Universitat Politècnica de València
Departamento de Máquinas y Motores Térmicos

Application of a flamelet-based combustion model to diesel-like reacting sprays

Doctoral Thesis
Presented by:
Eduardo Javier Pérez Sánchez
Directed by:
Prof. Francisco Payri González
and
Assoc. Prof. Ricardo Novella Rosa

Valencia, December 10, 2018

Doctoral Thesis

Application of a flamelet-based combustion model to diesel-like reacting sprays

Presented by: Eduardo Javier Pérez Sánchez
Directed by: Prof. Francisco Payri González
Assoc. Prof. Ricardo Novella Rosa

Examining Board:

President: Prof. Jesús Benajes Calvo
Secretary: Prof. Juan José Hernández Adrover
Examiner: Dr. Peter Priesching

Reviewing Board:

Assoc. Prof. Rosario Ballesteros Yáñez
Assoc. Prof. Blanca Giménez Olavarría
Dr. Peter Priesching

Valencia, December 10, 2018

Resumen

El objetivo de esta tesis es la investigación y análisis de la estructura interna de los chorros diésel reactivos y el efecto de las condiciones de contorno en los parámetros asociados a la combustión. Este objetivo se consigue por medio de la simulación numérica del chorro con modelos de turbulencia RANS y LES usando un modelo de combustión avanzado basado en el concepto *flamelet*.

Para este estudio, se aplica una aproximación simplificada de las *flamelets* de difusión, conocidas en la literatura como *Flamelets* de Difusión Aproximadas (ADF en inglés), como fundamento del modelo de combustión. En una primera etapa, el modelo se valida con combustibles de diferente complejidad química en regímenes estacionarios y transitorios para el conjunto de posibles velocidades de deformación. Una vez se confirma su idoneidad para condiciones encontradas en chorros diésel, se aplica a la simulación del chorro A del *Engine Combustion Network* (ECN), representativo de chorros diésel.

Para proporcionar un cuadro completo de los fenómenos subyacentes, la combustión se analiza inicialmente para condiciones homogéneas y llamas laminares para las distintas condiciones de contorno de este experimento. Después este análisis se complementa con la simulación de diferentes mecanismos químicos para determinar cómo las características del encendido predichas por el esquema de oxidación afectan a la propagación de llama. Los resultados obtenidos en esta etapa se enlazan con el análisis del chorro turbulento en el contexto de simulaciones RANS y LES para describir cómo el fenómeno de la combustión se modifica con los diferentes niveles de complejidad física. La estructura del chorro turbulento se describe profundamente para las distintas condiciones de contorno y mecanismos químicos en términos de mezcla y escalares reactivos para las fases temporales y las regiones espaciales de la llama.

La satisfactoria concordancia con los resultados experimentales muestran que el concepto *flamelet*, y más particularmente el modelo ADF, es adecuado para las simulaciones de chorros diésel.

Resum

L'objectiu d'esta tesi és la investigació i anàlisi de l'estructura interna dels dolls dièsel reactius i l'efecte de les condicions de contorn en els paràmetres associats a la combustió. Este objectiu s'aconsegueix per mitjà de la simulació numèrica del doll amb models de turbulència RANS i LES usant un model de combustió avançat basat en el concepte *flamelet*.

Per a este estudi, s'aplica una aproximació simplificada de les *flamelets* de difusió, conegudes a la literatura com *Flamelets* de Difusió Aproximades (ADF en anglés), com a fonament del model de combustió. En una primera etapa, el model es valida amb combustibles de diferent complexitat química en règims estacionaris i transitoris per al conjunt de possibles velocitats de deformació. Una vegada es confirma la seua idoneïtat per a condicions trobades en dolls dièsel, s'aplica a la simulació del doll A del *Engine Combustion Network* (ECN), representatiu de dolls dièsel.

Per a proporcionar un cuadre complet dels fenòmens subjacents, la combustió s'analitza inicialment per a condicions homogènies i flames laminars per a les distintes condicions de contorn d'aquest experiment. Després esta anàlisi es complementa amb la simulació de diferents mecanismes químics per a determinar com les característiques de l'encesa predites per l'esquema d'oxidació afecten la propagació de flama. Els resultats obtinguts en esta etapa s'enllacen amb l'anàlisi del doll turbulent en el context de simulacions RANS i LES per a descriure com el fenomen de la combustió es modifica amb els diferents nivells de complexitat física. L'estructura del doll turbulent es descriu profundament per a les distintes condicions de contorn i mecanismes químics en termes de mescla i escalars reactius per a les fases temporals i les regions espacials de la flama.

La satisfactòria concordança amb els resultats experimentals mostren que el concepte *flamelet*, i més particularment el model ADF, és adequat per a les simulacions de dolls dièsel.

Abstract

The objective of this thesis is the investigation and analysis of the internal structure of diesel-like reacting sprays and the effect of boundary conditions on combustion related parameters. This objective is achieved by means of the numerical simulation of the spray with RANS and LES turbulence models using an advanced combustion model based on the flamelet concept.

For this study, a simplified approach for diffusion flamelets, known in the literature as Approximated Diffusion Flamelet (ADF), is applied as the basis of the combustion model. In a first step, this model is validated for fuels with different chemical complexity in steady and transient regimes for the whole set of possible strain rates. Once its suitability is confirmed for conditions found in diesel sprays, it is applied to the simulation of spray A from the Engine Combustion Network (ECN), representative of diesel-like sprays.

In order to provide a complete picture of the underlying phenomena, combustion is initially analysed in homogeneous conditions and laminar flames for the different boundary conditions of this experiment. Later, this analysis is complemented with the simulation of different chemical mechanisms in order to determine how the ignition characteristics predicted by the oxidation scheme affect to the flame propagation. The results obtained at this stage are connected with the analysis of the turbulent spray in the context of RANS and LES simulations as a way to track how combustion phenomenon is modified at the different levels of physical complexity. The turbulent spray structure is thoroughly described for the different boundary conditions and chemical schemes in terms of mixing and reactive variables for both temporal phases and spatial flame regions.

The satisfactory agreement with experimental results shows that the flamelet concept, and more particularly the ADF model, is suitable for diesel-like sprays simulations.

Agradecimientos

Quiero expresar en estas líneas mi más sincero reconocimiento al Instituto Universitario de Investigación CMT - Motores Térmicos, y muy en particular a su director Dr. J. M. Desantes, por darme la oportunidad, primeramente, de cursar los estudios de doctorado y, posteriormente, de llevar a cabo la consiguiente labor de investigación que ha dado lugar a esta tesis. Merecen mi más profunda estima y agradecimiento el Dr. F. Payri y el Dr. R. Novella, directores de esta tesis, por su confianza y dirección y con los que me encuentro en deuda por todas las discusiones tan instructivas que hemos mantenido a lo largo de estos años mostrándome, en todo momento y circunstancia, su apoyo incondicional.

También quiero agradecer al Dr. J. M. García y al Dr. J. M. Pastor sus siempre valiosas y acertadas observaciones y al Dr. R. Payri su ánimo constante. Asimismo quiero hacer esta gratitud extensiva al resto de compañeros del Instituto con los que he compartido esta etapa. De entre ellos, especial mención quiero hacer de los doctores A. Hernández, A. Pandal y J. Winklinger con los que he tenido la oportunidad de intercambiar interesantes puntos de vista sobre muy diversas cuestiones.

Por último, quiero manifestar mi aprecio al Dr. B. Naud que me ha proporcionado tantos preciados consejos y al Dr. D. Mira con el que colaboré en el último período de esta tesis durante una estancia de investigación en el Barcelona Supercomputing Center que me resultó especialmente constructiva.

Esta tesis se ha desarrollado en el marco de una ayuda para la Formación de Profesorado Universitario (FPU 14/03278) perteneciente a los subprogramas de Formación y de Movilidad financiada por el Ministerio de Educación, Cultura y Deporte de España.

Table of Contents

Nomenclature

Latin

A	Depending on the context, constant of proportionality in Arrhenius law or instantaneous flame area
a	Flame strain rate
B	Beta function
B_0, B_1, C_τ, CBU	Constants from the DDM model used in this work
C_{EBU}	Constant of proportionality for the EBU combustion model
C_{ij}	(i, j) component of cross stress tensor
C_{sgs}, C'_{sgs}	Constant of proportionality defining the eddy viscosity in some LES models
$C_{\varepsilon 1}$, $C_{\varepsilon 2}$, $C_{\varepsilon 3}$	Constants appearing in ε equation in $k - \varepsilon$ model
C_μ	Turbulent viscosity constant in $k - \varepsilon$ model
C_χ	Constant of proportionality for the mean scalar dissipation rate model
c, c_F, d	Normalized progress variable
c_p	Mass heat capacity at constant pressure
c_2	Flamelet normalized progress variable
D_i	Mass diffusivity for species i
Da	Damköhler number
D/Dt	Total derivative
d_d	Droplet diameter
d_{eq}	Nozzle equivalent diameter
d_0	Diameter of the nozzle in a round jet
E	Energy spectrum function
E_a	Activation energy

F_i	External force in direction i
f	Probability density function (PDF) or filtered density function (FDF)
$\vec{f}_i$	Species mass flux for species i
$f_{\nu 1}$	Wall damping function in Spalart-Allmaras model
G	Depending on the context, LES filter function or non-reacting scalar used in the level set approach for premixed combustion
h	Specific total enthalpy
h_s	Specific sensible enthalpy
J	Ratio between the mean scalar dissipation rate and mean stoichiometric scalar dissipation rate
K	Total kinetic energy
Ka, Ka_δ	Karlovitz number
k	Turbulent kinetic energy
$k_{b,j}$	Backward specific reaction rate for reaction j
$k_{f,j}$	Forward specific reaction rate for reaction j
k_{sgs}, K_{sgs}	Subgrid scale turbulent kinetic energy
k_v	Constant defining the temporal variation of the square of the droplet diameter
L	Flow scale
L_f	Flame length
L_{ij}	(i,j) component of Leonard stress tensor
Le	Lewis number
ℓ	Characteristic eddy size
ℓ_D	For non-premixed flames, diffusion thickness
ℓ_F	Flame thickness
ℓ_δ	Reaction layer thickness
ℓ_0	Integral scale
M_i	Species M_i in the system
$[M_i]$	Molar concentration for species M_i
$\dot{m}$	Mass flow rate
$\dot{m}_{ev}$	Evaporation mass flow rate for a droplet immersed in a convective stream
$\dot{m}_{ev,0}$	Evaporation mass flow rate for a droplet in a quiescent environment
N_r	Total number of reactions in the chemical system
N_s	Total number of species in the system
$\vec{n}$	Normal vector to the flame surface

$n_{elem,k}$	Number of atoms of element *elem* in species k
$\wp$	Production of turbulent kinetic energy
$\wp_z$	Production of mixture fraction variance
$\wp_\phi$	Production for the variance of a general scalar variable
P	Probability density function
P_Z	Probability density function for mixture fraction
P_χ	Probability density function for scalar dissipation rate
Pr	Prandtl number
p	Pressure
p_{amb}	Ambient pressure
$\vec{q}$	Heat flux
$\dot{q}_j$	Rate of progress for reaction j
R	Universal perfect gas constant
R_{ij}	Velocity autocorrelation for velocity components i and j
Re	Reynolds number
RR	Characteristic reaction rate
r	Radial direction in the cylindrical coordinate system of a round jet
$\vec{r}$, $\vec{x}$	Position vector
$r_{1/2}$	Radius for each axial position of the round jet
$\vec{S}$	Surface vector
S	Depending on the context, spray vapour/tip penetration or segregation factor for mixture fraction variance
S_h	Source term for total enthalpy
S_k	Evaporative source term for species k
S_Z	Evaporative source term for fuel mixture fraction
S_ϕ	Source term for a general variable
Sc	Schmidt number
Sc_v	Schmidt number for mixture fraction variance
Sh	Sherwood number
$\|\bar{s}\|$	Characteristic filtered rate of strain
s_{ij}	(i,j) component of strain rate tensor
s_L	Laminar burning velocity
s_L^0	Laminar burning velocity for a plane flame
s_T	Turbulent burning velocity
T	Temperature

T_{amb}	Ambient temperature
T_{ij}^{sgs}	(i,j) component of subgrid scale stress tensor
$\widetilde{T}_{max}$	Maximum Favre-averaged temperature in the domain
t	Time
t_{ID}, t^*	Ignition delay
$U(\ell)$	Characteristic velocity of vortex of size ℓ
u	Axial velocity in the cylindrical coordinate system of a round jet
$\vec{u}$	Velocity vector
$\overline{u}_{ax}$	Mean axial velocity on the axis of a round jet
u_0	Mean axial velocity at the exit of the nozzle of a round jet
V	Volume
$\vec{V}_i$	Diffusion velocity vector for species i
v	Radial velocity in the cylindrical coordinate system of a round jet
W	Lambert function
W_i	Molecular weight for species i
w	Azimuthal velocity in the cylindrical coordinate system of a round jet
X_{O_2}	Oxygen molar fraction
x	Axial direction in the cylindrical coordinate system of a round jet
Y_c	Progress variable
$\dot{Y}_c$	$\partial Y_c/\partial t$
Y_i	Mass fraction for species i
$\widetilde{Y}_i^{max}$	Maximum Favre-averaged mass fraction for species i in the domain
Z	Fuel mixture fraction
$\widetilde{Z}$	Mean fuel mixture fraction
$\widetilde{Z''^2}$	Fuel mixture fraction variance
Z_{MR}	Most reactive fuel mixture fraction
Z_{O_2}	Oxygen mixture fraction
Z_{rms}	Fuel mixture fraction root mean square
Z_s	Saturation fuel mixture fraction
$\widetilde{Z''^2_{sgs}}$	Subgrid fuel mixture fraction variance
Z''_{st}	Characteristic fuel mixture variance at for the stoichiometric mixture

Greek

α	Depending on the context, thermal conductivity or exponent that defines the chemical source terms limitation for ADF model
β	Exponent for temperature in Arrhenius law

Γ	Depending on the context, diffusivity coefficient for a general variable or gamma function
γ	Half-angle of the round jet
Δ, $\widehat{\Delta}$	Filter width
$\Delta h_{f,i}$	Specific formation enthalpy for species i
Δt	Time step
$(\Delta Z)_F$	For non-premixed flames, flame thickness in mixture fraction space
$(\Delta Z)_R$	For non-premixed flames, reaction layer thickness in mixture fraction space
ε	Rate of dissipation of turbulent kinetic energy
ε_ϕ	Rate of dissipation of a general scalar variable
η	Kolmogorov length scale
θ	Azimuthal direction in the cylindrical coordinate system of a round jet
ϑ	Integral velocity
κ	Wavenumber
λ	Thermal diffusivity
μ	Depending on the context, dynamic viscosity or parameter related to the mean of the scalar dissipation rate for the log-normal function
ν	Kinematic viscosity
$\widetilde{\nu}$	Kinematic viscosity parameter in Spalart-Allmaras model
$\nu_{i,j}$	$\nu''_{i,j} - \nu'_{i,j}$
$\nu'_{i,j}$, $\nu''_{i,j}$	Stoichiometric molar coefficients for species i in reaction j
ρ	Mass density
ρ_a	Air mass density
ρ_f	Fuel mass density
ρ_{ij}	Autocorrelation coefficient for velocity components i and j
Σ	Flame surface density
σ	Parameter related to the variance of the scalar dissipation rate for the log-normal function
σ_{ij}	(i, j) component of the stress tensor
σ_k	Ratio between turbulent viscosities for velocity and turbulent kinetic energy
σ_ε	Ratio between turbulent viscosities for velocity and dissipation of turbulent kinetic energy
τ_{chem}	Characteristic chemical time

τ_{ij}	(i,j) component of the shear stress tensor
τ_{ij}^{R}	(i,j) component of the Reynolds stress tensor
τ_{ij}^{sgs}	(i,j) component of the subgrid scale stress tensor
τ_{physic}	Characteristic physical time
$\tau(T,p)$	Ignition delay for fixed (T,p) conditions
Φ	Dissipation function
Φ_{ij}	(i,j) component of velocity spectrum tensor
ϕ	Depending on the context, it denotes a general scalar variable or equivalence ratio
ϕ_{norm}, $\phi_{norm,2}$	In the round jet normalized variable of ϕ
χ	Scalar dissipation rate
Ψ, ψ	It denotes any reactive scalar
ω	Turbulence frequency
$\vec{\omega}$	Vorticity
$\dot{\omega}_c$	Chemical source term for normalized progress variable c
$\dot{\omega}_i$	Mass chemical source term for species i
$\dot{\omega}_T$	Chemical source term for temperature
$\dot{\omega}_{Y_c}$	Chemical source term for progress variable

Superscripts

d	Deviatoric component of a tensor
$equil$	Referred to equilibrium conditions
HR	Related to homogeneous reactor
$inert$	Referred to inert conditions
sgs	Subgrid scale
$steady$	Referred to steady conditions

Subscripts

b	Related to burned gas
DI	Limit between the inertial subrange and the dissipation range
EI	Limit between the energy-containing range and the inertial subrange
eff	Related to an effective parameter (composed of laminar and turbulent contributions)
$elem$	Referred to element $elem$

eq	Referred to equilibrium conditions
i	In the context, of non-premixed combustion, Da, χ or a at the limit between the auto-ignition and reignition-extinction ranges
$inert$	Referred to inert conditions
P	Referred to combustion products
q	In the context, of non-premixed combustion, maximum Da, χ or a in the reignition-extinction range
sgs	Subgrid scale
st	Referred to the value at the stoichiometric mixture
T	Related to a turbulent parameter
u	Related to unburned gas

Symbols, operators and functions

δ	Dirac function
δ_{ij}	Kronecker symbol
∇	Hamilton's nabla operator
$\bar{}$, $\widehat{}$	Reynolds average or filtering
$\tilde{}$	Mass weighted Favre average or filtering
$'$	Fluctuating component for Reynolds average or filtering
$''$	Fluctuating component for mass weighted Favre average or filtering
$\langle\rangle$	Average in LES simulations

Initials and acronyms

ADF	Approximated diffusion flamelet model
BML	Bray-Moss-Libby model
CFD	Computational fluid dynamics
CFM	Coherent flamelet model
CMC	Conditional moment closure
CPF	Constant-pressure flow rigs
CSEM	Conserved scalar equilibrium model
CVP	Constant-volume pre-burn combustion vessel
DASSL	Differential/algebraic system solver
DDM	Discrete droplet method
DF	Diffusion flamelet model
DI	Direct injection system

DNS	Direct numerical simulation
DS	Dynamic structure model
EBU	Eddy break-up model
ECN	Engine Combustion Network
EDC	Eddy dissipation concept
EGR	Exhaust gas recirculation
FDF	Filtered density function
FGM	Flamelet generated manifold
FPDF	Filtered probability density function
FPI	Flame prolongation of ILDM
HCCI	Homogeneous charge compression ignition
HP-LTC	Highly premixed low temperature combustion
ID	Ignition delay
IDI	Indirect injection system
ILDM	Intrinsic low dimensional manifold
ISAT	*In situ* adaptive tabulation
LEM	Linear eddy model
LES	Large eddy simulation
LIF	Laser induced fluorescence
LOL	Lift-off length
LTC	Low temperature combustion
MC-LTC	Mixing controlled low temperature combustion
NTC	Negative temperature coefficient
ODE	Ordinary differential equation
PAHs	Polycyclic aromatic hydrocarbons
PDE	Partial differential equation
PDF	Probability density function
PISO	Pressure implicit with splitting of operators
PIV	Particle image velocimetry
PM	Particle matter
PPCI	Partially premixed compression ignition
PV	Progress variable
RANS	Reynolds averaged Navier-Stokes
RIF	Representative interactive flamelet model

rms	Root mean square
RNG	Renormalization group
RSM	Reynolds stress equation model
SC	Surface control
SCR	Selective catalytic reduction
SFM	Steady flamelet model
sgs	Subgrid scale
SOC	Start of combustion
SOI	Start of injection
TCI	Turbulence-chemistry interaction
TDC	Top dead center
UFPV	Unsteady flamelet progress variable model
UHC	Unburned hydrocarbons
URANS	Unsteady Reynolds averaged Navier-Stokes
USFM	Unsteady flamelet model
VC	Volume control

Chapter 1

Introduction

Contents

1.1 Motivation of the study and background

The critical role that combustion plays in mankind development is evidenced when considering how extended is in so varied purposes such as electric power generation, propulsion systems, furnaces and other industrial applications. Turbomachinery and internal reciprocating engines cover almost all the spectrum of industrial devices designed to transform the chemical energy contained in fuel molecules bounds into mechanical energy.

The limitations of turbomachinery for applications where variable regimes and loads are required, apart from other aspects, relegates them from these applications and leaves the internal reciprocating engines as the only possibility for these practical purposes. The Diesel engine is clearly the most competitive option for devices where very high power is demanded due to its low specific consumption and, therefore, its high efficiency as well as its high specific power.

Since its creation at the end of the nineteenth century by the engineer Rudolf Diesel [1] it has expanded from industrial machinery to the automotive

sector during the 80s of the past century, with indirect injection systems (IDI), and the 90s, with a remarkable successful market penetration with the direct injection technology (DI).

However, despite DI diesel engines unquestionable potentiality, they are not exempt of issues related to pollutant emissions that engineers have been facing during the last 30 years due to the social ever-increasing concerning. The most important pollutants in diesel engines are nitrogen oxides, NO_x, produced when reaching high temperatures in zones rich in oxygen, and particles or soot, formed in an ambient where oxygen lacks and temperatures are limited to intermediate values. Monoxide carbon, CO, and unburned hydrocarbons, UHC, are generated in negligible amounts in typical working conditions.

Regulations have become more stringent and since the first of them in the 80s, pollutant emissions have been reduced two orders of magnitude. Clearly this is is a very remarkable reduction but unfortunately it is not enough. Figure 1.1 shows the evolution of the maxima admissible pollutant emission values of NO_x and particle matter (PM) for Euro regulations for passenger cars and heavy-duty diesel engines [2]. The difficulty to fulfil this regulation is even greater when considering that for lots of strategies the reduction of NO_x increases soot formation and vice versa, that is, there exists a trade-off between them.

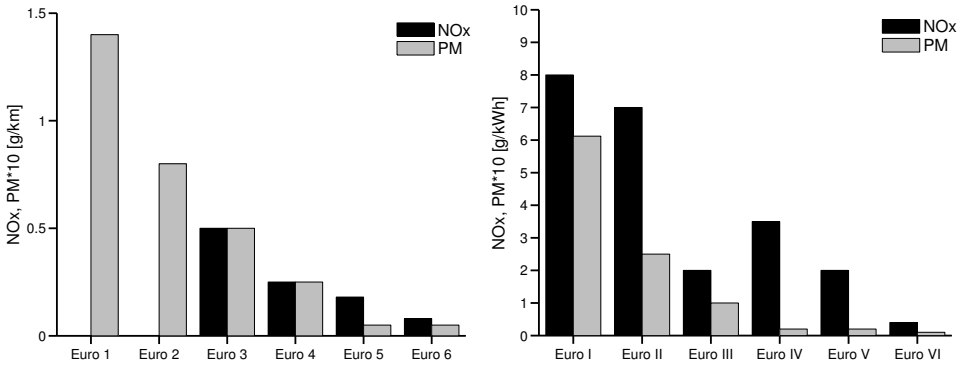

Figure 1.1. *Maxima admissible values of* NO_x *and PM for Euro regulations for passenger cars (left) and heavy-duty diesel engines (right).*

It is evidenced how the continuous search of engines that fulfil the regulations with high efficiencies minimizing the penalty in consumption requires a great effort in research. This research in experimental and numerical

fields is expected to contribute to an understanding that will improve the current technology or even lead to envisage new revolutionary concepts.

In the last years, there has been a remarkable improvement of the injection systems and they have been combined with air management aspects as well as other strategies in order to reduce drastically the pollutant formation and emissions. Other parallel lines have focused on developing new combustion concepts that face the same problem from a different point of view.

Regarding the improvements in conventional diesel combustion, it is worth mentioning that the injection systems have been refined. The common-rail technology, which allows reaching injection pressures of the order of 1500 bar, that lead to a very fast spray atomization and evaporation, together with the control of the injection rate, used to delay or split injection in several events, are the most important achievements in the injection system related to the improvement of spray mixing and soot formation reduction.

In addition, it is quite extended the use of Exhaust Gas Recirculation (EGR) to decrease flame temperature due to dilution of air with burnt gases avoiding the generation of NO_x as well as the application of supercharging in order to increase the specific engine power.

These strategies and technologies are used in conjunction with exhaust gas after-treatment systems that catalyse reactions, like the Selective Catalytic Reduction (SCR) to reduce NO_x, and the particle filter that accumulates soot until it is oxidised when the particle filter regeneration takes place. However, all these after-treatment systems have some drawbacks that have prevented from being imposed as the definitive solution, apart from the increase in pump power that they produce and the consequent efficiency loss.

In parallel to these technologies other lines have appeared in the last decades that intend to eliminate pollutant emissions formation by a drastic modification of the combustion concept and open new paths in the research field. They are known as Low Temperature Combustion (LTC) [3] and two main types can be distinguished. They are all characterized by reducing the flame temperature, avoiding NO_x formation, and homogenizing the mixture where reaction occurs intending to avoid rich mixture regions and preventing, in this way, soot formation.

The first one is Mixing Controlled Low Temperature Combustion (MC-LTC) where injection and combustion are superimposed in time. Fuel is injected close to the top dead center (TDC) and high injection pressures are

used in order to improve mixing and increase the lift-off length (LOL)[1] that entails a reduction of soot formation. In addition, high EGR rates are used in order to drastically reduce NO_x formation.

However, the extreme temperature reduction may lead to some operating problems because chemistry might be slowed down, since it shows an exponential relationship with temperature, preventing the total conversion from CO to CO_2. This affects directly to the engine efficiency as well as CO emissions while, although soot formation is decreased, its reduction may not be enough.

The other type is the Highly Premixed Low Temperature Combustion (HP-LTC) for which a strong mixing takes place for air and fuel before the start of combustion (SOC) due to a premature injection during admission or start of compression strokes avoiding local rich mixture regions.

Two main ways are found in the literature in order to apply this concept. On the one hand, in the Homogeneous Charge Compression Ignition (HCCI) [4] a very premature injection leads to highly homogenized mixture. Ignition delay is controlled by chemical kinetics and is decoupled from injection. An excess of air leads to low flame temperatures and prevents from NO_x and soot formation. However, there exist control problems related to CO and UHC formation and knocking, limiting the work conditions to low and medium loads.

On the other hand, the Partially Premixed Compression Ignition (PPCI) [5] is in-between HCCI and conventional diesel combustion. The mixing times are more moderate leading to a not completely homogeneous mixture although fuel injection during compression stroke avoids to superimpose injection and combustion events. It requires high injection pressures as well as massive EGR rates. Knocking may occur if load is not limited to moderate values.

In order to prevent this, the previous concept combined with less reactive fuels may lead to high efficiency and low NO_x and soot formation. This reduction of reactivity is accomplished blending fuels with different octane number, like diesel and gasoline, and gives rise to concepts like dual-fuel [6].

Previous concepts are quite promising but although some of them are found in a very advanced stage, they have not reached probably a complete matureness degree and some issues still remain unsolved[2]. It stems from this

[1] Modern diesel flames are detached or lifted from the nozzle and the distance from the nozzle to the base of the flame, that is the lift-off length, is one of the most important characteristics of the flame. This concept is further explained in chapter 2.

[2] Apart from the fact that drastic technological changes require usually some time to expand and be adopted.

that conventional diesel engines are going to remain as a solution for a large spectrum of applications for the incoming years. Even if this spectrum is narrowed in the automotive sector, heavy duty diesel engines, like those found in trucks, will still presumably cover the market for high power applications.

Due to all the reasons above exposed it arises that research is required in the field of DI diesel combustion. This can be done by experiments and/or numerical simulations. The very high computational power achieved during the last years has prompted numerical investigation to a place that could not be envisaged some decades ago. More particularly, Computational Fluid Dynamics (CFD) is a fruitful research field that has lead to an advancement in the understanding of the fluid mechanics field and its application in the design of aerofoils, burners, engines, turbomachinary, etc. is quite extended.

Although numerical simulations are subjected to numerical uncertainties due to domain and equations discretization, resolution of the system equations together with the physical models, that intend to describe the large range of scales and flow and chemical interactions in the context of turbulent combustion, it is unquestionable that they provide an extremely valuable information. Fields for all the solved variables at every point and instant are obtained and lead to 'see' and understand phenomena for which is almost impossible to obtain information by any other way with a very reduced cost compared to laboratory experiments. Notwithstanding, it is important to emphasize that despite all these positive features one should not fall in the mistake of believing simulation results without a critical spirit.

All this shows that, nowadays, experiments and numerical simulations have become an inseparable binomial in the research field. And this spirit is reflected in the Engine Combustion Network (ECN) [7] which combines the most advanced experimental techniques with numerical simulations in order to deepen in the DI diesel combustion understanding. In the frame of the ECN several research institutions contribute and share information in order to enrich the state of the art. In addition, experiments are carried out in special vessels with optical accesses. The particular configuration of the experiments leads to discard uncertainties that would be found in a real engine. Therefore, it is intended to minimize the interaction with other phenomena that would only darken the analysis in order to understand the own intrinsic nature of the combustion process. Some experimental information used along this work is found in the context of the ECN [7].

The aim of this work is to contribute to the current knowledge of DI diesel combustion in these special ECN configurations by means of numerical simulations as is further developed in next section.

1.2 Objectives

Previous section gave a sketch of the state of the art and the current research lines in diesel combustion. This thesis is developed in the context of conventional diesel combustion and its main objective is to numerically investigate and model in RANS and LES[3] turbulence frameworks a diesel-like spray by means of an advanced combustion model, assessing the boundary condition effects as well as other critical modelling aspects.

The adopted combustion model in this work is based on the flamelet concept which has been demonstrated to be extremely suitable for diesel combustion [8–11]. However, an accurate description of the local conditions of the turbulent flame together with the use of complex mechanisms required for diesel sprays simulations may soar the computational cost when considering wide ranges of boundary conditions. To give response to this issue a simplified model, known as Approximated Diffusion Flamelet (ADF) [12], was suggested some years ago and used along this investigation. Nevertheless, its validation was not completely accomplished and, in consequence, its application to further calculations requires to be assessed.

Therefore, the main objective of this thesis can be decomposed in several steps required to reach the end of this work:

1. The ADF is first validated in order to sustain further calculations. To encompass a great variety of configurations it is assessed for fuels of different chemical complexity in steady as well as transient regimes.

2. The model is applied to the ECN spray A which is representative of modern diesel-like sprays in the frame of RANS turbulence models. The analysis is composed of three objectives:

   (a) To investigate how the flame structure is modified when adding new physical content to the auto-ignition process. For this purpose, homogeneous reactors ignition are first described, followed by the study of diffusion laminar flames where diffusion and convection compete with chemistry. Finally, the turbulent flame is described.

   In the case of the ADF, its flame modelling invites to carry out this analysis that arises as a natural step of its workflow, as will be described in chapter 3.

[3] RANS stands for Reynolds Averaged Navier-Stokes while LES for Large Eddy Simulation.

(b) The effect of the boundary conditions is fundamental in order to understand the reactive spray characteristics. This is accomplished analysing different temperature and oxygen parametric variations. In the light of this analysis the internal spatial structure as well as the spray auto-ignition are described.

(c) In order to shed light on the effect of the chemical mechanism on the flame structure several well-known oxidation schemes are modelled at all the stages of combustion (homogeneous reactors, flamelets and turbulent spray) to determine their similarities and differences and how their solutions are modified when adding new physical phenomena.

3. Spray A is modelled in the frame of LES turbulence models. Despite the LES remarkable higher cost compared to RANS, it provides some valuable information related to flow fluctuations impossible to obtain in the RANS context.

It is thought that an analysis from so different points of view contrasts the results providing a picture of the spray that complements and improves the state of the art.

1.3 Document structure

Once the objectives have been posed the document structure and the content of the following chapters can be described.

A bibliographical review is given in chapter 2. Due to the theoretical character of the work but at the same its practical application a balance between the underlying physical theories and the most prominent results for sprays at typical diesel work conditions has been searched. Special emphasis has been placed on the physical content of the theories and models to the detriment of a highly mathematical description. In order to accomplish this, the chapter first describes the main results of turbulence theory and turbulence models after a brief description of fluid mechanics equations. It follows with the explanation of combustion theory, starting from the chemical kinetics and auto-ignition theory and the subsequent insight into laminar and turbulent combustion theories for premixed, non-premixed and partially premixed combustion. This gives rise to a description of the combustion models available in the literature. Finally, and with all this background,

the chapter is closed with a description of the general spray theory and the characteristics of the reactive diesel spray.

Chapter 3 gives a more specific vision of the models based on the flamelet concept and describes in detail the combustion model applied in this work. After this, a detailed validation of the ADF model, which is used along this work, is given by its comparison with the complete laminar flame solution for different fuels and steady and transient regimes.

After this validation, chapters 4 and 5 explain the main results obtained in this thesis for diesel-like sprays by the application of the ADF model to spray A by means of RANS and LES turbulence models, respectively. Not only the impact of reactivity on the flame structure by changing the boundary conditions is analysed, but combustion structure at configurations with different physical content (homogeneous reactors, flamelets and turbulent spray) as well as the influence of the chemical mechanism are the goal of this investigation. This last analysis is limited to the RANS description due to the high computational cost involved in LES simulations.

Finally, chapter 6 gathers the main conclusions obtained along the work as well as some recommended future works in order to increase the knowledge beyond the scope of the present thesis.

References

[1] Diesel R. "Internal combustion engine". *U.S. Patent 608845*, 1898.

[2] *https://www.dieselnet.com/*, 2018.

[3] Agarwal A. K., Singh A. P. and Maurya R. K. "Evolution, challenges and path forward for low temperature combustion engines". *Progress in Energy and Combustion Science*, Vol. 61, pp. 1–56, 2017.

[4] Ryan T. W. and Callahan T. J. "Homogeneous charge compression ignition of diesel fuel". *SAE Technical Paper*, 1996.

[5] Okude K., Mori K., Shiino S. and Moriya T. "Premixed compression ignition (PCI) combustion for simultaneous reduction of NOx and soot in diesel engine". *SAE Technical Paper*, 2004.

[6] Olsson J. O., Tunestål P. and Johansson B. "Closed-loop control of an HCCI engine". *SAE Technical Paper*, 2001.

[7] Pickett L. M., Bruneaux G. and Payri R. "Engine combustion network". *Sandia National Laboratories, Livermore, CA, https://ecn.sandia.gov/*, 2018.

[8] Barths H., Hasse C., Bikas G. and Peters N. "Simulation of combustion in direct injection diesel engines using a eulerian particle flamelet model". *Proceedings of the Combustion Institute*, Vol. 28 n^o 1, pp. 1161–1168, 2000.

[9] Dhuchakallaya I., Rattanadecho P. and Watkins P. "Auto-ignition and combustion of diesel spray using unsteady laminar flamelet model". *Applied Thermal Engineering*, Vol. 52 n^o 2, pp. 420–427, 2013.

[10] Tillou J., Michel J. B., Angelberger C., Bekdemir C. and Veynante D. "Large-Eddy Simulation of Diesel Spray Combustion with Exhaust Gas Recirculation". *Oil & Gas Science and Technology-Revue de l'IFP*, Vol. 69 n^o 1, pp. 155–165, 2014.

[11] Kahila H., Wehrfritz A., Kaario O., Masouleh M. G., Maes N., Somers B. and Vuorinen V. "Large-eddy simulation on the influence of injection pressure in reacting spray A". *Combustion and Flame*, Vol. 191, pp. 142–159, 2018.

[12] Michel J. B., Colin O. and Veynante D. "Modeling ignition and chemical structure of partially premixed turbulent flames using tabulated chemistry". *Combustion and Flame*, Vol. 152 n^o 1, pp. 80–99, 2008.

Chapter 2

Bibliographical review

Contents

2.1 Introduction

Turbulent combustion is one of the most complex phenomena of fluid mechanics that may be found due to the different physical and chemical processes that appear and interact. Its extended use in industry as a way to obtain work has prompted the need of the theoretical study of the underlying processes appearing in industrial devices in order to optimize their design and increase their efficiency while diminishing pollutant emissions.

A simple analysis of the reactive flow that may be found in industrial combustion systems reveals the complexity of this scientific field:

1. The fuel may be found in solid (coal), liquid (gasoline and gas-oil) or gas (natural gas) phase. As the reactions take place at molecular level the first step is to pulverize or evaporate the fuel in order to be able to obtain a fuel-air mixture. To do so, high velocities are induced with the aim to gasify or vaporize the fuel in the minimum space.

2. A mixing process between fuel and air is required to burn fuel since chemistry is only able to occur when there exists a mixing at molecular level.

3. High velocities may be induced in order to create a turbulent flow that generates high gradients enhancing and accelerating air and fuel mixing. Turbulence is a complex phenomenon not completely understood even for incompressible flows. Although there exists a vast theory, the difficulties of facing a chaotic phenomenon have not been completely overcome and extending results to a general flow is a matter not covered yet.

4. Fuel chemical oxidation is other of the critical difficulties of combustion description. The high number of species produced and consumed, of the order of several hundreds, due to thousands of reactions gives a measure of its complexity and makes almost an impossible task including all the chemical steps in numerical simulations. Fortunately, not all the species

are fundamental in determining fuel oxidation and minor species and radicals may be omitted or considered in an equilibrium state with not appreciable losses in the calculations.

When dealing with pollutants like soot, the difficulties are still more evident since its formation and growth is described by both chemical and physical processes.

5. Heat losses to walls, including radiative effects, are important since they may decrease flame temperature or even quench the flame. Radiation may be especially critical when predicting pollutants such as NO_x (nitrogen oxides) which show a sensitive dependence with high temperatures.

6. In real devices impingement of the spray with the wall may be found. This may induce critical heat losses and modify the spray structure creating new vortexes that generate products recirculation.

This enumeration reveals the difficulty of constructing a complete combustion theory that has the ability to describe the whole process with a high level of physical content. Clearly this is a complex task, however, the application of the theories formulated for the different phenomena, and having in mind that they were constructed under restrictive hypotheses, may lead to an approximated description. Notwithstanding, and as a consequence of the several hypotheses introduced, results are expected to show some divergences.

A fundamental aspect that should be always born in mind when understanding the different approaches or models proposed is that their formulation intends to describe the physics with the more realistic vision while reducing the computational cost. Probably, the most illustrative case for this is the turbulence problem. At first glance it may seem paradoxical the need of using models to describe a problem whose exact equations are completely known. Nevertheless, its chaotic nature, although deterministic[1], forces to adopt some kind of simplified approach where the flow is not solved at all the scales.

These simplifications lead to a loss of the physics that has to be included in some way since there exists an 'exchange of information' between the solved and the unresolved parts. How the the unresolved part interacts with the

[1]It is deterministic because physical laws are deterministic, however, it is chaotic because small perturbations in the initial and/or boundary conditions may produce large changes in the flow. Hence, it is almost impossible to predict the flow state after an amount of time from the initial and boundary conditions because of measuring precision, uncertainties, etc.

solved variables is what the turbulence model intends to describe assuming some hypotheses.

The success of the model to predict the flow state depends on the physics retained by the model and tends to occur when the level of abstraction is high. From a practical point of view this has to be accompanied by a low computational cost since in other case the benefits are not compensated by the resources penalties.

In addition, except for simplified cases, no analytical expressions can be developed forcing to apply numerical simulations for the resolution of the problems. Numerical methods constitute a scientific field itself and which methods and how they are applied are one of the cornerstones to obtain successful calculations.

Consequently, improving the ability and performance of the models should be understood as an asymptotic development that may lead to more refined results when formulating more general models and when increasing the computational power in order to include more phenomena with a more reliable description.

The reacting diesel spray is an example where all the aforementioned facts concur and, hence, its modelling is challenging and complex. A fuel in liquid phase is injected a very high velocities of the order of 500 m/s and Reynolds numbers of the order of 40000. The liquid vein has to atomize and break-up into droplets that evaporate at states that transitionally may reach supercritical conditions [1, 2]. Then, an intense mixing between fuel and air occurs in a turbulent flow where high swirl is typically induced and, subsequently, mixture auto-ignites. After a time a developed flame is established. Soot is produced in the inner region of the spray while nitrogen oxides are found on the border of the flame. In addition, it is highly probable that spray impinges with the cylinder provoking high heat losses together with local quenching of the flame.

This work is devoted to analyse numerically the auto-ignition process and internal structure of a reacting spray at diesel-like conditions in the frame of different turbulence approaches with an advanced combustion model. To achieve this goal it is mandatory to expose the different physical and chemical aspects that may influence in the study of such problem. This is carried out along this chapter which only intends to condensate the fundamentals of such rich theories like turbulence and combustion theories. First, the physical grounds of the theory are described adding in each section new physical aspects. Subsequently, the most extended models available in literature are exposed. The interested reader may find in classical and indispensable

books the grounds to understand fluid mechanics, turbulence and combustion theories [3–10]. Finally, all this information is used as the basis to describe and sustain the most relevant results for diesel sprays.

2.2 Fluid mechanics equations

Before starting to explain more advanced features of fluid mechanics it is unavoidable to expose briefly the fluid mechanics instantaneous equations. They are simply obtained by applying the physical conservation laws, namely, mass conservation, Newton and thermodynamic laws, to a differential mass or volume which is called volume control (VC). The border of the volume control is the surface control (SC).

The direct application of the equations to the control volume leads to a Lagrangian formulation where particles are tracked along their trajectories. However, it is very extended and useful to obtain the equations on fixed positions which may lead to an Eulerian formulation. The chain rule is the basic tool that relates derivatives between both formulations. Equations in differential or integral form may be obtained.

The concept of total derivative D/Dt is introduced, which determines the total change per unit time that a variable ϕ [2] suffers for a VC. It is defined as

$$\frac{D\phi}{Dt} = \frac{\partial \phi}{\partial t} + \vec{u} \cdot \nabla \phi \tag{2.1}$$

The first term on the right hand side (r.h.s.) of equation 2.1 is the temporal derivative while the second expresses the inner product of velocity $\vec{u}$ and the gradient (denoted by operator ∇) and is the convective derivative. From its definition it is seen that D/Dt is a linear operator. Changes in the value of ϕ are due to some external agents related by a physical law.

Multiplying equation 2.1 by density ρ and integrating, the total variation of the volume control is obtained yielding to[3]

$$\int_{VC} \rho \frac{D\phi}{Dt}\, dV = \frac{\partial}{\partial t} \int_{VC} \rho\, \phi\, dV + \int_{SC} \rho\, \phi\, \vec{u} \cdot d\vec{S} \tag{2.2}$$

where the first integral is extended to the volume control while the second to the surface control. Therefore, the left hand side (l.h.s.) is composed of the

[2] ϕ measures a variable per unit mass.

[3] ρ and $\vec{u}$ may be included inside the derivatives from equation 2.1 by virtue of the continuity equation that is given in the following.

temporal change in the volume control and the fluxes that go in and out of the volume control through the surface control[4].

Apart from the convective transport (determined by $\vec{u}$) the other fundamental transport phenomenon is diffusion. Diffusion tends to reduce the spatial inhomogeneities and generates fluxes proportional to the gradients. For the momentum, in the case of Newtonian fluids, it is created by the strain rate and produces a shear between the different layers of the fluid motion. Defining the components of the strain rate tensor $[s]$ as

$$s_{ij} = \frac{1}{2}\left(\frac{\partial u_i}{\partial x_j} + \frac{\partial u_j}{\partial x_i}\right) \tag{2.3}$$

the stress tensor $[\sigma]$ is given by

$$\sigma_{ij} = -p\,\delta_{ij} + 2\mu\left(s_{ij} - \frac{1}{3}\nabla\cdot\vec{u}\;\delta_{ij}\right) \tag{2.4}$$

where p is the pressure, δ_{ij} is the Kronecker symbol and μ is the dynamic viscosity. It is useful to define the kinematic viscosity, ν, given by $\nu = \mu/\rho$ with units of length^2/time. Diffusion for momentum is, hence, the second term of the r.h.s. of equation 2.4 which is denoted as the shear stress tensor $[\tau]$.

For energy, diffusion flux is given by Fourier's law and is provoked by temperature gradients. With α the thermal conductivity, Fourier's law takes the form

$$\vec{q} = -\alpha\,\nabla T \tag{2.5}$$

where $\vec{q}$ is the heat flux and T is temperature. In the same way that the kinematic viscosity was given, a thermal diffusivity may be defined as $\lambda = \alpha/(\rho\,c_p)$ where c_p is the mass heat capacity at constant pressure. Again λ has units of length^2/time.

Finally, for the species diffusion, gradients in concentrations produce additional velocities (different for each species) that are superimposed to the mean flow. The total velocity for species i is then written as $\vec{u} + \vec{V_i}$ where $\vec{V_i}$ is the diffusion velocity for species i, that is, the additional velocity caused by

[4]Equation 2.2 may be directly obtained by a balance of variable ϕ in the volume control or starting from equation 2.1 and using Gauss divergence theorem.

species gradients. As $\vec{u}$ is the mean velocity of the whole set of species it has to be fulfilled by definition the condition

$$\sum_{i}^{N_s} Y_i \, \vec{V}_i = 0 \tag{2.6}$$

where N_s is the total number of species and Y_i is the mass fraction for species i. The exact equation for diffusion velocities may be found from solving a linear system of equations at each point and instant [8, 11] that may lead to a high computational cost. In order to reduce its cost, Hirchsfelder and Curtis approximation is used [12]. In other cases, Fick's law is adopted although it is only valid for binary mixtures. Although these two last approximations are extremely useful one has to bear in mind that they do not necessarily conserve mass. According to Fick's law, species mass flux $\vec{f}_i$ would be given by

$$\vec{f}_i = \rho \, Y_i \, \vec{V}_i = -\rho \, D_i \, \nabla Y_i \qquad i = 1, \ldots, N_s \tag{2.7}$$

where D_i is the mass coefficient for species i and has units of length^2/time.

When applying the diffusion transport to a control volume there are fluxes that enter while other exit from the volume control leading to a net flux given by the divergence of the flux. Thus, assuming previous laws, the diffusion term is the divergence of a gradient. In the case that the diffusivity (μ, α or ρD) is constant the term becomes a Laplacian.

In addition, volumetric or surface sources[5] may appear e.g. gravitational force or chemical heat release and species mass production/consumption due to chemical reactions.

The whole transport phenomena leads to write a general equation for any specific variable ϕ with the following terms

$$\rho \, \frac{D\phi}{Dt} = \rho \, \frac{\partial \phi}{\partial t} + \rho \, \vec{u} \cdot \nabla \phi = \nabla(\rho \, \Gamma \, \nabla \phi) + S_\phi \tag{2.8}$$

where Γ is the diffusivity coefficient. The terms from the l.h.s. are the temporal derivative and the convective transport. The first term from the r.h.s. is the diffusion and the last term of the equation corresponds to the source term.

[5] In general, we will not distinguish between positive (source) and negative (sink) contributions and will denote all of them with the word source.

With these elements it is possible to write transport conservations equations for mass, species, momentum and energy. With regards to energy, different quantities may be considered depending on the problem that is addressed. Three basic variables account for the energetic content of a fluid particle: sensible, chemical and kinetic energies. The first two types of energy may be expressed in terms of internal energy or enthalpy. In the following lines only enthalpy is used due to its suitability for open systems. The sensible enthalpy accounts for changes in temperature T and phase changes. If there is no phase change the specific sensible enthalpy h_s takes the form

$$\Delta h_s = \int_{T_0}^{T} c_p \, dT \tag{2.9}$$

where T_0 is a reference temperature. The chemical enthalpy for species i is the formation enthalpy $\Delta h_{f,i}$ which is the energy required to form a mass unity of species i from its elements at a given temperature. If this temperature is the standard temperature the formation enthalpy is denoted by $\Delta h^o_{f,i}$. Finally, the kinetic energy is defined as $K = \frac{1}{2}\vec{u}\cdot\vec{u} = \frac{1}{2}u_i\,u_i$.

Equations for the different combinations of energies may be easily obtained and are explained in detail in [8]. In the following, only equations for the kinetic energy and the total enthalpy h, that accounts for the sum of the three energies, are given.

The instantaneous equations for continuity (2.10), species (2.11), momentum (2.12), total enthalpy (2.13) and kinetic energy (2.14) are the following:

$$\frac{\partial \rho}{\partial t} + \frac{\partial (\rho\, u_i)}{\partial x_i} = 0 \tag{2.10}$$

$$\frac{\partial (\rho\, Y_j)}{\partial t} + \frac{\partial (\rho\, Y_j\, u_i)}{\partial x_i} = -\frac{\partial (\rho\, Y_j\, V_{ij})}{\partial x_i} + \rho\, \dot{\omega}_j \qquad j = 1, \ldots, N_s \tag{2.11}$$

$$\frac{\partial (\rho\, u_j)}{\partial t} + \frac{\partial (\rho\, u_j\, u_i)}{\partial x_i} = -\frac{\partial p}{\partial x_j} + \frac{\partial \tau_{ij}}{\partial x_i} + F_j \qquad j = 1, 2, 3 \tag{2.12}$$

$$\frac{\partial (\rho\, h)}{\partial t} + \frac{\partial (\rho\, h\, u_i)}{\partial x_i} = \frac{\partial p}{\partial t} - \frac{\partial q_i}{\partial x_i} + \frac{\partial (\tau_{ij}\, u_j)}{\partial x_i} + \rho \sum_{j=1}^{N_s} (Y_j\, F_{ij}\, u_i + Y_j\, F_{ij}\, V_{ij}) + S_h \tag{2.13}$$

$$\frac{\partial(\rho K)}{\partial t} + \frac{\partial(\rho K u_i)}{\partial x_i} = u_j \frac{\partial \sigma_{ij}}{\partial x_i} + \rho \sum_{j=1}^{N_s} Y_j F_{ij} u_i \tag{2.14}$$

where F_j are external forces in direction j, S_h is the source term for total enthalpy, $\dot{\omega}_j$ is the chemical source term for species j and V_{ij} is the i-th component of vector $\vec{V_j}$ [6]. In these equations Einstein notation has been used[7].

Direct substitution of Newton's, Fick's and Fourier's laws lead to obtain typical fluid mechanics equations for Newtonian compressible reactive flows. The momentum equation for a Newtonian fluid is known as Navier-Stokes equation. It is worth mentioning that for flows where the variations of density and diffusion coefficients are negligible, as most of the incompressible flows, diffusion terms are remarkably simplified and become proportional to Laplacians of the variables. In addition, from the continuity equation it is observed that for incompressible flows the stress tensor for Newtonian fluid is simplified to $\sigma_{ij} = -p\,\delta_{ij} + 2\,\mu\,s_{ij}$.

Although energy equation has been written for total enthalpy it is interesting to note that a term of paramount importance appears in equations for sensible enthalpy (similarly for sensible internal energy) in the form $\tau_{ij}\,\frac{\partial u_i}{\partial x_j}$. For Newtonian flows it takes the form

$$\Phi = \tau_{ij} \frac{\partial u_i}{\partial x_j} = 2\,\mu\,s_{ij}\,s_{ij} - \frac{2}{3}\,\mu \left(\frac{\partial u_k}{\partial x_k}\right)^2 \tag{2.15}$$

This is the dissipation function where the main contribution $2\,\mu\,s_{ij}\,s_{ij}$ is non-negative since it is the sum of squared terms. It is an energetic contribution that describes how energy is taken from the kinetic energy of the flow and transferred into thermal energy due to viscous friction. With the proper operations this term gives rise to the turbulent kinetic energy dissipation that, as will be seen in section 2.3, is one of the most important variables that characterize a turbulent flow.

Finally, to say that the previous coefficients ν, λ and D, lead to define the following important dimensionless numbers which measure the intensity of diffusion between different phenomena

$$Sc_i = \frac{\nu}{D_i} \tag{2.16}$$

[6] In equations 2.11 and 2.12 j is fixed.

[7] Einstein and vectorial notations are used indistinctly along this text.

$$Pr = \frac{\nu}{\lambda} \tag{2.17}$$

$$Le_i = \frac{\lambda}{D_i} \tag{2.18}$$

where Pr is Prandtl number and Sc_i and Le_i are the Schmidt and Lewis numbers, respectively, for species i. For gases their values are close to unity since diffusion is a molecular process and, hence, the intrinsic mechanism for diffusion is the same for all the quantities. This allows the calculation of fluxes for different variables and is called the Reynolds analogy [5, 10].

2.3 Turbulence theory

2.3.1 Introduction and fundamentals

Turbulence is one the most complex phenomena that may be found in physics and this is clearly patent when considering the tremendous effort that engineers have done in order to understand its nature and the great variety of models that may be found in literature. The intrinsic complexity of the problem has made these models to be devised for specific configurations and, hence, they lack generality. As was explained before, this may seem paradoxical since the governing equations are completely known but the practical impossibility of solving them forces the search of alternative descriptions that may contain the most important aspects of the physics while their equations resolution is still feasible.

To make more abstruse this matter, it is difficult to find a definition which describes the intrinsic nature of turbulence. On the contrary, most of the definitions only enumerate a set of characteristics of the turbulent flow [13]. Some features characterize turbulence [5, 13]:

1. Although the governing equations are deterministic they show a chaotic nature, that is, they are extremely sensitive to any changes in the initial and boundary conditions. This makes almost impossible the prediction of a given flow since there are errors related to measurements and experiments are non-repeatable [8].

[8] For the instantaneous initial and boundary conditions. Clearly they are repeatable in terms of average values.

2. Turbulence is caused by perturbations in the flow. When Reynolds number is high inertial forces are large compared to viscous forces and perturbations increase in magnitude. This leads to a fluid motion where particles do not move along ordered layers as in a laminar flow.

3. Turbulence is three dimensional, time dependant, rotational and intermittent.

4. Although the instantaneous flow may be chaotic it may not be chaotic in statistical terms. Averaging between different samples of the same experiment reveals that the variables show averaged values with a deviation. Consequently, turbulence may be described in statistic terms by soft profiles. This is the base of the (Unsteady) Reynolds Averaged Navier-Stokes (URANS and RANS) models widely extended in the modelling of turbulent flows.

5. A structure composed of vortexes or eddies of different lengths is observed. This gives rise to the energy cascade description, which explains that there is a transfer of energy from the largest eddies, for which energy is provided, to the smallest ones where energy is dissipated into heat.

6. Turbulence accelerates momentum, energy and species transport. This transport is caused by a strong convection between the different spatial regions producing highly inhomogeneous fields where there exist sharp gradients. These high gradients provoke strong diffusion processes leading to the homogenization of the fields. In a generalized meaning of the concept of mixing, the strong gradients, created by the chaotic and erratic flow motion, intensify the mixing process due to the high diffusion fluxes.

   This means that, in the case of momentum, its exchange is enhanced due to high shear stresses. In the same way, homogeneous mixture formation is accelerated due to the important mass fluxes established between adjacent fluid layers with heterogeneous composition.

   Similar to the intensified transport, the dissipation of the quantities, which depends on the gradients of the fields, is augmented too.

7. This enhanced transport or exchange of quantities in the fluid motion may be desirable as in the case of mixing or, on the contrary, may be an inconvenient as in the pressure losses produced by the friction of the fluid with a wall or in the quenching of the flame.

8. The turbulent flow is rotational. The strain of rotation is measured with the vorticity $\vec{\omega}$ defined by the curl of velocity, that is, $\vec{\omega} = \nabla \times \vec{u}$. The alignment of the strain rate with the vorticity increases the magnitude of $\vec{\omega}$ producing vortex stretching.

The previous aspects highlight the most important characteristics of turbulence. However, some of them should be emphasized due to the relevance in subsequent results. In fact, the infeasibility of solving the instantaneous equations has forced to adopt more simplified approaches which are build on some simple observations.

The visual aspect of a turbulent flow shows that, as was previously stated, the fluid motion is composed of eddies of different sizes and the range of sizes depends on the Reynolds number. The largest vortexes, called the integral scales, are the most energetic ones with the largest characteristic time scales[9] and receive the energy from an external source. These eddies are unstable and break up into smaller vortexes transferring energy to eddies of smaller sizes. The kinetic energy contained in theses vortexes is transferred to smaller ones with smaller time scales too and so on. Finally, there exists a critical vortex size for which kinetic energy is dissipated into heat due to friction of adjacent fluid layers. These eddies, known as the Kolmogorov scales, show the smallest temporal scales. This vision corresponds to the energy cascade notion and was first described by Richardson in 1922 [14].

The length of the integral scale is denoted by ℓ_0 while the symbol η is used for the Kolmogorov scales. If the flow scale is L then ℓ_0 is of the same order of magnitude. Another important length scale is Taylor scale, which, although different to the previous length scales has not an easy interpretable physical meaning, it is related to eddies for which dissipative effects are not strong. For a general eddy its length scale is denoted by ℓ.

For each length scale a Reynolds number is defined as

$$Re(\ell) = \frac{\ell\, U(\ell)}{\nu} \tag{2.19}$$

where $U(\ell)$ is the characteristic velocity for an eddy of size ℓ. For Kolmogorov scale Reynolds number is unity.

The energy cascade description of turbulence for very high Reynolds numbers leads to define three main ranges where eddies may be found depending on their size [6]

[9] Sometimes understood as the turn-over time of an eddy.

1. The energy-containing range corresponds to the largest eddies. External energy is injected in this range. This energy (added at some rate) is called production of turbulence $\wp$. The range is delimited by the scales ℓ_{EI} and L.

2. The universal equilibrium range: corresponds to eddies with length scales smaller than those belonging to the energy-containing range and is divided in two subranges:

   (a) Inertial subrange: in this region energy is transferred (without losses) from larger to smaller eddies. It is limited between ℓ_{DI} and ℓ_{EI}.

   (b) Dissipation range: corresponds to the smallest eddies (Kolmogorov vortexes) where kinetic energy is dissipated into heat due to viscous stresses.

The ranges form a continuum in the size of the scales. A sketch of the ranges is shown in figure 2.1.

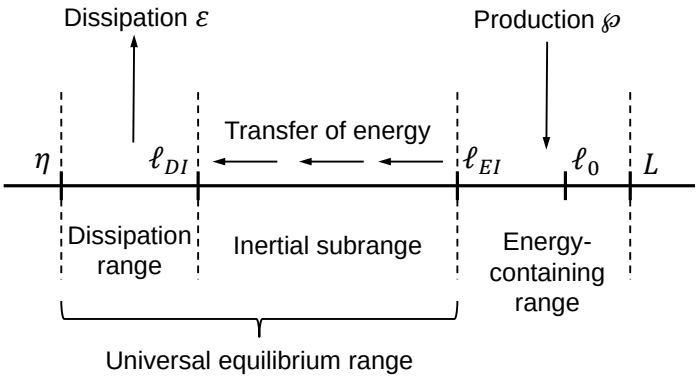

Figure 2.1. *Energy fluxes for the whole range of turbulent scales.*

As in the inertial subrange there is only a transfer of energy without sources or sinks, this means that for lengths ℓ in the inertial subrange it holds $\varepsilon = U^2(\ell)/(\ell/U(\ell)) = U^3(\ell)/\ell$ where ε denotes the rate of dissipation of turbulent kinetic energy, that is, the rate at which turbulent kinetic energy is transformed into heat. A precise definition of this concept is given in 2.3.2.

One of the most prominent advancements in turbulence theory is due to A. N. Kolmogorov, who in 1941 published a set of papers [15, 16], which constitute a theory sometimes known as K41, where he stated some important laws related to the behaviour of turbulent statistics and the spectral content of energy, that is, how energy is distributed depending on the size of the vortex for high Reynolds flows. It is developed assuming homogeneous turbulence and high Reynolds numbers. However, as a first step and previous to describing these results, we provide the following definitions:

1. Homogeneous turbulence: it occurs when the statistics do not change with position. It may occur in one or several directions.
2. Isotropic turbulence: it occurs when the statistics do not change with rotations and reflections.

To describe turbulence Kolmogorov assumed the following hypotheses:

1. Hypothesis of local isotropy: at sufficient high Reynolds number the smallest scales ($\ell \ll \ell_0$) show statistical isotropy.
2. First similarity hypothesis: at sufficient high Reynolds number the statistics at the universal equilibrium range are uniquely determined by ν and ε.
3. Second similarity hypothesis: at sufficient high Reynolds number the statistics at the inertial subrange are uniquely determined by ε independently of ν.

The hypothesis of local isotropy explains that, although the large scales are deformed by the domain geometry and the boundary conditions and, hence, are anisotropic, this anisotropy is lost when energy is transferred to smaller vortexes. This implies that the smallest eddies tend to be isotropic[10] and, consequently, in some sense, their statistics are universal. The similarity hypotheses explain what these statistics depend on. With this description and based on dimensional arguments expressions for different variables can be obtained.

In the light of these hypotheses the names given to the different ranges are clearly understood. They contain a deep meaning of the physics and the results

[10]Isotropy has to be understood in statistical terms since it does not necessarily occur at each instant even for the smallest eddies.

deduced from them have been corroborated by a large number of experiments [17, 18].

On the one hand, from the first similarity hypothesis it is deduced that $\eta = \eta(\varepsilon, \nu)$ and the only product that may be formed between ε and ν (not considering multiplicative constants) in order to yield a length is [11]

$$\eta = \left(\frac{\nu^3}{\varepsilon}\right)^{1/4} \tag{2.20}$$

Similarly we have

$$U(\eta) = (\nu\,\varepsilon)^{1/4} \tag{2.21}$$

On the other hand, from the energy cascade description we have that $\varepsilon \sim U(\ell_0)^3/\ell_0$ [12]. With the previous relationships it is obtained that

$$\frac{\eta}{\ell_0} \sim Re(\ell_0)^{-3/4} \tag{2.22}$$

2.3.2 Statistical description of turbulence

Before proceeding with a deeper analysis of turbulence it is mandatory to introduce the statistic concepts related to turbulence which play a fundamental role in turbulence description since the origins of its analysis.

If velocity or other field signal is recorded at one given point the erratic nature of turbulence is patent. Dealing with such functions is almost impossible and the use of statistics arises in a natural way. Denoting the mean value with an overline, $\overline{\phi}$, the signal, ϕ, may be decomposed into a mean value and a fluctuating component ϕ' as

$$\phi = \overline{\phi} + \phi' \tag{2.23}$$

If the flow is statistically stationary the statistics may be obtained recording the signal during a temporal window. On the contrary, if the flow

[11] It is typical in turbulence theory to use dimensional arguments in order to find expressions and formulas.

[12] This time it is used the symbol $\sim$ instead of $=$ in order to clarify that the equality does not necessarily holds but both members only scale, that is, they are proportional since the expression is applied out of the inertial subrange.

is not statistically stationary the statistics may be found for different samples of the same experiment [6]. This is called Reynolds decomposition and gives rise to Reynolds means.

Averaging equation 2.23 it is obtained that $\overline{\phi'} = 0$. The value $\overline{\phi'^2}$ measures the variance of the signal and it is one of the most important characterization of a fluctuating variable together with the mean value. Standard deviation $\sqrt{\overline{\phi'^2}}$ may reach values of the 20 % of the mean $\overline{\phi}$.

Clearly, higher moments may be defined, such as $\overline{\phi'^3}$ and $\overline{\phi'^4}$, which give a measure of the skewness or asymmetry and the kurtosis or flatness of the signal, respectively.

In the same way that different statistics have been defined from the temporal signal or the values obtained from different samples, a probability density function (PDF) may be defined for each point (and time for not statistically stationary flows). Then the PDF may be written as $f(\phi; \vec{x}, t)$ where the semicolon fixes the point and time for which the PDF is obtained[13]. From this PDF all the moments may be easily written as

$$\overline{\phi^n(\vec{x}, t)} = \int_{-\infty}^{\infty} \phi^n(\vec{x}, t)\, f(\phi; \vec{x}, t)\, d\phi \tag{2.24}$$

from which the values $\overline{\phi'^n}$ are easily deduced.

Transport equations for the averaged variable may be easily obtained from decomposing the instantaneous variables in a mean and fluctuating components and averaging the instantaneous equations [6, 10]. As the fluid mechanic equations are non-linear products between the different terms appear. The terms that contain products of the mean and fluctuating components vanish when averaging, however, the products of the fluctuating components are not zero in general. These terms represent the flux of the turbulent components due to turbulent convection and are of paramount importance.

In incompressible flows turbulent fluxes only contain the product of the fluctuating velocity and the fluctuation of any variable ϕ. However, for compressible flows where the density shows a pulsating component new terms appear complicating the equations. In order to avoid this issue density-weighted or Favre averages [19] are introduced

$$\phi = \widetilde{\phi} + \phi'' \tag{2.25}$$

[13] For statistically steady flows the PDF is $f(\phi; \vec{x})$.

with

$$\widetilde{\phi} = \frac{\overline{\rho\,\phi}}{\overline{\rho}} \tag{2.26}$$

It is easily deduced that $\overline{\rho\,\phi''} = 0$. With this definition to average, transport equations are formally equal for incompressible flows (Reynolds averages) and compressible flows (Favre averages)[14]. In principle, both averages provide different results when applied to a compressible flow and we should not compare density-weighted averages when solving transport equations with experimental Reynolds averages. Notwithstanding, this is a quite extended practice since it is quite difficult to measure the density field and, except for a little number of experiments [20, 21], this information is not available.

Due to the formal similarity for the equations for both averages they will be used indistinctly in the following. The concepts defined for one of them may be easily extended to the other one.

The averaged equations (written for Favre averages) for a general flow are written as

$$\frac{\partial\overline{\rho}}{\partial t} + \frac{\partial(\overline{\rho}\,\widetilde{u_i})}{\partial x_i} = 0 \tag{2.27}$$

$$\frac{\partial(\overline{\rho}\,\widetilde{Y_j})}{\partial t} + \frac{\partial(\overline{\rho}\,\widetilde{Y_j}\,\widetilde{u_i})}{\partial x_i} = -\frac{\partial(\overline{\rho}\,\widetilde{Y_j\,V_{ij}} + \overline{\rho}\,\widetilde{u_i''\,Y_j''})}{\partial x_i} + \overline{\rho}\,\widetilde{\dot{\omega}_j} \qquad j = 1, \ldots, N_s \tag{2.28}$$

$$\frac{\partial(\overline{\rho}\,\widetilde{u_j})}{\partial t} + \frac{\partial(\overline{\rho}\,\widetilde{u_j}\,\widetilde{u_i})}{\partial x_i} = -\frac{\partial\overline{p}}{\partial x_j} + \frac{\partial(\overline{\tau_{ij}} - \overline{\rho}\,\widetilde{u_i''\,u_j''})}{\partial x_i} + \overline{F_j} \qquad j = 1, 2, 3 \tag{2.29}$$

$$\frac{\partial(\overline{\rho}\,\widetilde{h})}{\partial t} + \frac{\partial(\overline{\rho}\,\widetilde{h}\,\widetilde{u_i})}{\partial x_i} = \frac{\partial\overline{p}}{\partial t} - \frac{\partial(\overline{q_i} - \overline{\rho}\,\widetilde{u_i''\,h''})}{\partial x_i} + \frac{\partial(\overline{\tau_{ij}\,u_j})}{\partial x_i} + \overline{\rho}\sum_{j=1}^{N_s}(\widetilde{Y_j\,F_{ij}}\,u_i + \widetilde{Y_j\,F_{ij}}\,V_{ij}) + \overline{S_h} \tag{2.30}$$

As observed additional terms appear in the averaged transport equations that correspond to the product of the fluctuating components of any variable

[14] Although they may contain different source terms.

and the velocity $(-\overline{\rho}\,\widetilde{u_i''\,\phi''})$. Physically, they are interpreted as a turbulent transport, that is, the transport of a fluctuating component due to the fluctuating velocity and are understood as additional stresses or fluxes to which the averaged fields are submitted. It is worth mentioning that averaged equations show that these terms may be written as divergences of the vector fields $-\overline{\rho}\,\widetilde{\phi'\,\vec{u'}}$ and, consequently, they are transport terms[15].

More particularly, in the case of the momentum equation the products of the fluctuating velocities, $-\rho\,\overline{u_i'\,u_j'}$ (or $-\overline{\rho}\,\widetilde{u_i'\,u_j'}$ in compressible flows), are understood as additional stresses that act on the averaged fields. For this reason they are called Reynolds stresses τ_{ij}^R which lead to define the Reynolds stresses tensor. In the context of incompressible flows and, depending on the author, Reynolds stresses may denote $-\rho\,\overline{u_i'\,u_j'}$ or simply $\overline{u_i'\,u_j'}$. In this text the last nomenclature is adopted, that is, refer to $\overline{u_i'\,u_j'}$ as the Reynolds stresses[16]. These terms are unknown and require a closure model in order to solve the averaged transport equations.

The fluctuating components of the velocity may lead to the definition of the turbulent kinetic energy

$$k = \frac{1}{2}\overline{u_i'\,u_i'} \tag{2.31}$$

This is a very important variable and is the simplest characterization of turbulence. Turbulent kinetic energy equation for incompressible flows is

$$\frac{\partial k}{\partial t} + \frac{\partial(\overline{u_i}\,k)}{\partial x_i} = -\frac{\partial}{\partial x_i}\left(\frac{1}{\rho}\overline{u_i'\,p'} - 2\nu\,\overline{u_j'\,s_{ij}'} + \overline{u_i'\,k}\right) - \overline{u_i'\,u_j'}\,\overline{s_{ij}} - 2\nu\,\overline{s_{ij}'\,s_{ij}'} \tag{2.32}$$

From this equation the most important terms of the right hand side are $\overline{u_i'\,u_j'}\,\overline{s_{ij}}$, which is the production term of turbulent kinetic energy $\wp$, and $2\nu\,\overline{s_{ij}'\,s_{ij}'}$, denoted as ε, that represents the rate of dissipation of turbulent kinetic energy. It is clearly seen that $\varepsilon \geq 0$ and, hence, it is a sink term

[15] In this context, transport refers to a redistribution of the variable if no external fluxes feed the volume control. This is easily seen writing the divergence term as a flux by means of the Gauss theorem.

[16] As said before, Reynolds and Favre averages lead to formally similar equations, however, equations for incompressible flows are remarkably simpler than for compressible flow. For this reason and for the turbulence theory description, in the following, results correspond to incompressible flows most of the times. This is done because adding compressibility phenomena does not provide a deeper understanding in the context of this exposition and adds a new degree of difficulty.

in the turbulent kinetic energy equation. It represents the energy that is transformed into heat due to viscous effects which, according to the energy cascade description, occurs at the smallest eddies. Defining the characteristic velocity for the integral scale as $k^{1/2}$ the integral scale is approximated as $L \sim k^{3/2}/\varepsilon$ [17].

The production term $\wp$ appears in the mean kinetic energy equation $(\frac{1}{2}\overline{u_i}\ \overline{u_i})$ with opposite sign. Therefore it is an exchange of energy from the largest scales to the smallest scales, that is, a conversion of mean kinetic energy to turbulent kinetic energy and is a power caused by Reynolds stresses. In general, it takes a positive value. At this point it is important to note that the energy cascade should be understood as the description of a statistical process and not a local process. This is, the energy is transferred statistically from the largest eddies to the smallest although this does not mean that locally the energy is not transferred from the smallest eddies to the largest ones. This phenomenon may occur in the flow and it is called backscatter.

Note that the rest of the terms in the r.h.s. of equation 2.32 take the form $\partial M_i/\partial x_i$ or $\partial M_{ijj}/\partial x_i$. This implies that they are affected by the operator divergence and, therefore, by virtue of Gauss theorem they represent a flux of energy. If no external fluxes appear through the surface volume they only redistribute energy inside the volume control.

From the previous description the turbulent kinetic energy equation has an easy interpretation. Integrating over a volume control, it describes that the volume control total turbulent kinetic energy variation is due to external energy fluxes $+\ \wp - \varepsilon$.

In a pure shear flow $\wp = \varepsilon$ [5] while, in shear free flows the equilibrium between production and dissipation may be observed only in some regions. For wall flows production equals dissipation in the near-wall region comprising the log-law region [22].

In a similar way, the behaviour for the variance of a general variable[18] $\overline{\phi'^2}$ is given by the following equation[19]

[17] Note that the use of a variable such as ε related to the smallest scales to define an integral scale is valid in the light of the energy cascade which argues that, for high Reynolds numbers and with some additional assumptions, the energy taken from the mean flow (large scales) equals the dissipation (small scales).

[18] To simplify we assume that the variable has no source terms.

[19] In the same way that for the turbulent kinetic energy this equation is written for incompressible flow too.

$$\frac{\partial\overline{\phi'^2}}{\partial t}+\frac{\partial(\overline{u_i}\,\overline{\phi'^2})}{\partial x_i}=-\frac{\partial}{\partial x_i}\left(-\Gamma\frac{\partial\overline{\phi'^2}}{\partial x_i}+\overline{u_i'\,\phi'^2}\right)-2\overline{u_i'\,\phi'}\frac{\partial\overline{\phi}}{\partial x_i}-2\Gamma\overline{\frac{\partial\phi'}{\partial x_i}\frac{\partial\phi'}{\partial x_i}} \quad (2.33)$$

Again a scalar variance production term arises and is given by $\wp_\phi = -2\overline{u_i'\,\phi'}\frac{\partial\overline{\phi}}{\partial x_i}$ while the scalar dissipation rate is $\varepsilon_\phi = 2\Gamma\overline{\frac{\partial\phi'}{\partial x_i}\frac{\partial\phi'}{\partial x_i}} \geq 0$. Similar considerations to those given for k about equation physical interpretation can be established for scalar variance. In fact, it is observed that equations 2.32 and 2.33 are formally identical (this is clearly seen when developing the s_{ij} terms in equation 2.32).

So far, the moments only provide information at a given point and time but not about how the signal interacts with itself in the spatial or temporal directions. This interaction is described by the autocorrelation function. For homogeneous turbulence, the spatial autocorrelation for velocity is given by

$$R_{ij}(\vec{r},t)=\overline{u_i'(\vec{x},t)\,u_j'(\vec{x}+\vec{r},t)} \quad (2.34)$$

which may be normalized as

$$\rho_{ij}(\vec{x},t)=\frac{R_{ij}(\vec{r},t)}{R_{ij}(0,t)}=\frac{R_{ij}(\vec{r},t)}{\overline{u_i'u_j'}(t)} \quad (2.35)$$

known as the autocorrelation coefficient[20]. A similar definition may be given for temporal autocorrelation. ρ_{ij} is unity at the origin where it is maximum and tends to vanish for distant points from the origin. In addition, it has null slope at the origin.

Since according to Kolmogorov's hypotheses vortexes depending on their length show a particular behaviour and relationship with some variables it is natural to inquire about the nature of turbulence in the frequency/wavenumber domain. For this purpose Fourier transform is applied to the temporal signals. It is interesting to do this with the autocorrelation function applied to the velocity. This yields a Fourier transform pair defined by the velocity autocorrelation function and the velocity spectrum tensor Φ_{ij}

$$\Phi_{ij}(\vec{\kappa})=\frac{1}{(2\pi)^3}\int_{-\infty}^{\infty}\int_{-\infty}^{\infty}\int_{-\infty}^{\infty}R_{ij}(\vec{r})\exp(-i\,\vec{r}\,\vec{\kappa})\,d\vec{r} \quad (2.36)$$

[20] $R_{ij}(\vec{r},t)$ does not depend on $\vec{x}$ due to homogeneous turbulence assumption.

$$R_{ij}(\vec{r}) = \int_{-\infty}^{\infty}\int_{-\infty}^{\infty}\int_{-\infty}^{\infty} \Phi_{ij}(\vec{\kappa}) \exp(i\,\vec{r}\,\vec{\kappa})\, d\vec{\kappa} \tag{2.37}$$

where the symbol i in the exponential terms is the imaginary unity. The rest of dependencies have been omitted for the sake of clarity. The notation $d\vec{r}$ means $dr_1\, dr_2\, dr_3 = dV$ where V is the volume.

κ is the wavenumber defined for a vortex of size ℓ as $\kappa = 2\pi/\ell$ and $\vec{\kappa}$ is the wavenumber vector. For nomenclature purposes we define $\kappa_L = 2\pi/L$, $\kappa_{EI} = 2\pi/\ell_{EI}$, $\kappa_{DI} = 2\pi/\ell_{DI}$ and $\kappa_\eta = 2\pi/\eta$.

The energy spectrum function is defined as

$$E(\kappa) = \frac{1}{2}\oint \Phi_{ii}(\vec{\kappa})\, dS(\kappa) \tag{2.38}$$

where the integration is carried out on spherical surfaces centred at the origin.

From equation 2.38 it follows that

$$k = \int_0^\infty E(\kappa)\, d\kappa \tag{2.39}$$

Similar definitions may be provided for the temporal autocorrelations [5].

Kolmogorov deduced that in the inertial subrange the energy spectrum takes the form

$$E(\kappa) = C\varepsilon^{2/3}\kappa^{-5/3} \tag{2.40}$$

where C is a universal constant called Kolmogorov constant and takes a value of 1.5 approximately. This is the well-known Kolmogorov -5/3 spectrum and has been experimentally confirmed [17]. Different laws have been proposed for the dissipation range, such as Pao spectrum [23], but all of them provide an exponential decay in this range. In the energy-containing range, $E(\kappa)$ is supposed to change with κ^2. These results are shown in figure 2.2.

As a final note it is important to insist that turbulence theory is an asymptotic theory[21] (for very high Re numbers) that intends to give a

[21] Asymptotic theory refers to a theory developed assuming very large values for some variables.

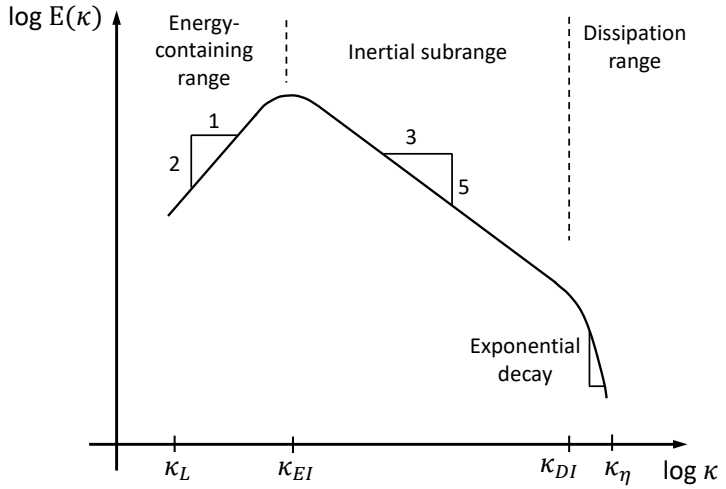

Figure 2.2. *Energy content as a function of the wavenumber.*

qualitative picture (with some quantitative results) of a phenomenon that otherwise would remain inextricable. Clearly it cannot substitute the physical laws for the conservative variables and it has to be understood as a a guide that provides an approximated vision of the problem. The asymptotic theories have been applied successfully to the combustion theory too.

This is only a concise description of turbulence but contains the most important aspects. For the engineer the main goal is solving the transport equations. As was said before the resolution of the instantaneous equations is unaffordable forcing to solve the averaged or filtered equations (as will be seen later) as the best approach to the problem. However, these equations contain extra terms related to the fluctuating components of the fields that require to be modelled. The theoretical knowledge gained during the years for the turbulence description leads to pose such models based on physical grounds that are described in next section.

2.3.3 Turbulence models

2.3.3.1 Introduction to the different approaches

This section is devoted to describe the most important approaches proposed to solve turbulence, that is, how transport equations for a turbulent flow are approximated. As was said before, solving the instantaneous equations is almost an impossible task except for very particular problems. These problems do not correspond to the modelling of industrial devices and are purely academic. In these cases, the domain is taken small enough to maintain the number of nodes and time steps inside the possibilities of the current computational power [24].

The infeasibility of solving all the spatial and temporal scales is clear when noting that the Kolmogorov scales are proportional to $\ell_0 Re^{-3/4}(\ell_0)$. In an engineering problem ℓ_0 may be of the order of some decimetres or metres while η may measure some tens or some few hundreds of micrometres while the temporal scales related to the Kolmogorov scales are of the order of some few hundreds of microseconds [10]. This means that solving all the scales requires a number of nodes (in the three spatial and temporal directions) that goes further from the current possibilities. It is easy to see, from the proportionality between the integral and Kolmogorov scales, that the computational cost increases with $Re^3(\ell_0)$.

The resolution of the instantaneous equations is known as Direct Numerical Simulation (DNS) and, currently, is limited to small domains with low-moderate Reynolds numbers [22, 24–26]. In a DNS almost all the computational effort is used to solve the dissipative scales [6].

To tackle with engineering problems, in the literature two approaches have been proposed that provide a feasible resolution of equations. They basically consist of averaging or filtering the instantaneous equations in order to obtain new equations where not all the scales are solved and, hence, the resolution of these averaged or filtered flows does not involve so many computational resources. However, due to the non-linearity of the fluid mechanic equations the average and filter operations introduce new terms in the equations that have to be modelled. These new terms express the interaction between the not solved vortexes with the solved part of the flow. Their modelling is the goal of the turbulence models.

The first approach is the Reynolds Averaged Navier-Stokes (RANS) for statistically steady flows or the Unsteady Reynolds Averaged Navier-Stokes

(URANS) for not statistically stationary flows[22]. They are based on the concept of averaging the equations when the variables are decomposed in a mean and a fluctuating part as was explained in the previous section. This average may be performed with Reynolds or Favre averages and the averaged equations are equations 2.27, 2.28, 2.29 and 2.30. The fundamentals of the method were explained in section 2.3.2.

The second approach is known as Large Eddy Simulation (LES) and consists of filtering the fields in the vicinity of each point. This implies that only the information of the field related to high frequencies is lost due to the filtering process and, consequently, the largest eddies are solved while the smallest are still modelled. This is different to the RANS approach where all the scales are modelled since the averages extend over all the time or for the complete set of possible samples. Consequently, RANS models have to describe the whole set of scales what is clearly extremely complex since, different to the small eddies, large vortexes are strongly affected by the boundary conditions as well as the geometry and they are anisotropic.

It is expected that the universal behaviour of the smallest eddies, which has to be modelled in LES simulations, leads to the formulation of easier and more general models than those required for RANS, where the description of the whole range of scales complicates this task. This explains the great variety of models that may be found for RANS simulations and why it is expected that the results obtained with LES simulations are more reliable than those provided by RANS simulations. Notwithstanding, the more accurate resolution of the flow for LES simulations is accompanied of a considerable increase of the computational cost.

These features show how the increase in the ability to describe the flow goes together with an increase in the required computational power.

It is important to note that all the flows are unsteady for LES and DNS although being statistically steady. Only with RANS it is possible to make use of simplifications in the equations or the domain when the flow to be solved is statistically steady and/or homogeneous in any direction.

Coming back to the LES approach, the (low-pass) filtering is done by means of a filter function G defined by a filter width Δ. In general, the value of Δ gives a measure of the size of the vortexes that are not being solved. For a general field ϕ the filtering operation is defined as

[22] In the following we will designate, in a general way, RANS to this approach even if we are dealing with a statistically unsteady problem.

$$\overline{\phi}(\vec{x},t) = \int_{-\infty}^{\infty}\int_{-\infty}^{\infty}\int_{-\infty}^{\infty} G(\vec{x},\vec{r},\Delta)\,\phi(\vec{r},t)\,d\vec{r} \tag{2.41}$$

If the filter does not depend on the origin i.e. it is of the form $G(\vec{r}-\vec{x},\Delta)$ it is called a homogeneous filter. Note that filtering is a linear operation. Moreover, Δ is usually taken twice the size of the mesh[23].

Different filters have been proposed such as the cut-off filter in spectral space, which only retains informations of the vortexes larger than 2Δ, the box filter in physical space, which averages the values in a cube of side Δ and the Gaussian filter.

The filter function has to verify the normalization condition, that is

$$\int_{-\infty}^{\infty}\int_{-\infty}^{\infty}\int_{-\infty}^{\infty} G(\vec{x},\vec{r},\Delta)\,d\vec{r} = 1 \tag{2.42}$$

The instantaneous field may be written as

$$\phi = \overline{\phi} + \phi' \tag{2.43}$$

Moreover, density-weighted or Favre filtering, used for variable density flows, may be defined in a similar way than those used for averages in RANS

$$\phi = \widetilde{\phi} + \phi'' \tag{2.44}$$

with

$$\widetilde{\phi} = \frac{\overline{\rho\,\phi}}{\overline{\rho}} \tag{2.45}$$

Again both decompositions are formally identical and the operations done for one are easily extended to the other one.

However, different to the averaging approach, in the case of filtering it occurs, in general, that $\overline{\phi'} \neq 0$ and $\overline{\overline{\phi}} \neq \overline{\phi}$. In addition, commuting the filter and derivatives requires the filter width to be spatially uniform which in turn

[23] In any case it cannot be smaller than the mesh size.

implies the mesh to be spatially uniform too[24]. In practice, commutation errors are typically neglected.

If the transport equations are filtered then the filtered equations for LES are obtained. The filtering of the convective non-linear terms produces the filtered quantities $\overline{u_i\,\phi}$ (or $\overline{\rho}\,\widetilde{u_i\,\phi}$). As the solved variables are $\overline{u_i}$ and $\overline{\phi}$ (or $\widetilde{u}_i$ and $\widetilde{\phi}$), the non-linear terms require some type of modelling. In this way it is written $\overline{u_i\,\phi} = \overline{u_i}\,\overline{\phi} + (\overline{u_i\,\phi} - \overline{u_i}\,\overline{\phi})$ and then the term $\overline{u_i}\,\overline{\phi}$ becomes the convective term in the transport equation while $\overline{u_i\,\phi} - \overline{u_i}\,\overline{\phi}$ passes to other side of the equality as a subgrid stress[25]. If ϕ is the velocity, the subgrid scale stress tensor $[\tau^{sgs}]$ is obtained, where each of its terms is $\tau_{ij}^{sgs} = \overline{u_i\,u_j} - \overline{u_i}\;\overline{u_j}$.

Note that different to RANS, $\tau_{ij}^{sgs} \neq \overline{u_i'\,u_j'}$ since $\overline{u_i'} \neq 0$ and $\overline{\overline{u_i}} \neq \overline{u_i}$ [26]. In fact, τ_{ij}^{sgs} may be decomposed in the following way [27]

$$\tau_{ij}^{sgs} = \overline{u_i\,u_j} - \overline{u_i}\;\overline{u_j} = (\overline{\overline{u_i}\,\overline{u_j}} - \overline{u_i}\;\overline{u_j}) + (\overline{\overline{u_i}\,u_j'} + \overline{u_i'\,\overline{u_j}}) + \overline{u_i'\,u_j'} \tag{2.46}$$

The first term between parenthesis of the right hand side is the Leonard stresses L_{ij} caused by effects of the resolved scales, the second term between parenthesis is the cross stresses C_{ij} which expresses the interaction between the subgrid scales and the resolved flow and, finally, the last term is the subgrid scale Reynolds stresses.

Substituting τ_{ij}^{sgs} (or $\widetilde{u_i\,u_j} - \widetilde{u}_i\,\widetilde{u}_j$) in equation 2.29 instead of $\widetilde{u_i''\,u_j''}$ and the corresponding fluxes $\overline{u_i\,\phi} - \overline{u_i}\,\overline{\phi}$ (or $\widetilde{u_i\,\phi} - \widetilde{u}_i\,\widetilde{\phi}$) instead of $\overline{u_i'\,\phi'}$ (or $\widetilde{u_i''\,\phi''}$) in equations 2.28 and 2.30, LES equations are obtained. It arises, then, that LES equations are formally identical to RANS equations[27]. Equations 2.47, 2.48, 2.49 and 2.50 are continuity, species, momentum and enthalpy written in the LES frame.

$$\frac{\partial\overline{\rho}}{\partial t} + \frac{\partial(\overline{\rho}\,\widetilde{u}_i)}{\partial x_i} = 0 \tag{2.47}$$

[24] If the ratio between the mesh size and filter width is constant.

[25] Term $\overline{u_i\,\phi} - \overline{u_i}\,\overline{\phi}$ is due to not solved motions that have smaller characteristic length scales than Δ. For this reason it is said that they act as a subgrid stress.

[26] In RANS it is fulfilled $\overline{u_i'\,u_j'} = \overline{u_i\,u_j} - \overline{u_i}\;\overline{u_j}$.

[27] As a consequence, in the following we will use the same notation for both RANS and LES making no distinction between them and subsequent development applies to both approaches unless otherwise stated.

$$\frac{\partial(\overline{\rho}\,\widetilde{Y_j})}{\partial t}+\frac{\partial(\overline{\rho}\,\widetilde{Y_j}\,\widetilde{u_i})}{\partial x_i}=-\frac{\partial(\overline{\rho}\,\widetilde{Y_j\,V_{ij}}+\overline{\rho}\,(\widetilde{u_i\,Y_j}-\widetilde{u_i}\,\widetilde{Y_j}))}{\partial x_i}+\overline{\rho}\,\widetilde{\dot{\omega}_j}\qquad j=1,\ldots,N_s \tag{2.48}$$

$$\frac{\partial(\overline{\rho}\,\widetilde{u_j})}{\partial t}+\frac{\partial(\overline{\rho}\,\widetilde{u_j}\,\widetilde{u_i})}{\partial x_i}=-\frac{\partial\overline{p}}{\partial x_j}+\frac{\partial(\overline{\tau_{ij}}-\overline{\rho}\,(\widetilde{u_i\,u_j}-\widetilde{u_i}\,\widetilde{u_j}))}{\partial x_i}+\overline{F_j}\qquad j=1,2,3 \tag{2.49}$$

$$\begin{aligned}\frac{\partial(\overline{\rho}\,\widetilde{h})}{\partial t}+\frac{\partial(\overline{\rho}\,\widetilde{h}\,\widetilde{u_i})}{\partial x_i}=&\frac{\partial\overline{p}}{\partial t}-\frac{\partial(\overline{q_i}-\overline{\rho}\,(\widetilde{u_i\,h}-\widetilde{u_i}\,\widetilde{h}))}{\partial x_i}+\frac{\partial(\overline{\tau_{ij}\,u_j})}{\partial x_i}+\\&+\overline{\rho}\sum_{j=1}^{N_s}(\widetilde{Y_j\,F_{ij}\,u_i}+\widetilde{Y_j\,F_{ij}\,V_{ij}})+\overline{S_h}\end{aligned} \tag{2.50}$$

When comparing LES simulations with experiments this is done typically in terms of average fields. In the LES context we will denote the averaging process by the symbol $\langle\rangle$. This averaging is usually carried out in time for statistical stationary flows but sometimes it is useful to average in spatial directions if turbulence is homogeneous. This is the case for round jets where there exists homogeneity in azimuthal direction. In the case where the flow is not statistically stationary and does not show homogeneity, average can be done between repetitions of the same experiment [6] in the same way that averages may be defined for URANS.

When computing scalar variance or subgrid stresses it is important to note that the LES subgrid model only provides one part of these variables since there exists a contribution from the solved motions. In order to calculate it, we note that the variance of an instantaneous variable ϕ values $\langle\phi^2\rangle - \langle\phi\rangle^2$. Assuming that $\langle\phi\rangle \simeq \langle\overline{\phi}\rangle$ and $\langle\phi^2\rangle \simeq \langle\overline{\phi^2}\rangle$ the total variance of ϕ is approximated as

$$\langle\phi^2\rangle-\langle\phi\rangle^2\simeq[\langle\overline{\phi}^2\rangle-\langle\overline{\phi}\rangle^2]+[\langle\overline{\phi^2}-\overline{\phi}^2\rangle] \tag{2.51}$$

The first term between brackets corresponds to the solved variance since it is computed from the filtered field $\overline{\phi}$ while the second term is the variance contribution computed from the subgrid model that will be described in subsequent sections.

This reasoning may be applied to τ_{ij}^{sgs} assuming similar hypotheses

$$\langle u_i\, u_j\rangle - \langle u_i\rangle\langle u_j\rangle \simeq [\langle \overline{u_i}\ \overline{u_j}\rangle - \langle \overline{u_i}\rangle\langle \overline{u_j}\rangle] + [\langle \overline{u_i\, u_j} - \overline{u_i}\ \overline{u_j}\rangle] \tag{2.52}$$

Again the first term in brackets is obtained from solved motions while the second terms is modelled and corresponds to the subgrid scale stress tensor.

2.3.3.2 Turbulent fluxes modelling

In the previous sections RANS and LES equations, which are formally identical, were presented. These equations contain new terms due to the turbulent fluxes that represent new unknowns and require to be modelled. This is the closure problem and since there are more unknown than equations the system is said to be unclosed. The modelling of these terms is the goal of the turbulent model and in order to tackle with it, different approaches have been proposed.

It is important to remark again that RANS turbulence models have to describe all the scales of the flow including the largest ones, which take the energy from the mean flow and are affected by the boundary conditions and the domain geometry and, hence, are anisotropic. Due to the great variety of flows that may be found, these scales show different behaviour and it is almost impossible to formulate a model of general purpose. For this reason there exists a large number of them, each one addressed to specific flow configurations.

On the contrary, LES models are expected to be more universal since they solve only the small vortexes which tend to be isotropic. Therefore, LES simulations are in principle more reliable than RANS and this is one of the strongest points in favour of them. Obviously, the success of an LES simulation does not only depends on the model itself but on the quality of the mesh and the boundary conditions. In fact, as part of the turbulent kinetic energy is solved there exist recommendations in the literature that estimate that an accurate LES simulation should solve at least 80% of the total turbulent kinetic energy [28].

In addition, as the computational cost of an LES simulation is several orders of magnitude higher than a RANS simulation, LES turbulence models tend to be simpler with only one transport equation as much.

For both frames there exist two types of models in order to describe the turbulent fluxes[28]

1. Models based on the eddy viscosity hypothesis: they are based on the Boussinesq or turbulent-viscosity hypothesis and the gradient diffusion hypothesis which relate the turbulent fluxes with the solved quantities by means of a turbulent viscosity/diffusivity. Then the problem is reduced to find this turbulent viscosity/diffusivity.

2. Models not based on the eddy viscosity hypothesis: do not make use of the Boussinesq and the gradient diffusion hypotheses. Instead they pose equations for the Reynolds stresses or are based on scale similarity arguments in order to solve the turbulent fluxes.

In the following the turbulent-viscosity and the gradient diffusion hypotheses are explained since they have played a prominent role in the theory of turbulence for more than one century and are the base for a great number of RANS and LES turbulence models.

First, consider the anisotropic or deviatoric tensor of the Reynolds stress tensor, $(\tau_{ij}^R)^d$, which is defined as

$$(\tau_{ij}^R)^d = \overline{u_i' \, u_j'} - \frac{2}{3} k \, \delta_{ij} \tag{2.53}$$

The turbulent-viscosity or Boussinesq hypothesis establishes a similarity between Newton's stresses law and the anisotropic part of Reynolds stresses and states that

$$-\rho \, (\tau_{ij}^R)^d = -\rho \, \overline{u_i' \, u_j'} + \frac{2}{3} \rho \, k \, \delta_{ij} = 2\rho \, \nu_T \, \overline{s_{ij}} = 2\mu_T \, \overline{s_{ij}} \tag{2.54}$$

where μ_T is the turbulent or eddy viscosity and ν_T is the kinematic turbulent viscosity[29]. In principle, ν_T and μ_T depend on $(\vec{x}, t)$.

In the same way, the gradient diffusion hypothesis extends Fourier and Fick's laws to the context of turbulent modelling assuming that the turbulent flux of any variable ϕ (different from the velocity) is

[28] It is important to note that most of the turbulence models were conceived for incompressible flows although they are directly applied (or with slight modifications) to compressible flows and, more particularly, to reactive flows.

[29] For compressible flows Boussinesq hypothesis is rewritten as $-\overline{\rho} \widetilde{u_i'' \, u_j''} + \frac{2}{3} \overline{\rho} k \, \delta_{ij} = 2\mu_T \, (\widetilde{s_{ij}} - \frac{1}{3} \frac{\partial \widetilde{u_k}}{\partial x_k} \, \delta_{ij})$. Note its similarity with equation 2.4.

$$-\overline{u_i'\,\phi'} = \Gamma_T \frac{\partial \overline{\phi}}{\partial x_i} \tag{2.55}$$

where Γ_T is the turbulent diffusivity. In general, Γ_T is a function of $(\vec{x}, t)$.

Substituting equations 2.54 and 2.55 into averaged/filtered fluid mechanics equations leads to diffusion terms of the form $\nabla \cdot (\mu_{eff} \nabla u_i)$ and $\nabla \cdot (\Gamma_{eff} \nabla \phi)$. The subscript eff refers to the effective diffusivity which is the sum of the laminar and the turbulent ones, that is, $\mu_{eff} = \mu + \mu_T$ and $\Gamma_{eff} = \Gamma + \Gamma_T$. In RANS $\mu \ll \mu_T$ and then, it may be approximated $\mu_{eff} \simeq \mu_T$. However, for LES it is expected that μ is non-negligible compared to μ_T and both contributions to μ_{eff} have to be considered. Idem for Γ_{eff}.

Assuming Boussinesq and gradient diffusion hypotheses leads to $\wp \geq 0$ and $\wp_\phi \geq 0$, that is, these terms are source terms or equivalently they produce turbulent kinetic energy and scalar variance[30]. This means that these hypotheses do not allow backscattering. This may be acceptable for RANS approach but not always in LES context [29].

Dimensionless numbers for the turbulent viscosity and diffusivity are defined in a similar way to those given previously in 2.16, 2.17 and 2.18 and take values close to unity for gases.

It is worth mentioning that, for high Reynolds numbers, turbulent viscosity scales with velocity and length characteristic scales of the flow [6].

Regarding the validity of previous hypotheses, it is important to note that Newton, Fourier and Fick's laws establish a relationship between fluxes and variables at molecular level. On the contrary, Boussinesq and gradient diffusion hypotheses assume similar laws for fluxes that gather the impact of the whole range of scales and variables related to the largest scales. More particularly, the turbulent-viscosity hypothesis assumes that Reynolds stresses and the mean strain rate tensor are aligned. Similar considerations for the gradient diffusion hypothesis between the turbulent flux and the mean gradient.

In fact, Boussinesq hypothesis will be only valid when the flow evolves slow enough to allow that such flow reaches an equilibrium with the local conditions leading to a proportionality between mean strain rates and Reynolds stresses

[30] To be rigorous $\wp \geq 0$ always occurs for incompressible flows. For compressible flows production is the sum of a non-negative term $2\mu_T \widetilde{s}_{ij}\, \widetilde{s}_{ij}$ and a term related to velocity divergence that could be negative. Nevertheless, it is expected this term to be small compared to $2\mu_T \widetilde{s}_{ij}\, \widetilde{s}_{ij}$ in most engineering flows [10].

as in the case of jets, wakes, boundary layers, etc. Again, similar considerations are valid for the gradient diffusion hypothesis.

However, these hypotheses may fail in a general flow as some experiments confirm [30]. Notwithstanding, they provide the easiest procedure to solve the closure problem and, as said before, in some flows, like shear flows, the hypotheses are fulfilled [6].

With all these tools it is possible to proceed to explain briefly the most important RANS and LES turbulence models, as described in the following section.

2.3.3.3 RANS turbulence models

Mixing length model

It is the simplest model based on the eddy viscosity hypothesis. This model is only valid for two dimensional flows where only one of the Reynolds stresses is important and, hence, there is only one characteristic length scale in the flow. We call x_1 the flow preferential direction and x_2 its perpendicular direction[31] and u_1 and u_2 their respective velocities. Based on dimensional arguments, it is established that

$$\nu_T = C\,\vartheta\,\ell'_m \tag{2.56}$$

where ϑ and ℓ'_m are integral velocity and length characteristic scales, respectively, and C is a constant. Writing ϑ as

$$\vartheta = c\,\ell'_m \left|\frac{\partial \overline{u_1}}{\partial x_2}\right| \tag{2.57}$$

where c is a constant it is deduced that

$$\nu_T = \ell_m^2 \left|\frac{\partial \overline{u_1}}{\partial x_2}\right| \tag{2.58}$$

$$-\rho\overline{u_1' u_2'} = \rho\ell_m^2 \left|\frac{\partial \overline{u_1}}{\partial x_2}\right| \frac{\partial \overline{u_1}}{\partial x_2} \tag{2.59}$$

[31] As the model is addressed to two dimensional flows, x_3 corresponds to the spanwise direction.

ℓ_m is the mixing length and comprises the previous constants C, c and ℓ'_m. ℓ_m is a measure of the flow characteristic length that is algebraically related to the mean flow length scale.

The model provides excellent results for free shear flows as well as wall flows with slow changes in the flow direction.

*$k-\varepsilon$ **model***

The $k-\varepsilon$ model [31] is one of the most extended models because it describes the dynamics of turbulence with two transport equations making the model completely affordable from a computational point of view. Based on similar arguments that those exposed for the mixing length model and with previous relationships it is found that

$$\nu_T = C\,\vartheta\,\ell'_m = C_\mu \frac{k^2}{\varepsilon} \tag{2.60}$$

with C_μ a constant. The variables k and ε are modelled with the following transport equations (standard $k-\varepsilon$ model)

$$\frac{\partial(\rho\,k)}{\partial t} + \frac{\partial(\rho\,\overline{u_i}\,k)}{\partial x_i} = \frac{\partial}{\partial x_i}\left[\left(\mu + \frac{\mu_T}{\sigma_k}\right)\frac{\partial k}{\partial x_i}\right] + 2\mu_T\,\overline{s_{ij}}\;\overline{s_{ij}} - \rho\varepsilon \tag{2.61}$$

$$\frac{\partial(\rho\,\varepsilon)}{\partial t} + \frac{\partial(\rho\,\overline{u_i}\,\varepsilon)}{\partial x_i} = \frac{\partial}{\partial x_i}\left[\left(\mu + \frac{\mu_T}{\sigma_\varepsilon}\right)\frac{\partial \varepsilon}{\partial x_i}\right] + C_{\varepsilon 1}\,\frac{\varepsilon}{k}\,2\mu_T\,\overline{s_{ij}}\;\overline{s_{ij}} - C_{\varepsilon 2}\,\rho\frac{\varepsilon^2}{k} \tag{2.62}$$

The transport terms (those written with a divergence) are modelled with the transport gradient diffusion hypothesis. Due to this term equations are elliptic. The other terms correspond to the production and the dissipation of k and ε. Production and dissipation for ε are assumed proportional to the corresponding terms for k by a factor ε/k (and the constant factors). Physically, this intends to reproduce the fact that the variations of k and ε are linked, that is, the increase/decrease of k produces an increase/decrease of ε [10].

Table 2.1 gives the standard values for the $k-\varepsilon$ model constants.

When dealing with wall flows wall functions are used and, consequently, it is not necessary to integrate the equation in the boundary layer.

Table 2.1. *Standard values for the $k-\varepsilon$ model constants.*

$C_\mu = 0.09$	$\sigma_k = 1$	$\sigma_\varepsilon = 1.3$	$C_{\varepsilon 1} = 1.44$	$C_{\varepsilon 2} = 1.92$

The model provides accurate results for internal flows where Reynolds shear stresses are the most important ones and there exists a balance between production and dissipation of the turbulent kinetic energy. However, there exist discrepancies when dealing with free shear flows where the equality between production and dissipation is not fulfilled in all the flow regions. In the case of jets, the $k-\varepsilon$ model overestimates the spreading rate and, consequently, underestimates the spray penetration[32]. In these cases, the model constants are adjusted or new terms are introduced in the equations [32]. The model fails when describing highly strained flows and swirling flows too.

Spalart-Allmaras model

It is a model based on the eddy viscosity hypothesis devised to calculate external flows with an economical computational cost [33]. The model poses a transport equation for the kinematic viscosity parameter $\widetilde{\nu}$ and an algebraic expression for a characteristic length scale. Then

$$\nu_T = \widetilde{\nu} f_{\nu 1} \tag{2.63}$$

where $f_{\nu 1}$ is a wall-damping function which modulates the ratio $\nu_T/\widetilde{\nu}$ from 0 to 1 depending on the Reynolds number.

The model gives accurate results for external aerodynamic applications. It has been applied to turbomachinary calculations too.

$k-\omega$ model

This model solves the transport equations for k and ω, where ω is defined as the turbulence frequency $\omega = \varepsilon/k$ [34]. Then the turbulent viscosity is proportional to $\rho\, k/\omega$.

This model does not require the use of wall-damping functions for low Reynolds applications. However, it shows a high sensitivity to the value of ω in the free stream boundary condition. To avoid these problems hybrid models that solve $k-\omega$ model in the near-wall region and $k-\varepsilon$ far from the wall have been formulated [35, 36].

[32] All these concepts will be explained in detail in section 2.5.

All the models described so far make use of the Boussinesq hypothesis which assumes some kind of isotropy for all the normal stresses that may lead to some deviations. In addition, they fail when describing extra strain and body forces. In order to solve these problems the Reynolds stress equation model (RSM), which is described in the following, was devised.

Reynolds stress equation model

The Reynolds stress equation model (RSM) or the second-moment closure model [37] is not based on the eddy viscosity hypothesis and has the ability to describe anisotropy for the Reynolds stresses. Transport equations for each of the Reynolds stresses (6 in total) together with one for ε are required. These equations describe the total derivative of the Reynolds stresses as the combination of production, dissipation, diffusion, transport due to turbulent pressure-strain rate interactions and rotation for the Reynolds stresses.

This model involves a high computational cost, however, this drawback is compensated by its ability to describe accurately a great deal of flows.

Algebraic stress model

The high computational cost involved in solving the transport for the Reynolds stresses prompted the search of new approaches that while retaining the ability of the model to describe the anisotropy of the Reynolds stresses reduced drastically the use of computational resources. In the algebraic stress model [38, 39] the convective and diffusive terms for the Reynolds stresses equations are removed or modelled reducing the set of equations to an algebraic system. This system is solved in conjunction with the transport equations for k and ε.

Although this model may incorporate anisotropic effects for Reynolds stresses it does not show a clear improvement compared to $k-\varepsilon$ model [10].

Other models

There exist in the literature other models such as the non-linear $k-\varepsilon$ model. In this model it is assumed that turbulence does not depend only on the local variables but on the rate of change of the mean strain rate of the fluid particle [40]. Other models include additional quadratic terms written as a function of the product of mean strain rate and vorticity [41].

In order to improve the results for highly strained flows models the Renormalization Group (RNG) $k-\varepsilon$ model was proposed [42]. However, there does not exist an evident improvement of this model compared to standard $k-\varepsilon$ model for all flow configurations.

2.3.3.4 LES turbulence models

Smagorinsky model

Proposed by Smagorinsky in 1963, it is the first and simplest model in the LES context. It is argued that as the smallest scales tend to be isotropic, then Boussineq hypothesis may provide good predictions of the flow since the largest vortexes are solved. This leads to write[33]

$$\overline{u_i' \, u_j'} = -2\nu_T \, \overline{s_{ij}} + \frac{1}{3}\overline{u_k' \, u_k'} \, \delta_{ij} \tag{2.64}$$

Notwithstanding, in practice, Leonard and cross stresses are included in the previous expression leading to

$$\tau_{ij}^{sgs} = \overline{u_i \, u_j} - \overline{u_i} \; \overline{u_j} = -2\nu_T \, \overline{s_{ij}} + \frac{1}{3}\tau_{kk}^{sgs} \, \delta_{ij} \tag{2.65}$$

Based on similar arguments that the mixing length model and taking the characteristic length scale as Δ this yields

$$\mu_T = \rho \, (C_{sgs}\Delta)^2 \, |\overline{s}| = \rho \, (C_{sgs}\Delta)^2 \sqrt{2 \, \overline{s_{ij}} \; \overline{s_{ij}}} \tag{2.66}$$

$|\overline{s}| = \sqrt{2 \, \overline{s_{ij}} \; \overline{s_{ij}}}$ is the characteristic filtered rate of strain. The constant value C_{sgs} ranges from 0, for laminar flows, to 0.2 forcing to adjust this value which depends on the flow configuration. To improve the performance of this issue the dynamic model was proposed, as described in the following.

Moreover, as C_{sgs} is always positive it is easily deduced that the production term of the subgrid scale turbulent kinetic energy $k_{sgs}(= 1/2 \, \tau_{ii}^{sgs})$ [34] is always positive. This means that energy is transferred from the filtered scales to the unresolved scales, that is, the model does not allow backscatter. However, this does not correspond with reality since it is known that small vortexes may transfer energy to the large ones and, in this case, the production term would be negative [29].

Dynamic Smagorinsky model

In order to improve the performance of the Smagorinsky model the idea of the dynamic model [43] is to compute the value of C_{sgs} at each point and

[33] We will use the same nomenclature that that given for the turbulent viscosity in RANS models, ν_T, to refer to the eddy viscosity of the residual motions for LES models.

[34] From a rigorous point of view this is not a subgrid scale turbulent kinetic energy.

instant in the flow. For this purpose, the subgrid stresses are written for two filters (related to the filter widths Δ and $\widehat{\Delta}$).

$$\tau_{ij}^{sgs} = \overline{u_i\, u_j} - \overline{u_i}\ \overline{u_j} \tag{2.67}$$

$$T_{ij}^{sgs} = \widehat{\overline{u_i\, u_j}} - \widehat{\overline{u_i}}\ \widehat{\overline{u_j}} \tag{2.68}$$

Hence, subtracting previous expressions, Germano's identity may be obtained

$$L_{ij} = T_{ij}^{sgs} - \widehat{\tau_{ij}^{sgs}} = \widehat{\overline{u_i}\ \overline{u_j}} - \widehat{\overline{u_i}}\ \widehat{\overline{u_j}} \tag{2.69}$$

Then, using the Smagorinsky model and assuming the same constant C_{sgs} for both subgrid stresses

$$L_{ij}^{d} = C_{sgs}(2\Delta^2\, \widehat{\overline{s}\, \overline{|s_{ij}|}} - 2\widehat{\Delta^2}\, \widehat{|\overline{s}|}\ \widehat{\overline{s_{ij}}}) \tag{2.70}$$

where $L_{ij}^{d} = L_{ij} - 1/3\, L_{kk}\, \delta_{ij}$ is the deviatoric part for L_{ij}. L_{ij} may be understood as a Leonard stress and is computed from the solved filtered velocity field $\vec{\overline{u}}$.

Combining subscripts equation 2.70 leads to five independent equations where the only unknown is C_{sgs}. In order to minimize the error of C_{sgs} computation, it is usual to find it from applying least-square calculation. This procedure gives rise to large fluctuations of C_{sgs} and unstable LES calculations. To avoid this, the value of C_{sgs} is averaged in time or space providing more accurate results.

One eddy equation model

Another approach is to transport k_{sgs} leading to a similar transport equation to 2.32 [44]. Then

$$\mu_T = \rho\, C'_{sgs}\, \Delta\, \sqrt{k_{sgs}} \tag{2.71}$$

with C'_{sgs} a constant model.

It is clear that this model contains a higher physical level than the Smagorinsky model since the dynamics of k_{sgs} are solved. In addition, other of the benefits of transporting k_{sgs} is that it allows the use coarser meshes.

This model may be used in conjunction with the dynamic model in order to better adjust the constant C'_{sgs}.

Dynamic structure model

Different to the previous models based on the Boussinesq hypothesis, the dynamic model [29] was proposed as a way to improve results of models based on the eddy viscosity hypothesis since such hypothesis is not completely fulfilled in general. The dynamic model does not make use of Boussinesq hypothesis and states that

$$\tau_{ij}^{sgs} = c_{ij}\, k_{sgs} \tag{2.72}$$

where c_{ij} are the elements of a tensor that has to be determined. Then, in a similar way that other models, the subgrid stress tensor is written for other filter size and it is assumed that c_{ij} does not change with the filter size

$$T_{ij}^{sgs} = c_{ij}\, K_{sgs} \tag{2.73}$$

where K_{sgs} is the subgrid scale turbulent kinetic energy for this filter size. Then, with the aid of Germano's identity

$$L_{ij} = T_{ij}^{sgs} - \widetilde{\tau_{ij}^{sgs}} = c_{ij}\, K_{sgs} - \widetilde{c_{ij}\, k_{sgs}} \tag{2.74}$$

If the coefficients c_{ij} are extracted from the filtering operation (fields not depending strongly on position) algebraic equations are obtained. On the contrary, if they are not extracted integral equations are found. In the first case, it is easily deduced that

$$\tau_{ij}^{sgs} = L_{ij} \frac{2\, k_{sgs}}{L_{mm}} \tag{2.75}$$

In addition, k_{sgs} is transported expressing the budget of energy in a similar way than in the one eddy equation model.

It is worth mentioning that the model fulfils some additional constrains that would be desirable for any turbulence model such as frame invariance, solvability, etc. This model has been successfully applied to the calculation of diesel sprays [45–47] and is applied to the LES calculations of this work.

Other models

In a similar way than the RSM model for RANS, the Reynolds stresses may be transported in the LES frame. This type of models are especially useful when dealing with flows that show a clear anisotropic behaviour.

Another approach is the scale similarity model [48] where it is assumed that the subgrid stresses are controlled by the smallest resolved motions in the same way that they are determined by the largest unresolved motions leading to $\tau_{ij}^{sgs} = C(\overline{\overline{u_i}\,\overline{u_j}} - \overline{\overline{u_i}}\,\overline{\overline{u_j}})$. Due to numerical instabilities a term in the form given by expression 2.64 is added. It has been proved that this model provides accurate results.

2.4 Combustion theory

This section describes the fundamentals of combustion theory. In a general sense, combustion is the ignition of a fuel in a fluid medium. Fluid mechanics and turbulence have been described in the previous sections while the chemical aspects have been postponed for next paragraph 2.4.1. Subsequently, they will be put all together in order to provide a theoretical background of turbulent combustion most important aspects and models.

2.4.1 Auto-ignition

In this section a brief description of the chemical kinetics taking place during auto-ignition is given. It is only focused on chemistry itself and no additional processes (convection, diffusion, etc.) are considered.

Auto-ignition is the spontaneous ignition (no external sources) and burning of a fuel for given thermodynamic conditions. Only systems with species composed by atomic elements C, H, O and N are considered since they are the most typical in engineering applications[35].

During auto-ignition molecular bounds are broken releasing an amount of energy that increases the mean kinetic energy of the molecules and, hence, augments system temperature. During this process hundreds of species are produced and thousands of reactions occur, taking place with very different time scales. It is apparent that the diversity of time scales complicates the numerical resolution and, in general, the differential system of equations that governs this process is stiff.

[35] Clearly fuel may contain impurities such as S, additives like Pb and small concentrations of Ar.

A general reaction j may be written in the form

$$\sum_{i=1}^{N_s} \nu'_{i,j} M_i \leftrightarrows \sum_{i=1}^{N_s} \nu''_{i,j} M_i \qquad j = 1, \ldots, N_r \tag{2.76}$$

This system is composed by N_r reactions and N_s species denoted by M_i. $\nu'_{i,j}$ and $\nu''_{i,j}$ are the molar stoichiometric coefficients. It is defined $\nu_{i,j} = \nu''_{i,j} - \nu'_{i,j}$. The arrows in both directions indicate that the reaction may occur in both directions, that is, it is reversible.

Each reaction develops at an instantaneous rate of progress $\dot{q}_j$. Then, the reaction rate of species i, $\dot{\omega}_i$, is easily obtained from the whole set of reactions as

$$\dot{\omega}_i = W_i \sum_{j=1}^{N_r} \nu_{i,j}\, \dot{q}_j \tag{2.77}$$

where W_i is the molecular weight for species i. Clearly, by virtue of mass conservation $\sum_{i=1}^{N_s} \dot{\omega}_i = 0$.

The objective of chemical kinetic theory is to predict the temporal evolution of the set of species mass fractions Y_i and thermodynamic variables once the system of chemical equations 2.76 and the initial and boundary conditions are known. For this purpose, equations for $\dot{\omega}_i$ and energy are required.

If the pressure of the system is constant during the reaction then the total enthalpy is conserved. Regarding the composition evolution, and denoting molar concentration for species M_i as $[M_i]$, it is known from experimental observations that the reaction rate for reaction j can be expressed as

$$\dot{q}_j = k_{f,j} \prod_{i=1}^{N_s} [M_i]^{\nu'_{i,j}} - k_{b,j} \prod_{i=1}^{N_s} [M_i]^{\nu''_{i,j}} \tag{2.78}$$

where $k_{f,j}$ and $k_{b,j}$ are forward and backward specific reaction rates, respectively. The most common approach is to describe $k_{f,j}$ and $k_{b,j}$ by means of the Arrhenius theory which expresses any specific reaction rate k as

$$k = A\, T^{\beta} \exp\left(-\frac{E_a}{RT}\right) \tag{2.79}$$

where E_a is the activation energy, that is, the minimum required energy for the molecules to react, R is the universal perfect gas constant and A and β are constants. From this expression an interesting observation is revealed, namely, chemistry is strongly affected by temperature. In fact, it shows an exponential dependence with T. This is the reason why chemistry is very slow at low temperatures while once the reaction initiates, that is, substantial increments of temperature are detected, it occurs in extremely reduced amounts of time.

When the chemical equilibrium is reached then $\dot{q}_j = 0$ and $k_{f,j}$ and $k_{b,j}$ are related by the equilibrium constant k_{eq}

$$k_{eq} = \frac{k_f}{k_b} = \frac{\prod_{i=1}^{N_s} [M_i]_{eq}^{\nu''_{i,j}}}{\prod_{i=1}^{N_s} [M_i]_{eq}^{\nu'_{i,j}}} = \prod_{i=1}^{N_s} [M_i]_{eq}^{\nu_{i,j}} \tag{2.80}$$

k_{eq} is tabulated and may be computed from Gibbs free energy and temperature.

Then the transient chemical evolution may be found solving the energy equation, from which the temperature is obtained knowing the composition, coupled with the ODE system[36] $dY_i/dt = \dot{\omega}_i$, where the source term is computed from equations 2.77, 2.78, 2.79 and 2.80.

For large times equilibrium is reached. In the combustion context, equilibrium temperature is typically called adiabatic flame temperature when there are not heat losses, that is, the temperature reached when all the energy released during the complete reaction is converted into thermal energy. The adiabatic flame temperature shows strong dependence with the equivalence ratio, oxygen concentration in air, initial temperature, etc.

In general, during the auto-ignition process different types of reactions can be distinguished. These groups of reactions may be written schematically in the following form:

$$A \rightarrow C\cdot \tag{2.81}$$

$$A + C\cdot \rightarrow P + \alpha\, C\cdot \tag{2.82}$$

$$C\cdot \rightarrow P \tag{2.83}$$

[36] Acronym stands for ordinary differential equation.

where $C\cdot$ represents a radical or chain carrier, P are products and α is a multiplicative factor. Reaction 2.81 is an initiating reaction where a radical $C\cdot$ is produced from reactant A. Initiating reactions are the first that take place and are very slow and endothermic.

Reaction 2.82 is a propagation reaction where new radicals are produced from radical $C\cdot$. When $\alpha > 1$ the propagation reaction is known as a branching reaction since several radicals are produced from one radical. These reactions are fundamental during auto-ignition since they increase the radical pool and lead to explosion. Moreover, they are not necessarily fast reactions.

Finally, termination reactions 2.83 recombine radicals to give stable products or new radicals with low reactivity.

It is revealed the importance of achieving a radical pool or a critical concentration of radicals in order to start ignition. As will be seen later, Livengood and Wu integral is based on this observation in order to predict ignition delay. In addition, this radical pool cannot be achieved for all the thermodynamics conditions and compositions. On the one hand, for given thermodynamics conditions the inflammability limits provide the minimum and maximum values of the equivalence ratio for which the reaction may propagate once ignition has been initiated. On the other hand, for a given composition and pressure the ignition temperature is the minimum temperature value for which combustion occurs and delimits the explosion limits or the auto-ignition line.

In addition, from the description of the different reaction types, it is revealed that, when boundary conditions are such that lead to explosion, ignition is composed of different stages. First, a period where initiating and some propagation reactions take place and negligible amounts of heat are released occurs. This period of time is called ignition delay or induced time and finishes when the radical pool reaches a critical concentration. Then, explosion takes place where very fast reactions occur and release high amounts of heat that lead to equilibrium conditions.

This behaviour is found in short hydrocarbons chains, however, for long chains this process may be more complex since ignition proceeds in two stages: after ignition delay a first ignition occurs, where temperature increases around 200 K, followed by a second ignition delay where chemical activity drops that, finally, leads to a fast combustion where high temperatures are reached. The state during the second ignition delay is known as cool flame due to the modest temperature increment and the blue luminosity produced by formaldehyde (CH_2O) which is accumulated during this stage [9, 49].

For these long chain hydrocarbons, the auto-ignition line drawn in the temperature-pressure or $T - p$ representation is not decreasing in the whole range of temperatures. In fact, it is decreasing for low temperatures, increasing for temperatures around 900 K and again decreasing for higher temperatures. The shape of this line explains why the ignition delay, when represented against temperature, first decreases with temperature, then increases and finally decreases again. This behaviour, higher ignition delays when increasing the temperature (only for a range of temperatures), is known as the negative temperature coefficient (NTC).

In order to understand why the two stage ignition and the NTC zone is observed it is necessary to explain briefly the reactions that take place during the auto-ignition process. More details are found in [9, 49, 50].

Depending on the initial temperature different chemical paths may be followed. For low temperatures ($T < 1400K$) fuel (with generic composition RH where R is any organic radical) oxidation is initiated due to an H atom abstraction by the oxygen molecule. This abstraction may be carried out by other radicals different to O_2 once they are produced. For $T < 900$ K, R reacts with O_2 giving RO_2 that transforms into alkyl hydroperoxid (QOOH) which in turn reacts yielding OH radicals. This accumulation of radicals leads to explosion.

However, at intermediate temperatures two relevant chemical paths take place. In the first one, as happens for lower temperatures, QOOH reacts with O_2 and ketohydroperoxide + 2 OH + radical is obtained. This is a branching reaction at intermediate temperatures. However, in the second one, QOOH dissociation produces olefins, ether, HO_2, OH and other products. These reactions do not branch and, hence, provoke a decrease in reactivity. Therefore, for temperatures around 900 K there exists a competition between these two chemical paths that induce a reduction of reactivity and generate the cool flame as well as the the NTC zone.

The second path produces HO_2 which reacts to provide H_2O_2, which is a very stable species. When the temperature slowly increases and overtakes a threshold value the peroxide H_2O_2 decomposes into 2 OH (branching reaction). OH concentration soars and this leads to the end of the cool flame and the start of the high temperature combustion.

During the cool flame, the concentration of aldehydes, such as CH_2O, and peroxides, like H_2O_2, increases. At the end of the cool flame these species are consumed while OH concentration increases exponentially. Therefore, species such as CH_2O and H_2O_2 may be used as low temperature combustion tracers while OH traces high temperature combustion.

During the high temperature reactions, CH_2O combines with OH and generates CO which in turn reacts with OH in order to produce CO_2. Oxidation from CO to CO_2 is one of the most important reactions in fuel oxidation since great amounts of heat are released during this reaction.

At high temperature fuel decomposition is produced via thermal dissociation yielding olefins which are very unstable at these high temperatures and decompose or react with oxygen producing H_2O and CO. In the same way that previously, CO oxidises into CO_2.

The two stage ignition is fundamental in order to explain how combustion proceeds in diesel sprays and, hence, predicting both ignition delays is a relevant issue. In order to illustrate previous process figure 2.3 shows the temporal evolution for temperature and different species related to the low and high temperature combustion.

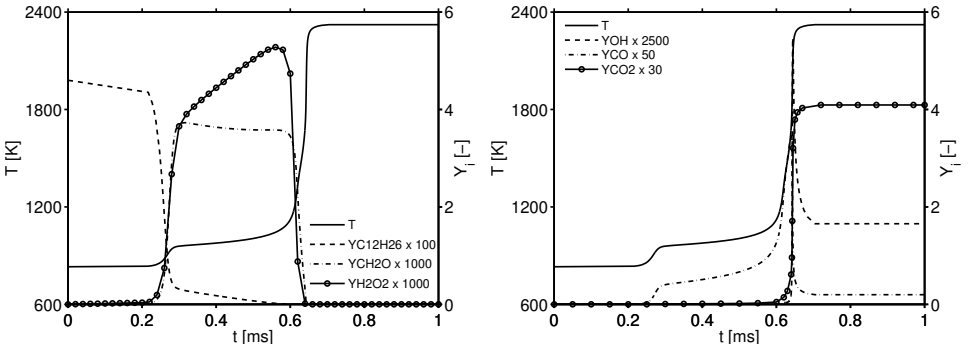

Figure 2.3. *Temporal evolution for temperature and different species. Left figure shows species related to low temperature chemistry while species in right figure appear during high temperature combustion. Evolution corresponds to a stoichiometric mixture of dodecane auto-ignition with diesel representative boundary conditions.*

In figure 2.3 the two stage ignition separated by the cool flame period is clearly distinguished. It is interesting to mention that during the first ignition delay only small amounts of fuel are consumed. When the mixture ignites at low temperature, fuel is almost depleted and species such as CH_2O, H_2O_2 and CO are produced. During the cool flame there exists an accumulation of these species until a critical temperature is reached and OH is produced consuming previous species and releasing high amounts of heat. At the second stage, final species like CO_2 are produced.

In addition, during high temperature combustion for rich mixtures, acetylene (C_2H_2) is produced. It generates benzene which is a highly stable molecule due to its resonant structure. This molecule combines with other benzenes to form pyrene and other complex molecules. These molecules, known as polycyclic aromatic hydrocarbons (PAHs), contain great amounts of carbons and their coagulation form soot which is a characteristic pollutant of diesel engines. Soot models are quite complex since chemical and physical processes take place and they are not completely known. However, the prediction of molecules such acetylene and benzene, which are soot precursors, is important since they can provide qualitative information about the trends of soot formation.

Therefore, soot, which is caused by fuel pyrolysis, is formed in the rich mixture regions, since there exists an excess of carbon atoms, and temperatures higher than 1300 K [51]. As will be seen later, in a diesel spray, soot oxidation occurs when passing through the stoichiometric surface due to the high temperatures. The characteristic yellow/orange colour of diffusion flames is due to soot oxidation when crossing across the stoichiometric surface.

Other important pollutant formed during the last stages of combustion are nitrogen oxides (NO_x). They are produced when there exists an excess of oxygen (lean mixtures) and very high temperatures (around 1900 K and higher) are reached. Different mechanisms explain its formation although the thermal via described by Zeldovich [9, 52] is one of the most important, especially in the diesel flame.

Moreover, it is worth mentioning that when reaching high temperatures dissociation reactions occur converting part of the thermal energy into chemical energy (endothermic reactions) [9]. They may have noticeable effect on the adiabatic flame temperature and some minor species concentrations.

The reactions and species appearing during fuel oxidation are gathered in the chemical mechanism together with some properties. Due to the extremely high number of reactions and species they are simplified by means of different sensitivity techniques which mainly evaluate the relevance of each species and reaction in order to decide if they should be included assuming a given degree of accuracy. It is usual to impose equilibrium for fast reactions and radicals that react in very short times.

Finally, and due to its relevance, Livengood and Wu integral is described. Previously, the ignition delay concept was explained together with the auto-ignition curves. These curves are for constant thermochemical conditions and cannot be directly applied when the mixture suffers a temporal evolution of such variables as happens in a reciprocating engine.

Livengood and Wu integral [53] provides an estimation of the ignition delay for variable thermodynamic conditions. As ignition delay lasts until a critical concentration of radicals is cumulated, say $[X]_{crit}$, and chemistry advances with a chemical reaction rate fixed only by the instantaneous conditions $(T(t), p(t))$ [37], it can be stated that, if τ is the ignition delay for given (T, p) conditions, then

$$\frac{d[X]}{dt} = \dot{\omega}(t) = \frac{[X]_{crit}}{\tau(T(t), p(t))} \tag{2.84}$$

where the instantaneous reaction rate $\dot{\omega}$ is approximated as the mean reaction rate found for constant conditions (T, p) during its ignition delay. Equation 2.85 is easily integrated during ignition delay[38]

$$\int_0^{[X]_{crit}} \frac{d[X]}{[X]_{crit}} = \int_0^{t_{ID}} \frac{dt}{\tau(T(t), p(t))} \;\rightarrow\; 1 = \int_0^{t_{ID}} \frac{dt}{\tau(T(t), p(t))} \tag{2.85}$$

where t_{ID} is the ignition delay for the $(T(t), p(t))$ transient evolution. Then, the value t_{ID} is computed as the upper bound of the curve that encloses unity area for the function $1/\tau(T(t), p(t))$, where the evolution $(T(t), p(t))$ is imposed.

This is an extremely useful and simple relationship that has been used not only to predict ignition delays in diesel engines but to predict detonation in gasoline engines [53]. Improvements to this approximation may be found in [49].

With the whole theoretical background described along this chapter we can proceed to the explanation of the fundamentals of general combustion. Historically, combustion theory has been divided in premixed and non-premixed combustion and, more recently, in partially premixed combustion. Although the underlying physical and chemical processes are similar for all of them, most of the models take advantage of the own characteristics of each combustion type and, hence, are constrained to the combustion type for which they were formulated. In this chapter we follow this traditional description and sketch only the main aspects of premixed combustion while special attention is devoted to non-premixed and partially premixed combustion due to their

[37] It depends on composition too but previous to ignition only small radicals concentrations are produced and, hence, this dependence is omitted.

[38] $[X]_{crit}$ is assumed constant for all thermodynamic conditions.

relevance in diesel sprays. Only combustion by deflagration, that is, for low Mach numbers, is considered.

Additionally, due to the fundamental role played by scale separation concepts and asymptotic theories in turbulent theories, the explanation is first devoted to laminar combustion description which is the base of several turbulent combustion models. Subsequently, turbulent combustion theory and its modelling are described.

2.4.2 Laminar combustion

Laminar combustion is the cornerstone of several theories and models applied to turbulent combustion. Consequently, a separated paragraph is devoted to describe its most fundamental notions. First, and although this work is focused on diesel flame description and, hence, on partially premixed and non-premixed combustion, for the sake of completeness, premixed combustion is explained too[39]. Then, non-premixed laminar combustion theory is described.

2.4.2.1 Premixed combustion

Premixed combustion occurs when fuel and air are mixed prior to combustion. It is clear that in this case the limiting process is chemistry since reactants are already mixed.

A very important dimensionless number in the context of combustion is the Damköhler number which relates a characteristic physical time τ_{physic} (related to mixing) with a characteristic chemical time τ_{chem}

$$Da = \frac{\tau_{physic}}{\tau_{chem}} \tag{2.86}$$

From this it is observed that for premixed flames Damköhler number is close to 0. One of the simplest devices based on the premixed combustion is the Bunsen burner where fuel and air are mixed along a pipe. At the end of the pipe they are homogeneously mixed and a conical flame front is established which is first initiated by an external source. The flame front is a thin layer that separates the fresh mixture from the burnt gases. Moreover, due to the heat release there exists a drop in density between unburned and burnt gases

[39] In addition, some concepts of premixed combustion are required to understand partially premixed combustion.

and, in order to fulfil continuity, such drop induces an acceleration of the flow when passing through the flame front. The colour of the flame front is blue for lean mixtures, due to CH radicals, while yellow/red for rich mixtures as a consequence of soot oxidation.

The existence of a flame front that separates two flow regions with different energetic content and species concentration implies heat and species mass diffusion fluxes from burnt to unburned gases. This diffusion may be conceptualized as an advancement of the flame front superimposed to the flow velocity field and gives rise to the laminar burning velocity s_L concept. Therefore, s_L is the relative velocity at which the flame front propagates normal to itself with regards to the mean flow[40]. Typically, it is referred from fresh gases, that is, the flame front relative velocity seen from the flow at fresh gases.

The laminar burning velocity is a very useful concept that simply expresses the strength of diffusion and the different premixed combustion theories have been developed in the light of this concept. It is part of the solution of the transport equations and arises as an eigenvalue of the problem.

The laminar burning velocity is typically measured for plane flames and then is denoted as s_L^0. However, the flame front may be curved by hydrodynamic or Landau-Darrieus instabilities [54, 55] and/or thermophysical instabilities. The first one occurs as a consequence of the density jump at both sides of the flame front while the second one happens due to non-unity Lewis numbers implying different fluxes for energy and species. Depending on the flow these instabilities may reduce the flame front area or, on the contrary, increase it.

The curvature induced by the flow or the instabilities affects the laminar burning velocity. The corrected laminar burning velocity s_L may be found from s_L^0 and a curvature term which depends on the flame front curvature and a characteristic length known as Markstein length [56]. In the same way, density differences at both sides of the flame front modify the velocity field and induce new contributions known as gas expansion that may curve stream lines.

Finally, note that the existence of a sustained flame front implies an equilibrium between chemical production and diffusion transport (characterized by s_L). However, if diffusion fluxes increase in intensity too much, they cannot be compensated by chemical generation and flame extinguishes. This is clearly

[40]In the context of laminar combustion mean flow should be understood as the flow resulting from all species velocities.

seen near walls where heat losses quench flame. For this reason, the flame front does not reach the nozzle rim in a Bunsen burner and such phenomenon is also applied to mine lamps.

Until this point the flame front has been described as an extremely thin layer and no attention has been devoted to its inner structure. However, its analysis reveals that the flame front is composed of two main regions, namely, a preheat zone or diffusion layer and a reaction layer. The first one does not show chemical activity and delimits the region where diffusion is intense due to heat release and species production/consumption taking place in the reaction region. In the preheat zone diffusion and convection are of the same order of magnitude. Chemical activity is limited to the reaction zone where chemistry is balanced by diffusion. It is estimated that the reaction layer thickness ℓ_δ is one tenth of the preheat region thickness which ranges between 0.1 and 1 mm [57]. The sum of both thickness is the flame thickness ℓ_F.

Premixed combustion has been studied analytically by means of asymptotic theories. The main objective of such theories is to estimate the laminar burning velocity as well as describe the inner flame front structure. These theories assume typically one step irreversible and infinitely fast chemistry and for this reason the expressions correspond to an asymptotic behaviour.

The first description of the premixed flame dates back to 1883 and is due to Mallard and Le Chatelier [58]. It consists of an analysis based on integral quantities but provides a fundamental estimation of s_L, namely, $s_L \propto \sqrt{\lambda\ RR} = \sqrt{\lambda/\tau_{chem}}$, where λ is the thermal diffusivity and RR is a characteristic reaction rate inversely proportional to the chemical characteristic time τ_{chem}. However, the first theory were the asymptotic concepts were applied is due to Zeldovich, Frank-Kamenetskii and Semenov [59]. In this theory the different regions of the flame were solved and analytical expressions were obtained for temperature as well as an expression for s_L. The physical content which expresses the proportionality between s_L and $\sqrt{\lambda\ RR}$ obtained by Mallard and Le Chatelier was confirmed.

2.4.2.2 Non-premixed combustion

The other type of combustion occurs when fuel and oxidant are not mixed when entering in the combustion chamber and is called non-premixed combustion. In this case, fuel and oxidant first mix and then they burn. This type of combustion appears in candles or jets and sprays. One remarkable advantage of non-premixed combustion compared to premixed combustion is

that, since the flame cannot recede inside the nozzle, burners are safer (no flashback).

Typically, the mixing process is slower than the chemical oxidation and, consequently, these flames show high Damköhler numbers. Since mixing occurs owing to diffusive fluxes and is the limiting process this type of combustion is also known as diffusion combustion. In addition, as a consequence of the limiting combustion rate imposed by the velocity at which fuel and oxidant mix, it is said that is a mixing controlled combustion.

The most important configurations correspond to counterflow flames, where fuel and oxidant streams flow in opposite directions, and reactive mixing layers and sprays where they move in the same direction. Similar to the premixed combustion the flame can be separated in a diffusion layer and a reaction layer. However, different to the premixed flame, the diffusion flame does not show a characteristic velocity although it can be strained with different intensity. The more strained the diffusion flame is, the lower its thickness is.

One of the most important concept in non-premixed combustion is the mixture fraction. It can be defined for each atomic element and represents the total mass for that element found at a given mixture. From this definition, it is easily seen that it is given by

$$\frac{Z_{elem}}{W_{elem}} = \sum_{k=1}^{N_s} n_{elem,k} \frac{Y_k}{W_k} \tag{2.87}$$

where Z_{elem} is the mixture fraction for element $elem$, W is the molecular weight and $n_{elem,k}$ is the number of atoms of element $elem$ in species k. The interest of the mixture fraction is that although the species are generated and consumed and, therefore, their masses change, the mass of the atomic elements is conserved during the chemical reactions.

Combining the mixture fractions of the elements composing the fuel, the fuel mixture fraction Z is obtained. Therefore, Z measures the mass coming from the fuel for any mixture. As it does not change with chemical reactions this means that it is a conserved passive scalar[41] and is transported according to

$$\frac{\partial(\rho Z)}{\partial t} + \frac{\partial(\rho u_i Z)}{\partial x_i} = \frac{\partial}{\partial x_i}\left(\rho D \frac{\partial Z}{\partial x_i}\right) \tag{2.88}$$

[41]It is conserved because no source terms appear in its equation. It is passive because it does not affect density neither diffusivity and, therefore, has no effect on the flow.

If it is assumed that any reactive scalar ψ, that is, species mass fractions or temperature, only depends on the coordinates (Z, t) in a reactive flow, transport equations for these variables may be written in the mixture fraction space instead of the physical space by means of Crocco transformation leading to [7, 8]:

$$\frac{\partial \psi}{\partial t} = \frac{\chi}{2}\frac{\partial^2 \psi}{\partial Z^2} + \dot{\omega}_i \tag{2.89}$$

In physical terms this transformation implies assuming small changes in the tangent directions to mixture fraction level surfaces compared to the normal direction. In equation 2.89, χ is the scalar dissipation rate defined by

$$\chi = 2D\frac{\partial Z}{\partial x_i}\frac{\partial Z}{\partial x_i} \tag{2.90}$$

Note its similarity with the scalar dissipation rate term from equation 2.33 that justifies the name given to χ. In addition, χ measures the strength of convection and diffusion in the mixture fraction space since it is related to the strain rate a to which the flame is submitted. Equation 2.89 applied to the set of reactive scalars is used to solve the combustion structure in laminar flames.

This description of the laminar flames is applied to turbulent combustion in the frame of the flamelet concept. A detailed description of this relevant concept is given in chapter 3.

If chemistry is irreversible and infinitely fast (or extremely fast compared to other physical processes, such as mixing), then it only occurs at the stoichiometric mixture while at the rest of mixtures only products of this oxidation plus air at lean mixtures and fuel at rich mixtures are found[42]. This means that combustion takes place only at stoichiometry while in the rest of mixtures only diffusion happens. This situation was described by Burke and Schumann [60]. The structure of this combustion is given in figure 2.4 and is independent of χ.

In addition, this figure shows the chemical equilibrium solution, that corresponds to a reversible infinitely fast reaction and forces χ to be null. In this case fuel, oxidizer and products may coexist at the same location and time. Note how in complex hydrocarbons Burke-Schumann and chemical equilibrium solutions may differ significantly in the rich mixtures region.

[42] Considering infinitely fast chemistry implies that air and fuel react instantaneously when they meet. As combustion is supposed to occur at stoichiometry reactants cannot coexist in the rest of mixtures.

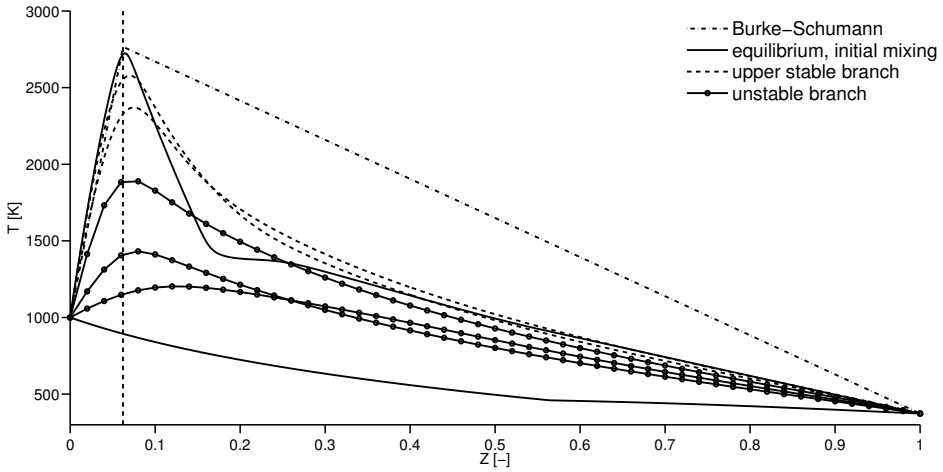

Figure 2.4. *Burke-Schumann, chemical equilibrium and several strained flames solutions as a function of mixture fraction. Vertical black dashed line indicates the stoichiometric mixture fraction. Profiles for heptane at representative diesel engine conditions.*

However, if chemistry is not so fast, finite rate chemistry effects are observed. Figure 2.4 gathers some examples of this situation where it is revealed that the final state of the flame depends on how strained the flame is (these solutions are referred as 'upper stable branch' and 'unstable branch' due to reasons given in the following). This strain rate is measured by χ and may be related to Damköhler number. In these cases there exists a region in the vicinity of the stoichiometric mixture fraction where combustion takes place while, in the rest of the domain, only diffusion is observed.

If we consider all the possible strained flames and fix the value of Z, we observe a relationship between temperature and Da with a S-shape as figure 2.5 shows. This curve is known as the S-curve. As the Damköhler number is proportional for a given mixture to the inverse of the scalar dissipation rate at stoichiometry, χ_{st}, the S-curve may be represented as a function of χ_{st}^{-1} too. The curve is sometimes directly represented as a function of χ_{st} and then takes the shape of an inverted S.

Different branches are observed in this curve. For high Damköhler numbers the steady temperature is close to the adiabatic temperature and defines a region where the flame may evolve from inert conditions to the upper branch.

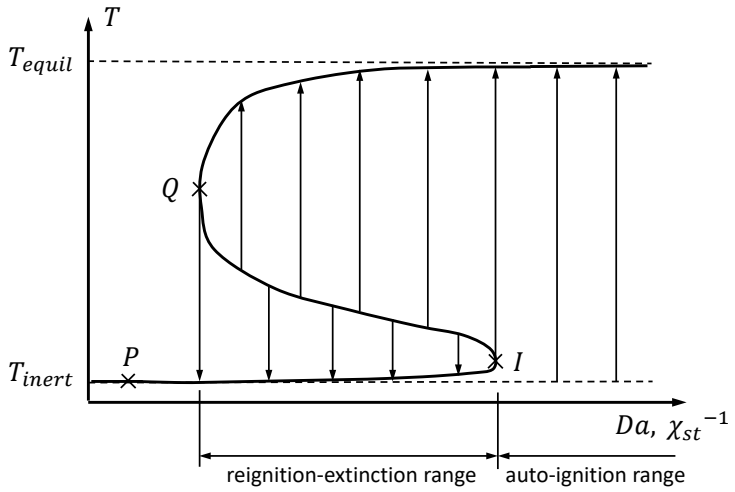

Figure 2.5. *S-curve composed by the whole set of temperature values as a function of Damköhler number or* χ_{st}^{-1}.

However, when increasing the strain rate (reducing Da) diffusion may be too large compared to chemical production leading to a possible extinction of the flame or directly to the impossibility of igniting.

This is illustrated in figure 2.5. Points with Damköhler numbers higher than that corresponding to point I, Da_i, may evolve from inert conditions to the upper branch and define the auto-ignition range. The interval from Da_q (Da at Q) to Da_i is referred to as the reignition-extinction range. For points with $Da < Da_i$ flames that start at inert conditions only evolve to branch PI, where temperature increments are marginal.

In the region defined by $Da_q < Da < Da_i$ three solutions or branches are observed. The intermediate branch QI is said to be unstable since small perturbations provoke that the flame ignites to the upper branch or quenches to the lower branch [61, 62]. The lower branch is reached from the extinction of a perturbed flame that starts from the unstable branch QI or from ignition starting at inert conditions (although this ignition produces negligible changes in temperature and composition). The scalar dissipation rate for point Q is denoted by χ_q and represents the maximum scalar dissipation rate belonging to the intermediate branch QI. For higher χ (or lower Da) the flame does not show chemical activity. Solutions belonging to the auto-ignition range are

shown in figure 2.4 as a function of Z and labelled as 'upper stable branch'. Likewise, solutions found in the reignition-extinction range are gathered in figure 2.4 and referred as 'unstable branch'. More details are found in next chapter.

2.4.3 Turbulent combustion

In this section the physical grounds of turbulent combustion are first explained and subsequently the most important models available in the literature are described. It is quite extended in turbulent combustion theory to describe the different combustion regimes by the comparison of laminar flame scales with characteristic turbulent scales. In this way, the result of this comparison leads to state how chemical and physical processes interact between them.

Based on the scales comparison, the scale separation concept, that is, one of the scales is much larger than the others, may be invoked to formulate the model. Thus, one of the processes is dominant and the problem dimensionality can be drastically reduced. The greater part of the turbulent combustion models makes use of this concept [7] since it is a way to circumvent the complex interaction between chemistry and turbulence. In addition, most of industrial devices working conditions are found in combustion regimes where these simplifications can be applied.

The main goal of any turbulence combustion model is to describe, on the one hand, how chemistry modifies the flow due to gradients generated by chemical reactions and, on the other hand, how turbulence influences on chemical production due to the gradients created by the flow motion. This is called turbulence-chemistry interaction (TCI) and describes the mutual action between chemistry and turbulence.

It is worth mentioning that combustion occurs at the smallest scales of the flow or even at scales smaller than Kolmogorov eddies. This means that in the frame of RANS or LES simulations, it is unavoidable to use some kind of TCI model since chemistry cannot be directly solved [28, 63]. Notwithstanding, it is expected, especially in the context of LES, that the better the flow is solved, the more accurate the simulation will be since some of the combustion model hypotheses will have less impact.

In the following, a qualitative description of combustion regimes for each of the three combustion modes is given.

2.4.3.1 Premixed combustion

Borghi, Peters and other authors have introduced a taxonomy for the regimes in premixed combustion [64, 65] by the comparison of the characteristic length scales ℓ_0 and ℓ_F, where ℓ_0 is the integral scale and ℓ_F is the flame thickness, and the integral velocity scale ϑ and the flame burning velocity s_L. Defining Karlovitz numbers as

$$Ka = \frac{\ell_F^2}{\eta^2} \tag{2.91}$$

$$Ka_\delta = \frac{\ell_\delta^2}{\eta^2} = \delta^2 Ka \tag{2.92}$$

Peters classified the different combustion regimes in a diagram similar to that shown in figure 2.6 [65]. In equation 2.92 ℓ_δ is the reaction layer thickness and δ is ℓ_δ/ℓ_F. In general, it is estimated that $\delta \sim 0.1$.

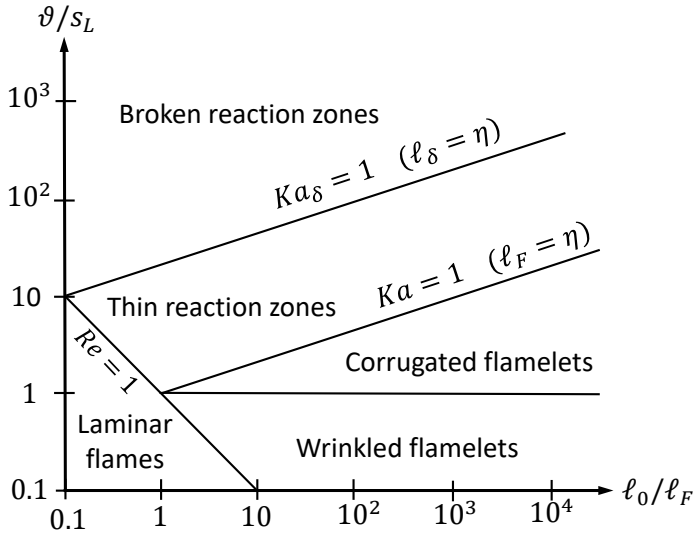

Figure 2.6. *Turbulent premixed flame diagram.*

Apart from the laminar regime, four turbulent combustion regimes ($Re > 1$) are identified:

1. Wrinkled flamelets: of no practical interest due to the extremely low turbulent velocities.

2. Corrugated flamelets: in this regime $Ka < 1$ and, hence, $\ell_F < \eta$, that is, the entire flame is embedded in the Kolmogorov eddies. As a consequence, the flame structure remains laminar since the smallest vortexes cannot distort the inner flame region. Thus, in this regime the interaction between the turbulent eddies and the flame is purely kinematic. The line $Ka = 1$ is called the Klimov-Williams criterion.

3. Thin reaction zone: in this combustion regime $Ka_\delta < 1$ and $Ka > 1$ and, hence, $\ell_\delta < \eta < \ell_F$. Thus, Kolmogorov eddies can enter in the preheat zone and modify it but not the reaction zone which remains laminar.

4. Broken reaction zone: in this regime $Ka_\delta < 1$ and, therefore, $\eta < \ell_\delta$. Turbulence can penetrate in the reaction layer and extinguish the flame as a consequence of the intense heat and species fluxes.

The corrugated and thin reaction zones regimes are those where combustion traditionally develops in industrial devices and, in consequence, they have been extensively studied. In the same way that the laminar burning velocity s_L is defined, it is useful to define a turbulent burning velocity s_T which is the burning velocity observed when averaging/filtering and is defined by

$$\dot{m} = \rho_u s_L A = \rho_u s_T A_T \tag{2.93}$$

where $\dot{m}$ is the mass burning rate, A is the instantaneous flame area, A_T is the averaged flame area and subscript u refers to unburned gases.

In 1940 Damköhler gave an estimation for s_T for the corrugated and thin reaction zone regimes [66]. In the first one, as the interaction between the flame front and the turbulent flow is kinematic, Damköhler established that

$$\frac{s_T}{s_L} = \frac{A}{A_T} \sim \frac{\vartheta}{s_L} \rightarrow s_T \sim \vartheta \tag{2.94}$$

On the contrary, for the thin reaction zone regime, turbulence modifies the intensity of transport phenomena in the preheat zone, that is, between the fresh gas and the reaction layer. Since $s_L \sim \sqrt{\lambda/\tau_{chem}}$ an analogy between the laminar and turbulent flows is assumed in the form $s_T \sim \sqrt{\lambda_T/\tau_{chem}}$ where λ_T is a turbulent thermal diffusivity and, hence

$$\frac{s_T}{s_L} \sim \sqrt{\frac{\lambda_T}{\lambda}} \sim \sqrt{\frac{\vartheta}{s_L}\frac{\ell_0}{\ell_F}} \tag{2.95}$$

where in the last expression it has been used that $\lambda \sim s_L\,\ell_F$ and $\lambda_T \sim \vartheta\,\ell_0$.

Combining expressions 2.94 and 2.95 it is seen that in general

$$\frac{s_T}{s_L} = 1 + C\left(\frac{\vartheta}{s_L}\right)^n \tag{2.96}$$

with $0.5 < n < 1$ [43]. A value around 0.7 is taken for general calculations [7].

2.4.3.2 Non-premixed combustion

In the same way that for premixed combustion, a diagram describing the different regimes in turbulent non-premixed combustion is given in the following. It is less frequent to find this type of diagrams for non-premixed combustion since these flames do not exhibit a characteristic velocity scale like premixed flames. However, from the strain rate a, to which the flame is submitted, a characteristic length scale, that measures the diffusion thickness, may be found as $\ell_D \sim \sqrt{\lambda/a}$. A flame thickness $(\Delta Z)_F$ in mixture fraction space is given by

$$(\Delta Z)_F = |\nabla Z|_{st}\,\ell_D \sim \sqrt{\frac{\chi_{st}}{a}} \tag{2.97}$$

where subscript *st* refers to stoichiometric conditions. In addition, a characteristic length scale measured in the mixture fraction space may be defined for the reaction layer and is denoted by $(\Delta Z)_R$.

Then a diagram defined by the ratios $Z''_{st}/(\Delta Z)_F$, where $Z''_{st} = (\widetilde{Z''^2})^{1/2}_{st}$, that is, a measure of the mixture fraction variance, and $\chi_{st,q}/\widetilde{\chi}_{st}$, where $\chi_{st,q}$ is the stoichiometric scalar dissipation rate for quenching conditions (see section 2.4.2.2), may be constructed [7]. The diagram is shown in figure 2.7.

Four regimes are distinguished:

[43] For the corrugated flamelets it was obtained $s_T/s_L = C\vartheta/s_L$. However, in equation 2.96, 1 is added to previous expression in order to recover $s_T \to s_L$ when $\vartheta \to 0$.

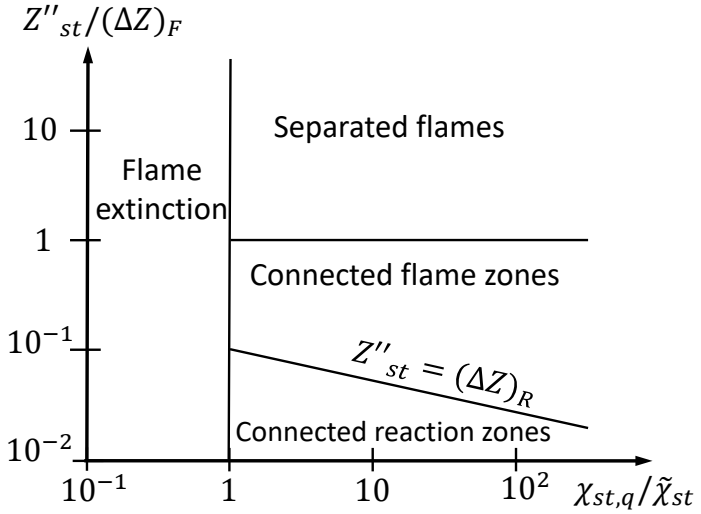

Figure 2.7. *Turbulent non-premixed flame diagram.*

1. Flame extinction: due to the high scalar dissipation rate (compared to the quenching value) transport is so intense that the flame cannot be further sustained.

2. Connected reaction zones: mixture fraction fluctuations are low compared to the flame reaction thickness ($Z''_{st} < (\Delta Z)_R$). This means an almost homogeneous mixture fraction field and, hence, the whole flame is connected.

3. Connected flame zones: in this zone $(\Delta Z)_R < Z''_{st} < (\Delta Z)_F$ and, in consequence, only the diffusion layer is connected but not the reaction layers.

4. Separated flames: as $(\Delta Z)_F < Z''_{st}$ flames are separated.

In a turbulent diffusion flame, extinction regime may be found close to the nozzle. When moving downstream, the flame is found in the separated flames regime and far away from the nozzle the connected flame zones regime dominates [7].

The role of the scalar dissipation rate in the context of turbulence ($\widetilde{\chi}$) is of paramount importance. It arises in the mixture fraction formulation and

is the dissipative term of the mixture fraction variance (see equation 2.33). $\widetilde{\chi}$ is related to $\widetilde{Z''^2}$ in a similar way as ε to k. Hence, accepting the energy cascade hypothesis, it is deduced that $\widetilde{\chi}$ is an invariant in the inertial subrange of turbulence [7].

As a final remark, it is interesting to say that in practice, depending on the flow velocities, some kind of stabilization mechanism is required in order to burn the mixture since, in other case, combustion quenches or does not proceed. The most extended mechanisms are the pilot flame where small premixed flames burn close to the nozzle to accelerate ignition, heating one (or both) air/fuel streams, creating a recirculation region of hot products or inducing swirl flows that may decelerate the flow in some regions [8]. These stabilization mechanisms are required since the high velocities induced in turbulent flames force to use them as the only way to develop and sustain combustion.

2.4.3.3 Partially premixed combustion

Finally, the partially premixed combustion is reviewed. This is a combustion mode where fuel and oxidant enter in the combustion chamber initially separated and mix to some degree prior to ignition, leading to a combustion that occurs in a stratified mixture. It is observed in gas turbines, direct injection gasoline engines and diesel engines.

In the case of sprays, partially premixed combustion occurs when the flame does not reach the nozzle and the flame is anchored at some distance. This distance is known as the flame lift-off length (LOL). As will be seen later in more detail, the flame is lifted when the velocity at the exit of the nozzle exceeds a critical value. Lifted flames have the advantage that any thermal contact between the flame and the nozzle is avoided, however, are less stable than purely diffusion flames that are attached to the nozzle.

The fact that the flame is lifted and stabilizes at some distance indicates that some kind of flame stabilization mechanism may exist in order to sustain the flame. Different theories exist in the literature that intend to explain this phenomenon although no one agrees with the whole set of experimental information. Only the main theories, summarized in [67, 68], are here briefly described.

1. Theory of the premixed flame [69–71]: this theory advocates that the base of the flame is premixed and the lift-off length is found at the point where the turbulent burning velocity equals the mean flow velocity. In

consequence, according to this theory the stabilization occurs by flame propagation. Although it is a very extended theory the scaling laws derived from it do not predict correctly the lift-off length as a function of the burning velocity for diesel flames [72].

2. Critical scalar dissipation rate concept [73]: according to this theory the flame stabilization is controlled by the extinction of diffusion laminar flames, that is, the lift-off length is established where the scalar dissipation rate exceeds the critical value χ_q. This theory does not account for the premixing upstream of the flame arguing that is not significant and for this reason is not widely accepted by the scientific community.

3. Large eddy concept [74, 75]: large vortexes recirculate hot products to the flame edge upstream of the lift-off length which are entrained and ignite reactants. This transport seems not to be totally confirmed by experimental results [67].

4. Auto-ignition: it is supposed to be the one of key stabilization mechanisms for diesel sprays [72, 76–78] and is due to a chemical activity that starts developing in the path between the exit nozzle and the lift-off length as a consequence of the high temperature and pressures found in the combustion chamber. In this case, the mixture spontaneously ignites and hot pockets appear upstream and detached from the main flame [72].

The triple flame is one of the most important type of edge flames that are typically found in the context of partially premixed combustion and was first observed by Phillips [79]. It is composed of two premixed flames, one at the lean side and the other at the rich side, that propagate at the burning velocity, and a diffusion flame found in-between, where intermediate products coming from the premixed flames, such as CO and H_2, are oxidized. The closer point to the nozzle is the triple point and is close to the stoichiometric mixture.

It is important to mention that there exist evidences that the flame stabilization does not occur with the same mechanisms for atmospheric gaseous flames and diesel flames [72]. This will be discussed in detail in section 2.5.4.

2.4.3.4 Combustion models

In previous sections the physical fundamentals of laminar and turbulent combustion have been reviewed. With these physical grounds it is possible

to describe successfully the most important combustion models, which make extensive use of combustion theory results.

Historically, infinitely fast chemistry models were first developed and applied to real calculations due to their very low computational cost. This assumption is equivalent to assume that chemistry is extremely fast compared to other physical processes. In addition, these models do not require any information about how chemistry develops during auto-ignition. With the increase of computational power transient effects were incorporated.

Some of the models presented in the following were explicitly formulated for premixed or non-premixed combustion while others may be applied to both regimes. However, as was mentioned previously, almost all of them assume scale separation between chemical and physical processes [7]. This means that they are addressed to specific combustion regimes, such as corrugated flamelets or thin reaction zones regimes. Although this is a clear constraint in terms of general purpose applicability, it is important to notice that industrial devices usually work at these regimes.

The following paragraphs do not intend to describe the models in an extensive manner. On the contrary, it is attempted to emphasize the physical aspects of each model omitting the mathematical description when possible in order to highlight their advantages, shortcomings and applicability.

1. Moment method for reactive scalars: the first attempt to tackle with turbulent reaction rates is to average/filter the instantaneous reaction rates. However, as the instantaneous reaction rate is proportional to $T^{\beta}\exp(-\frac{E_a}{RT})$ averaging/filtering implies to expand previous expression in Taylor series in order to write it in terms of $\widetilde{T''^n}$. This is a very expensive task since new relationships are required to calculate these moments making almost infeasible the application of this method[44]. In addition, lots of terms have to be considered in order to obtain accurate results.

   Sometimes this method is applied neglecting the turbulent fluctuations with some additional modifications. In this case, the mean chemical reaction rate is directly calculated from the mean reactive scalar values [80]. Clearly there are important losses of physical content when neglecting fluctuating contributions and, in general, these simplifications should not be applied since they may lead to spurious results [81].

[44] In the complete expression crossed products of the form $\widetilde{Y_i''^m T''^n}$ are obtained complicating even more the application of this method.

Since it is almost impossible to apply this method to real calculations, new models based on physical grounds have to be posed as exposed in the following.

2. Eddy break-up model (EBU): it is the simplest model for premixed combustion and assumes infinitely rate chemistry (scale separation). According to this model chemical reactions are controlled by turbulent motions [82, 83]. This implies that the averaged chemical reaction rate can be written in terms of only turbulent mixing variables yielding a products reaction rate in the form (similar expressions for reactants or heat release):

$$\widetilde{\dot{\omega}}_P = C_{EBU} \frac{\varepsilon}{k} \sqrt{\widetilde{Y_P''^2}} \tag{2.98}$$

C_{EBU} is a constant to be adjusted. Obviously, this model eliminates the influence of chemical kinetics and represents a limit for very fast chemistry.

3. Eddy dissipation concept (EDC): this model proposed by Magnussen [84] makes use of concepts from EBU model but applied to non-premixed combustion. A similar expression to 2.98 is posed for the fuel reaction rate but taking instead of $\sqrt{\widetilde{Y_P''^2}}$ the mean mass fraction of the deficient species. Again it can only be applied when chemistry is very fast compared to other flow scales.

   This model, as the EBU, depends on two constants that have to be adjusted *ad hoc* for each problem and may range in very wide intervals making the model to lose generality. In addition, this model, as any model based on infinitely rate chemistry, cannot predict ignition or lifted flames since reaction occurs instantaneously once fuel and oxidant meet.

4. Flamelet model: this model describes the turbulent flame as a set of strained laminar flames [85]. To apply this concept it is required that the flame is thin enough to not be perturbed by the turbulent flow and, therefore, remains laminar (at least the flame reaction layer[45]). Corrugated flamelet and thin reaction zone regimes fulfil this requirement since in both $\ell_\delta < \eta$ (scale separation). In this model laminar flames are typically known as flamelets.

[45]The flamelet concept can be applied provided that the reaction layer thickness ℓ_δ is smaller than the Kolmogorov eddy size η [7].

The flamelet model is able to incorporate finite rate chemistry and may be applied to both premixed and non-premixed combustion.

Different to other models, this approach is focused on the location of the surface flame which is defined by the surface level for a non-reactive variable. By virtue of the scale separation the model solves two flows at distinct scales that are coupled: the first one is the turbulent flow (large scales) while the second one are the flamelets (small scales). Chemical information from flamelet solutions is used to solve the turbulent flame.

Flamelet equations are obtained deriving transport equations along lines normal to surface levels for a specific non-reactive variable and doing a coordinate transformation. This non-reactive variable is G variable for premixed combustion and mixture fraction for non-premixed combustion.

- Premixed combustion: the model can be based on two different approaches, namely, the progress variable or the level set approximation.

  Progress variable

  The progress variable is a variable that measures the advancement of combustion and is defined as

  $$c = \frac{T - T_u}{T_b - T_u} \tag{2.99}$$

  or alternatively, from a linear combination of species mass fractions. In the same way that transport equations may be found for temperature or species mass fractions, it is possible to derive a transport equation for the progress variable:

  $$\frac{\partial(\overline{\rho}\,\widetilde{c})}{\partial t} + \frac{\partial(\overline{\rho}\,\widetilde{u_i}\,\widetilde{c})}{\partial x_i} + \frac{\partial(\overline{\rho}\,\widetilde{u_i'' c''})}{\partial x_i} = \overline{\rho}\,\widetilde{\dot{\omega}}_c \tag{2.100}$$

  The terms to be modelled in this equation are $\overline{\rho}\,\widetilde{u_i'' c''}$ and the chemical source term $\widetilde{\dot{\omega}}_c$.

  A limit case is the Bray-Moss-Libby model (BML) where the flame is considered to be infinitely thin (infinitely fast chemistry) implying that only $c = 0$ or 1 may be found in the instantaneous flow. In this model it is shown that gradient hypothesis is not applicable due to the expansion gas effects that generate a counter-gradient diffusion.

  Chemical source term $\widetilde{\dot{\omega}}_c$ may be defined proportional to the flame surface density Σ (flame surface per unit volume) which is modelled

by an algebraic model or a transport equation as in the Coherent Flamelet Model (CFM) [86]. This model belongs to the category of the flame surface density models. Based on these ideas, it is possible to extend flame surface density formulation to complex chemistry.

Level set approach

In the level set approach the flame surface is defined by the surface level of a non-reacting scalar called G [7, 65]. Then, the flame surface is given by $G(\vec{x}, t) = G_0$. Typically G_0 is taken equal to 0. Since the velocity at which the flame surface displaces in the flow is $\vec{u} + s_L \vec{n}$, where $\vec{n}$ is the normal vector to the flame surface pointing to fresh gases and it can be written in terms of G as

$$\vec{n} = -\frac{\nabla G}{|\nabla G|} \tag{2.101}$$

it is easily deduced that scalar G is described by the equation

$$\frac{\partial G}{\partial t} + \vec{u} \cdot \nabla G = s_L \, |\nabla G| \tag{2.102}$$

In principle, G is only defined on the flame surface but not in the rest of the domain. In this sense, G may be arbitrarily defined although it is sometimes taken equal to the distance from each point to the flame surface.

s_L may be expanded in different terms, namely, a non-stretched one-dimensional laminar burning velocity s_L^0, a term that accounts for the flame curvature and other that considers the strain rate (see section 2.4.2.1).

As scale separation is assumed, one-dimensional laminar flames (related to the small scales) depending on $(G, |\nabla G|, \ldots)$ are solved which are composed of a convective, diffusive and reaction term. Solutions may be integrated according to presumed PDFs[46] which are parametrized in terms of $(\widetilde{G}, \widetilde{G''^2}, \widetilde{|\nabla G|}, \ldots)$ in order to obtain averaged/filtered solutions for the reactive scalars. Finally, expressions or transport equations are required for $\widetilde{G}$, $\widetilde{G''^2}$, $\widetilde{|\nabla G|}$, etc. In the case of $\widetilde{G}$ and $\widetilde{G''^2}$, averaged and filtered equations are obtained from equation 2.102. In these equations the turbulent burning velocity s_T appears and may be calculated from expressions like equation 2.96.

[46] Probability density functions.

- Non-premixed combustion: the flamelet concept for non-premixed combustion applies similar ideas that the level set approximation. Instead of using scalar G, the mixture fraction Z, that has a clear physical meaning and is uniquely defined in the whole domain, is used. When the flame thickness is small enough, the turbulent flow is described as an ensemble of one-dimensional strained flamelets which, for $Le = 1$, are described by equations in the form of equation 2.89. The scalar dissipation rate χ, which plays a similar role to $|\nabla G|$ in premixed combustion, is a diffusivity in the mixture fraction space and measures how strained the flame is.

  As is assumed that all the reactive scalars depend on the instantaneous mixture fraction field, the turbulent transport of reactive scalars is only caused by the turbulent transport of mixture fraction. In addition, reactive scalars may show a dependence with time if transient effects are retained.

  As in the BML model for premixed combustion, the limit of infinitely fast chemistry leads to the Burke-Schumann solution, which used in conjunction with presumed PDFs, gives raise to the Conserved Scalar Equilibrium Model (CSEM). Clearly this model does not depend on χ.

  The use of steady strained flamelet solutions to solve turbulent combustion is equivalent to assume that the flow characteristics change slow enough that the flamelet is able to adapt to the local conditions.

  The procedure to apply this model is similar to the previous described for the level set in premixed combustion replacing $\widetilde{G}$ by $\widetilde{Z}$, $\widetilde{G''^2}$ by $\widetilde{Z''^2}$ and $\widetilde{|\nabla G|}$ by $\widetilde{|\nabla Z|}$ which in turn is proportional to $\widetilde{\chi}$. As this model is applied to the results of this work, a detailed description of the flamelet concept for non-premixed combustion is postponed to chapter 3.

5. Conditional moment closure model (CMC) [87, 88]: it was initially formulated for non-premixed combustion for finite rate chemistry. As in the flamelet concept for non-premixed combustion, reactive scalars fluctuations are assumed to be related to mixture fraction fluctuations and equations for reactive scalars conditioned to specified mixture fraction values Z^* are deduced, that is, equations for $\overline{\rho Y_i|Z^*}$ are found, where the symbol | represents conditioning.

   It is a method with a high computational cost since an additional transport equation is required for each combination of Z^* values and species. Moreover, a large number of Z^* values are required in order to obtain accurate results. Presuming the PDF for mixture fraction,

$P(Z)$, may lead to the calculation of different unclosed terms, such as the averaged chemical reaction rate. Moreover, it is easily seen that

$$\overline{\rho}\,\widetilde{Y_i} = \overline{\rho\,Y_i} = \int_0^1 \overline{\rho Y_i|Z^*}\,P(Z^*)\;dZ^* \tag{2.103}$$

CMC equations are similar to those derived with the flamelet model [7]. This should not be a surprise if we notice that both models assume that the reactive scalars depend directly on the mixture fraction and, hence, the physics retained by both models is similar.

The model has been applied to diesel sprays [89] and extended to premixed combustion too [90].

6. Linear eddy model (LEM) [91]: it is a model that accounts for finite rate chemistry effects and may be applied to both premixed and non-premixed combustion. In a first step, the model simulates one-dimensional molecular mixing (clearly at scales not solved in the simulation). For such purpose, one-dimensional equations are solved for reactive scalars. In a second step, solutions from these equations are rearranged as a way to account for the smallest eddies that cause an increase of shear stresses and fluxes in the flow.

   The method has been extended to hydrogen-air flames [92] and premixed flames [93]. However, it is important to note that is an expensive method in computational terms.

7. PDF transport equation model: this model describes combustion with finite rate chemistry and may be applied to both premixed and non-premixed combustion. Instead of presuming the PDFs shape, joint PDFs for velocity and reactive scalars are transported in the flow and computed [6, 94, 95].

   In the turbulent combustion context it is advocated that the main advantage of this method is that, different to other combustion models, the chemical source terms appear in a closed form and do not have to be modelled. The closure problem is limited to model molecular mixing and additional gradient terms due to pressure fluctuations and viscous stresses.

   In terms of computational cost it is a very expensive model that makes almost prohibitive its use for industrial applications. In order to reduce its cost it is used in conjunction with Monte-Carlo method, ILDM or

ISAT [47]. Notwithstanding, it has been applied to the simulation of diesel-like sprays [77, 96] with successful results.

Finally, there exists a group of methods that reduce the cost of the simulations when using complex chemistry with previous combustion models. It is important to note that these reduction methods are not combustion models themselves but only some techniques devised to decrease the computational cost related to the use of previous models. We do not include here chemical schemes reduction techniques since such techniques are applied to the chemical scheme, considered here an input, prior to the calculation of the reactive flow.

The Intrinsic Low Dimensional Manifold (ILDM), devised by Maas and Pope [97], is based on the idea that the thermo-chemical paths described by a set of chemical systems with different initial conditions but identical equilibrium solutions follow the same evolution (they overlap) after a small amount of time. Hence, there exists an attracting surface, called low-dimensional manifold, where evolutions with same equilibrium conditions tend to fall. This means that after a short period of time the chemical system depends only on some few variables. The method identifies these variables, by the analysis of the characteristic time scales of the system from the Jacobian matrix, and tabulate the chemical evolution of the system as a function of these variables.

This method provides good results for high temperature chemistry but shows some deviations for low temperature chemistry [98]. For this reason the ILDM has been applied together with the flamelet concept giving rise to the Flamelet Generated Manifold (FGM) [98] and the Flame Prolongation of ILDM (FPI) [99] which improved substantially the results. In both models flamelet equations are solved with complex mechanisms and solutions are tabulated as functions of few input variables.

Another reduction method is the *in situ* adaptive tabulation (ISAT) [100, 101]. The underlying idea of this method is that when applying pre-tabulated models only a small region of the look-up tables is accessed during the CFD[48] calculation, making superfluous the computation of the whole database. Then, the computational cost would be drastically reduced if this look-up table was generated during the CFD calculation as needed, that is, *in situ*. This method has been applied in the context of transported PDFs leading to a reduction of computational time of three orders of magnitude [8].

[47] ILDM and ISAT will be described in next paragraph.

[48] CFD stands for Computational Fluid Dynamics.

Finally, table 2.2 classifies the turbulent combustion models previously described.

Table 2.2. *Turbulent combustion models.*

	Premixed combustion	**Non-premixed combustion**
Infinitely fast chemistry	EBU model BML model Coherent Flamelet Model	EDC model CSEM
Finite rate chemistry	Moment method for reactive scalars	
	Flamelet model based on the progress variable (Flame surface density model) Flamelet model based on G equation	Flamelet model based on Z Conditional moment closure
	PDF transport equation model Linear eddy model	

2.5 Spray description and theory

The chapter is closed with the application of all the previous concepts to the analysis of the spray and, more particularly, to the diesel spray whose study in reactive conditions is the purpose of this work. A detailed description of the spray theory is given in the following prior to the analysis of combustion in the case of the diesel spray.

In a diesel spray, fuel is injected in liquid phase, vaporizes, mixes with air and finally burns. Therefore, it is natural to study as a first step how mixing occurs for a gas-gas jet[49] and, then, add new levels of physical content and complexity.

2.5.1 Gas-gas jet

Sprays or jets together with other flows such as wakes and mixing layers belong to the category of free shear flows and have the characteristic that they develop far from walls that confine the flow. Transfer of momentum is due to streams that flow with different velocities and, hence, generate a gradient. In

[49]Fuel is injected in gas phase.

the case of wakes, velocity gradients are produced by the non-slip condition on the wall of an obstacle that takes or adds (propulsion system) momentum to the flow.

The turbulent round jet, that is, a jet with cylindrical symmetry for statistical variables, shows the axial direction as preferential. Radial velocity is one order of magnitude lower than the axial component and radial gradients are clearly higher than gradients in axial direction.

It is composed of an initial core at the exit of the nozzle not perturbed by the surrounding flow. Downstream and at some distance of this core, once the turbulent jet is developed, experimental measurements show that radial profiles for different variables are self-similar. This is one of the most prominent properties of sprays and means that if the radial cuts are properly normalized they all fall on a single curve. The minimum distance from which this is observed hinges on each particular variable.

Taking a cylindrical coordinate system (x, r, θ), with the axial direction coincident with the spray axis, and calling (u, v, w) the instantaneous velocity vector in this coordinate system, applying the proper order of magnitude analysis and neglecting high-order terms, continuity and momentum equations in the axial direction for a developed and statistically stationary spray in the RANS context are

$$\frac{\partial \overline{u}}{\partial x} + \frac{1}{r}\frac{\partial (r\,\overline{v})}{\partial r} = 0 \tag{2.104}$$

$$\overline{u}\,\frac{\partial \overline{u}}{\partial x} + \overline{v}\,\frac{\partial \overline{u}}{\partial r} = \frac{\nu}{r}\frac{\partial}{\partial r}\left(r\frac{\partial \overline{u}}{\partial r}\right) - \frac{1}{r}\frac{\partial}{\partial r}\left(r\,\overline{u'v'}\right) \tag{2.105}$$

The analytical solutions for the round jet entering in a chamber with quiescent air were obtained by Schlichting, who solved these equations in 1933 assuming the gradient hypothesis[50] [4]. A similar equation to 2.105 can be written for passive scalars and if both the velocity and the passive scalar have similar boundary conditions their solutions are linearly related. This is the case for the mixture fraction for which we have

$$\frac{\overline{u}(x, r, \theta)}{u_0} = \overline{Z}(x, r, \theta) \tag{2.106}$$

[50] If we accept the gradient hypothesis, solutions for laminar and turbulent sprays are the same substituting ν by ν_{eff}. This is easily seen since the term $\frac{1}{r}\frac{\partial}{\partial r}\left(r\,\overline{u'v'}\right)$ becomes $\frac{\nu_{eff}}{r}\frac{\partial}{\partial r}\left(r\frac{\partial \overline{u}}{\partial r}\right)$. To do this we assumed ν_T approximately constant in the spray as deduced from self-similarity.

where u_0 is the mean axial velocity at the exit of the nozzle[51]. Naming d_0 the diameter of the nozzle it can be shown that the velocity on the axis $\overline{u}_{ax} = \overline{u}(x, 0, 0)$ falls following an hyperbola ($\propto 1/x$) for $x/d_0 > 30$ [6]. From Schlichting's solution we have for a radial profile

$$\frac{\overline{u}}{\overline{u}_{ax}} = \frac{1}{(1+\Omega^2)^2} \tag{2.107}$$

where $\Omega \propto r/x$. As a consequence, the spray spreading rate $\tan\gamma$, with γ the half-angle of the spray, is constant. Indeed if we define the limit of the spray for each axial position as the radius $r_{1/2}$ for which the velocity halves the velocity on the axis, we have from equation 2.107

$$\tan\gamma = \frac{dr_{1/2}}{dx} = constant \tag{2.108}$$

This means that the sprays spreads linearly in a conical shape. The spray spreads due to the mixing with the surrounding air which is dragged and accelerated by the spray core. This mixing entrains air in the spray and dilutes the fuel concentration. Then, the mass flow rate $\dot{m}$ across normal planes to spray axis depends on the axial position. From the previous solution it can be deduced that

$$\dot{m}(x) = \dot{m}_{fuel} + \dot{m}_{air} = 8\pi\mu_T\, x \tag{2.109}$$

As the momentum flow rate is conserved along all the sections normal to the spray[52], air entrainment provokes an acceleration of the surrounding air while decelerates the spray core, whose axial velocity falls following an hyperbola, as was previously described.

Reynolds stress tensor is

$$\begin{pmatrix} \overline{u'^2} & \overline{u'v'} & 0 \\ \overline{u'v'} & \overline{v'^2} & 0 \\ 0 & 0 & \overline{w'^2} \end{pmatrix} \tag{2.110}$$

[51]This proportion between $\overline{u}$ and $\overline{Z}$ only happens if the Schmidt number is unity. In other cases equation 2.106 is only approximated.

[52]Since we assumed that there are no external forces and pressure is almost constant in the domain.

Due to symmetry reasons $\overline{u'w'} = \overline{v'w'} = 0$ while $\overline{u'^2}$, $\overline{v'^2}$ and $\overline{w'^2}$ are pair functions and $\overline{u'v'}$ is an odd function and, hence, is zero on the axis.

In a radial cut, $\overline{v'^2}$ and $\overline{w'^2}$ are almost identical and decrease monotonically with the radius. On the contrary, $\overline{u'^2}$ shows higher values than the other normal Reynolds stresses and when moving away from the axis, first, it increases slightly and then decreases monotonically. The different values of these stresses show that the spray is anisotropic.

In the same way that the average fields are self-similar, Reynolds stresses show self-similarity too [5, 6, 102]. From this it is deduced that the turbulent kinematic viscosity ν_T is in turn self-similar. In addition, ν_T does not show strong variations along a radial cut between $r = 0$ and $r = r_{1/2}$ [6].

Regarding the turbulent flux for passive scalars a turbulent Schmidt number $Sc_T = 0.7$ has been experimentally found [6].

Finally, dissipation is dominant in the whole spray while production is reduced near the axis and has its maximum at $\sim 0.7r_{1/2}$. The mean flow convection and the turbulent transport complete the turbulent kinetic energy budget [103].

Turbulent spray visualization shows that there exists a sharp, irregular and contorted surface that separates the region of turbulent flow, with large vorticity, from the non-turbulent flow which is mainly irrotational. The surface that divides these two regions is the viscous superlayer. Given a fixed position the turbulent and the non-turbulent flow are seen to alternate with some probability. The flow is said to be intermittent and the intermittency function measures this probability. As for other variables the intermittency function is self-similar.

Previous considerations have been explained for a developed and statistically steady spray, however, in the context of diesel sprays it is important to consider the transient evolution. Related to the transient regime, the concept of the vapour penetration S is fundamental. It measures the distance from the nozzle to the most distant point of the spray, which is found on the axis. It can be shown that it can be approximated $S \propto \sqrt{t}$, where t is time, after a threshold time [104].

As was commented in section 2.3.3.3, it is worth emphasizing that the vapour penetration is underestimated when applying the $k - \varepsilon$ model with the standard values [32, 105] since the spreading rate is overestimated. In this case it is quite extended to increase the value $C_{\varepsilon 1}$ in order to improve predictions [105].

2.5.2 Liquid-gas spray

When the fuel is injected in liquid phase it has to vaporize prior to mixing with air. The velocity at which the fuel stream exits from the nozzle and the thermodynamic conditions in the air environment determine the velocity at which vaporization takes place.

In order to vaporize, the first step is to break of the liquid vein into droplets. This is called atomization and is produced as a consequence of the Kelvin-Helmholtz instabilities induced on the liquid vein surface. This break-up of the liquid vein takes a distance called break-up length that depends on the exit velocity u_0 giving rise to different atomization regimes.

In modern diesel engines working conditions, experimental investigations show that only the complete atomization regime is found in the spray [106], for which the break-up length is independent of u_0 and is of the same order of magnitude than d_0.

Downstream of the break-up length, fuel is found in droplets that suffer drag due to the relative velocity with the air environment entrained by the spray. They suffer Kelvin-Helmholtz instabilities as well as Rayleigh-Taylor instabilities caused by aerodynamic forces. When these forces are higher than the internal forces, which maintain the cohesion of the droplet, that is, the Weber number exceeds a critical value, the droplet breaks. This is the break-up process. In addition, droplets may suffer coalescence, collision, etc.

Once the droplets are small enough and show very high surface per unit volume most of vaporization takes place. In order to understand the evaporation process first the evaporation for a single droplet in a quiescent environment is studied.

It has been experimentally observed that the droplet diameter d_d follows the law

$$\frac{d(d_d^2)}{dt} = -k_v \tag{2.111}$$

where k_v is a positive constant. From equation 2.111 it is deduced that evaporation mass flow rate $\dot{m}_{ev,0}$ is proportional to d_d. Spalding found an analytical expression for k_v assuming saturated vapour conditions in the vicinity of the droplet surface [9].

Once evaporation mass flow rate for a single droplet is known it can be corrected for a droplet immersed in a convective stream by means of the Ranz-Marshall model which estimates the dimensionless Sherwood number Sh [53] as

$$Sh = 2 + 0.6\, Sc^{\frac{1}{3}}\, Re^{\frac{1}{2}} \tag{2.112}$$

With the aid of this expression it can be found that

$$\frac{\dot{m}_{ev}}{\dot{m}_{ev,0}} = \frac{Sh}{2} = 1 + 0.3\, Sc^{\frac{1}{3}}\, Re^{\frac{1}{2}} \tag{2.113}$$

where $\dot{m}_{ev}$ is the evaporation mass flow rate for the droplet in the stream. In addition, evaporation mass flow rate is increased if combustion develops surrounding the droplet.

The previous relationships hold for a cloud of droplets if the droplets are far enough to not interact between them. This is a basic hypothesis for different models based on a Lagrangian description of the liquid phase available in the literature, implying that they will only provide accurate results when the liquid volume fraction is lower than a threshold value typically chosen equal to 0.1 [107].

In order to model the liquid phase it has been adopted historically a Lagrangian description where droplets, grouped in parcels[54], exchange mass, momentum and energy with the environment. This description of the liquid phase gives rise to the Discrete Droplet Method (DDM) [108]. However, as mentioned previously, this model fails when the liquid volume fraction exceeds a critical value [107] and, hence, even being the most extended model approach, it arises that its hypotheses are not fulfilled in a diesel spray close to the nozzle. These shortcomings prompted the formulation of the Eulerian $\Sigma - Y$ model [109] which describes the liquid-gas mixture as a pseudo-fluid and makes use of the fact that, as will be explained later in more detail, in a diesel spray evaporation is mixing controlled, that is, air entrainment is the limiting process. Comparisons between both models for a diesel-like spray can be found in [110] where it is shown that the Eulerian approach is more suitable for the simulation of such sprays although its computational cost is higher.

Finally, to say that the distance from the nozzle to the point where the fuel is totally vaporized is called the liquid length or liquid penetration. For

[53] Sherwood number compares the total diffusion flux due to conduction and convection and the diffusion flux due to only conduction in a fluid.

[54] Statistical representations of sets of droplets with the same properties.

diesel sprays, it increases with d_0 but does not depend on the injection pressure since, for typical work conditions, evaporation is controlled by mixing, that is, the limiting process is air entrainment and not mass, momentum and energy diffusion from the droplet to the environment [111]. This implies that the increase of the liquid length induced by the higher velocities, as a consequence of the increase of the injection pressure, is compensated by higher air entrainment which tends to reduce the liquid length, and, therefore, liquid length is not affected by the injection pressure.

2.5.3 General comments on the reactive spray

Once fuel has vaporized and mixed with air, the spray may burn if there is high pressure and temperature in the environment. In a similar way to homogeneous mixtures auto-ignition (see section 2.4.1) the time elapsed from the start of injection (SOI) until the mixture ignites is known as the ignition delay (ID). Once the flame stabilizes, a diffusion flame is found in the vicinity of the stoichiometric mixture. Burke and Schumann were the first who solved analytically the reactive spray assuming that combustion only happens at stoichiometry independently of the rest of local flow conditions[55] [60].

Combustion reduces air entrainment and, consequently, velocity on the axis is higher for the reactive case compared to the inert one. This in turn produces a faster penetration of the spray and a possible radial expansion, that is, an increase of the spreading rate [112]. In the reactive case, spray penetration is known as tip penetration instead of vapour penetration since after combustion fuel is transformed into products.

The distance from the nozzle to the point on the axis where the mixture fraction equals stoichiometric mixture fraction is the flame length L_f. It can be shown from the analysis of section 2.5.1 that $L_f \propto Re_0\, d_0$ where $Re_0 = d_0\, u_0/\nu$. From this, it is observed that L_f is proportional to u_0 in the laminar regime. In order to calculate L_f in the turbulent regime, it suffices to substitute ν by ν_T. However, as the turbulent viscosity may be written as the product of a characteristic length and a velocity scale, that is, $\nu_T \propto d_0\, u_0$, it is deduced that L_f does not depend on u_0 in the turbulent regime. Both regimes are connected by a transient regime.

In addition, if u_0 exceeds a critical value the flame is not attached to the injector and there exists a distance between the nozzle and the base of the

[55] This implies that combustion always occurs if air and fuel meet in stoichiometric proportions. Needless to say that this model cannot reproduce transient phenomena including flame extinction or lifted flames.

flame. This distance is known as lift-off length, described in section 2.4.3.3, and shows a linear relationship with u_0 [7]. In this case, apart from the diffusion flame, a partially premixed combustion region is found in the vicinity of the lift-off length. If the velocity u_0 increases too much the flame blows-off.

The dependence of the flame length and the lift-off length is summarized in figure 2.8. Lifted flames may be found in diesel sprays and gas turbines and its modelling requires advanced combustion models that consider finite rate chemistry.

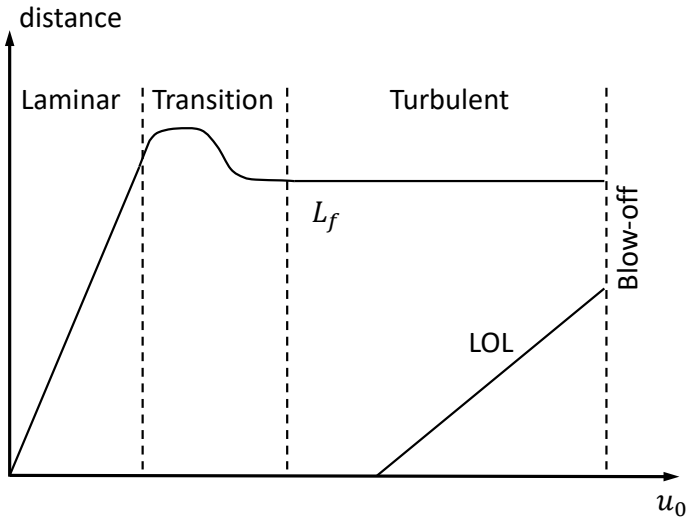

Figure 2.8. *Flame length L_f and lift-off length (LOL) as a function of the exit nozzle velocity.*

It is worth mentioning that upstream of the lift-off length the spray shows an extremely reduced chemical activity and, in consequence, it can be considered inert.

2.5.4 The reacting diesel spray

The previous section provided the grounds to explain any spray and, in particular, the diesel spray that develops in a DI (direct injection) diesel engine. However, the particular conditions of very high pressure and temperature at which it occurs and the lack of visual images until the 90s made

its description, at least, elusive for the scientific community during years. And the proof of this is that during a long time there existed several misconceptions which explained combustion in diesel sprays consisting of small diffusion flames that were established surrounding individual droplets or a diffusion flame that wrapped the periphery of the spray fed by the vapour of the droplets cloud.

However, spray visualization by means of optical techniques revealed a quite different picture. From experimental information Dec [51] devised a conceptual model of the diesel spray and its systematic investigation by means of experiments and CFD has lead to deepen the nature of the whole process [72, 76, 77, 111, 113–115].

According to Higgins [113], the temporal stages that compose the diesel combustion event are initiated by an ignition delay where different periods are distinguished. First, a physical induction period takes place, where atomization, air entrainment and evaporation occur, as described previously. According to Siebers [111], from the relationships that liquid length shows with boundary conditions, it is deduced, as explained previously, that evaporation is mixing controlled. Moreover, atomization, air entrainment and evaporation are not only characteristic of this stage but extend during the whole injection.

During the second period of the spray, ignition delay, and once fuel has mixed with air, the first stage of ignition occur. Reactions crack fuel molecules and produce radicals releasing extremely low amounts of heat. During this stage and although possible sparse soot spots are observed, formaldehyde and CH radicals chemiluminescence is observed extending either uniformly on a wide region of the spray or in its periphery depending on the reactivity of the mixture [113].

After these periods, the spray ignition delay stage concludes and a second stage of ignition, that corresponds to the premixed-burn period, takes place. Fast and exothermic reactions occur with high amounts of heat release detected that produce an important pressure increase in the combustion chamber. A great amount of the injected fuel mass, that has mixed during the ignition delay period and is found inside the flammability limits, burns. This explains why this period is known as the premixed combustion stage.

From this description it is observed that this stage is controlled by the mixing air-fuel rate and the ignition delay. Sparse soot pockets are visualized, however, the main combustion occurs in the volume of the spray in a distributed region as chemiluminescence images show.

Finally, a diffusion combustion is established which is mixing controlled since the burning rate is limited by the mixing rate and not by chemical

kinetics. This stage shows more moderate burning rates than those found during the premixed combustion stage.

Regarding flame spatial structure, a detailed picture of its morphology during this period is given in the following according to Dec's conceptual model [51].

The diesel spray vaporizes in some few millimetres and suffers a strong mixing with air due to the enhanced turbulence induced by the the high fuel velocity. Downstream of the liquid length the diesel flame is established. It is a lifted flame[56] composed of a partially premixed combustion that develops at rich mixtures, positioned in the vicinity of the lift-off length and a diffusion flame that wraps the spray. In addition, some chemiluminescence is observed upstream of the rich flame.

Visualization of the spray reveals that soot is formed in the central regions of the spray implying temperatures of the order of 1300 K. The heat release required to augment the temperature can be only caused by a flame which develops in a region of equivalence ratios that range between 2 and 4 (this flame corresponds to the aforementioned partially premixed combustion).

In the inner region limited by the rich premixed and the diffusion flames, no oxygen is found since it is consumed by the rich premixed combustion and the diffusion flame prevents from its entrance. Therefore, negligible amounts of heat are released in this zone. Regarding species, only partially oxidised products and not saturated hydrocarbons are found. These not saturated hydrocarbons of short chain generate PAHs (polycyclic aromatic hydrocarbons) and, therefore, act as soot precursors (see section 2.4.1). Soot size increases when moving downstream in the spray due to the increase of residence times as well as the increase of temperature owing to diffusion.

In the periphery of the spray a diffusion flame is found in the vicinity of the stoichiometric mixture. This diffusion flame oxidises the products of the partially premixed combustion and soot, which is attacked by OH radicals. Finally, wrapping the diffusion flame at the lean side, there exists a sheet were NO_x are thermally produced since it is a region with excess of oxygen and very high temperatures.

A sketch of the diesel flame according to Dec's conceptual model is shown in figure 2.9.

Regarding the influence of the main boundary conditions, ambient or air temperature has a very remarkable impact on the ignition delay as well as

[56] Common rail technology allows to reach extremely high injection pressures of the order of 150 MPa. The fuel velocity at the exit of the nozzle is around 500 m/s.

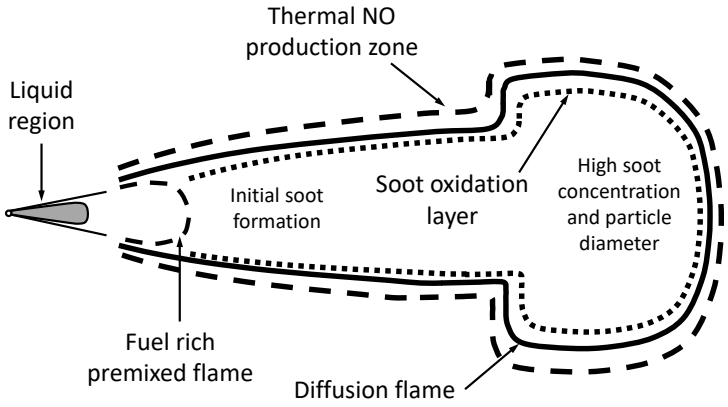

Figure 2.9. *Sketch of a developed diesel flame according to Dec's conceptual model.*

the lift-off length since chemical activity shows a very strong dependence with temperature (see Arrhenius law in section 2.4.1). The influence of these parameters with oxygen concentration is moderate. Both ambient temperature and air oxygen concentration play an important role in flame morphology as well as in pollutants formation but do not determine air entrainment, although ambient temperature influences in the evaporation process. Finally, it seems that increasing the injection pressure may cause a modest decrease of the ignition delay [116].

Other experimental and modelling works have corroborated and completed the picture of how diesel combustion proceeds. Regarding auto-ignition, an abundant set of experiments and simulations confirm that high-temperature combustion kernels are first observed in rich mixtures with low scalar dissipation rates and mixture fraction variances [77, 117]. In addition, a recession of the lift-off length to the nozzle has been measured during the transient flame evolution from auto-ignition until reaching statistical steady conditions [81, 118].

Different works have emphasized the importance of the lift-off length in combustion since it determines the maximum reactive mixture in the spray and, therefore, this length is deeply connected with soot formation [119]. This is clear when considering that if the rich partially premixed flame is placed in very rich mixtures high soot formation is expected. However, moving lift-off length downstream (due to air and/or fuel thermodynamic

conditions) increases air entrainment (dilutes fuel in mixture) and places, hence, combustion at leaner mixtures. As a consequence of this combustion displacement, soot formation is reduced. It has been observed that if the equivalence ratio is lower than 2 at the lift-off length the flame is non-sooting [120].

Concerning oxygen concentration in air it has been experimentally shown that its decrease produces a first increase in soot mass formation and a reduction of NO_x mass due to the reduction of the maximum flame temperature. This is the trade-off between soot and NO_x. However, when reducing oxygen concentration to very low values (of the order of 0.1), although the averaged equivalence ratio at the lift-off length section shows negligible changes, a stringent decrease of the soot mass formation is observed [114]. Regarding ambient temperature, its increase reduces the lift-off length and augments soot formation [76, 121].

Taking advantage of this idea, advanced combustion techniques like dual-fuel have been suggested [122]. In this technique, fuels with high and low reactivity are mixed as a way to inhibit fast combustion shown by highly reactive fuels. In this way, lift-off length is moved downstream to equivalence ratios where only marginals amounts of soot are produced.

Another very interesting aspect related to the spray transient regime is that the instantaneous fields rapidly stabilize around the averaged steady fields once the spray passes through a region [123]. Once they stabilize it is said that the quasi-steady regime has been reached in that region[57].

Finally, regarding the stabilization mechanism at the lift-off length, experimental measurements show that pockets of formaldehyde appear upstream and detached from the base of the flame [72, 124]. Different numerical investigations have confirmed these observations [76–78, 115], as well as simulations carried out in this work and described along this document [125], which suggest that auto-ignition is important in the flame stabilization. In addition, scaling laws found for lift-off length for atmospheric gaseous flames based on flame propagation (premixed flame at the lift-off length) as the main flame stabilization mechanism [7] are found not to be fulfilled in diesel flames when changing some parameters as the nozzle diameter or the ambient oxygen concentration [126].

In line with these facts, and regarding the relationship between ignition delay and lift-off length, it is observed that decreasing the ignition delay by

[57]The term quasi-steady refers to the fact that, in most cases, the modification of the controlling factors is slow compared to the flow dynamics and, hence, the spray rapidly adapts to the new boundary conditions.

means of the boundary conditions or fuel reactivity the lift-off length decreases too [72, 81]. This has been defended as an argument in order to indicate that the diesel flame stabilization mechanism is probably not only determined by flame propagation.

All these evidences seem to suggest that even if different stabilization mechanisms may concur (see section 2.4.3.3) in the diesel flame stabilization, auto-ignition plays an important role. However, it is worth noting that is probable that flame propagation or even other mechanisms are still relevant in diesel flame stabilization. The relative importance of each one is expected to depend on the boundary conditions too.

Finally, it is emphasized that this description corresponds to a simplified situation since in real engines other effects, such as swirl movement, sprays interaction or wall impingement, omitted here, are usually relevant.

References

[1] Dahms R. N. and Oefelein J. C. "On the transition between two-phase and single-phase interface dynamics in multicomponent fluids at supercritical pressures". *Physics of Fluids*, Vol. 25 n^o 9, pp. 092103, 2013.

[2] Falgout Z., Rahm M., Wang Z. and Linne M. "Evidence for supercritical mixing layers in the ECN spray A". *Proceedings of the Combustion Institute*, Vol. 35 n^o 2, pp. 1579–1586, 2015.

[3] Batchelor G. K. *An introduction to fluid dynamics*. Cambridge university press, 2000.

[4] Schlichting H. and Gersten K. *Boundary-layer theory*. Springer, 2016.

[5] Tennekes H. and Lumley J. L. *A first course in turbulence*. MIT press, 1972.

[6] Pope S. B. *Turbulent flows*. IOP Publishing, 2001.

[7] Peters N. *Turbulent combustion*. Cambridge University Press, 2000.

[8] Poinsot T. and Veynante D. *Theoretical and numerical combustion*. RT Edwards Inc., 2005.

[9] Glassman I., Yetter R. A. and Glumac N. G. *Combustion*. Academic press, 2014.

[10] Versteeg H. K. and Malalasekera W. *An introduction to computational fluid dynamics: the finite volume method*. Pearson Education, 2007.

[11] Williams F. A. *Combustion theory*. Benjamin Cummings, Menlo Park, CA, 1985.

[12] Hirschfelder J. O., Curtiss C. F. and Bird R. B. *Molecular theory of gases and liquids*, volume 26. Wiley New York, 1969.

[13] McDonough J. M. *Introductory lectures on turbulence: physics, mathematics and modeling*. University of Kentucky, 2007.

[14] Richardson L. F. *Weather prediction by numerical process*. Cambridge University Press, 1922.

[15] Kolmogorov A. N. "The local structure of turbulence in incompressible viscous fluid for very large Reynolds numbers". *Proc. R. Soc. Lond. A*, Vol. 434 n^o 1890, pp. 9–13, 1991.

[16] Kolmogorov A. N. "Dissipation of energy in the locally isotropic turbulence". *Proc. R. Soc. Lond. A*, Vol. 434 n^o 1890, pp. 15–17, 1991.

[17] Saddoughi S. G. and Veeravalli S. V. "Local isotropy in turbulent boundary layers at high Reynolds number". *Journal of Fluid Mechanics*, Vol. 268, pp. 333–372, 1994.

[18] Sreenivasan K. R. "On the universality of the Kolmogorov constant". *Physics of Fluids*, Vol. 7 n^o 11, pp. 2778–2784, 1995.

[19] Favre A. J. "The equations of compressible turbulent gases". *Aix-Marseille University (France). Inst. de Mecanique Statistique de la Turbulence*, 1965.

[20] Cabra R., Myhrvold T., Chen J. Y., Dibble R. W., Karpetis A. N. and Barlow R. S. "Simultaneous laser Raman-Rayleigh-LIF measurements and numerical modeling results of a lifted turbulent H2/N2 jet flame in a vitiated coflow". *Proceedings of the Combustion Institute*, Vol. 29 n^o 2, pp. 1881–1888, 2002.

[21] Cabra R., Chen J. Y., Dibble R. W., Karpetis A. N. and Barlow R. S. "Lifted methane–air jet flames in a vitiated coflow". *Combustion and Flame*, Vol. 143 n^o 4, pp. 491–506, 2005.

[22] Kim J., Moin P. and Moser R. "Turbulence statistics in fully developed channel flow at low Reynolds number". *Journal of fluid mechanics*, Vol. 177, pp. 133–166, 1987.

[23] Pao Y. H. "Structure of turbulent velocity and scalar fields at large wavenumbers". *The Physics of Fluids*, Vol. 8 n^o 6, pp. 1063–1075, 1965.

[24] Borghesi G., Krisman A., Lu T. and Chen J. H. "Direct numerical simulation of a temporally evolving air/n-dodecane jet at low-temperature diesel-relevant conditions". *Combustion and Flame*, 2018.

[25] Spalart P. R. "Direct simulation of a turbulent boundary layer up to Rθ = 1410". *Journal of Fluid Mechanics*, Vol. 187, pp. 61–98, 1988.

[26] Le H., Moin P. and Kim J. "Direct numerical simulation of turbulent flow over a backward-facing step". *Journal of fluid mechanics*, Vol. 330, pp. 349–374, 1997.

[27] Leonard A. "Energy cascade in large-eddy simulations of turbulent fluid flows". In *Advances in geophysics*, volume 18, pp. 237–248. Elsevier, 1975.

[28] Pope S. B. "Ten questions concerning the large-eddy simulation of turbulent flows". *New journal of Physics*, Vol. 6 n^o 1, pp. 35, 2004.

[29] Pomraning E. and Rutland C. J. "A dynamic one-equation nonviscosity large-eddy simulation model". *AIAA journal*, Vol. 40 n^o 4, pp. 689–701, 2002.

[30] Tavoularis S. and Corrsin S. "Experiments in nearly homogenous turbulent shear flow with a uniform mean temperature gradient. Part 1". *Journal of Fluid Mechanics*, Vol. 104, pp. 311–347, 1981.

[31] Launder B. E. and Spalding D. B. "The numerical computation of turbulent flows". In *Numerical Prediction of Flow, Heat Transfer, Turbulence and Combustion*, pp. 96–116. Elsevier, 1983.

[32] Pope S. B. "An explanation of the turbulent round-jet/plane-jet anomaly". *AIAA journal*, Vol. 16 n^o 3, pp. 279–281, 1978.

[33] Spalart P. R. and Allmaras S. R. "A one-equation turbulence model for aerodynamic flows". In *30th Aerospace Sciences Meeting and Exhibit*, pp. 439–439, 1992.

[34] Wilcox D. C. "Reassessment of the scale-determining equation for advanced turbulence models". *AIAA journal*, Vol. 26 n^o 11, pp. 1299–1310, 1988.

[35] Menter F. R. "Improved Two-Equation k-ε Turbulence Models for Aerodynamic Flows". *NASA Technical Memorandum*, Vol. 103975, 1992.

[36] Menter F. R. "Two-equation eddy-viscosity turbulence models for engineering applications". *AIAA journal*, Vol. 32 n^o 8, pp. 1598–1605, 1994.

[37] Launder B. E., Reece G. Jr. and Rodi W. "Progress in the development of a Reynolds-stress turbulence closure". *Journal of fluid mechanics*, Vol. 68 n^o 3, pp. 537–566, 1975.

[38] Naot D. and Rodi W. "Calculation of secondary currents in channel flow". *Journal of the Hydraulics Division*, Vol. 108 n^o 8, pp. 948–968, 1982.

[39] Demuren A. O. and Rodi W. "Calculation of turbulence-driven secondary motion in non-circular ducts". *Journal of Fluid Mechanics*, Vol. 140, pp. 189–222, 1984.

[40] Speziale C. G. "On nonlinear k-l and k-ε models of turbulence". *Journal of Fluid Mechanics*, Vol. 178, pp. 459–475, 1987.

[41] Pope S. B. "A more general effective-viscosity hypothesis". *Journal of Fluid Mechanics*, Vol. 72 n^o 2, pp. 331–340, 1975.

[42] Yakhot V., Orszag S. A., Thangam S., Gatski T. B. and Speziale C. G. "Development of turbulence models for shear flows by a double expansion technique". *Physics of Fluids A: Fluid Dynamics*, Vol. 4 n^o 7, pp. 1510–1520, 1992.

[43] Germano M., Piomelli U., Moin P. and Cabot W. H. "A dynamic subgrid-scale eddy viscosity model". *Physics of Fluids A: Fluid Dynamics*, Vol. 3 n^o 7, pp. 1760–1765, 1991.

[44] Yoshizawa A. and Horiuti K. "A statistically-derived subgrid-scale kinetic energy model for the large-eddy simulation of turbulent flows". *Journal of the Physical Society of Japan*, Vol. 54 n^o 8, pp. 2834–2839, 1985.

[45] Bharadwaj N., Rutland C. J. and Chang S. M. "Large eddy simulation modelling of spray-induced turbulence effects". *International Journal of Engine Research*, Vol. 10 n^o 2, pp. 97–119, 2009.

[46] Bharadwaj N. and Rutland C. J. "A large-eddy simulation study of sub-grid two-phase interaction in particle-laden flows and diesel engine sprays". *Atomization and Sprays*, Vol. 20 n^o 8, 2010.

[47] Mompó Laborda J. M. *Engineering Large Eddy Simulation of Diesel Sprays*. Doctoral Thesis, Universitat Politècnica de València, 2014.

[48] Bardina J., Ferziger J. and Reynolds W. "Improved subgrid-scale models for large-eddy simulation". In *13th Fluid and Plasma Dynamics Conference*, pp. 1357–1357, 1980.

[49] López Pintor D. *Theoretical and experimental study on the autoignition phenomena of homogeneous reactive mixtures*. Doctoral Thesis, Universitat Politècnica de València, 2017.

[50] Shen H. P. S., Steinberg J., Vanderover J. and Oehlschlaeger M. A. "A shock tube study of the ignition of n-heptane, n-decane, n-dodecane, and n-tetradecane at elevated pressures". *Energy & Fuels*, Vol. 23 n^o 5, pp. 2482–2489, 2009.

[51] Dec J. E. "A conceptual model of DI diesel combustion based on laser-sheet imaging". *SAE Technical paper*, 1997.

[52] Zeldovich Y. B. "Acta Physicochim". *USSR*, Vol. 21, pp. 577, 1946.

[53] Livengood J. C. and Wu P. C. "Correlation of autoignition phenomena in internal combustion engines and rapid compression machines". In *Symposium (international) on combustion*, volume 5, pp. 347–356. Elsevier, 1955.

[54] Darrieus G. "Propagation d'un front de flamme". *La Technique Moderne*, Vol. 30, pp. 18, 1938.

[55] Landau L. D. "On the theory of slow combustion". *Acta Physicochim (USSR)*, Vol. 19, pp. 77–85, 1944.

[56] Markstein G. H. *Nonsteady flame propagation*, volume 75. Elsevier, 2014.

[57] Veynante D. and Vervisch L. "Turbulent combustion modeling". *Progress in Energy and Combustion Science*, Vol. 28 n^o 3, pp. 193–266, 2002.

[58] Mallard E. and Le Chatelier H. "Combustion of explosive gas mixtures". *Ann. mines*, Vol. 8, pp. 274, 1883.

[59] Semenov N. N. "Thermal Theory of Combustion and Explosion: III. Theory of Normal Flame Propagation". *Technical Memorandums National Advisory Committee for Aeronautics*, 1942.

[60] Burke S. P. and Schumann T. E. W. "Diffusion flames". *Industrial & Engineering Chemistry*, Vol. 20 n^o 10, pp. 998–1004, 1928.

[61] Kirkbey L. L. and Schmitz R. A. "An analytical study of the stability of a laminar diffusion flame". *Combustion and Flame*, Vol. 10 n^o 3, pp. 205–220, 1966.

[62] Schmitz R. A. "A further study of diffusion flame stability". *Combustion and Flame*, Vol. 11 n^o 1, pp. 49–62, 1967.

[63] Pitsch H. "Large-eddy simulation of turbulent combustion". *Annu. Rev. Fluid Mech.*, Vol. 38, pp. 453–482, 2006.

[64] Borghi R. "On the structure and morphology of turbulent premixed flames". In *Recent advances in the Aerospace Sciences*, pp. 117–138. Springer, 1985.

[65] Peters N. "The turbulent burning velocity for large-scale and small-scale turbulence". *Journal of Fluid mechanics*, Vol. 384, pp. 107–132, 1999.

[66] Damköhler G. "Der einfluss der turbulenz auf die flammengeschwindigkeit in gasgemischen". *Zeitschrift für Elektrochemie und angewandte physikalische Chemie*, Vol. 46 n^o 11, pp. 601–626, 1940.

[67] Lyons K. M. "Toward an understanding of the stabilization mechanisms of lifted turbulent jet flames: experiments". *Progress in Energy and Combustion Science*, Vol. 33 n^o 2, pp. 211–231, 2007.

[68] Venugopal R. and Abraham J. "A review of fundamental studies relevant to flame lift-off in diesel jets". *SAE technical paper*, 2007.

[69] Wohl K., Kapp N. M. and Gazley C. "The stability of open flames". In *Symposium on Combustion and Flame, and Explosion Phenomena*, volume 3, pp. 3–21. Elsevier, 1948.

[70] Vanquickenborne L. and Van Tiggelen A. "The stabilization mechanism of lifted diffusion flames". *Combustion and Flame*, Vol. 10 n^o 1, pp. 59–69, 1966.

[71] Eickhoff H., Lenze B. and Leuckel W. "Experimental investigation on the stabilization mechanism of jet diffusion flames". In *Symposium (International) on Combustion*, volume 20, pp. 311–318. Elsevier, 1985.

[72] Pickett L. M., Siebers D. L. and Idicheria C. A. "Relationship between ignition processes and the lift-off length of diesel fuel jets". *SAE technical paper*, 2005.

[73] Peters N. and Williams F. A. "Liftoff characteristics of turbulent jet diffusion flames". *AIAA journal*, Vol. 21 n^o 3, pp. 423–429, 1983.

[74] Broadwell J. E., Dahm W. J. A. and Mungal M. G. "Blowout of turbulent diffusion flames". In *Symposium (international) on combustion*, volume 20, pp. 303–310. Elsevier, 1985.

[75] Miake-Lye R. C. and Hammer J. A. "Lifted turbulent jet flames: a stability criterion based on the jet large-scale structure". In *Symposium (International) on Combustion*, volume 22, pp. 817–824. Elsevier, 1989.

[76] Gong C., Jangi M. and Bai X. S. "Large eddy simulation of n-dodecane spray combustion in a high pressure combustion vessel". *Applied Energy*, Vol. 136, pp. 373–381, 2014.

[77] Pei Y., Hawkes E. R., Bolla M., Kook S., Goldin G. M., Yang Y., Pope S. B. and Som S. "An analysis of the structure of an n-dodecane spray flame using TPDF modelling". *Combustion and Flame*, Vol. 168, pp. 420–435, 2016.

[78] Kahila H., Wehrfritz A., Kaario O., Masouleh M. G., Maes N., Somers B. and Vuorinen V. "Large-eddy simulation on the influence of injection pressure in reacting spray A". *Combustion and Flame*, Vol. 191, pp. 142–159, 2018.

[79] Phillips H. "Flame in a buoyant methane layer". In *Symposium (International) on Combustion*, volume 10, pp. 1277–1283. Elsevier, 1965.

[80] Lucchini T., d'Errico G., Ettorre D. and Ferrari G. "Numerical investigation of non-reacting and reacting diesel sprays in constant-volume vessels". *SAE International Journal of Fuels and Lubricants*, Vol. 2 n^o 1, pp. 966–975, 2009.

[81] Bhattacharjee S. and Haworth D. C. "Simulations of transient n-heptane and n-dodecane spray flames under engine-relevant conditions using a transported PDF method". *Combustion and Flame*, Vol. 160 n^o 10, pp. 2083–2102, 2013.

[82] Spalding D. B. "Mixing and chemical reaction in steady confined turbulent flames". In *Symposium (International) on Combustion*, volume 13, pp. 649–657. Elsevier, 1971.

[83] Spalding D. B. "Development of the eddy-break-up model of turbulent combustion". In *Numerical Prediction of Flow, Heat Transfer, Turbulence and Combustion*, pp. 194–200. Elsevier, 1983.

[84] Magnussen B. F. and Hjertager B. "On mathematical modeling of turbulent combustion with special emphasis on soot formation and combustion". In *Symposium (international) on Combustion*, volume 16, pp. 719–729. Elsevier, 1977.

[85] Williams F. A. *Recent advances in theoretical descriptions of turbulent diffusion flames*. Springer, 1975.

[86] Marble F. E. and Broadwell J. E. "The coherent flame model for turbulent chemical reactions". *Purdue University Lafayette*, 1977.

[87] Klimenko A. Y. "Multicomponent diffusion of various admixtures in turbulent flow". *Fluid dynamics*, Vol. 25 n^o 3, pp. 327–334, 1990.

[88] Bilger R. W. "Conditional moment closure for turbulent reacting flow". *Physics of Fluids A: Fluid Dynamics*, Vol. 5 n^o 2, pp. 436–444, 1993.

[89] Bolla M., Gudmundsson T., Wright Y. M. and Boulouchos K. "Simulations of diesel sprays using the conditional moment closure model". *SAE International Journal of Engines*, Vol. 6 n^o 2013-01-1618, pp. 1249–1261, 2013.

[90] Klimenko A. Y. and Bilger R. W. "Conditional moment closure for turbulent combustion". *Progress in energy and combustion science*, Vol. 25 n^o 6, pp. 595–687, 1999.

[91] Kerstein A. R. "A linear-eddy model of turbulent scalar transport and mixing". *Combustion Science and Technology*, Vol. 60 n^o 4-6, pp. 391–421, 1988.

[92] McMurthy P. A., Menon S. and Kerstein A. R. "A linear eddy sub-grid model for turbulent reacting flows: application to hydrogen-air combustion". In *Symposium (International) on Combustion*, volume 24, pp. 271–278. Elsevier, 1992.

[93] Smith T. and Menon S. "Model simulations of freely propagating turbulent premixed flames". In *Symposium (International) on Combustion*, volume 26, pp. 299–306. Elsevier, 1996.

[94] Pope S. B. "PDF methods for turbulent reactive flows". *Progress in energy and combustion science*, Vol. 11 n^o 2, pp. 119–192, 1985.

[95] O'Brien E. E. *The probability density function (pdf) approach to reacting turbulent flows*. Springer, 1980.

[96] Pei Y., Hawkes E. R., Kook S., Goldin G. M. and Lu T. "Modelling n-dodecane spray and combustion with the transported probability density function method". *Combustion and Flame*, Vol. 162 n^o 5, pp. 2006–2019, 2015.

[97] Maas U. and Pope S. B. "Simplifying chemical kinetics: intrinsic low-dimensional manifolds in composition space". *Combustion and flame*, Vol. 88 n^o 3-4, pp. 239–264, 1992.

[98] van Oijen J. A. and de Goey L. P. H. "Modelling of premixed laminar flames using flamelet-generated manifolds". *Combustion Science and Technology*, Vol. 161 n^o 1, pp. 113–137, 2000.

[99] Gicquel O., Darabiha N. and Thévenin D. "Laminar premixed hydrogen/air counterflow flame simulations using flame prolongation of ILDM with differential diffusion". *Proceedings of the Combustion Institute*, Vol. 28 n^o 2, pp. 1901–1908, 2000.

[100] Pope S. B. "Computationally efficient implementation of combustion chemistry using in situ adaptive tabulation". *Combustion theory and modelling*, 1997.

[101] Yang B. and Pope S. B. "Treating chemistry in combustion with detailed mechanisms— In situ adaptive tabulation in principal directions— Premixed combustion". *Combustion and Flame*, Vol. 112 n^o 1-2, pp. 85–112, 1998.

[102] Hussein H. J., Capp S. P. and George W. K. "Velocity measurements in a high-Reynolds-number, momentum-conserving, axisymmetric, turbulent jet". *Journal of Fluid Mechanics*, Vol. 258, pp. 31–75, 1994.

[103] Panchapakesan N. R. and Lumley J. L. "Turbulence measurements in axisymmetric jets of air and helium. Part 1. Air jet". *Journal of Fluid Mechanics*, Vol. 246, pp. 197–223, 1993.

[104] Desantes J. M., Payri R., Salvador F. J. and Gil A. "Development and validation of a theoretical model for diesel spray penetration". *Fuel*, Vol. 85, pp. 910–917, 2006.

[105] Novella R., García A., Pastor J. M. and Domenech V. "The role of detailed chemical kinetics on CFD diesel spray ignition and combustion modelling". *Mathematical and Computer Modelling*, Vol. 54 n^o 7, pp. 1706–1719, 2011.

[106] Payri F., Desantes J. M. and Arrègle J. "Characterization of D.I. diesel sprays in high density conditions". *SAE Technical Paper*, 1996.

[107] Subramaniam S. "Lagrangian-Eulerian methods for multiphase flows". *Progress in Energy and Combustion Science*, Vol. 39 n^o 2-3, pp. 215–245, 2013.

[108] Dukowicz J. K. "A particle-fluid numerical model for liquid sprays". *Journal of computational Physics*, Vol. 35 n^o 2, pp. 229–253, 1980.

[109] Vallet A. and Borghi R. "Modélisation Eulerienne de l'atomisation d'un jet liquide". *Comptes Rendus de l'Académie des Sciences-Series IIB-Mechanics-Physics-Astronomy*, Vol. 327 n^o 10, pp. 1015–1020, 1999.

[110] Desantes J. M., García-Oliver J. M., Pastor J. M. and Pandal A. "A comparison of diesel sprays CFD modeling approaches: DDM versus Σ-Y Eulerian atomization model". *Atomization and Sprays*, Vol. 26 n^o 7, 2016.

[111] Siebers D. "Liquid-phase fuel penetration in Diesel sprays". *SAE Technical paper*, 1998.

[112] Payri R., García-Oliver J. M., Xuan T. and Bardi M. "A study on diesel spray tip penetration and radial expansion under reacting conditions". *Applied Thermal Engineering*, Vol. 90, pp. 619–629, 2015.

[113] Higgins B., Siebers D. L. and Aradi A. "Diesel-spray ignition and premixed-burn behavior". *SAE Technical Paper*, 2000.

[114] Idicheria C. A. and Pickett L. M. "Soot formation in diesel combustion under high-EGR conditions". *SAE Technical Paper*, 2005.

[115] Pei Y., Som S., Pomraning E., Senecal P. K., Skeen S. A., Manin J. and Pickett L. M. "Large eddy simulation of a reacting spray flame with multiple realizations under compression ignition engine conditions". *Combustion and Flame*, Vol. 162 n^o 12, pp. 4442–4455, 2015.

[116] Molina S. A. *Estudio de la influencia de los parámetros de inyección y la recirculación de gases de escape sobre el proceso de combustión, las prestaciones y las emisiones de un motor diésel de 1.8 litros de cilindrada.* Doctoral Thesis, Universitat Politècnica de València, 2003.

[117] Epaminondas M. "Ignition of turbulent non-premixed flames". *Progress in Energy and Combustion Science*, Vol. 35 n^o 1, pp. 57–97, 2009.

[118] Idicheria C. A. and Pickett L. M. "Effect of EGR on diesel premixed-burn equivalence ratio". *Proceedings of the Combustion Institute*, Vol. 31 n^o 2, pp. 2931–2938, 2007.

[119] Idicheria C. A. and Pickett L. M. "Formaldehyde visualization near lift-off location in a diesel jet". *SAE Technical Paper*, 2006.

[120] Idicheria C. A. and Pickett L. M. "Quantitative mixing measurements in a vaporizing diesel spray by Rayleigh imaging". *SAE Technical Paper*, 2007.

[121] Pei Y., Davis M. J., Pickett L. M. and Som S. "Engine combustion network (ECN): global sensitivity analysis of Spray A for different combustion vessels". *Combustion and Flame*, Vol. 162 n^o 6, pp. 2337–2347, 2015.

[122] Agarwal A. K., Singh A. P. and Maurya R. K. "Evolution, challenges and path forward for low temperature combustion engines". *Progress in Energy and Combustion Science*, Vol. 61, pp. 1–56, 2017.

[123] García-Oliver J. M., Malbec L. M., Toda H. B. and Bruneaux G. "A study on the interaction between local flow and flame structure for mixing-controlled Diesel sprays". *Combustion and Flame*, Vol. 179, pp. 157–171, 2017.

[124] Tagliante F., Malbec L. M., Bruneaux G., Pickett L. M. and Angelberger C. "Experimental study of the stabilization mechanism of a lifted Diesel-type flame using combined optical diagnostics and laser-induced plasma ignition". *Combustion and Flame*, Vol. 197, pp. 215–226, 2018.

[125] Desantes J. M., García-Oliver J. M., Novella R. and Pérez-Sánchez E. J. "Application of a flamelet-based CFD combustion model to the LES simulation of a diesel-like reacting spray". In *Tenth International Conference on Computational Fluid Dynamics (ICCFD10), Barcelona, Spain*, 2018.

[126] Siebers D. L., Higgins B. and Pickett L. "Flame lift-off on direct-injection diesel fuel jets: oxygen concentration effects". *SAE Technical Paper*, 2002.

Chapter 3

Combustion model description and validation

Contents

3.1 Introduction and overview to the flamelet concept

This chapter deals with describing in detail the combustion model implemented and used for the development of the current work. As was

pointed out in previous chapters, it is based on the flamelet concept which has been extensively applied to non-premixed and partially premixed turbulent combustion occurring in devices such as gas turbines, furnaces and diesel engines, and provides very interesting results as is found in the literature [1–5].

Description of the different combustion models in chapter 2 made patent that there exists a great variety of models that gather different physical and chemical aspects with a wide range of computational cost. The choice of a model based on the flamelet concept as the combusiton model applied to the current calculations responds to a triple objective: to find a model with the ability to manage complex chemistry while retaining transient effects and with a low computational cost.

On the one hand, modelling a transient phenomenon as the ignition of a spray that, in addition, is lifted precludes applying models based on infinitely chemistry rate. On the other hand, not all the models that account for finite rate chemistry seem suitable: CMC, PDF transport equation and linear eddy models, despite their rich physical and chemical content, lead to a high computational cost, especially with large chemical mechanisms which are mandatory for accurate diesel simulations and, more particularly, for pollutant predictions. The moment method is discarded due to its poor description of turbulent fluctuations. However, the flamelet concept arises as an approach for which a good balance between physical and chemical content and computational cost is achieved. These reasons justify the choice of this model for the present research work.

As was explained in chapter 2, the basic idea that underlies to any flamelet model is to describe the turbulent flame as an ensemble of reactive-diffusive laminar flames called flamelets [6]. This means that chemistry is fast enough for not being instantaneously and locally affected by turbulence or, in other words, the chemical characteristic time is small compared to the physical characteristic time or, equivalently, Damköhler number is high. If this happens, turbulence cannot modify the thin layer where combustion develops and, hence, the structure of this layer remains laminar [7–9].

In general, this constrain is formulated stating that the thickness of the combustion layer is smaller than Kolmogorov turbulent scale η. However, it seems that the flamelet assumption is valid even if Kolmogorov eddies enter in the diffusive layer provided that the reaction layer thickness is still smaller than η [7].

Although the wide range of application where the flamelet concept is suitable notice that, as the vast majority of combustion models, it assumes

scale separation forcing chemistry to be fast compared to physical processes (turbulence). Figure 3.1 shows a sketch of how a turbulent reacting spray can be described by a set of flamelets in counterflow configuration with their axis normal to the stoichiometric surface level.

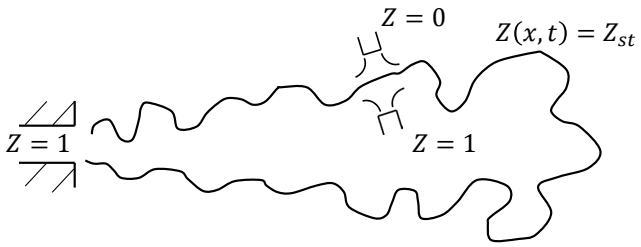

Figure 3.1. *Sketch of a turbulent spray described by a set of laminar flames according to the flamelet concept.*

The previous ideas provide the key to outline the model. Since the turbulent flame is composed of laminar flames, it is necessary to compute a set of laminar flames, previous or during the CFD, whose solutions are used to solve the turbulent flame. Evidently, if a RANS or LES description of the flow is adopted, part of the interactions between chemistry and turbulence are not solved and flamelet solutions should not be directly used. As the mixing process, chemistry occurs at the smallest scales of the flow [1] [10, 11] and, therefore, cannot be computed from the solved motions of the turbulent flow. On the contrary, these processes are related to the smallest scales which are described by means of the flamelets. Flamelets and turbulent flow interact mutually (TCI)[2] and this interaction is described by means of presumed probability density functions (PDFs) for RANS or presumed filtered probability density functions (FPDFs) for LES [12]. These functions in conjunction with flamelet solutions provide a vector of averaged/filtered chemical source terms for the reactive scalars transport equations. It is worth mentioning that as in none of the turbulence approaches (RANS and LES) chemistry is solved[3], it is typical to use similar functions for both PDFs and FPDFs.

[1] Mixing is a consequence of diffusion processes and, hence, only occurs at the smallest scales of the flow. Chemistry happens due to molecules collisions and, then, takes place at the smallest scales of the flow too.

[2] See section 2.4.3.

[3] Chemistry is solved for the flamelet but not in the turbulent flow itself.

Therefore, it is patent that the flow is solved at two scales: a micro-scale, described by flamelet equations where the interaction between mixing and chemistry is solved for a laminar flow, and a macro-scale, related to the large eddies of the flow which are computed by means of RANS or LES turbulence models. The PDFs or FPDFs are the bridge that connect the flow at both scales.

Which laminar flames controlling variables are considered to describe the flamelet depend on the problem to be solved, the accuracy of the calculations, etc. Clearly, one of the key parameters is the fuel mixture fraction Z which was defined in section 2.4.2.2 and follows equation 2.88.

Refined definitions for Z may be found in the literature when different fuel streams are injected in the combustion chamber o non-unity Lewis numbers are considered for different species [13].

Z is a conserved passive scalar, however, if it only accounts for fuel in gas phase but fuel is injected in liquid phase, as is the case of diesel engines, a source term that accounts for evaporation, S_Z, has to be included in equation 2.88. Once the fuel is vaporized this source term is null. Therefore, in the region where combustion develops mixture fraction equation does not usually show any source term.

S_Z is modelled by means of evaporation sub-models that describe the liquid phase evolution and may have an important impact on the liquid length estimation. In addition, in this case Z does not range from 0 to 1 but from 0 to the saturation mixture fraction Z_s defined as the maximum mixture fraction value for which fuel does not condensate for given thermodynamic conditions.

Usually, it is considered that non-premixed turbulent combustion takes place in a stabilized diffusion flame in the vicinity of the stoichiometric surface. This was the basic hypothesis in the Burke-Schumann solution which is one of the pioneer works in describing diffusion flames and dates from 1928 [14]. According to this solution and once a steady regime is reached, combustion occurs only at the stoichiometric surface where fuel and oxygen are consumed to generate products following an irreversible one-step reaction. This implies that for the rest of the mixtures only a diffusion process takes place and, therefore, the solution of a diffusion flame in the mixture fraction space is composed of two straight lines with a jump in the slope positioned at the stoichiometric mixture fraction. This was shown in figure 2.4 from chapter 2 and it is here reproduced for the sake of clarity in figure 3.2. This figure includes the chemical equilibrium solution as well other curves that will be described in the following.

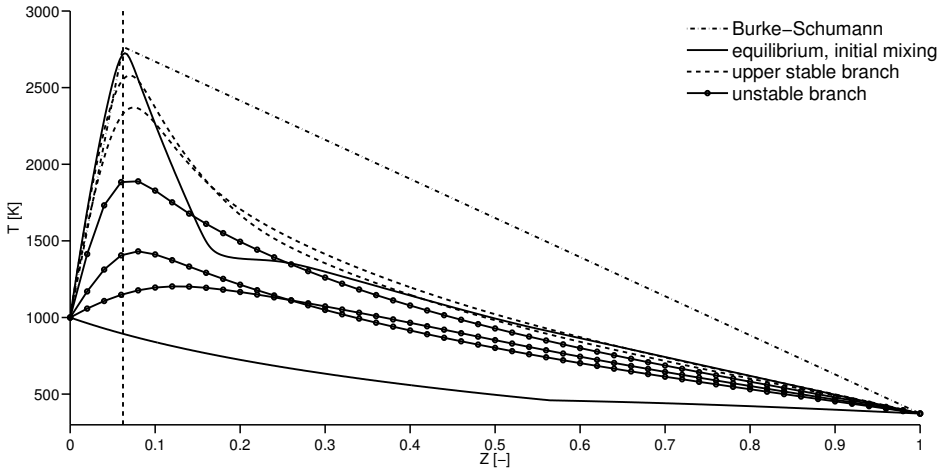

Figure 3.2. *Burke-Schumann, chemical equilibrium and several strained flames solutions as a function of mixture fraction. Vertical black dashed line indicates the stoichiometric mixture fraction. Profiles for heptane at representative diesel engine conditions.*

It is important to distinguish between Burke-Schumann and equilibrium solutions. The first one supposes a structure for the diffusion flame, that can be strained, where only the stoichiometric mixture shows chemical activity while the rest of mixtures are chemically inert. Different to this model, the equilibrium solution is the profile obtained for an unstrained flame for steady regime where there is no chemical activity for any mixture. Both solutions show similar profiles for lean mixtures since in this region equilibrium solution is well-described by a straight line, however, important differences may arise for the rich mixtures where the equilibrium solution may show a curvature that Burke-Schumann model does not exhibit.

The key role that mixture fraction plays invites to rewrite the reactive scalars (species and temperature) transport equations in the mixture fraction space by means of the Crocco transformation [7, 13] leading to equation 2.89. This coordinate transformation implies to consider negligible the transport tangent to the mixture fraction level surfaces compared to their normal direction. This equation is written here for species (equation 3.1) and temperature (equation 3.2) assuming unity Lewis number and constant c_p and gives rise to the Unsteady Flamelet Model (USFM).

$$\frac{\partial Y_i}{\partial t} = \frac{\chi}{2}\frac{\partial^2 Y_i}{\partial Z^2} + \dot{\omega}_i \qquad i = 1, \ldots, N_s \tag{3.1}$$

$$\frac{\partial T}{\partial t} = \frac{\chi}{2}\frac{\partial^2 T}{\partial Z^2} + \dot{\omega}_T \tag{3.2}$$

where Y_i denotes the mass fraction for species i and T the temperature. Moreover, N_s is the total number of species appearing in the chemical mechanism. Equations 3.1 and 3.2 are composed of a transient term, $\partial/\partial t$, a diffusion term $\chi\partial^2/\partial Z^2$ and a chemical source term, $\dot{\omega}_i$ or $\dot{\omega}_T$. As explained in section 2.4.1, the chemical term is obtained from the solution of the ODE chemical system. It is typical to conceptualize a flamelet geometrically in a counterflow configuration and this disposition is adopted in the following.

Thus solving flamelet combustion implies solving for each of the species appearing in the chemical mechanism as well as the temperature the transport equations given by equations 3.1 and 3.2 together with the ODE chemical system. As any PDE[4] system, it is required to provide the corresponding boundary conditions, defined at the fuel and oxidant nozzles, and the initial conditions given by the profiles of the species mass fractions and temperature prior to ignition, that is, the profiles defined by fuel and oxidant mixing.

Equations 3.1 and 3.2 show one clear advantage when compared to the equations in physical space $(\vec{x}, t)$, namely, that the convective term vanishes since there is no relative velocity between the reactive scalars and the mixture fraction [1]. However, not all the links with the physical space have disappeared since the scalar dissipation term χ is retained. This is a fundamental parameter that is defined as

$$\chi = 2D\frac{\partial Z}{\partial x_i}\frac{\partial Z}{\partial x_i} \tag{3.3}$$

From this it is seen that χ measures locally the strength of convection and diffusion normal to the mixture fraction surfaces. In addition, from equation 3.3 it is seen that χ is a non-negative value and is formally identical[5] to the dissipative term ε_ϕ from the scalar variance transport equation 2.33.

In a flamelet there exists a competition between chemical and diffusion processes. Diffusion may contribute to the combustion of mixtures with low reactivity accelerating their ignition while it may slow down the ignition of

[4]Partial differential equation.
[5]Omitting the average operation.

highly reactive mixtures. If χ, or, equivalently, the diffusion intensity is too high for the chemical advancement this may lead to the extinction of the flame or the impossibility of the flame to ignite.

From equations 3.1 and 3.2 and cancelling the transient term (steady regime) it is easily devised the Burke-Schumann solution for one-step irreversible chemistry, advanced in previous paragraphs. In the same way, the mixing line is obtained if chemistry is frozen, the transient term is null and $\chi \neq 0$.

An interesting feature of the Burke-Schumann solution is that it decouples mixing from chemistry, that is, the reactive scalar fields are known once Z field is solved. Assuming some additional hypotheses Burke and Schumann obtained the analytical solution for a reactive jet by solving separately mixing from chemistry [14].

It is worth mentioning that Burke-Schumann solution holds equations 3.1 and 3.2 except for the stoichiometric mixture. As it imposes frozen chemistry in the diffusion regions ($Z \neq Z_{st}$) the value of χ may be arbitrary. On the contrary, if we impose that equations 3.1 and 3.2 hold in the whole range for steady regime and $\chi = 0$, then $\dot{\omega}_i = 0$. The only situation for which a reactive mixture fulfils this condition is the chemical equilibrium. In general, as was noted previously, Burke-Schumann and the equilibrium solutions are close except in the rich region for complex hydrocarbons.

The behaviour of the flame with χ or, equivalently, the Damköhler number[6] is summarized by the so-called S-curve shown in figure 2.5 from chapter 2. The S-curve has been described by means of the asymptotic theory assuming a one-step irreversible reaction and large activation energies and the well-known Liñán's paper [15] is a landmark in its study.

As was explained in section 2.4.2.2, two zones are distinguished: low (high) χ (Da) values define the auto-ignition range where the flame may evolve from inert conditions to a state close to the equilibrium. Increasing (decreasing) χ (Da) enhances diffusion compared with chemistry and defines a new range, known as reignition-extinction range, where there exists an unstable steady branch which may ignite to high temperatures or extinguish to inert conditions when χ (Da) is slightly modified [16, 17]. The reignition-extinction range extends in the interval $[\chi_i, \chi_q]$ ($[Da_q, Da_i]$). For $\chi > \chi_q$ ($Da < Da_q$) diffusion is so intense that combustion does not proceed.

[6] χ may be interpreted as the inverse of a physical time. If the chemical time is considered constant, Da and χ are inversely proportional.

As was previously suggested, the appearance of χ in the flamelet equation forces to link the mixture fraction space to the physical space. In order to avoid solving the mixing process in physical space coupled with flamelet equations, it is usual to prescribe χ (since it depends on Z) and impose the solution obtained for a strained steady constant density counterflow configuration which is given by the following expression [7]

$$\chi(a, Z) = \frac{a}{\pi} Z_s^2 \exp[-2(\text{erfc}^{-1}(2Z/Z_s))^2] \tag{3.4}$$

a is the strain rate, which measures the gradient of the velocity field and, hence, is an indicator of the strength of the convection process. It is usual to approximate the strain rate by a constant value in the whole flame. Z_s corresponds to the saturation mixture fraction previously defined.

From equation 3.4 it is observed that χ can be written as the product of the strain rate and a function depending on the mixture fraction $F(Z)$, that is, $\chi = a\, F(Z)$. Then, it is easily deduced that

$$\chi = \chi_{st} \frac{F(Z)}{F(Z_{st})} \tag{3.5}$$

From equation 3.5 it is deduced that there exists a linear relationship between the strain rate and the scalar dissipation rate for any fixed mixture fraction and, in particular, for the scalar dissipation rate at the stoichiometric mixture, χ_{st}.

At first glance, prescribing the profile for χ could introduce some important discrepancies when comparing with the solution obtained by solving mixing in physical space, especially for transient evolutions. However, different studies show that slight differences are observed when applying equation 3.4 compared to the complete solution in physical space [18]. In the literature, some more refined profiles for χ for non-constant density flows may be found [19]. Nevertheless, in this work all the calculations have been carried out solving flamelet equations in the mixture fraction space with the χ profile given by equation 3.4.

At this point, the transient flamelets have been characterized by three variables, the mixture fraction Z, which measures the part of mass coming from the fuel, the scalar dissipation rate χ, an indicator of the strength of the convective and diffusive processes normal to the mixture fraction level surfaces and, finally, time t. Hence, denoting by ψ any reactive scalar or its chemical source term the solution for ψ for the whole set of flamelets may be written as

$$\psi = \psi(Z, \chi, t) \tag{3.6}$$

As χ shows a dependence with Z it is more useful to re-parametrize the previous equation as

$$\psi = \psi(Z, \chi_{st}, t) \tag{3.7}$$

Flamelet equations may consider additional effects such as flame curvature, heat losses, etc. [7, 20, 21] that introduce new parameters in the equations. Additionally, these equations could be formulated for non-unity Lewis numbers [22]. It is obvious that considering new aspects depends on the problem to be solved and, although they provide a more reliable description of the physical processes, they increase the computational cost. This last aspect has prompted the formulation of new hypotheses to simplify equations 3.1 and 3.2, as we shall see in the following sections.

In fact, a lot of work developed during years has been carried out considering only steady solutions, leading to the Steady Flamelet Model (SFM), or transient solutions but only for one χ_{st} value. In general, this decision is driven by the computational power available at each moment.

Equations 3.1 and 3.2 allow to solve the laminar flame structure and then, apply the solutions to the calculation of the turbulent flame by virtue of the flamelet concept. As was explained previously, the bridge between laminar and averaged/filtered quantities $\widetilde{\psi}$ is given by PDFs in RANS and FPDFs in LES. Additionally, the variables that define the flamelet solution (Z, χ, t) are not further available in the RANS or LES solutions. Instead their corresponding averaged/filtered values are solved in the flow, that is, $(\widetilde{Z}, \widetilde{\chi}_{st}, \ldots)$. In this way, equations for these averaged/filtered input variables are solved in the flow and then, the corresponding values for $\widetilde{\psi}$, which are gathered in a manifold that depends on $(\widetilde{Z}, \widetilde{\chi}_{st}, \ldots)$, are obtained.

Apart from $\widetilde{Z}$, solving mixture fraction variance $\widetilde{Z''^2}$ is normally required since PDFs and FPDFs are typically defined by an average value and a variance. Regarding $\widetilde{\chi}$, although it can be transported [7], it is usual to use some algebraic expression for its calculation as will be explained in section 3.2.

For time variable, if we consider unsteady flamelets, two approaches could be considered. The first one is to solve the flamelet equations *in situ* during the CFD calculation [1]. In this case the flamelet time is taken equal to the CFD time. The second one is to solve the flamelet equations prior to the CFD

calculation making use typically of the progress variable concept, as will be further described in section 3.2.

According to section 2.3.2, $\widetilde{\psi}$ is obtained from presumed PDFs or PDFFs as

$$\widetilde{\psi} = \int \int \dots \int_{\Omega} \psi(Z, \chi_{st}, \dots)\, P(Z, \chi_{st}, \dots; \vec{x}, t)\, dZ\, d\chi_{st} \dots \tag{3.8}$$

where the multiple integral indicates that integration is extended to the whole domain Ω defined by all the flamelet controlling variables $(Z, \chi_{st}, \dots)$. The semicolon indicates that the shape of P depends on $(\vec{x}, t)$.

If $(\widetilde{Z},\ \widetilde{Z''^2},\ \widetilde{\chi}_{st}, \dots)$ are the moments of the different input variables at the point $(\vec{x}, t)$ equation 3.8 can be alternatively written as

$$\widetilde{\psi} = \int \int \dots \int_{\Omega} \psi(Z, \chi_{st}, \dots)\, P(Z, \chi_{st}, \dots; \widetilde{Z}, \widetilde{Z''^2}, \widetilde{\chi}_{st}, \dots)\, dZ\, d\chi_{st} \dots \tag{3.9}$$

Hence equation 3.9 relates $\widetilde{\psi}$ with the the turbulent values of the variables that define the flamelet, namely, $\widetilde{Z}$, $\widetilde{Z''^2}$, $\widetilde{\chi}_{st}$, etc.

If the variables that define the flamelet act at different scales, as the mixture fraction and the scalar dissipation rate, it is possible to argue that their PDFs or PDFFs are statistically independent [13] yielding

$$P(Z, \chi_{st}; \widetilde{Z}, \widetilde{Z''^2}, \widetilde{\chi}_{st}) = P(Z; \widetilde{Z}, \widetilde{Z''^2})\, P(\chi_{st}; \widetilde{\chi}_{st}) \tag{3.10}$$

Once integration has been performed a manifold in the form $\widetilde{\psi} = \widetilde{\psi}(\widetilde{Z}, \widetilde{Z''^2}, \widetilde{\chi}_{st}, \dots)$ is obtained and it is possible to couple the flamelet model with the CFD. To do so there exist different approaches, as will be explained in next section.

Additionally, different information from the flamelet may be used. One method is to transport only the turbulent variables that define the flamelets and then obtain $\widetilde{\psi}$ at each CFD cell from the manifold. The other method is to transport the controlling manifold variables as well as the reactive scalars, for whose equations the chemical source terms are in turn obtained from the database or manifold [13].

The second one is a more general view although computationally more expensive. It enables to account for acoustic waves or fuel evaporation and other phenomena of interest that have not be considered in the flamelet

formulation and, hence, this method is more suitable for problems such as diesel engine simulations [13, 23]. This approach is the one adopted for the current work.

3.2 Description of the model

The previous section provided a general vision of the flamelet concept, describing its advantages, characteristics, etc. and sketched the coupling with CFD. A great variety of ways to do this is found in literature. In most cases, models have been formulated in function of the available computational power, however, the increasing computational resources have prompted new proposals aimed at better solving the combustion process.

On the one hand, the Representative Interactive Flamelet model (RIF) and later, the multi-RIF where the first methods that integrated the flamelet concept [1, 7, 24]. These models solve a set of flamelets *in situ*, that is, together with CFD solution. However, in spite of their promising results, there is a loss of accuracy when considering only some few flamelets to solve the whole combustion. This is due to the fact that these models solve flamelets that are representative of a certain spatial region and do not account for the local conditions reached at each point.

On the other hand, the potential of the pre-tabulated methods has made that these formulations received special attention in the last years. The Intrinsic Low Dimensional Manifold (ILDM), suggested by Maas et al. [25] (see section 2.4.3.4), describes a chemical system evolution in function of very few variables. As the method is not suitable for low temperature combustion it was improved obtaining the chemical information from premixed laminar flames solutions giving rise to the Flamelet Generated Manifold (FGM) [20, 21] and Flame Prolongation of ILDM (FPI) [26] models. These ideas have been extended to non-premixed combustion too.

This last formulation is used for the implementation and calculations of this thesis. As unsteady effects are considered by means of the progress variable concept, this formulation is included in the category of Unsteady Flamelet Progress Variable models (UFPV). Different to RIF approach, the values provided by the model at each cell of the flow are found for the local conditions.

As explained in section 2.4.3.4, progress variable c has its origins in premixed combustion and is used as a variable which discerns between fresh and burnt gases. An easy way to define this variable is

$$c = \frac{T - T_u}{T_b - T_u} \tag{3.11}$$

where T_u and T_b are the temperature of unburned and burnt gases, respectively. Since this definition was typically used for models that considered simplified chemistry and, hence, no dissociation effects, etc. were included, T only ranged between T_u and T_b and, consequently, c was bounded between 0 and 1 [7].

The concept of the progress variable can be extended to other types of combustion as non-premixed combustion [27]. It traces combustion evolution and leads to re-parametrize equation 3.7 in the following way

$$\psi = \psi(Z, \chi_{st}, c) \tag{3.12}$$

This change of variable imposes that a bijective relationship has to exist between c and t. Since this bijection has to occur for all the mixtures and χ_{st}, it is clear that finding a proper definition for c in the case of complex chemistry is not a straightforward task. One option could be the use of previous definition 3.11, however, for long chain fuels the bijective relationship between time and temperature does not necessarily hold. Other option could be to define c in terms of enthalpy [28]. In this work, progress variable is described as a linear combination of species mass fractions. A very extended definition of the non-normalized progress variable Y_c [8] is [29]

$$Y_c = Y_{\mathrm{CO}} + Y_{\mathrm{CO_2}} \tag{3.13}$$

As this definition provides a strictly increasing Y_c variable with time, it is deduced that c, given by

$$c = \frac{Y_c - Y_c^{inert}}{Y_c^{equil} - Y_c^{inert}} \tag{3.14}$$

ranges between 0 and 1. Y_c^{inert} and Y_c^{equil} are the values of Y_c at inert and equilibrium conditions, respectively. From the previous equation, it is

[7] In fact, in different models, such as the Bray-Moss-Liby model, c could only take the values 0 and 1 in the instantaneous field.

[8] In the following, we shall refer to Y_c as the progress variable and c as the normalized progress variable. However, if it is not relevant to distinguish between both in the particular context, we shall refer to c as the progress variable too.

seen that the chemical source terms $\dot{\omega}_c$ and $\dot{\omega}_{Y_c}$ for c and Y_c, respectively, are simply related by

$$\dot{\omega}_c = \frac{\dot{\omega}_{Y_c}}{Y_c^{equil} - Y_c^{inert}} \tag{3.15}$$

Apart from the bijection that has to exist between time and the progress variable, it would be desirable that c fulfilled other properties such as a soft relationship with species in order to describe accurately the whole combustion [30]. Optimisation algorithms have been applied to tackle with the problem of defining proper progress variables [30].

With equation 3.12, evolution of the reactive scalars during combustion is written in terms of intrinsic or internal combustion variables that provide a clear structure of the process. These variables are more meaningful than physical space variables $(\vec{x}, t)$ [9]. The reactive scalars usually show softer evolutions in (Z, χ_{st}, c) than in $(\vec{x}, t)$ reducing memory resources to storage them. In order to illustrate this, figure 3.3 shows the evolution with time and c for some relevant species and temperature for a stoichiometric auto-ignition of dodecane, which is a diesel surrogate that will be used in simulations in next chapters. Figure 3.3 reveals that, except during the cool flame, very high chemical reaction rates are observed when auto-ignition proceeds at both stages in the temporal representation. This makes patent that very fine meshes in temporal direction are required in order to suitably tabulate chemical evolutions different to the tabulation in c, where changes are softer and more gradual.

The more suitable description of combustion in terms of c instead of time is a consequence of the disparity of chemical time scales found during auto-ignition and between mixtures. This was pointed out in chapter 2 and is one of the motivations that prompted the formulation of some methods such as ILDM.

With all these elements, we are in position to describe the particular formulation of the model that has been developed and further applied along this thesis. The description of the model is exposed in detail in the following lines. First, an extensive description of the flamelets calculations is given and, then, how TCI is accounted for is explained. Finally, the coupling between CFD and the combustion database completes the model description.

[9] However, the dependence $c = c(Z, \chi_{st}, t)$ has to be retained to be able to relate reactive scalars evolutions with time.

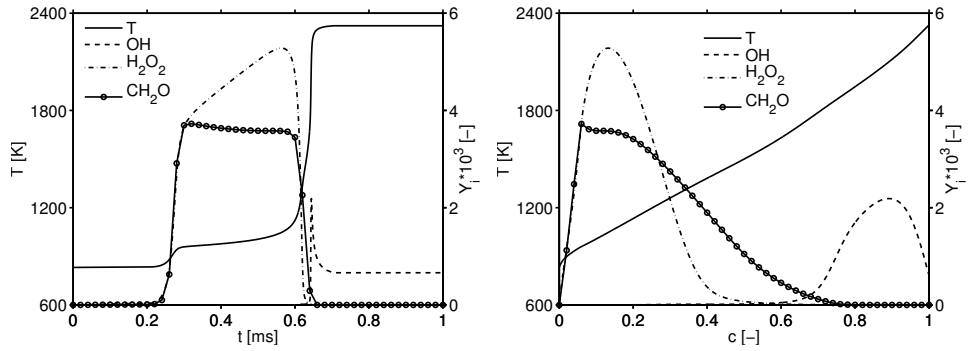

Figure 3.3. *Evolution for temperature and several relevant species as a function of time (left) and c (right). Profiles for a stoichiometric mixture fraction of dodecane and representative diesel engine conditions.*

3.2.1 Initial and boundary conditions

As in any transient flow problem, the first step is to provide the boundary and initial conditions for the flamelets. In this case, the boundary conditions are given by the particular conditions at the border of the domain, that is, thermodynamic conditions and composition at the oxidant and fuel sides together with the strain rate.

The initial conditions are defined by the mixing of fuel and air prior to combustion and such conditions, consisting of temperature and composition, have to be provided for each mixture fraction. The species mass fractions are easily obtained since they show a linear relationship with Z. For this work, as no heat losses are included in flamelet calculations, temperature is calculated from the conservation of enthalpy and the composition by means of Raoult's law. Consequently, an adiabatic ideal mixing between fuel and air is supposed. Fuel in gas phase and air are assumed to be real gases.

If fuel is injected in liquid phase, the enthalpy required to vaporise the fuel has to be included in the energetic balance. After mixing, fuel is completely vaporised for the mixtures $Z \in [0, Z_s]$, where Z_s is the saturation mixture fraction, that, as defined in section 3.1, is the maximum mixture fraction for which fuel does not condensate. When $Z > Z_s$ air and fuel in gas and liquid phases coexist in the same mixture. This means that the adiabatic mixing line is calculated assuming equilibrium between liquid and vapour and this is justified for typical diesel engine work conditions in the light of the fact that evaporation is mixing controlled [31], as explained in sections 2.5.2 and 2.5.4.

3.2.2 Flamelet equations

3.2.2.1 The DF model

The set of equations to solve the flamelet consists of the species and enthalpy transport equations and the ODE chemical system (see section 2.4.1 for equations 3.18, 3.19, 3.20 and 3.21).

$$\frac{\partial Y_i}{\partial t} = \frac{\chi}{2}\frac{\partial^2 Y_i}{\partial Z^2} + \dot{\omega}_i \qquad i = 1, \ldots, N_s \tag{3.16}$$

$$h(Z) = Z\, h_{fuel} + (1 - Z)\, h_{ox} = \sum_{j=1}^{N_s} Y_i h_i \tag{3.17}$$

$$\dot{\omega}_i = W_i \sum_{j=1}^{N_r} \nu_{i,j}\, \dot{q}_j \tag{3.18}$$

$$\dot{q}_j = k_{f,j} \prod_{i=1}^{N_s} [M_i]^{\nu'_{i,j}} - k_{b,j} \prod_{i=1}^{N_s} [M_i]^{\nu''_{i,j}} \tag{3.19}$$

$$k_{f,j} = A_{f,j}\, T^{\beta_{f,j}} \exp\left(-\frac{E_{a_{f,j}}}{RT})\right) \tag{3.20}$$

$$k_{b,j} = A_{b,j}\, T^{\beta_{b,j}} \exp\left(-\frac{E_{a_{b,j}}}{RT})\right) \tag{3.21}$$

where h is the total enthalpy used to obtain temperature. The advantage of using the total enthalpy is that if pressure changes, radiation, etc. are neglected it has no source terms and, if unity Lewis number is assumed, then the total enthalpy and the mixture fraction are linearly related. This means that no PDE for the total enthalpy is required [7] since it is simply computed from $h(Z) = Z\, h_{fuel} + (1 - Z)\, h_{ox}$, where h_{fuel} and h_{ox} are the total enthalpy for fuel and oxidant, respectively.

Different flamelets defined by their stoichiometric dissipation rate χ_{st} or, equivalently, the strain rate a are solved. Normally, the steady solutions are first obtained leading to the calculation of the S-curve. Once the S-curve is completely computed the unsteady or transient solutions are carried out. If the strain rate belongs to the auto-ignition range the flamelet evolves from inert conditions to the upper stable branch and, in this case, the initial solution

corresponds to the mixing line. However, if the strain rate is in the reignition-extinction range several flamelets may be solved. If the mixing line is provided as the initial condition the flamelet will only reach a state close to the mixing line defined by the lower stable branch. Nonetheless, if the unstable branch is given as initial condition, the flamelet evolves to the upper stable branch or the lower stable branch if the strain rate is slightly decreased or increased, respectively.

Once the flamelet equations have been solved in the whole range of strain rates for the steady and unsteady solutions, it is usual to re-parametrize time by the more suitable progress variable. This has several advantages since, as was commented previously, the profiles of the variables adopt soft profiles in the progress variable space. Consequently, to retain the flame structure, only the progress variable is stored as a function of time, $c = c(Z, a, t)$, or equivalently, $Y_c = Y_c(Z, a, t)$ and the rest of variables are re-parametrized with c instead of t, that is, $\psi = \psi(Z, a, c)$.

Important amounts of memory are saved when storing flamelet solutions as a function of c since, in general, around 100 values are typically needed in practice to trace most of the reactive scalars evolution accurately. In addition, it is not necessary to store the evolution for the whole set of species for further calculations since this would soar the computational requirements. Instead of this, the most important species, which constitute almost the whole mass of the mixture, are saved. The mass deficit generated by this procedure is later treated during the CFD calculation as will be explained.

Additionally, it is required to save the source term for the progress variable for subsequent CFD calculations. Since the progress variable is defined from other variables of the system, in our case from a linear combination of species mass fractions, it is easily obtained from the source terms of such species that define Y_c. If the chemical source terms $\dot{\omega}_i$ are used, the source term for the progress variable is $\dot{\omega}_{Y_c}$. However, if the species flamelet transient terms $\partial Y_i/\partial t$ are used, we shall refer to their linear combination as $\partial Y_c/\partial t$ or, equivalently, $\dot{Y}_c$.

At this point, the generated flamelet database is composed of $c = c(Z, a, t)$, $\psi = \psi(Z, a, c)$ and $\dot{Y}_c = \dot{Y}_c(Z, a, c)$. In this work, we call this model the Diffusion Flamelet model (DF). Figure 3.4 summarizes in a flowchart the steps to solve the DF model.

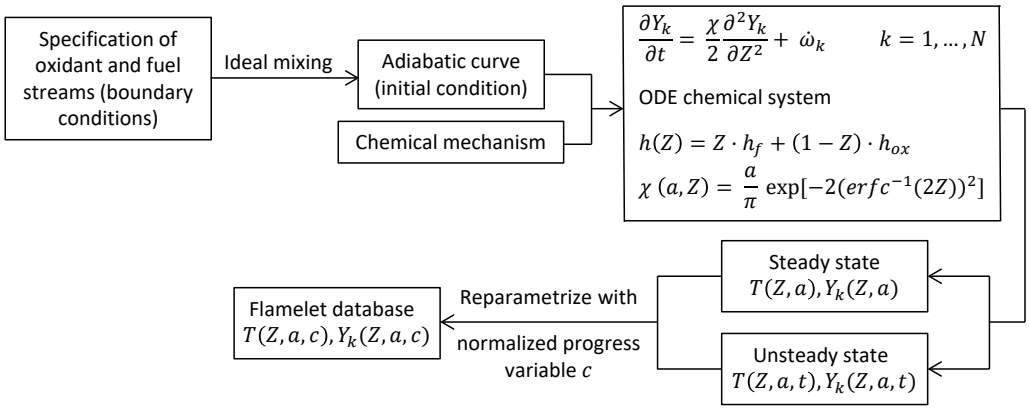

Figure 3.4. *DF model description flow chart.*

3.2.2.2 The ADF model

DF model requires to solve a PDE system and a ODE system of N_s equations each one. For complex hydrocarbons, hundreds of species may appear during fuel oxidation and thousands of reactions may take place. Additionally, when boundary conditions span over wide ranges as in the case of diesel engines, a high number of flamelets have to be solved to cover the whole set of strain rates, pressures, EGR, etc. The concurrence of these facts make infeasible the calculation of the flamelet database with complex mechanisms in a reasonable amount of time for diesel engine applications.

In this context, several years ago a new model of diffusion flamelets was proposed in order to tackle with these issues. The approach is called the Approximated Diffusion Flamelet model (ADF) [32] and assumes new hypotheses on the combustion structure of the flame. It makes extensive use of the progress variable concept for its formulation and is based on the following hypothesis: the relationship between any reactive scalar ψ or chemical source term and the progress variable Y_c does not depend on the strain rate.

This means that in the ADF model the relationships $\psi = \psi(Z, Y_c)$ and $\dot{\omega}_i = \dot{\omega}_i(Z, Y_c)$ are fixed for any strain rate. From this it is deduced that, as the previous relationships do not show any dependency with the strain rate, it would be enough to solve only one flamelet with the DF model to obtain such relationships. The most economical way to accomplish this is to solve a

flamelet corresponding to strain rate null or, equivalently, a set of homogeneous reactors (HRs) since no strain rate implies no diffusion and no convection and, hence, mixtures can be solved separately.

As each of the homogeneous reactors is solved separately (not coupled with the rest as the whole set of mixtures are in a flame), their resolution takes only a small amount of time compared to any flamelet (DF model) where the fastest species for the fastest mixture fraction limits the time step for all the rest of mixtures. In addition, no PDEs are solved.

Homogeneous reactors are computed imposing the same initial and boundary conditions at fuel and oxidant streams than those used for the DF model. In this work no heat losses are considered and, hence, adiabatic evolution with constant pressure is imposed in order to solve their chemical evolution [32].

Once the relationships $\psi = \psi(Z, Y_c)$ and $\dot{\omega}_i = \dot{\omega}_i(Z, Y_c)$ are calculated it is not necessary to solve the PDE system 3.16 since their dependence with Y_c is known. Instead only a PDE for Y_c is required to solve the flamelets for the different strain rates. This equation is a linear combination of species mass fractions equations and reads

$$\frac{\partial Y_c}{\partial t} = \frac{\chi(a, Z)}{2} \frac{\partial^2 Y_c}{\partial Z^2} + \dot{\omega}_{Y_c}^{HR}(Z, Y_c) \tag{3.22}$$

where the dependencies have been explicitly written.

In summary, solving the ADF model requires to compute

1. The set of homogeneous reactors with the corresponding boundary and initial conditions (the same that those used to solve the DF model).

2. The PDE transport equation defined for the progress variable and given by equation 3.22. $\dot{\omega}_{Y_c}^{HR}$ appearing in equation 3.22 is the chemical source term for the progress variable obtained from solving the homogeneous reactors. From this equation $\dot{Y}_c$ is obtained too.

3. The evolution for any reactive scalar $\psi = \psi(Z, a, t)$ is obtained from $\psi = \psi(Z, Y_c)$, computed from homogeneous reactors calculations, and $Y_c = Y_c(Z, a, t)$, found from the flamelet solution.

Hence, a database in the form $c = c(Z, a, t)$, $\psi = \psi(Z, c)$ and $\dot{Y}_c = \dot{Y}_c(Z, a, c)$, as in the DF model, is stored for subsequent calculations. A description of the steps of the ADF approach is gathered in the flowchart

shown in figure 3.5. Finally, note that as the DF model converges to the solution of homogeneous reactors when $a \to 0$, both DF and ADF models tend to provide the same solutions when $a \to 0$.

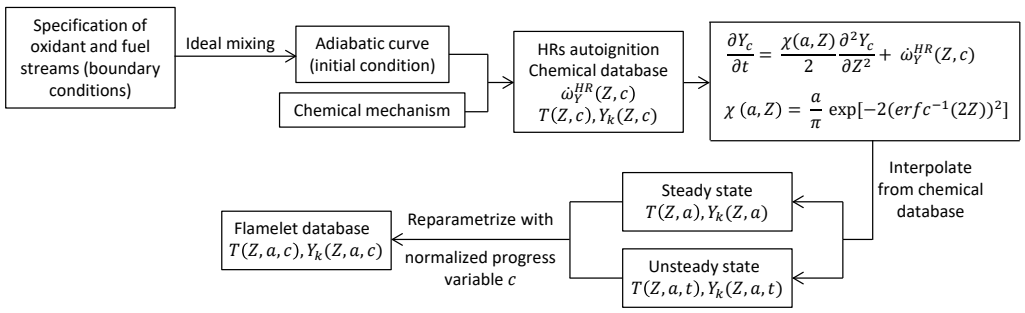

Figure 3.5. *ADF model description flow chart.*

It is clear that the ADF model makes an assumption that seems quite strong and, consequently, requires a detailed validation. For this purpose, section 3.3 assesses ADF model by means of the comparison of both DF and ADF solutions in steady and unsteady regimes in the whole range of strain rates for different representative fuels. It is emphasized that the ADF model was conceived to solve the flamelet equations with complex chemical schemes, necessary to reproduce pollutant emissions, lift-off length, etc. at a diesel spray, while reducing drastically the computational cost. In the light of this purpose this model has to be understood and the main objective of the validation to be exposed in section 3.3 consists of showing that the losses of accuracy are acceptable and largely compensated by the benefits in computational cost.

For the moment, we will explain different aspects of the ADF model that have been improved from other authors ideas or directly developed in this thesis which are necessary to consider in order to perform successful calculations. We will start with some useful definitions that we will use along the work and can be applied to both ADF and DF models.

A flame progress variable c_F normalized to the upper steady solution Y_c^{steady} instead of equilibrium (see definition 3.14 for the normalized progress variable c) is expressed as

$$c_F(Z,a,t) = \frac{Y_c(Z,a,t) - Y_c^{inert}(Z)}{Y_c^{steady}(Z,a) - Y_c^{inert}(Z)} \tag{3.23}$$

c_F range over the interval $[0,1]$ since all the flamelet states are limited by the inert solution and the corresponding value for the upper branch of the S-curve. In the auto-ignition range c_F is monotonic with time.

Moreover, to trace the evolution of the whole flame another normalized variable is useful. For that purpose, variable c_2, defined by the following formula, is used:

$$c_2(a,t) = \frac{\int_0^{Z_s}(Y_c(Z,a,t) - Y_c^{inert}(Z))\,dZ}{\int_0^{Z_s}(Y_c^{steady}(Z,a) - Y_c^{inert}(Z))\,dZ} \tag{3.24}$$

c_2 expresses the ratio between the areas enclosed by the inert and the Y_c profile at each instant and the inert and the steady profile Y_c^{steady} from the upper branch. In the auto-ignition range, as c_F is monotonic with time c_2 is monotonic too. Consequently, c_2 shows a one-to-one relationship with time for a fixed strain rate in such range[10].

In the following we will explain some methods developed in this work to improve the ability of the ADF model to describe combustion. The first aspect deals with the numerical treatment of the progress variable source term obtained from the homogeneous reactors. As it is known, the auto-ignition of a mixture may be separated in at least three main stages: a first period corresponding to the ignition delay where slow reactions take place and a radical pool is accumulated until a critical value is reached, a second period of rapid and exothermic reactions that release high amounts of heat[11] that lead to the third stage, the chemical equilibrium. It is a recommendable practice, when generating the homogeneous reactors database for the ADF model, to calculate both the transient evolution as well as the equilibrium solution, which is used to fill the values for the different variables related to $c = 1$.

In order to solve the ADF flamelet equation, first, it is necessary to verify that, when integrating the chemical source term from the homogeneous reactors database $\dot{\omega}_{Y_c}(Y_c)$ [12], the $Y_c = Y_c(t)$ profile given by homogeneous

[10] This relationship is different for each strain rate.

[11] In complex fuels, this stage may be composed of complex processes such as those observed during the cool flame.

[12] In the following we will omit superscript HR used in equation 3.22 since in the ADF context it is understood that the chemical source terms come from the homogeneous reactors database.

reactors auto-ignition is retrieved[13]. We will refer to this integration as reconstruction. It is clear that $\dot{\omega}_{Y_c}$ tabulation implies some losses that may provoke some deviations in $Y_c = Y_c(t)$ curve between the one given by homogeneous reactors auto-ignition and the reconstructed profile. However, these losses have a very different impact on the reconstruction depending on the value of $\dot{\omega}_{Y_c}$ [14].

In fact, as the chemical reaction rates are typically high during the second stage there are no appreciable losses when tabulating and subsequently reconstructing. However, the initial chemical reaction rate is critical to predict accurately the ignition delay when reconstructing since small changes in its values cause important deviations.

During ignition delay there is no appreciable progress variable evolution. This means that the first tabulated progress variable chemical reaction rate is extremely low (it may be several orders of magnitude lower than the values reached during combustion)[15]. Consequently, the initial value provided by solving homogeneous reactors auto-ignition has no necessarily real meaning and has to be adjusted *a posteriori* since small errors in this value dilate/compress artificially the ignition delay of the reconstructed curve.

How such value is adjusted depends on the interpolation method followed in the progress variable direction, that is, how the curve $\dot{\omega}_{Y_c}$ is interpolated. In this thesis, interpolations in all directions are performed by means of piecewise linear interpolations, including the progress variable direction. In this way, continuity is retained (not for the derivative). Although, at first glance, higher order interpolations would provide more exact solutions, this is not always the case for $\dot{\omega}_{Y_c}$. For example, if owing to the use of splines or other polynomials, zero values or negative chemical source terms were provided by the interpolation the reaction could not proceed further from an intermediate state during its reconstruction. Finally, some authors use discontinuous functions, such as step functions [23], however, this is deemed not to be the proper solution since discontinuities may cause different numerical disadvantages when solving flamelet equations. Consequently, it is though

[13] In this discussion, as we assume the mixture fixed, we omit the dependence of $\dot{\omega}_{Y_c}$ with Z.

[14] Note that $\dot{\omega}_{Y_c}$ is saved in terms of the progress variable and not of time. This makes the reconstruction sensitive to small changes in $\dot{\omega}_{Y_c}$ when it shows very small values.

[15] Even introducing fuel mass in the definition of the progress variable no appreciable changes in its value would occur during ignition delay. Considering radicals in the progress variable definition is an extremely complicated task due to the mathematical properties that the progress variable has to fulfil. Therefore, it seems unavoidable the treatment of these low chemical source terms.

that the use of piecewise linear interpolations provides desirable properties to solve the equations, namely, continuous and bounded functions.

The following method finds the necessary initial value for the progress variable chemical source term $\dot{\omega}_{Y_c,0} = \dot{\omega}_{Y_c}(c = 0)$ to reach a given value c_1 in a time t_1 when integrating $\dot{\omega}_{Y_c}$ with a linear interpolation in the interval $[0, c_1]$ [16]. In general, c_1 corresponds to the first non-null tabulated value of the vector c used for the chemical database. In addition, we will assume that $\dot{\omega}_{Y_c,1} = \dot{\omega}_{Y_c}(c = c_1)$ is known from the homogeneous reactors calculation and its value is reliable[17].

By virtue of the piecewise linear interpolation, we write $\dot{\omega}_{Y_c} = mc + \dot{\omega}_{Y_c,0}$ for $c \in [0, c_1]$ with $m = (\dot{\omega}_{Y_c,1} - \dot{\omega}_{Y_c,0})/c_1$ the slope of the line. From the definition of $\dot{\omega}_c$ and integrating in the interval $[0, c_1]$

$$\dot{\omega}_c = \frac{\dot{\omega}_{Y_c}}{Y_c^{equil} - Y_c^{inert}} = \frac{dc}{dt} \Rightarrow \int_0^{t_1} \frac{dt}{Y_c^{equil} - Y_c^{inert}} = \int_0^{c_1} \frac{dc}{\dot{\omega}_{Y_c}} = \int_0^{c_1} \frac{dc}{mc + \dot{\omega}_{Y_c,0}} \tag{3.25}$$

Solving

$$\frac{t_1}{Y_c^{equil} - Y_c^{inert}} = \frac{1}{m} \ln\left(\frac{mc_1 + \dot{\omega}_{Y_c,0}}{\dot{\omega}_{Y_c,0}}\right) = \frac{c_1}{\dot{\omega}_{Y_c,1} - \dot{\omega}_{Y_c,0}} \ln\left(\frac{\dot{\omega}_{Y_c,1}}{\dot{\omega}_{Y_c,0}}\right) \tag{3.26}$$

Calling $t_1' = \frac{t_1}{Y_c^{equil} - Y_c^{inert}}$ the expression is rewritten as

$$\frac{\exp\left(\frac{t_1'}{c_1}\,\dot{\omega}_{Y_c,1}\right)}{\frac{t_1'}{c_1}\,\dot{\omega}_{Y_c,1}} = \frac{\exp\left(\frac{t_1'}{c_1}\,\dot{\omega}_{Y_c,0}\right)}{\frac{t_1'}{c_1}\,\dot{\omega}_{Y_c,0}} \tag{3.27}$$

With the notation $A = \frac{\exp\left(\frac{t_1'}{c_1}\,\dot{\omega}_{Y_c,1}\right)}{\dot{\omega}_{Y_c,1}}$ and $B = \frac{t_1'}{c_1}$ the previous equation is written in the following form

$$-\frac{B}{A} = -B\,\dot{\omega}_{Y_c,0}\,\exp\left(-B\,\dot{\omega}_{Y_c,0}\right) \tag{3.28}$$

[16] In this work interpolations are carried out in c instead of Y_c since c may be defined on an orthogonal mesh and, therefore, the domain (Z, c) is a rectangle.

[17] With reliable it is meant that its integration leads to an increment of progress variable in a time step that matches with the homogeneous reactor calculation. To fulfil this, it is enough to be sufficiently high and this condition is usually achieved provided that chemical reactions have initiated and produced some amount of heat.

This equation is of the form $M = z \exp(z)$ where M is known (and corresponds to $-B/A$) and z is the variable to be solved (and corresponds to $-B\dot{\omega}_{Y_c,0}$). The solution to this equation is given by the inverse of the function $f(x) = x \exp(x)$ which is called Lambert W function and is shown in figure 3.6 for real values.

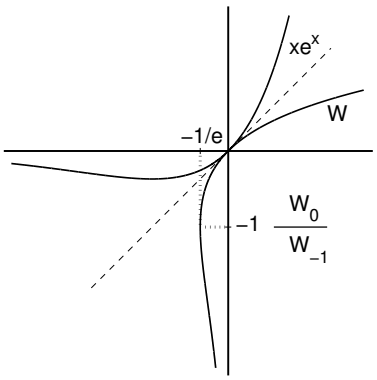

Figure 3.6. *$x \exp x$ and Lambert W functions.*

W is a multivalued function (except at 0) and for real values ranges over the interval $[-1/e, \infty[$. It is composed of two branches or solutions called branches 0 and -1, W_0 and W_{-1}, respectively. If $x \geq 0$ the only image is given by branch 0, W_0, however, for $x \in [-1/e, 0[$ is composed by branch 0, with $W_0 \geq -1$, and branch -1, with $W_{-1} < -1$.

Observing equation 3.27 it arises that $A, B > 0$ [18] and

$$-\frac{B}{A} = -\frac{t_1'}{c_1}\,\dot{\omega}_{Y_c,1}\,\exp\left(-\frac{t_1'}{c_1}\,\dot{\omega}_{Y_c,1}\right) \in \mathrm{Im}\,(x \exp x) \rightarrow -\frac{B}{A} \geq -\frac{1}{e} \qquad (3.29)$$

where Im denotes the image of a function. Consequently, it is deduced that $-1/e \leq -B/A \leq 0$ and, hence, the problem has always a solution defined by W_0 or W_{-1}. Notice that equation 3.28 has two solutions, the trivial one given by $\dot{\omega}_{Y_c,1}$ (replacing $\dot{\omega}_{Y_c,0}$ by $\dot{\omega}_{Y_c,1}$ the identity is obtained[19]) and a non-trivial solution.

[18] It is assumed that $\dot{\omega}_{Y_c} \geq 0$.

[19] In fact, from a rigorous point of view this is not a solution to the problem since in the development to achieve equation 3.26, it is implicitly assumed that $m \neq 0$.

As in the interval $[-1/e, 0[$ there is only one image per branch, it is deduced that the non-trivial solution $-B\dot{\omega}_{Y_c,0}$ and $-B\dot{\omega}_{Y_c,1}$ are given one of them by branch W_0 and the other one by W_{-1}. Therefore, solution $-B\dot{\omega}_{Y_c,0}$ is found on the branch where $-B\dot{\omega}_{Y_c,1}$ does not belong to. More explicitly, as $W_0 \geq -1$ and $W_{-1} < -1$, if $-B\dot{\omega}_{Y_c,1} \geq -1$ then it belongs to W_0 and, therefore, $-B\dot{\omega}_{Y_c,0}$ is defined by W_{-1} and vice versa. In summary, $\dot{\omega}_{Y_c,0}$ is obtained from the following solution

$$\dot{\omega}_{Y_c,0} = \begin{cases} -W_0(-B/A)/B & -B\dot{\omega}_{Y_c,1} < -1 \\ -W_{-1}(-B/A)/B & -B\dot{\omega}_{Y_c,1} \geq -1 \end{cases} \tag{3.30}$$

With the value $\dot{\omega}_{Y_c,0}$ provided by equation 3.30 and a linear interpolation in the progress variable direction, a value of c_1 is reached in a time t_1 with the prescribed source term $\dot{\omega}_{Y_c,1}$.

In the case that time t_1 is unknown or $\dot{\omega}_{Y_c,1}$ is not reliable, previous steps are applied to the first non-null tabulated c value with available information and, then, chemical reaction rates in-between are linearly interpolated. Once these rates are computed the corresponding values of time can be found from equation 3.26. It arises that using a linear interpolation in the progress variable provides a piecewise exponential curve when reconstructing the homogeneous reactor solution (see equation 3.26).

A comparison between solutions $c = c(t)$ provided by the homogeneous reactor numerical solution and the reconstructed profile obtained from applying previous adjustment is shown in figure 3.7. It is observed that an excellent reconstruction is obtained.

With this method, the problems related to capture the ignition delay are circumvented avoiding the use of very fine meshes which may not be so effective and increase the computational storage.

In a similar way, the method is applied to the tabulation of $\partial Y_c/\partial t$ at $c = 0$ for both DF and ADF models when solving the flamelets since otherwise an artificial delay would be introduced too.

The second aspect related to ADF model improvements deals with a phenomenon occurring during flamelet ignition when applying the ADF model to long chain hydrocarbons. It was first described in a paper by Michel et al. [32] where they suggested a correction in order to avoid this deviation. In the following paragraphs this phenomenon is described and an alternative adjustment, based on that given by Michel et al., is explained.

It is observed that for long chain hydrocarbons subjected to diesel-like boundary conditions, rich mixtures show an artificially rapid ignition during

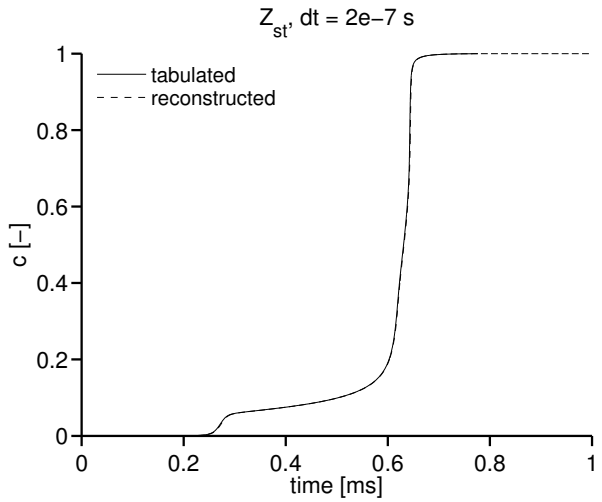

Figure 3.7. *Comparison between the tabulated and reconstructed profiles $c = c(t)$. Solutions for a stoichiometric mixture fraction of dodecane and representative diesel engine conditions. Time step for the reconstruction equal to $2 \cdot 10^{-7}$ s.*

ADF flamelet combustion. Figure 3.8 compares a $Y_c(Z)$ profile for both DF and ADF models for a flame with a strain rate of 200 1/s. For reference, the steady solution is included too. Moreover, $\dot{\omega}_{Y_c}(Z)$ curves corresponding to previous $Y_c(Z)$ profile for both DF and ADF models as well as the chemical source terms read in the homogeneous reactors database for the $Y_c(Z)$ DF profile, labelled as 'DF-HRs', are represented. Figures correspond to heptane flamelet combustion at representative diesel engine conditions.

As deduced from figures the ADF model predicts a remarkable faster ignition for rich mixtures compared to the DF model. In addition, it is very illustrative to compare $\dot{\omega}_{Y_c}(Z)$ for the DF model and the profile 'DF-HRs' since for the first curve the chemical source terms are extremely low for mixtures $Z \geq 0.35$. However, 'DF-HRs' profile predicts higher chemical source terms in all the range of mixture fractions. This evidences that the artificial acceleration of rich mixtures when solving the flamelet using the homogeneous reactors chemical source terms (ADF model) has a physical ground and is not due, at least in its totality, to numerical errors.

This fact is clearer seen in figure 3.9 where $\dot{\omega}_{Y_c}$ is represented as a function of c for strain rate 200 1/s and stoichiometric and rich mixtures for the homogeneous reactors and the DF model. A zoom is made for low c values. It

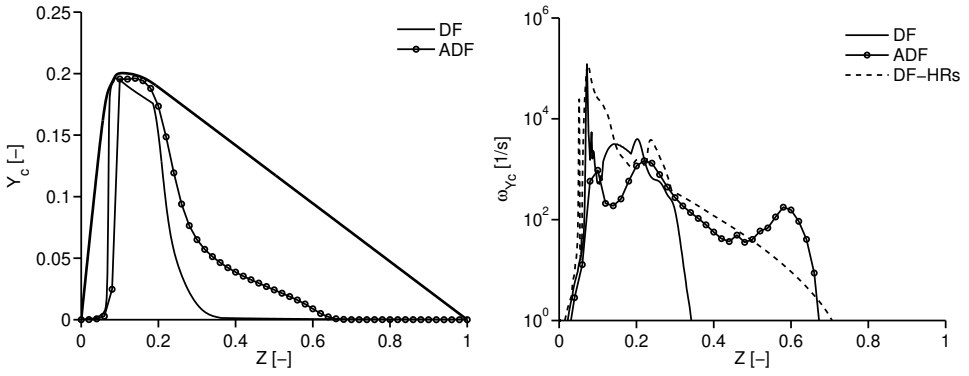

Figure 3.8. *$Y_c(Z)$ profiles during flamelet ignition for $a = 200$ 1/s for both DF and ADF models (left). Steady solution is included in bold. $\dot{\omega}_{Y_c}(Z)$ for both $Y_c(Z)$ profiles and homogeneous reactors chemical source terms $\dot{\omega}_{Y_c}^{HR}$ interpolated for $Y_c(Z)$ DF curve and labeled as DF-RHs (right). Solutions for heptane at representative diesel engine conditions.*

is observed that the discrepancies for $\dot{\omega}_{Y_c}$ between homogeneous reactors and DF flamelets are moderate for the stoichiometric mixture but increase when enriching the mixture leading to a substantial reduction of the chemical source term given by the DF model compared to homogeneous reactors solutions. Although not shown, these discrepancies are more important when increasing the strain rate. This explains the artificial acceleration of the ADF flamelet ignition, observed in figure 3.8, that requires some kind of limitation for the homogeneous reactors reactivity in order to improve its results.

This behaviour should not be seen as an impediment for the application of the ADF model. Deviations from the correct evolution are expected when introducing simplifications. However, if possible corrections can be adopted in order to retrieve the correct evolution and if the computational cost benefits are evident, a simplified approach has still space for solving the problem it was addressed to.

Based on the ideas presented by Michel et al. to mitigate this behaviour [32], we explain a correction based on the Livengood and Wu approximation [33], described in section 2.4.1. This correction moderates the chemical reaction rates of the mixtures while they do not overcome the ignition delay time and is composed of two aspects, the time for which it is applied and how the chemical source term is reduced.

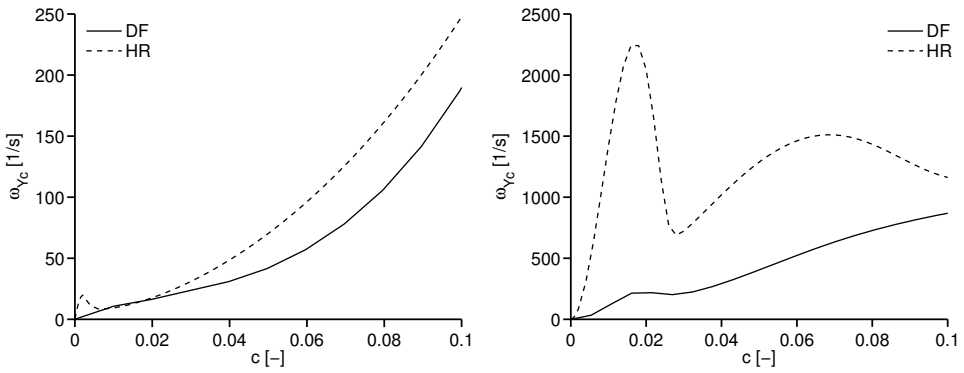

Figure 3.9. *$\dot{\omega}_{Y_c}(Z)$ for the homogeneous reactors and the DF model for $a = 200$ 1/s as a function of c for stoichiometric (left) and rich (right) mixtures in the interval of low c values. Solutions for heptane at representative diesel engine conditions.*

The time for which the correction extends is deduced from the Livengood and Wu integral which states that the ignition delay t^* of a transient evolution fulfils

$$\int_0^{t^*} \frac{dt}{\tau(Z, T(t), \vec{Y}(t))} = 1 \tag{3.31}$$

where $\tau(Z, T(t), \vec{Y(t)})$ is the ignition delay for a mixture subjected to the fixed initial conditions given by $(Z, T, \vec{Y})$, where $\vec{Y}$ is the vector of compositions. The dependence with flamelet time t in the term $\tau(Z, T(t), \vec{Y}(t))$ has been explicitly introduced to remark that temperature and composition are a function of time during flame ignition.

Assuming that the local conditions of the mixture do not strongly change until ignition occurs, a zero order approximation is adopted. Then, $\tau(Z, T(t), \vec{Y}(t)) \approx \tau(Z, T(0), \vec{Y}(0)) = \tau(Z)$, that is, the ignition delay $\tau(Z)$ for the mixture fraction at the thermochemical conditions defined by the mixing line. Substituting in equation 3.31, and as $\tau(Z)$ does not depend on the local conditions, it is easily seen that the condition 3.31 becomes

$$\frac{t^*}{\tau(Z)} = 1 \tag{3.32}$$

The value $\tau(Z)$ is simply obtained from the database of the homogeneous reactors evolutions. For this purpose, a threshold value of the progress variable

c^* is chosen and the ignition delay $\tau(Z)$ is defined as the time spent by a mixture to reach the value $c = c^*$. Then,

$$t^*(Z) = \tau(Z) = t^{HR}(Z, c = c^*) \tag{3.33}$$

where t^{HR} is in fact the time spent by a mixture fraction Z to reach a value c in homogeneous conditions. Consequently, the correction is applied only while $t \leq t^*(Z)$ for a mixture fraction Z, where t is the flamelet time. In this work, c^* has been chosen equal to $5 \cdot 10^{-4}$. It is not expected that the choice of c^* has a strong impact on the final results since once ignition delay is overcome combustion develops in a very short time.

The second part of the correction deals with how the chemical reaction rates are reduced. For this purpose, $\dot{\omega}_{Y_c}(Z, c)$ is multiplied by a factor of the form $(t/t^*)^\alpha$ with $\alpha \geq 0$. In this way, the intensity of the correction is moderated according to the ratio between the flamelet time and the mixture fraction ignition delay and continuity of $\dot{\omega}_{Y_c}$ is retained. As the correction is only applied for $t \leq t^*(Z)$ and $\alpha \geq 0$ we have $0 \leq (t/t^*)^\alpha \leq 1$.

Therefore, the correction takes the final form

$$\dot{\omega}_{Y_c}(Z, t) = \begin{cases} \left(\frac{t}{t^*(Z)}\right)^\alpha \dot{\omega}_{Y_c}^{HR}(Z, c(t)) & t < t^*(Z) \\ \dot{\omega}_{Y_c}^{HR}(Z, c(t)) & t \geq t^*(Z) \end{cases} \tag{3.34}$$

where $\dot{\omega}_{Y_c}^{HR}$ refers to the chemical source term from homogeneous reactors database.

If no correction is applied it suffices to take $\alpha = 0$ while $\alpha = \infty$ leads to

$$\dot{\omega}_{Y_c}(Z, t) = \begin{cases} 0 & t < t^*(Z) \\ \dot{\omega}_{Y_c}^{HR}(Z, c(t)) & t \geq t^*(Z) \end{cases} \tag{3.35}$$

This last case generates discontinuous chemical reaction rate profiles and is not recommended. On the contrary, using a finite and positive value for α modulates the intensity of the correction with time and provides a continuous $\dot{\omega}_{Y_c}(Z, t)$ profile[20] avoiding non-physical and numerical perturbations. The greater the exponent α is, the more reduced the reactivity of the mixture is, causing a more dilated flamelet ignition delay.

In practice, α is of the order of unity. The value of α may be adjusted from one DF flamelet reference case or, if not possible, with experimental

[20] Provided that $\dot{\omega}_{Y_c}^{HR}$ is continuous as it is in this work.

information from laminar or turbulent combustion. Moreover, from the definition of this chemical source term limitation, it is clear that it only affects flame transient evolution and has no influence on its steady regime.

In order to evaluate the influence of the limitation of the chemical source terms on the ADF solutions, figure 3.10 shows a similar representation to that appearing in figure 3.8 taking $\alpha = 2$. It is observed that the premature ignition of rich mixtures is inhibited providing a good agreement between both DF and ADF solutions.

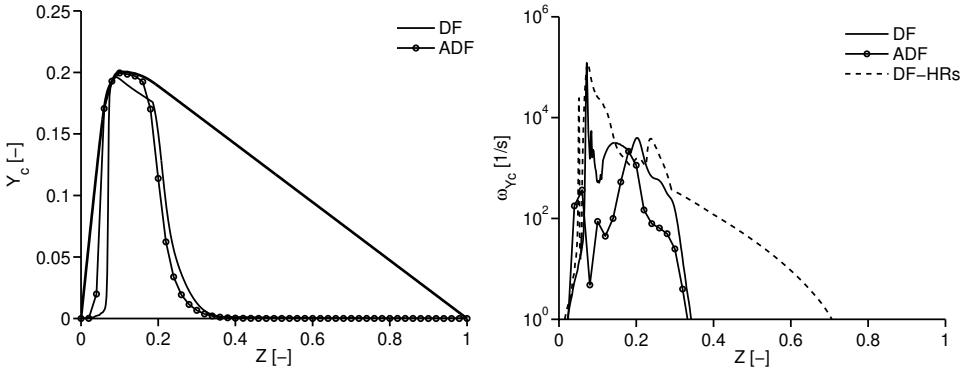

Figure 3.10. *$Y_c(Z)$ profiles during flamelet ignition for $a = 200$ 1/s for both DF and ADF models (left). Steady solution is included in bold. $\dot{\omega}_{Y_c}(Z)$ for both $Y_c(Z)$ profiles and homogeneous reactors chemical source terms $\dot{\omega}_{Y_c}^{HR}$ interpolated for $Y_c(Z)$ DF curve and labeled as DF-RHs (right). Chemical source terms are limited with $\alpha = 2$ for ADF calculation. Solutions for heptane at representative diesel engine conditions.*

The different features explained so far will be applied in section 3.3, devoted to the validation of ADF model by means of a detailed comparison with DF solutions. This comparison is carried out for several fuels of different chemical complexity for steady and unsteady solutions in order to cover a wide range of applicability of the ADF model. The boundary and initial conditions correspond to different experiments widely diffused in literature and considered to be relevant in practical applications.

3.2.3 Turbulent combustion database

Once the laminar flame database has been generated, functions that account for the fluctuations of the turbulent flow have to be applied to the

laminar solutions. As previously explained, these functions are presumed probability density functions (PDFs) for RANS or filtered probability density functions (FPDFs) for LES [12] and lead to calculate averaged/filtered values for reactive scalars and/or chemical source terms. They are presumed since they are defined by a family of curves known forehand that only depend on some parameters given by the local values of the combustion controlling variables solved in the turbulent flow.

In the context of LES the definition of the FPDF requires some additional comments. Given a realization of an experiment we could define from an instantaneous field ψ at each point and time a function that described the subfilter state of the field according to

$$f(\Psi;\, \vec{x}, t) = \int_{-\infty}^{\infty}\int_{-\infty}^{\infty}\int_{-\infty}^{\infty} G(\vec{x}, \vec{r})\, \delta(\psi(\vec{r}, t) - \Psi)\, d\vec{r} \tag{3.36}$$

where G is the LES filter function. This function f is the filtered density function (FDF) [34] and has interesting properties such as

$$\widetilde{\psi}(\vec{x}, t) = \int \Psi\, f(\Psi; \vec{x}, t)\, d\Psi \tag{3.37}$$

Property 3.37 and others are interesting when using models that solve the reactive flow at two levels, namely, the flow at the micro-scales, where the flamelet develops, and the flow solved in the LES simulation. However, the FDF f is a a function that depends on each realization of the experiment[21]. Consequently, it may not be statistically representative and its shape may be quite complex and cannot be presumed.

In order to solve this problem, the FPDFs are defined as the average of the FDFs for a set of samples of the experiment. Therefore, the FPDF is representative of such experiment, is feasible to presume its shape and can be used to find the filtered values of the reactive scalars in the LES simulation according to equation 3.9. The functions defined in the following describe the FPDFs used in the LES context as well as the PDFs applied to RANS.

In this work the variables defining the flamelets are (Z, a, t) or, equivalently, (Z, χ_{st}, t) and, hence, the corresponding presumed PDFs/FPDFs have to be defined as a function of the moments of these variables. Thus, the values of these moments, that is, the parameters of such presumed functions, are

[21] In a single DNS the FDF would be the function obtained from applying equation 3.36 to the instantaneous field.

solved in the CFD simulation in order to define the local shape of the PDFs or FPDFs. Once they are defined the average of reactive scalars or chemical source terms is then computed according to

$$\widetilde{\psi} = \int_0^\infty \int_0^{Z_s} \int_0^\infty \psi(Z, \chi_{st}, t)\, P(Z, \chi_{st}, t; \widetilde{Z}, \widetilde{Z''^2}, \widetilde{\chi}_{st}, \ldots)\, dt\, dZ\, d\chi_{st} \tag{3.38}$$

In practice, only the two first moments for the combustion controlling variables are retained, that is, the average value and its variance. Therefore, a function of the form $P(Z, \chi_{st}, t; \widetilde{Z}, \widetilde{Z''^2}, \widetilde{\chi}_{st}, \widetilde{\chi''^2_{st}}, \widetilde{t}, \widetilde{t''^2})$ should be provided. As was explained in section 3.1, it is a common practice to assume statistical independence between the different controlling variables leading to write previous expression as $P_Z(Z; \widetilde{Z}, \widetilde{Z''^2})\, P_\chi(\chi_{st}; \widetilde{\chi}_{st}, \widetilde{\chi''^2_{st}})\, P_t(t; \widetilde{t}, \widetilde{t''^2})$. This independence is justified advocating to the different scales that each of the variables affects to [13].

In the following, the presumed function used for each of the variables is described. The first variable to deal with is the mixture fraction. Since it is a variable that appears in all the combustion models, even the simplest, it is quite extended to apply a PDF or PDDF to account for its fluctuations. The common function to describe these fluctuations is the beta function [7, 8, 13] which depends on two parameters and, if it ranges over the interval $[0, Z_s]$, takes the form

$$P_Z(Z) = \frac{1}{B(\alpha, \beta)} \frac{Z^{\alpha-1}(Z_s - Z)^{\beta-1}}{Z_s^{\alpha+\beta-1}} \tag{3.39}$$

Function B appearing in equation 3.39 is the beta function defined by the integral

$$B(a, b) = \int_0^1 x^{a-1}(1-x)^{b-1}\, dx \tag{3.40}$$

The beta function is related to the gamma function by the expression

$$B(a, b) = \frac{\Gamma(a)\,\Gamma(b)}{\Gamma(a+b)} \tag{3.41}$$

Gamma function is defined by

$$\Gamma(x) = \int_0^\infty t^{x-1} \exp(-t)\, dt \tag{3.42}$$

α and β, appearing in equation 3.39, are related to the two first mixture fraction moments of beta function (average and variance) according to

$$\alpha = \frac{\widetilde{Z}}{Z_s}\left(\frac{\widetilde{Z}(Z_s - \widetilde{Z})}{\widetilde{Z''^2}} - 1\right) \tag{3.43}$$

$$\beta = \alpha\left(\frac{Z_s}{\widetilde{Z}} - 1\right) \tag{3.44}$$

As the maximum mixture fraction variance depends on the average mixture fraction $\widetilde{Z}$, it is practical to define a new variable S, called segregation factor, that normalizes the mixture fraction variance in the following way.

$$S = \frac{\widetilde{Z''^2}}{\widetilde{Z}(Z_s - \widetilde{Z})} \tag{3.45}$$

Equation 3.39 is a versatile function that may adopt a bell shape or one or two asymptotes on the extremes of the interval. However, despite these diverse morphologies it cannot reproduce two local maxima or one asymptote and one local maximum [7]. Figure 3.11 shows several shapes for this function.

From a numerical point of view, the integration of this function poses some difficulties as a result of the asymptotic behaviour that may appear in the extremes. This behaviour may require more iterations to reach convergence for the numerical integration than the rest of the domain. In this case, it is recommended to split the domain in several intervals to accelerate the convergence process.

With regards to the scalar dissipation rate it is typically used a Dirac δ [35] or a log-normal function [36]. As the first one is straightforward we shall focus on the second function. The log-normal function is defined by the following formula

$$P_\chi(\chi_{st}) = \frac{1}{\chi_{st}\,\sigma\sqrt{2\pi}} \exp\left(-\frac{(\ln\chi_{st} - \mu)^2}{2\sigma^2}\right) \tag{3.46}$$

where μ and σ are related to the two first moments according to

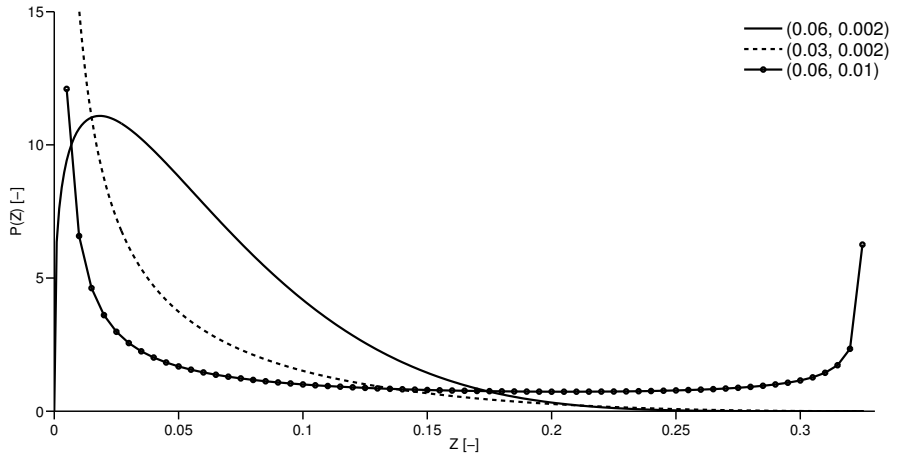

Figure 3.11. *Beta function for different pairs* $(\widetilde{Z}, \widetilde{Z''^2})$.

$$\widetilde{\chi}_{st} = \exp\left(\mu + \frac{\sigma^2}{2}\right) \tag{3.47}$$

$$\widetilde{\chi''^2_{st}} = \widetilde{\chi}^2_{st}\left(\exp(\sigma^2) - 1\right) \tag{3.48}$$

This function is defined only for non-negative values and is an asymmetric bell displaced to the origin. This means that it promotes low and intermediate χ_{st} values while dampens the impact of the high χ_{st} values. Figure 3.12 shows the shape of different log-normal functions.

The log-normal function is defined by two parameters, namely, μ and σ which are related to $\widetilde{\chi}_{st}$ and its variance $\widetilde{\chi''^2_{st}}$, as shown in equations 3.47 and 3.48. Transport equations for $\widetilde{\chi}$ and $\widetilde{\chi''^2}$ can be deduced. However, it is difficult to judge if the additional complexity introduced by the transport equations for these variables is compensated by the increase in accuracy of the calculations[22]. For this reason, an algebraic expression for $\widetilde{\chi}$ is normally used, that can be related to $\widetilde{\chi}_{st}$ as explained in section 3.2.4, and σ takes usually

[22]As any equation in RANS or LES context these equations contain unknown terms difficult to model.

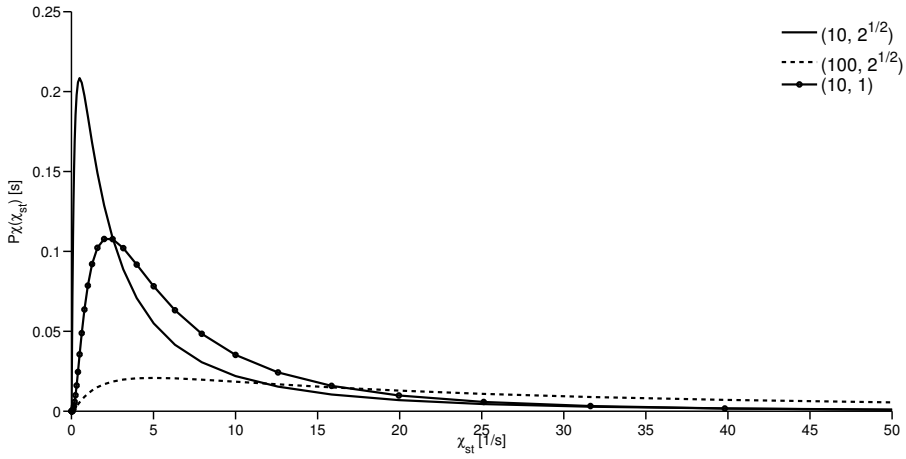

Figure 3.12. *Log-normal function for different pairs* $(\widetilde{\chi}_{st}, \sigma)$.

the constant values 1 or $\sqrt{2}$. This implies assuming $\sqrt{\widetilde{\chi''^2_{st}}}/\widetilde{\chi}_{st}$ constant and equal to 1.31 for $\sigma = 1$ or 2.53 for $\sigma = \sqrt{2}$ [23].

From figure 3.12 it is observed how in practice the bell is remarkably displaced to the origin. As log-normal function promotes low and intermediate χ_{st} values, it is recommendable not using linear distributions in χ_{st} when generating the laminar flame database. Attending to log-normal definition a logarithmic distribution is a suitable choice. Again splitting the interval of integration in smaller intervals accelerates convergence.

Finally, in this work, the function related to time fluctuations is taken a Dirac δ. It is considered that the use of PDFs or FPDFs in the other directions retains enough physical content to provide accurate results. In addition, it is difficult to define a suitable function for this variable based on physical grounds.

Hence, equation 3.38 takes the following final form

[23] The value $\sigma = 0$ transforms the log-normal into a Dirac δ.

$$\widetilde{\psi}(\widetilde{Z},S,\widetilde{\chi}_{st},\widetilde{t}\,)=\int_0^{\infty}\int_0^{Z_s}\int_0^{\infty}\psi(Z,\chi_{st},t)\,\delta(t-\widetilde{t}\,)\,P_Z(Z;\widetilde{Z},S)\,P_\chi(\chi_{st};\widetilde{\chi}_{st},\sigma)\,\mathrm{d}t\,\mathrm{d}Z\,\mathrm{d}\chi_{st} \tag{3.49}$$

which becomes[24]

$$\widetilde{\psi}(\widetilde{Z},S,\widetilde{\chi}_{st},\widetilde{t}\,)=\int_0^{\infty}\int_0^{Z_s}\psi(Z,\chi_{st},\widetilde{t}\,)\,P_Z(Z;\widetilde{Z},S)\,P_\chi(\chi_{st};\widetilde{\chi}_{st},\sigma)\,\mathrm{d}Z\,\mathrm{d}\chi_{st} \tag{3.50}$$

$\widetilde{\psi}(\widetilde{Z},S,\widetilde{\chi}_{st},\widetilde{t}\,)$ is re-parametrized with $\widetilde{Y}_c$ which is integrated too[25] leading to write $\widetilde{\psi}(\widetilde{Z},S,\widetilde{\chi}_{st},\widetilde{Y}_c\,)$.

In the current work, only reactive scalars and the chemical source term for the progress variable are integrated while species chemical reaction rates are obtained from their mass fractions as explained in section 3.2.4.

In the same way that the reactive scalars are integrated, χ has to be integrated[26] too and its integration yields

$$\begin{aligned}\widetilde{\chi}&=\int_0^{\infty}\int_0^{Z_s}\chi_{st}\frac{F(Z)}{F(Z_{st})}\,P_Z(Z;\widetilde{Z},S)\,P_\chi(\chi_{st};\widetilde{\chi}_{st},\sigma)\,\mathrm{d}Z\,\mathrm{d}\chi_{st}\\&=\left(\int_0^{\infty}\chi_{st}\,P_\chi(\chi_{st};\widetilde{\chi}_{st},\sigma)\,\mathrm{d}\chi_{st}\right)\left(\frac{1}{F(Z_{st})}\int_0^{Z_s}F(Z)\,P_Z(Z;\widetilde{Z},S)\,\mathrm{d}Z\right)\\&=\widetilde{\chi}_{st}\,J(\widetilde{Z},S)\end{aligned} \tag{3.51}$$

J depends only on the coordinates $(\widetilde{Z},S)$ and relates the value $\widetilde{\chi}$ found in CFD with the value $\widetilde{\chi}_{st}$ that defines the log-normal function and the combustion manifold.

The whole set of integrations provides relationships of the form $\widetilde{\psi}=\widetilde{\psi}(\widetilde{Z},S,\widetilde{\chi}_{st},\widetilde{Y}_c\,)$, for the reactive scalars and the chemical source term for $\widetilde{Y}_c$, and $\widetilde{\chi}=\widetilde{\chi}(\widetilde{Z},S,\widetilde{\chi}_{st})=\widetilde{\chi}_{st}J(\widetilde{Z},S)$ which constitute the turbulent combustion database.

[24] The dependence of $\widetilde{\psi}$ with σ is omitted since it is considered constant.

[25] $\widetilde{Y}_c$ is obtained directly applying its definition for the integrated species mass fractions.

[26] Note that log-normal function is defined as a function of $\widetilde{\chi}_{st}$ and not $\widetilde{\chi}$.

In order to simplify calculations it is recommendable to use an orthogonal mesh for the set of input variables that extends over a four dimensional parallelepiped. For this purpose, vectors $\widetilde{Z}_i$, S_j, $\widetilde{\chi}_{st,k}$ and d_l are defined and then, $\widetilde{\psi}_{i,j,k,l} = \widetilde{\psi}(\widetilde{Z}_i, S_j, \widetilde{\chi}_{st,k}, d_l)$ is assigned at each of the nodes of such parallelepiped. (i, j, k, l) takes all the possible combinations of natural values for which the indexes extend. In this case, d is defined similarly to c_F but applied to the turbulent manifold, that is,

$$d = \frac{\widetilde{Y}_c - \widetilde{Y_c^{inert}}}{\widetilde{Y_c^{steady}} - \widetilde{Y_c^{inert}}} \tag{3.52}$$

and is a normalization of the progress variable.

Apart from species mass fractions and other variables of interest, the progress variable chemical source term has to be tabulated in order to obtain the chemical advance during combustion. This source term may correspond to the integration of $\dot{\omega}_{Y_c}$ or $\partial Y_c/\partial t$ from equation 3.22. The first one only accounts for the chemical activity while the second compresses the chemical reaction and the diffusion that occurs at the smallest scales where the laminar flame develops. Since these scales are not solved in the CFD calculation, the integrated value of $\partial Y_c/\partial t$ is used as the CFD progress variable chemical source term in this work in order to retain their effect.

Finally, to say that this database is generated prior to CFD calculation and its values are retrieved during CFD simulation as explained in next section.

3.2.4 Flamelet model and CFD coupling

In this section the coupling of the flamelet model used in the current work with CFD is explained. Once the turbulent flame manifold composed of $\widetilde{\psi} = \widetilde{\psi}(\widetilde{Z}, S, \widetilde{\chi}_{st}, \widetilde{Y}_c)$ and $J = J(\widetilde{Z}, S)$ has been calculated, the turbulent flame can be solved as described in the following. Next equations are solved during the CFD temporal loop and may require several internal loops in order to achieve convergence. However, as this depends on the particular numerical algorithm we will not focus on this aspect and we will only enumerate the equations in the temporal loop to be solved. In the same way, the order for the resolution of the equations could be different depending on the implementation of the CFD solver. Finally, equations are written as they have been solved in this work and, therefore, contain some simplifications including turbulent flux modelling.

Notwithstanding, an effort has been done in order to abstract the model as much as possible with the purpose of providing generality. As a consequence,

the explicit reference to the models used in this work to describe turbulence, evaporation, etc. is omitted here and will be mentioned in the corresponding chapters. In the same way, although $\partial\widetilde{Y}_c/\partial t$ is used as the chemical source term for $\widetilde{Y}_c$ in this work, we shall refer to $\widetilde{Y}_c$ chemical source term with the generic nomenclature $\widetilde{\dot{\omega}}_{Y_c}$ along this section since, as said previously, such term can be obtained from different flamelet contributions and the way it is computed depends on the author. Moreover, apart from the model used in this work, alternative ways to couple flamelet model and CFD are sketched.

In the following, regarding diffusivity subscripts, no subscript refers to laminar, T to turbulent in RANS context, sgs to subgrid in LES frame and eff to effective, that is, the sum of the laminar component plus the turbulent one in RANS or the subgrid one in LES. Mass diffusivity is denoted by D. In addition, in this model Le number is assumed unity.

The flamelet model and CFD coupling consists of the following steps:

1. Solve the models for the liquid phase and obtain evaporative source terms, momentum exchange between liquid and gas, etc.
2. Solve continuity[27].
3. Solve Navier-Stokes equation.
4. For each cell take the 4-tuple $(\widetilde{Z}, S, \widetilde{\chi}_{st}, d)$ and find the chemical source terms from the combustion model. To do this, there exist two ways:
   - Strong coupling: find the chemical source term for the progress variable $\widetilde{\dot{\omega}}_{Y_c}$ from the turbulent manifold and solve the transport equation for the progress variable (equation 3.62 written for $\widetilde{Y}_c$ instead of $\widetilde{Y}_i$). The rest of variables (species, etc.) may be obtained during the post-processing from the values $(\widetilde{Z}, S, \widetilde{\chi}_{st}, \widetilde{Y}_c)$ for each cell and instant.
   - Weak coupling: find the chemical source terms for all the species and solve transport equations for these species. This method allows to consider some thermodynamic, chemical and dynamic additional effects, such as fuel evaporation, pollutants formation or compressibility, that have not been considered in the manifold [13, 23]. To do this, two methods may be found in literature:

     Option 1: tabulate the chemical source terms as a function of $(\widetilde{Z}, S, \widetilde{\chi}_{st}, \widetilde{Y}_c)$ and use them to solve species transport equations (see

[27] Since continuity, Navier-Stokes, energy equations, etc. were described in chapter 2 they are not reproduced here. The same equations explained in chapter 2 are used in this context but adding the corresponding source terms arising from the Lagrangian-Eulerian coupling.

equation 3.62). With this method the particles thermochemical paths may deviate due to numerical errors from the turbulent flame manifold since there is no mechanism that forces to remain in the vicinity of the manifold [23].

Option 2: tabulate species mass fractions and use them to find species chemical source terms. This is the procedure adopted in the current work.

To do this, first, we have to find which would be the species mass fraction vector at next step if only chemical effects took place, that is, 'advance' through the turbulent flame manifold and compare it with the current species mass fraction vector at the cell. In order to do this, the progress variable at next time step is computed from $\widetilde{\dot{\omega}}_{Y_c}$, retrieved from the manifold, according to[28]

$$\widetilde{Y}_c(t+\Delta t) = \widetilde{Y}_c(t) + \widetilde{\dot{\omega}}_{Y_c}(\widetilde{Z}, S, \widetilde{\chi}_{st}, \widetilde{Y}_c(t))\,\Delta t \tag{3.53}$$

where Δt is chosen equal to the CFD time step if it is small enough. In previous expression, values $(\widetilde{Z}, S, \widetilde{\chi}_{st}, \widetilde{Y}_c(t))$ correspond to those found at each cell. How to obtain the values $(\widetilde{Z}, S, \widetilde{\chi}_{st})$ is described in the following while $\widetilde{Y}_c$ is found applying its definition from the species mass fractions at the cell. Then we can find the chemical source term for each species $\widetilde{\dot{\omega}}_k$ as the following ratio:

$$\widetilde{\dot{\omega}}_k = \frac{\widetilde{Y_k}^{tab}(\widetilde{Z}, S, \widetilde{\chi}_{st}, \widetilde{Y}_c(t+\Delta t)) - \widetilde{Y_k}^{cell}(t)}{\Delta t} \tag{3.54}$$

where superscript *tab* refers to the value tabulated in the turbulent combustion database while *cell* to the CFD value at the current cell.

In addition, and as in this kind of approximations only a small set of the species appearing in the mechanism is transported (of the order of 10 species) additional species that act as mass sinks have to be included in order to conserve atomic elements masses. These species represent the mass that lacks in the system and it is assumed that they have representative thermo-physical properties for the not transported species. In these calculations, the only atomic elements that compose the molecules are carbon, hydrogen, oxygen and nitrogen. For each element of the system we choose a species (except for nitrogen): C_7H_{14} for carbon, H_2 for hydrogen and O_2 for oxygen. Their mass is obtained from equation 2.87 that is here reproduced.

[28] As previously said, for the sake of generality we use the $\widetilde{\dot{\omega}}_{Y_c}$ symbol for the progress variable chemical source term although in the current work such term corresponds to $\partial\widetilde{Y}_c/\partial t$.

$$\frac{Z_{elem}}{W_{elem}} = \sum_{k=1}^{N_s} n_{elem,k} \frac{Y_k}{W_k} \tag{3.55}$$

Z_{elem} refers to the mixture fraction of the element (C, H and O), W is the molecular weight, N_s is the total number of species and $n_{elem,k}$ is the number of atoms of element $elem$ in species k.

Once the mass fractions for the sink terms are computed from equation 3.55 for instant $t + \Delta t$ from the species vector $\widetilde{Y_k}^{tab}(\widetilde{Z}, S, \widetilde{\chi}_{st}, \widetilde{Y}_c(t + \Delta t))$, their chemical source terms are obtained from equation 3.54 (these sink species are transported too). Equation 3.55 requires transporting Z_{elem}, however, some simplifications can be applied as described in the following.

5. Solve fuel mixture fraction $\widetilde{Z}$ equation. In this case, an additional evaporative source term $\overline{S_Z}$ has to be considered too since $\widetilde{Z}$ only accounts for the fuel gas phase.

$$\frac{\partial(\overline{\rho}\,\widetilde{Z})}{\partial t} + \frac{\partial(\overline{\rho}\,\widetilde{u_i}\,\widetilde{Z})}{\partial x_i} = \frac{\partial}{\partial x_i}\left(\overline{\rho}\,D_{eff}\frac{\partial \widetilde{Z}}{\partial x_i}\right) + \overline{S_Z} \tag{3.56}$$

6. Solve elements mixture fractions, such as $\widetilde{Z}_{O_2}$ for oxygen, similarly to equation 3.56 [29]. Assuming similar laminar diffusivity for H and C [30] and Lewis unity (as in this work) leads to equations for Z_H and Z_C in the form of equation 3.56. As their boundary conditions are proportional it is deduced that Z_H and Z_C only differ by a constant of proportionality. This constant is the ratio between the number of hydrogen and carbon atoms in the fuel. Consequently, if fuel does not contain oxygen then $\widetilde{Z} = \widetilde{Z}_H + \widetilde{Z}_C$ and $\widetilde{Z}_H$ and $\widetilde{Z}_C$ are proportional to $\widetilde{Z}$ and, therefore, there is no need to transport them.

   $\widetilde{Z}_{O_2}$, $\widetilde{Z}_H$ and $\widetilde{Z}_C$ are used in equation 3.55 to find the mass fractions for the species that complete the atomic balance.

7. Solve mixture fraction variance $\widetilde{Z''^2}$ (RANS) or $\widetilde{Z''^2_{sgs}}$ (LES) equation. For RANS it takes the form

[29] For $\widetilde{Z}_{O_2}$ equation there is no evaporative term.

[30] This is only necessary in LES since in RANS laminar diffusivity is very small compared to turbulent diffusivity.

$$\frac{\partial(\overline{\rho}\,\widetilde{Z''^2})}{\partial t}+\frac{\partial(\overline{\rho}\,\widetilde{u}_i\,\widetilde{Z''^2})}{\partial x_i}=\frac{\partial}{\partial x_i}\left(\overline{\rho}\,D_{eff}\frac{\partial\widetilde{Z''^2}}{\partial x_i}\right)+2\overline{\rho}\,D_{eff}\frac{\partial\widetilde{Z}}{\partial x_i}\frac{\partial\widetilde{Z}}{\partial x_i}-\overline{\rho}\,\widetilde{\chi} \tag{3.57}$$

while in LES is

$$\frac{\partial(\overline{\rho}\,\widetilde{Z''^2_{sgs}})}{\partial t}+\frac{\partial(\overline{\rho}\,\widetilde{u}_i\,\widetilde{Z''^2_{sgs}})}{\partial x_i}=\frac{\partial}{\partial x_i}\left(\overline{\rho}\,D_{eff}\frac{\partial\widetilde{Z''^2_{sgs}}}{\partial x_i}\right)+2\overline{\rho}\,D_{sgs}\frac{\partial\widetilde{Z}}{\partial x_i}\frac{\partial\widetilde{Z}}{\partial x_i}-\overline{\rho}\,\widetilde{\chi_{sgs}} \tag{3.58}$$

For $\widetilde{Z''^2}$ and $\widetilde{Z''^2_{sgs}}$ we do not consider any evaporative source term but it is deemed that this should not have a noticeable impact for typical diesel engine conditions. In RANS framework $\widetilde{Z''^2}$ compresses the whole mixture fraction variance while in LES it corresponds only to the subgrid component.

D_T and D_{eff} may be computed from the thermal diffusivity (since $Le = 1$) or from the kinematic viscosity by means of the Schmidt number.

To solve previous equations, it is necessary to compute the scalar dissipation rate to which the flame is strained. Although a transport equation may be obtained for this term [37], in this work, widely accepted algebraic expressions are used. They are based on the idea that the mixture fraction variance is transported and dissipated in a similar way that the turbulent kinetic energy and, hence, a proportionality between their characteristic times can be found.

- In RANS context, the turbulent kinetic energy characteristic time is written as k/ε while the mixture fraction variance characteristic time is $\widetilde{Z''^2}/\chi$. Then,

$$\widetilde{\chi}=C_\chi\frac{\varepsilon}{k}\widetilde{Z''^2} \tag{3.59}$$

  where C_χ is a constant around 2 [38].
- In LES context, the turbulent kinetic energy characteristic time is written as Δ^2/D_{sgs} leading to the following expression for the subgrid scalar dissipation rate

$$\widetilde{\chi_{sgs}}=C_\chi D_{sgs}\frac{\widetilde{Z''^2_{sgs}}}{\Delta^2} \tag{3.60}$$

where Δ is the filter size. Then, the total scalar dissipation rate $\widetilde{\chi}$ is

$$\widetilde{\chi} = \widetilde{\chi_{sgs}} + 2D\frac{\partial\widetilde{Z}}{\partial x_i}\frac{\partial\widetilde{Z}}{\partial x_i} \tag{3.61}$$

The last term represents the solved scalar dissipation rate.

On the one hand, once $\widetilde{\chi}$ or $\widetilde{\chi_{sgs}}$ is found, equations 3.57 and 3.58 can be solved and the segregation factor S field is calculated using equation 3.45 and substituting $\widetilde{Z''^2}$ for RANS and $\widetilde{Z''^2_{sgs}}$ for LES. On the other hand, field $\widetilde{\chi}_{st}$ is computed from $\widetilde{Z}$ and S and function $J(\widetilde{Z}, S)$.

8. Solve species transport equations.

$$\frac{\partial(\overline{\rho}\,\widetilde{Y_k})}{\partial t} + \frac{\partial(\overline{\rho}\,\widetilde{u_i}\,\widetilde{Y_k})}{\partial x_i} = \frac{\partial}{\partial x_i}\left(\overline{\rho}\,D_{eff}\frac{\partial\widetilde{Y_k}}{\partial x_i}\right) + \overline{\rho}\,\widetilde{\dot{\omega}}_k + \overline{S_k} \tag{3.62}$$

where $\overline{S_k}$ is the evaporative source term for species k (only for those species contained in the fuel). As mentioned previously, an identical equation is written but only for the progress variable when adopting the strong coupling.

9. Solve energy equation.

10. Solve turbulence model equations.

3.3 Validation of the ADF model

The hypotheses assumed for the ADF model require to be tested in order to validate it and find the ranges where it can be applied. This was done by Michel et al. [32] in the work where they described the ADF model, however, although the interesting results provided, it is considered that the validation was not sufficiently detailed and extensive. A more systematic comparison between DF and ADF models is required and this is carried out in this section. Moreover, the ideas given in the previous section are applied and tested. The following discussion can be found in the author's works [39, 40].

In order to widely validate the ADF model, several fuels covering a practical range of hydrocarbons used for different industrial devices with boundary conditions corresponding to well-known experiments are assessed.

Table 3.1. *Boundary conditions for the hydrogen set of flamelets.*

	Fuel ($Z = 1$)	Hot coflow ($Z = 0$)
Temperature (K)	305	1055
Mole fractions	$X_{\mathrm{H2}} = 0.25$	$X_{\mathrm{O2}} = 0.1474$
	$X_{\mathrm{N2}} = 0.75$	$X_{\mathrm{N2}} = 0.7537$
		$X_{\mathrm{H2O}} = 0.0989$

Table 3.2. *Boundary conditions for the methane set of flamelets.*

	Fuel ($Z = 1$)	Hot coflow ($Z = 0$)
Temperature (K)	320	1350
Mole fractions	$X_{\mathrm{O2}} = 0.15$	$X_{\mathrm{O2}} = 0.12$
	$X_{\mathrm{N2}} = 0.52$	$X_{\mathrm{N2}} = 0.73$
	$X_{\mathrm{CH4}} = 0.33$	$X_{\mathrm{H2O}} = 0.15$

Table 3.3. *Boundary conditions for the heptane set of flamelets.*

	Fuel ($Z = 1$)	Oxidant ($Z = 0$)
Temperature (K)	373	1000
Mole fractions	$X_{\mathrm{C7H16}} = 1$	$X_{\mathrm{O2}} = 0.21$
		$X_{\mathrm{N2}} = 0.79$

These fuels are hydrogen, methane and heptane and the boundary conditions of the experiments are gathered in tables 3.1, 3.2 and 3.3.

Hydrogen is the simplest fuel and has the advantage that its chemistry is well-known. The mechanism used for its simulation is composed of 9 species and 21 reactions [41]. Increasing in chemical complexity, methane, which is the simplest hydrocarbon, is found. The GRI mechanism was chosen for its calculation with 53 species and 325 reactions [42]. The boundary conditions for the experiments considered for both fuels correspond to the nominal cases of the laboratory flames analysed by Cabra et al. from the University of Berkeley [43, 44] which develop at atmospheric pressure.

Finally, heptane is a long chain hydrocarbon typically used as a diesel surrogate and is described by Zeuch et al. chemical mechanism which is composed of 110 species and 1170 reactions [45]. In this case, boundary

conditions correspond to spray H experiment from the Engine Combustion Network (ECN), widely used for diesel spray models validation [46].

For these boundary conditions, the stoichiometric mixture fraction values are 0.479 for hydrogen, 0.176 for methane and 0.062 for heptane.

The following comparison for ADF validation is carried out in terms of the steady (S-curve) and unsteady solutions provided by both DF and ADF models. In addition, in order to analyse the impact of the progress variable definition on ADF solutions, two progress variable definitions are used for methane and heptane, assessing their results in steady and transient regimes too. It is clear that this comparison does not proceed for the DF model where the definition of the progress variable does not affect results since it is only used for tabulating purposes.

On the one hand, the progress variable used for hydrogen is defined by $Y_c = Y_{H_2O} + 10Y_{HO_2} + 3Y_{H_2}$ and was suggested by Naud et al. to simulate the hydrogen Berkeley flame [18]. On the other hand, methane and heptane calculations are performed with two progress variable definitions. The first one, abbreviated as PV1, is the commonly used $Y_c = Y_{CO} + Y_{CO_2}$ [29] while the second one, PV2, is given by $Y_c = Y_{CO} + Y_{CO_2} + Y_{H_2O} + 10Y_{HO_2} + 3Y_{H_2}$ and is obtained from the sum of PV1 plus the progress variable used for hydrogen.

PV1 is a progress variable definition composed of an intermediate species, such as CO, and the final product CO_2. Although in most of the cases it is enough to accurately describe homogeneous mixtures auto-ignition and flame evolution, it is believed that introducing species appearing in the first steps of combustion is convenient. This is accomplished by defining an alternative progress variable (PV2) that includes species such as HO_2.

It has been checked that these definitions fulfil progress variable constrains for the set of boundary conditions. In general, PV2 is used for methane calculations while PV1 is applied to heptane solutions unless otherwise stated.

In order to discard any possible numerical uncertainty related to solving equations, fine grids have been chosen for the different variables although it is feasible to use coarser meshes for practical calculations. For the homogeneous reactors mixture fraction tabulation, 201 points were taken for hydrogen, 251 for methane and 338 for heptane. In the case of heptane, mixture fraction distribution is not equally spaced, as in the other cases, since its grid spacing depends on the richness of the mixture. Evolution of mixtures auto-ignition is stored in a mesh, common for all the fuels, of 504 points for the normalized progress variable c which is equally spaced except for low c values. In the case of the DF model, 201 points were taken for hydrogen and 501 for methane and heptane in mixture fraction direction to solve properly flame equations.

Hydrogen and methane are injected in gas phase but heptane in liquid phase, however, and in order to use similar ranges for the combustion controlling variables, mixture fraction extends from 0 to 1 for all the cases. This simplification implies that evaporation is neglected in the case of heptane as if this fuel was injected in gas phase. However, it is important to emphasize that for the purpose of this comparison between flamelet models, this assumption is acceptable as it does not affect the main conclusions extracted from this validation.

The limitation for chemical rates described in section 3.2.2.2 is only applied to heptane as shall be explained. As will be discussed later, the start of ignition in the very lean mixtures and the reduced chemical reaction terms until reaching high values of c for hydrogen and methane flames make unnecessary the application of this limitation.

The solutions for the DF model are obtained by means of LFLAM code developed at CIEMAT [31] by Dr. Naud [18, 47] while the ADF model was developed by the author of this work.

3.3.1 Steady regime

The solutions for the steady regime are typically obtained with the Newton-Rapson algorithm. With this method, the flamelet equation for a given strain rate is solved taking as initial guess the solution of another strain rate which is close to the one that is desired to calculate. Proceeding in this way the whole S-curve is obtained. When the algorithm is applied for the first time, it is useful to take the equilibrium solution as the initial guess for the lowest strain rate.

First the surfaces (Z, χ, Y_c) for the steady solutions are shown. From these surfaces the S-curve for a mixture fraction Z^* is obtained cutting the surface by the plane $Z = Z^*$. These surfaces are interesting because they delimit the region of possible physical states for the flame during its ignition[32]. Figure 3.13 shows these surfaces for the three fuels and both DF and ADF models. Each branch is represented with a different colour. Scales are common for both figures corresponding to the same fuel.

[31] CIEMAT stands for 'Centro de Investigaciones Energéticas, Medioambientales y Tecnológicas' and is a Spanish public research center.

[32] Since the S-curve delimits the region of possible physical transient solutions for each mixture fraction. Regarding flame extinction, the transient evolutions are outside of the volume enclosed by these surfaces although the projection of such transient evolutions on the plane (Z, χ) remain inside the corresponding projection of the surface (Z, χ, Y_c).

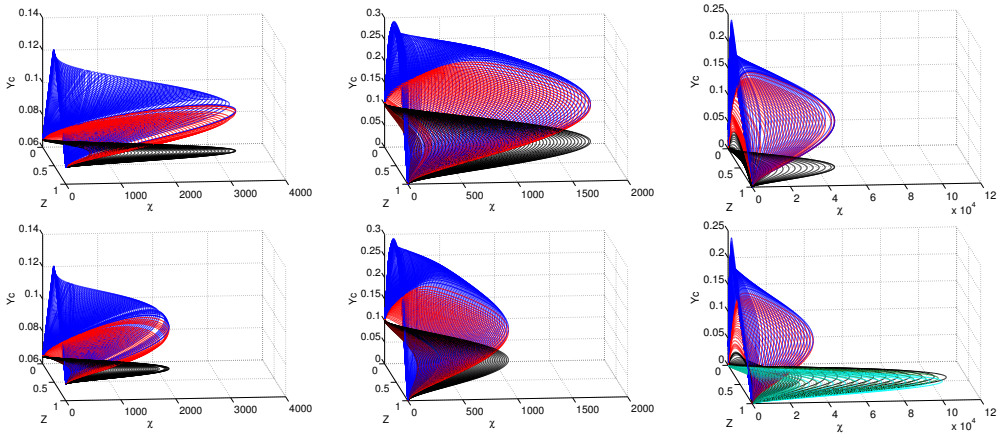

Figure 3.13. *Steady solutions for hydrogen (left), methane (center) and heptane (right). DF solutions at top row and ADF solutions at bottom row.*

The main differences are related to the quenching scalar dissipation rate χ_q, given by the maximum χ value where blue and red surfaces join, which is markedly greater in the case of the DF model than in the ADF approach. This implies that combustion may be sustained at higher strained flows when calculating with the DF model.

The other important discrepancy is related to the two unstable branches appearing for heptane in the case of the ADF model (red and green lines). This second χ_q reaches very high values (approximately three times the value of the other χ_q value) and is not predicted by the DF model. It is generated by the chemical kinetics as will be explained in a later discussion.

In order to have a more quantitative vision of the steady regime solutions, S-curves are plotted in figures 3.14 for hydrogen, 3.15 for methane and 3.16 for heptane considering lean, stoichiometric and rich mixtures. The strain rate a is used for the abscissa axis since, for a given mixture fraction, χ and a are directly proportional.

It is observed that for hydrogen case, values for a_i and a_q[33] are both greater in the DF model than in the ADF. For the DF model they reach values of 2000 and 10365 1/s, respectively, while for the ADF their values are 850 and 6550 1/s. This manifests how diffusion processes affect chemistry activity especially

[33]The values of a corresponding to χ_i and χ_q. See section 3.1 for their definition.

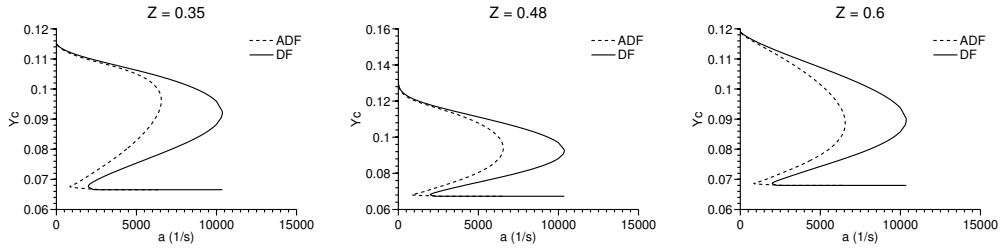

Figure 3.14. *S-curves obtained with DF and ADF models for hydrogen at lean (left), stoichiometric (center) and rich (right) mixtures.*

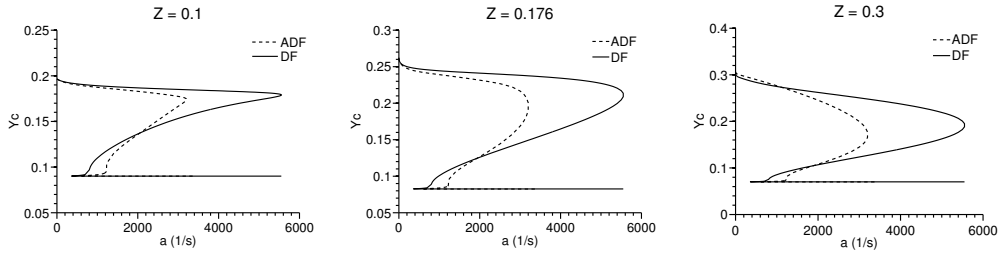

Figure 3.15. *S-curves obtained with DF and ADF models for methane at lean (left), stoichiometric (center) and rich (right) mixtures.*

in the reignition-extinction range. However, it is also observed that divergences between models in the auto-ignition range are reasonably small.

Figure 3.15 shows the steady solutions for methane. In this case a_q is still greater for the DF model, with a value of 5550 1/s, than for the ADF model, where it reaches only 3200 1/s. However, and different to the hydrogen case, a_i is lower for the DF model, 360 1/s, than for the ADF, 570 1/s.

Thus, one of the most important conclusions to be extracted from this comparison is that the validity of the ADF model is limited to the auto-ignition range, since, even for low molecular complexity fuels, there exist important differences in the reignition-extinction range which are not well-reproduced by the ADF model.

Finally, to close this analysis figure 3.16 gathers the steady solutions for the heptane case, where due to the wide range of strain rates where combustion

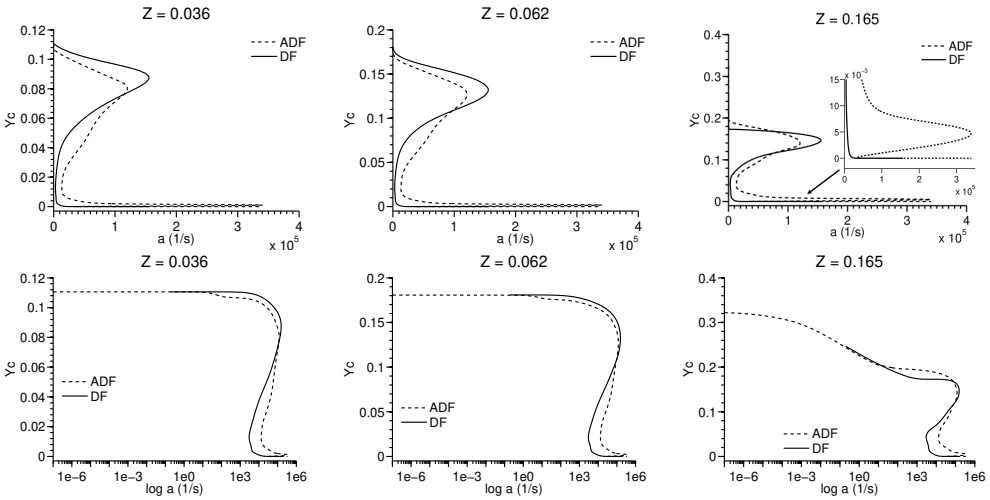

Figure 3.16. *S-curves obtained with DF and ADF models for heptane at lean (left), stoichiometric (center) and rich (right) mixtures. Linear scale for top figures and logarithmic scale for bottom figures.*

develops it has been represented in both linear and logarithmic scales. With regards to a_i and a_q values, the same comments to those pointed for methane are still valid in this case. DF model shows greater value for a_q, 155550 1/s, but lower a_i, 2990 1/s, than the ADF model, where the values are 120000 1/s and 13400 1/s, respectively. In addition, and as was pointed out before, ADF approach predicts a second quenching point for low Y_c values that extends until very high strain rate values as shown in figure 3.16 with a zoom for better visibility.

The reason for this behaviour is found in the chemical source terms provided by the homogeneous reactors calculations. In order to analyse these terms, figure 3.17 shows in colour maps the fields $\dot{\omega}_{Y_c}^{HR}(Z,c)$ obtained from the homogeneous reactors solutions for the three fuels, with some level curves for reference.

Only for the heptane case two relative maxima are observed, one at high c values in the vicinity of stoichiometry, as in the other fuels, and other in the region of low c values and very rich mixtures. Considering equation 3.22 for the steady regime (transient term cancelled) and figure 3.17 for heptane, the appearance of the second peak of the S-curve can be explained: noticing

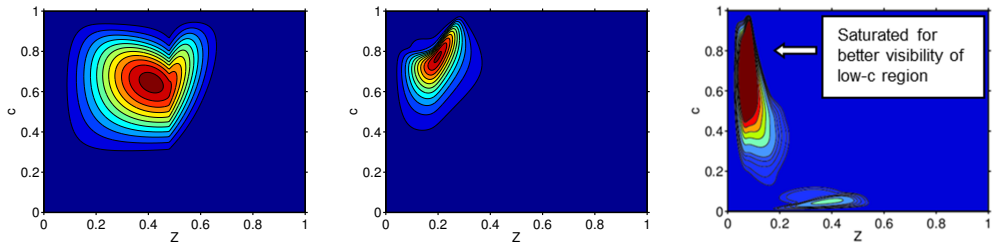

Figure 3.17. *Homogeneous reactors chemical source terms $\dot{\omega}_{Y_c}^{HR}(Z,c)$ for hydrogen (left), methane (center) and heptane (right). For reference, several level curves are included too.*

that the whole set of steady solutions covers all the possible states between inert and equilibrium solutions it arises that an increase of the chemical source term has to be compensated by an increase, in absolute value, of the mixing term when moving close to a maximum of $\dot{\omega}_{Y_c}^{HR}$. The mixing term is the product of the scalar dissipation rate χ, which is the product of the strain rate a and a fixed function that uniquely depends on Z, and the second derivative $\partial^2 Y_c/\partial Z^2$. As the increase of the chemical source term is not fully compensated by the increase of $\partial^2 Y_c/\partial Z^2$ this forces an increase of the strain rate[34]. This generates the different quenching points in the S-curves for the ADF model and, particularly, two quenching points for heptane with a very high strain rate value for the peak appearing in the low c region due to the very low values that $\partial^2 Y_c/\partial Z^2$ takes.

Therefore, this second peak is observed as a consequence of the low temperature chemistry which is in deep connection with cool flames. Even if it is expected that the ADF model introduces non-negligible discrepancies in the flamelet solutions for very high strain rates it is worth mentioning that other numerical studies have found double S-curves when solving complex fuels with the DF model [48].

This behaviour is clearly observed in figure 3.18 where several profiles corresponding to the different branches of the heptane S-curve for the ADF model have been represented in the (Z, Y_c) coordinates. In addition, some level curves of the $\dot{\omega}_{Y_c}^{HR}(Z, Y_c)$ map have been included in order to confirm that

[34] In a first approximation this second derivative can be associated to the curvature of the profile, especially for steady solutions close to the inert line which are those related to the second peak in the case of heptane.

the change of the branch occurs in the region of the local minimum/maximum chemical source term. It is seen that the low curvature of the profiles forces the decrease/increase of the strain rate in order to compensate the chemical source term. In general, the number of relative maxima composing the chemical source term gives the number of pairs of stable-unstable branches of the S-curve.

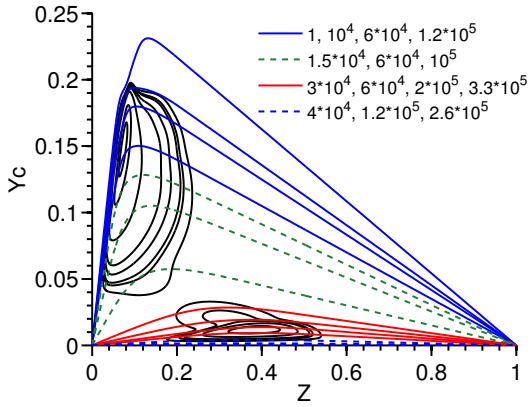

Figure 3.18. *Steady solutions (Z, Y_c) for the ADF model superimposed over the level curves of the chemical source field $\dot{\omega}_{Y_c}^{HR}$ (black lines) for heptane. Each type of line corresponds to a different branch of the S-curve. The values of the legend indicate the strain rate (1/s) of the represented solutions.*

Effect of the progress variable definition

In contrast to the DF model, the ADF model is based on solving only a transport equation for the progress variable. Therefore, its accuracy relies on the representativeness of the progress variable to describe the different combustion stages. It arises as a natural question to ask about the effect of the definition of this variable on the final solutions. To answer this question, the two progress variables defined previously for methane and heptane are compared in this section in terms of the steady solutions.

Figures 3.19 and 3.20 show the S-curves for methane and heptane with the progress variables named as PV1 and PV2 for lean, stoichiometric and rich mixtures. Again for heptane the representation is shown in linear and logarithmic scales due to the wide range where the strain rate spans. The comparison is performed in terms of temperature instead of progress variable due to the different used definitions.

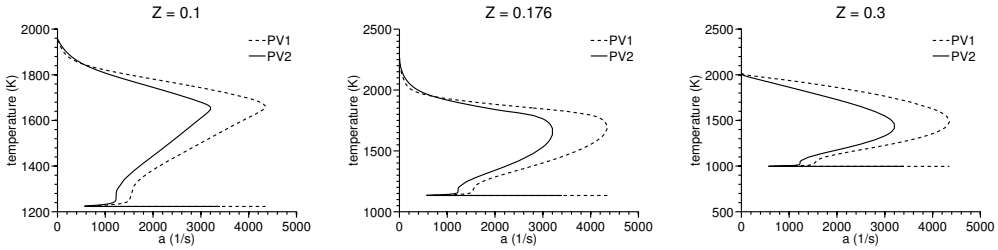

Figure 3.19. *S-curves obtained with PV1 and PV2 definitons for ADF model for methane. Figure gathers solutions at lean (left), stoichiometric (center) and rich (right) mixtures.*

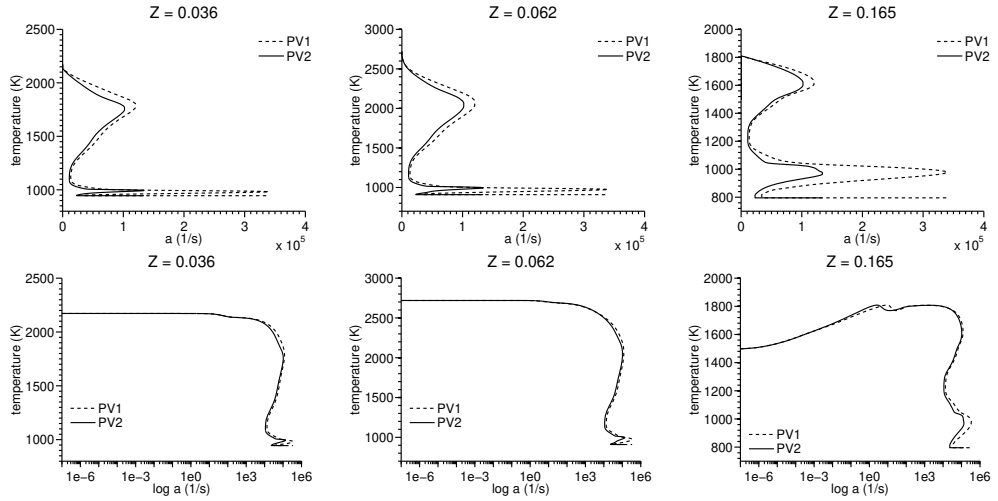

Figure 3.20. *S-curves obtained with PV1 and PV2 definitons for ADF model for heptane. Figure gathers solutions at lean (left), stoichiometric (center) and rich (right) mixtures in linear (top) and logarithmic (bottom) scales.*

Conclusions established when comparing DF and ADF models are ratified since the auto-ignition range is similarly reproduced by both definitions while the reignition-extinction range is the most affected by the choice of the progress variable. Additionally, the impact of the definition of this variable is more evident for rich mixtures than for lean or stoichiometric mixtures.

For heptane both definitions show a second quenching peak although the strain rate to which this unstable branch extends is different. In fact, for this fuel the main discrepancies between solutions given by PV1 and PV2 are mainly found in the region of the second peak.

The main conclusion of this detailed analysis is that the range of validity of the ADF model is limited to the auto-ignition range independently of the fuel complexity since in the reignition-extinction range this model does not describe the solutions provided by the DF model. This conclusion is in agreement with intuition since both models tend to provide the same solution as $a \to 0$ and, hence, it is deduced that in the vicinity of the homogeneous reactors solutions ($a = 0$) both models predict close solutions. It is worth mentioning that in industrial devices, and particularly in thermal engines, the combustion process usually develops in the auto-ignition range and the relevance of the reignition-extinction range is smaller [49]. Consequently, the ADF model may be applied to the simulation of diesel engines, gas turbines, etc. with a suitable level of accuracy.

The following section completes this analysis describing the transient solutions of the flames for the different fuels and validates the ADF model in this regime.

3.3.2 Unsteady regime

To solve the transient solutions with the DF model the DASSL algorithm [50] is used with second order for derivatives in mixture fraction and a variable order for temporal derivative that ranges between one and fifth order. The solutions are obtained by means of the program LFLAM developed at CIEMAT [18, 47].

In the case of the ADF, an implicit algorithm with adaptive time step is applied. For ADF calculations the time step is computed from the maximum transient term $\partial Y_c/\partial t$ from previous time step and a desired maximum advancement in the normalized progress variable direction. Additionally, this algorithm is complemented with another one which doubles or halves the time step if the advancement for the progress variable is too small or too large, respectively. Mixture fraction derivatives are calculated with a second order approximation while temporal derivatives are discretised following a first order scheme.

The main motivation of the ADF model, as was explained in section 3.2.2.2, is to develop a model with the ability to manage complex chemical schemes and solve the flame structure in small amounts of time while still retaining

complex physical aspects. Then, in order to validate the ADF model it is not enough to show its ability to reproduce the flame structure in a range relevant to simulate industrial combustion systems, but it is necessary to show that the reduction in computational time justifies its adoption.

This section opens with a comparison of the computational cost required to solve both DF and ADF models for the same combustion problem. The comparison is carried out in terms of the time spent to solve the transient evolutions for a set of strain rates that cover the auto-ignition range of heptane. The time required to find the steady solutions is not included since it is in general negligible. Since the ADF model takes its complete meaning when being applied to complex chemical schemes the comparison is only performed for heptane.

Table 3.4 gathers the computational time required to solve the transient evolution for heptane with DF and ADF models. It arises that ADF reduces by at least one order of magnitude the time spent to calculate these flamelets. In fact, if the flamelet database is composed by 30 flamelets and an average time of 55 minutes is taken to solve the transient evolution of one flamelet with the DF model, it is obtained that solving the whole set of flamelets takes 1650 minutes ($= 55 \times 30$). However, for the ADF approach, if an average time of 4 minutes/flame is assumed and the time to solve homogeneous reactors calculation is 45 minutes, the time is reduced to 165 minutes ($= 4 \times 30 + 45$). This means that the computational cost is reduced one order of magnitude.

Table 3.4. *Comparison of the computational time for DF and ADF models for heptane. Strain rate units in 1/s. Computational time units in minutes. Machine characteristics: RAM memory of 64 GB, clock frequency of 2.5 GHz. All the calculation launched at one core.*

	HRs	$a = 1$	$a = 10$	$a = 50$	$a = 100$	$a = 200$	$a = 1000$
DF	-	107	74	55	48	39	23
ADF	45	6	8	3	3	2	2

The previous calculations show that the ADF model is justified in terms of the reduction of the computational cost. When dealing with the modelling of diesel sprays in engines, that due to the boundary conditions requires solving a large flamelet database composed of hundreds of flames, the ADF model arises as a feasible approach. If the transient evolution of the ADF model is proved to predict DF results in the auto-ignition range, it will be concluded that the ADF approach has been validated and its use will be completely justified.

The analysis of the transient regime is carried out in terms of ignition delays and flame structure in mixture fraction space. A final section comparing the effect of progress variable definition on flame structure closes the study.

In this analysis, ignition delay is defined as the time spent for a mixture to reach a given value of the flame progress variable c_F. The c_F values considered for this comparison are 0.05, corresponding to the beginning of combustion (low temperature combustion), and 0.3 representing a more developed stage that corresponds to the high temperature chemistry [32, 51]. Due to the multiplicity of solutions in the reignition-extinction range this analysis is limited to the auto-ignition range.

Figures 3.21 and 3.22 gather results for hydrogen and methane flames for both values of c_F and three strain rates covering the auto-ignition range. Scales are common for figures corresponding to the same strain rate.

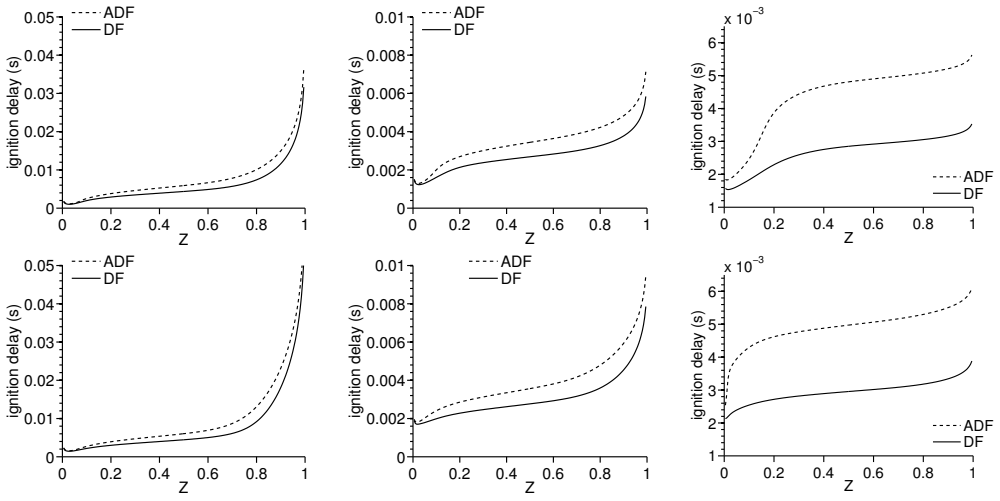

Figure 3.21. *Ignition delay for hydrogen until reaching $c_F = 0.05$ (top row) and 0.3 (bottom row) at strain rates $a = 10$ (left), 100 (center) and 600 (right) 1/s.*

From the figures it is observed that ADF model reproduces the shape of the profiles predicted by DF model and only for the highest strain rate, close to the value a_i, the discrepancies may be considered important. Again this is a consequence of the equality reached in the solutions between both models when $a \to 0$. Additionally, the agreement between the curves show that there is no need of limiting the chemical rates for hydrogen and methane flames.

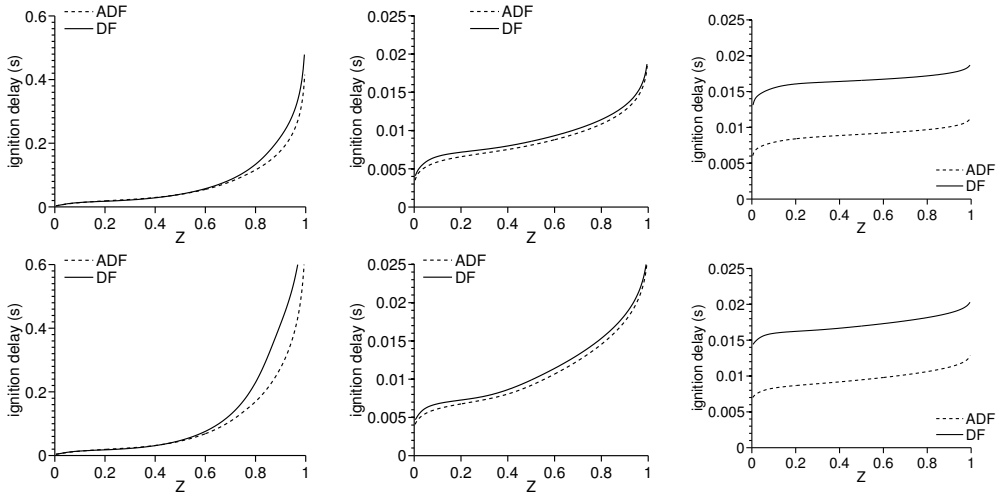

Figure 3.22. *Ignition delay for methane until reaching $c_F = 0.05$ (top row) and 0.3 (bottom row) at strain rates $a = 1$ (left), 50 (center) and 250 (right) 1/s.*

Finally, increasing the strain rate flattens ignition delay curves due to the intensification of diffusion fluxes that tend to smooth the ignition advancement between mixtures.

On the contrary, ignition features for heptane are different and make necessary including the chemical reaction term limitation for the transient flame development. In this case, this limitation is applied to the whole set of mixture fractions. Figures 3.23 and 3.24 show the ignition delays for several strain rates spanning on the auto-ignition range for c_F 0.05 and 0.3, respectively. In order to analyse the influence of exponent α appearing in the definition of the chemical rates limitation (see equation 3.34), the ignition delay for several values has been drawn. Clearly when increasing the value of α the ignition delay is extended.

It is observed that differences in ignition delay between DF model and ADF solutions with no limitation are more relevant when increasing the strain rate and, consequently, the importance of incorporating the chemical rate limitation is greater for high strain rates. Moreover, limiting the chemical source terms is necessary for rich mixtures for all the strain rates but when increasing a, it turns out that lean and stoichiometric mixtures have to be

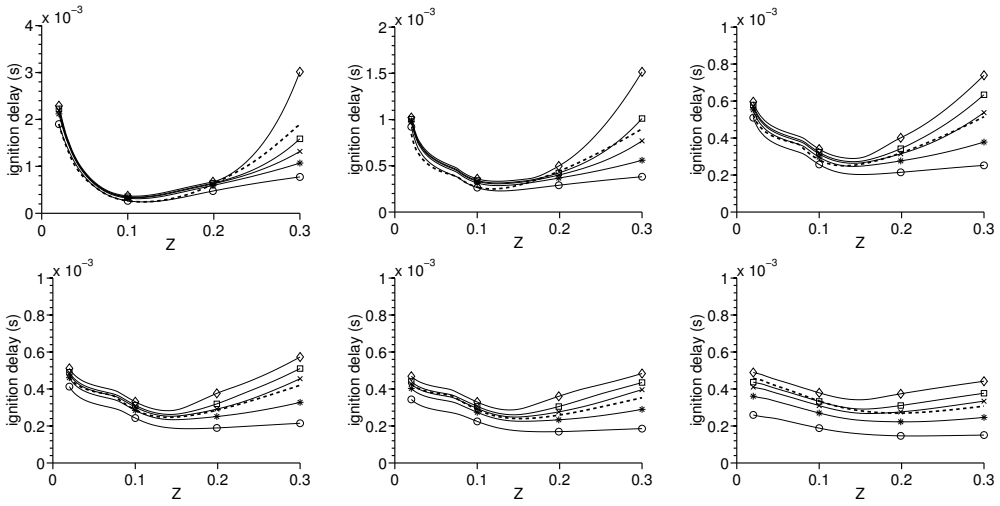

Figure 3.23. *Ignition delay for heptane until reaching $c_F = 0.05$ for strain rates $a = 1$ (top left), 10 (top center), 50 (top right), 100 (bottom left), 200 (bottom center) and 1000 (bottom right) 1/s. The dashed line corresponds to the DF solution. The solid lines correspond to the ADF solutions with the following legend: circles for no limitation, asterisks for $\alpha = 1$, crosses for $\alpha = 2$, squares for $\alpha = 3$ and diamonds for $\alpha = 10$.*

limited too. In addition, ignition delay sensitivity to α augments when increasing a.

From figures 3.23 and 3.24 it is observed that $\alpha = 2$ is the exponent which best fits the DF ignition delay curves even for very high strain rates and is the chosen value for further calculations. With the use of this limitation it is shown that the ability of the ADF model to reproduce combustion structure of complex fuels, such as heptane, improves significantly.

Continuing with the analysis, figures 3.25 and 3.26 show the combustion structure for hydrogen and methane flames. In both figures the transient evolution for four strain rates has been included, belonging the two first strain rates to the auto-ignition range and corresponding to the top figures, while the other two figures, on the bottom, are for strain rates in the reignition-extinction range. In this representation, profiles for DF and ADF models correspond to the same c_2 values (including inert and steady profiles), however, this does not imply that they correspond to the same instants. Therefore, the following analysis is focused on combustion structure by means

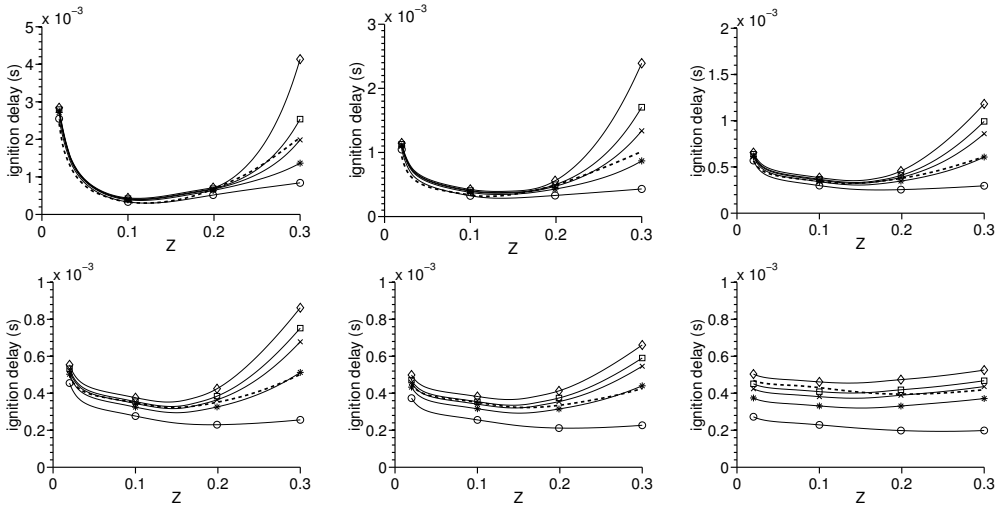

Figure 3.24. *Ignition delay for heptane until reaching $c_F = 0.3$ for strain rates $a = 1$ (top left), 10 (top center), 50 (top right), 100 (bottom left), 200 (bottom center) and 1000 (bottom right) 1/s. The dashed line corresponds to the DF solution. The solid lines correspond to the ADF solutions with the following legend: circles for no limitation, asterisks for $\alpha = 1$, crosses for $\alpha = 2$, squares for $\alpha = 3$ and diamonds for $\alpha = 10$.*

of the description of the profiles defined by variables (Z, Y_c) during ignition propagation across the flame. It is important to note that part of the discrepancies between the transient profiles are due to differences in the steady regime between models since the profiles shown correspond to the same c_2 values.

Profiles similarity between both models reveals how combustion structure is well-reproduced by the ADF model even for very high strain rates belonging to the reignition-extinction range. For high strain rates diffusion processes tend to smooth the curves provoking a synchronized advancement of all the mixtures as was observed in the ignition delay curves where the increase of the strain rate made the curves flatter.

From figures 3.25 and 3.26 it is observed that due to the boundary conditions, first ignition kernels appear in the very lean mixtures, which are the mixtures with the highest initial temperature for these hydrogen and methane flames in the auto-ignition range. The ignition kernels propagate across the

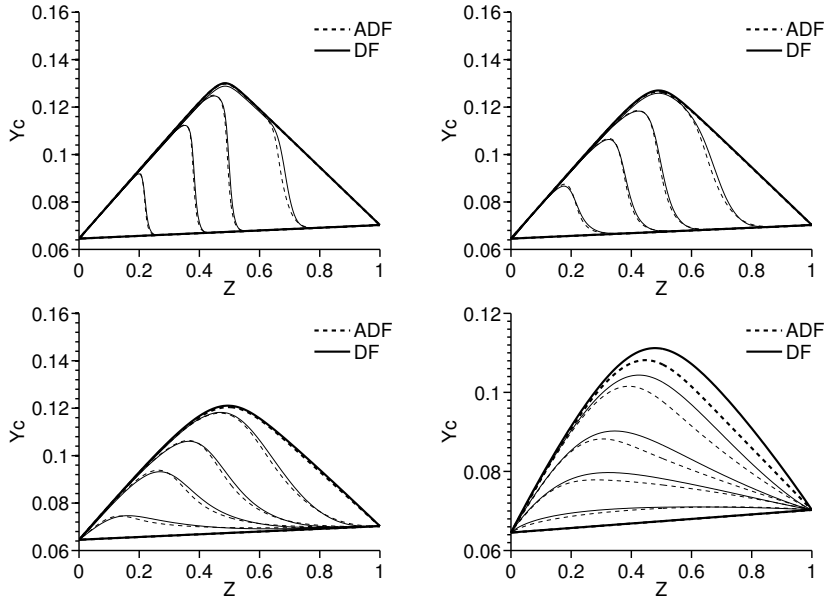

Figure 3.25. *(Z, Y_c) profiles for hydrogen for $c_2 = 0.1$, 0.3, 0.5 and 0.8 at strain rates $a = 10$ (top left), 100 (top right), 1000 (bottom left) and 5000 (bottom right) 1/s. Inert ($c_2 = 0$) and steady ($c_2 = 1$) solutions are included in bold.*

mixtures and promote the ignition of richer mixtures until the flame reaches a complete developed state. Finally, to say that the similarity between the profiles for both models corroborate, as shown in the ignition delay analysis, that no chemical rate limitation is required in these flames.

In a similar way, profiles for heptane comparing the morphology of the curves (Z, Y_c) for both models are shown in figure 3.27. ADF model is computed with a value $\alpha = 2$ for the exponent of the chemical limitation since this value was the one that best fitted the ignition delay curves (see figures 3.23 and 3.24). All the flamelets appearing in figure 3.27 correspond to strain rates belonging to the auto-ignition range.

Figure 3.27 reveals that this limitation avoids an artificial generation of progress variable in the rich mixtures. Curves (Z, Y_c) provided by both models for the different strain rates are remarkably similar leading to the important conclusion that the ADF model has the ability to reproduce the combustion structure of a laminar flame in the auto-ignition range, independently of the

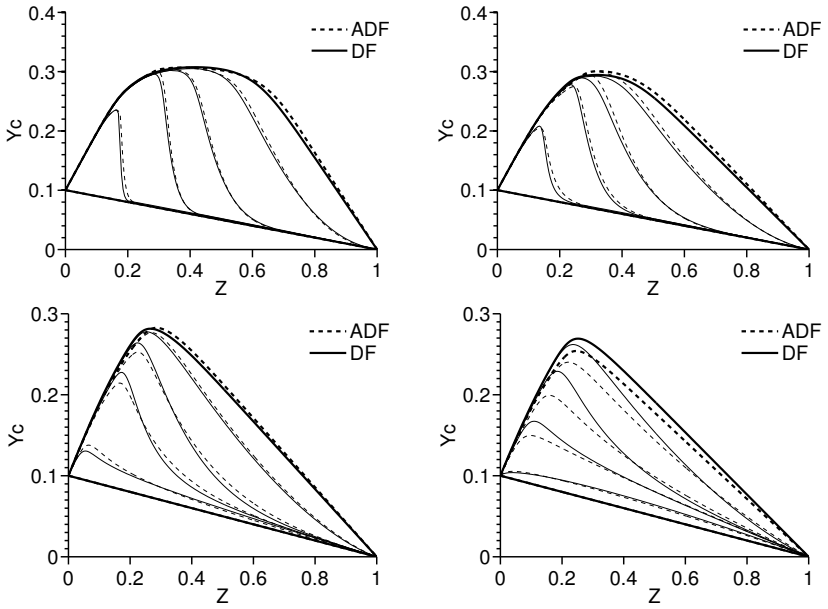

Figure 3.26. *(Z, Y_c) profiles for methane for $c_2 = 0.1$, 0.3, 0.5 and 0.8 at strain rates $a = 10$ (top left), 100 (top right), 800 (bottom left) and 2000 (bottom right) 1/s. Inert ($c_2 = 0$) and steady ($c_2 = 1$) solutions are included in bold.*

fuel molecular complexity, if the suggested chemical rate limitation is applied when necessary.

Finally, solving the whole set of flames where the S-curve extends allows to represent the transient flamelet term $\partial Y_c/\partial t$ in the coordinates (a, Y_c) once mixture fraction is fixed. $\partial Y_c/\partial t$ accounts for diffusion and chemical contributions and is a variable of paramount importance since, as was explained in section 3.2.3, it is the source term to advance in the turbulent manifold in the current formulation of the model. This source term is represented in figures 3.28 and 3.29 for hydrogen and methane flames, respectively, for both DF and ADF models.

From figures 3.28 and 3.29, it is observed that the maximum $\partial Y_c/\partial t$ value is found at intermediate values of Y_c as a consequence of the fact that the maximum chemical source term for these fuels is found at intermediate/high values of c, as seen from figure 3.17. In addition, the figures show how for lean mixtures the highest $\partial Y_c/\partial t$ values are found for low strain rates. This

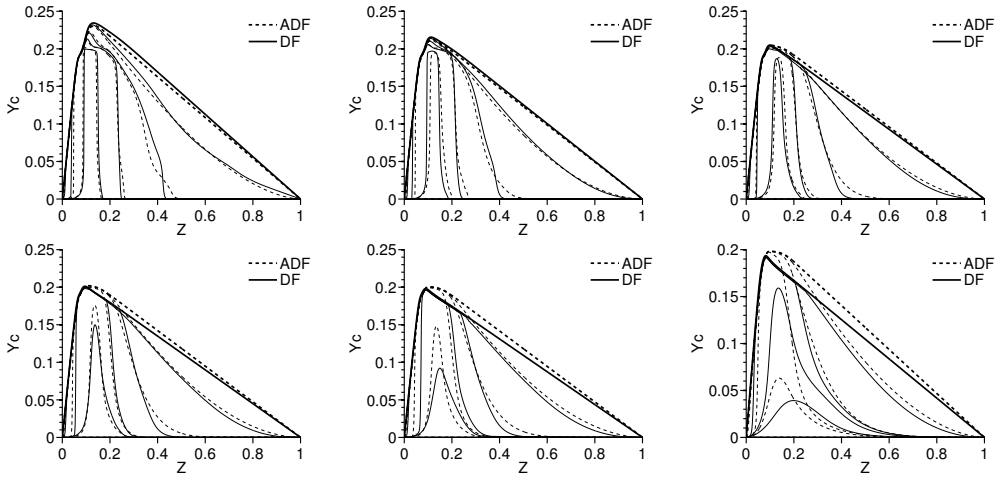

Figure 3.27. *(Z, Y_c) profiles for heptane for $c_2 = 0.1$, 0.3, 0.5 and 0.8 at strain rates $a = 1$ (top left), 10 (top center), 50 (top right), 100 (bottom left), 200 (bottom center) and 1000 (bottom right) 1/s. Inert ($c_2 = 0$) and steady ($c_2 = 1$) solutions are included in bold.*

stems from the appearance of the first ignition kernels at very lean mixtures, as was explained previously. When a is low almost all the production of the progress variable is used to advance in the completeness of combustion for the mixture where production occurs and very small amounts of Y_c are diffused to the adjacent mixtures. However, when increasing the strain rate, greater fractions of Y_c are diffused to other mixtures reducing the term $\partial Y_c/\partial t$ for lean mixtures since they are very reactive. On the contrary, rich mixtures are not very reactive and the transport of Y_c from lean mixtures favours their combustion development making the highest values of $\partial Y_c/\partial t$ to be found at intermediate strain rates for these mixtures.

Finally, to say that DF model shows systematically higher $\partial Y_c/\partial t$ values for both flames compared to ADF model indicating a more vigorous combustion.

Effect of the progress variable definition

In the same way that in section 3.3.1 there was a paragraph devoted to study the impact of the progress variable definition on the ADF results for steady regime, in the following lines a brief analysis intends to understand similar effects for the transient evolution. This is done in figures 3.30 and

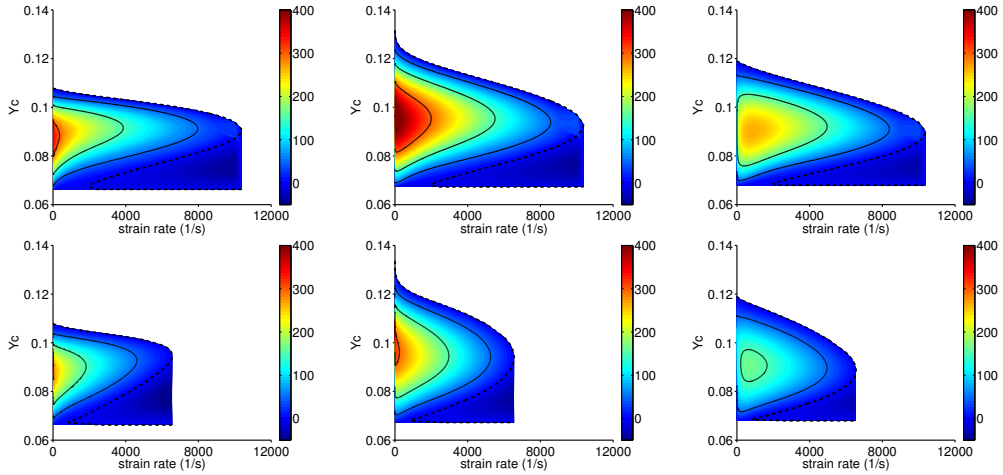

Figure 3.28. *Contour plot of $\partial Y_c/\partial t$ for hydrogen using DF (top) and ADF (bottom) models at lean (left), stoichiometric (center) and rich (right) mixture fractions. Black dashed lines represent steady regime while solid black lines correspond to $\partial Y_c/\partial t$ isolines with values 50, 150 and 300 1/s.*

3.31 comparing combustion structure in terms of (Z, T) profiles [35] for both progress variables PV1 and PV2 for methane and heptane flames. In the case of heptane, calculations have been carried out with $\alpha = 2$ (exponent for the chemical rate limitation) for both progress variables. In the case of methane, top figures are for flamelets with strain rates belonging to the auto-ignition range while bottom figures are for strain rates in the reignition-extinction range. For heptane all the flamelets are found in the auto-ignition range. Profiles correspond to the same c_2 values.

For both fuels an excellent agreement is observed for all the strain rates between the profiles given by both progress variables even for those belonging to the reignition-extinction range in the case of the methane flame. Part of the discrepancies are due to the fact that profiles correspond to the same c_2 values and there exist slight differences between the steady solutions for both progress variables.

Thus, the flame structure provided by ADF model does not strongly depend on progress variable definition, especially in the auto-ignition range.

[35] Again the temperature is used as the variable to compare results.

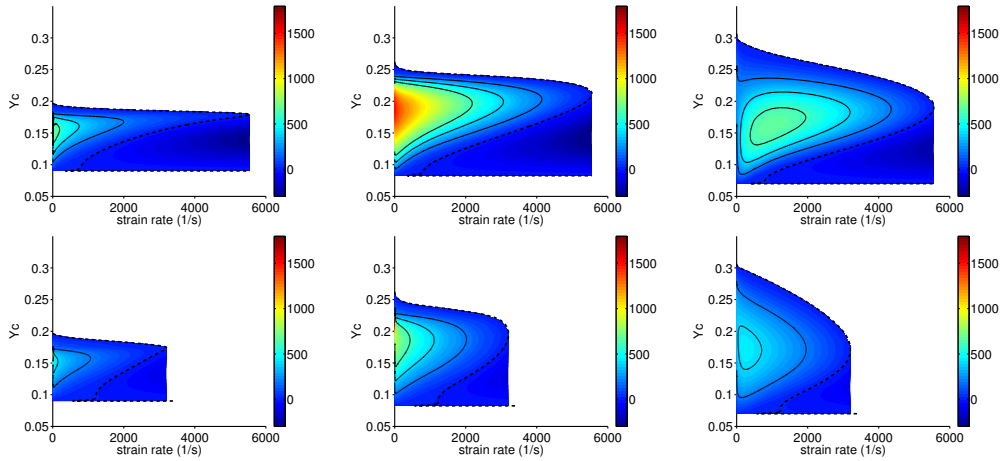

Figure 3.29. *Contour plot of $\partial Y_c/\partial t$ for methane using DF (top) and ADF (bottom) models at lean (left), stoichiometric (center) and rich (right) mixture fractions. Black dashed lines represent steady regime while solid black lines correspond to $\partial Y_c/\partial t$ isolines with values 200, 400 and 600 1/s.*

3.3.3 Conclusions

The analysis performed so far has lead to the formulation of several conclusions.

1. Depending on the boundary conditions and the chemical development of combustion it may be necessary to use some kind of chemical rate limitation. Based on the work of Michel et al. [32] a limitation in the chemical source terms has been suggested and it has been proved to provide excellent results.

2. The validity of the ADF model is limited to the auto-ignition range even for fuels with very low chemical complexity. Along this chapter it has been shown that the S-curve, ignition delay and combustion structure are well-reproduced by the ADF model in this range.

   Although the transient evolution of the flame may be properly reproduced even for strain rates belonging to the reignition-extinction range, the important discrepancies observed for very high strain rates in

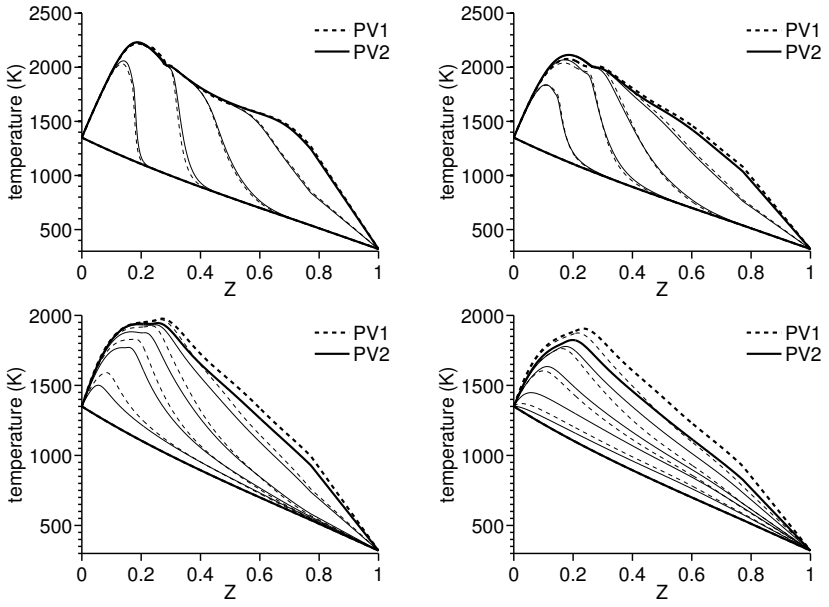

Figure 3.30. *(Z,T) profiles for methane using PV1 and PV2 for $c_2 = 0.1$, 0.3, 0.5 and 0.8 at strain rates $a = 10$ (top left), 100 (top right), 800 (bottom left) and 2500 (bottom right) 1/s. Inert ($c_2 = 0$) and steady ($c_2 = 1$) solutions are included in bold.*

the S-curve limit the application of the ADF model to the auto-ignition range.

3. The results of the ADF model depend slightly on the progress variable definition in the auto-ignition range. This means that if the progress variable has the ability to trace the different stages of combustion it can be considered that ADF results are quite independent of the definition of this variable.

The previous conclusions validate the ADF model and allow to apply this model to industrial devices, such as diesel engines, since in most of these devices the main combustion develops in the auto-ignition range. Together with these conclusions, the computational economy related to the ADF approach (see section 3.3.2) justify the use of this model as an alternative to the complete DF model when the use of complex mechanisms and the wide

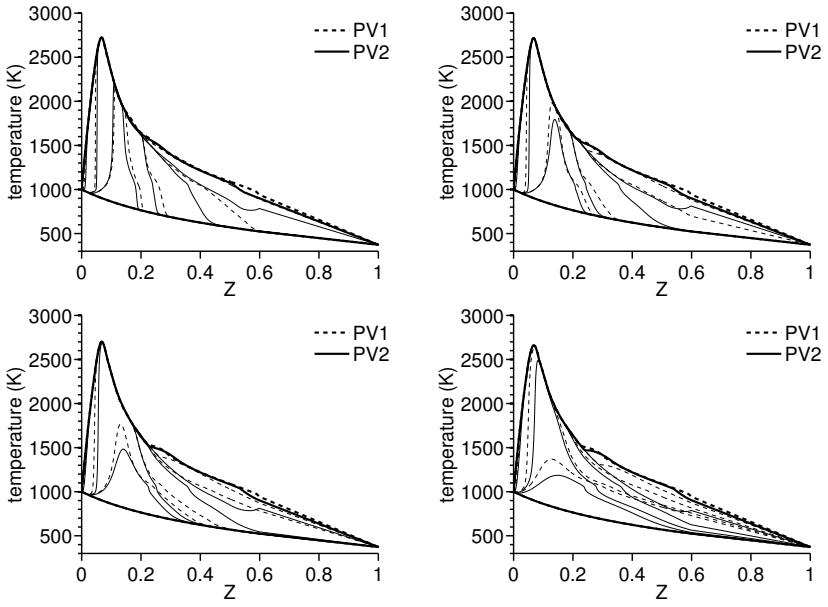

Figure 3.31. *(Z,T) profiles for heptane using PV1 and PV2 for $c_2 = 0.1$, 0.3, 0.5 and 0.8 at strain rates $a = 10$ (top left), 50 (top right), 200 (bottom left) and 1000 (bottom right) 1/s. Inert ($c_2 = 0$) and steady ($c_2 = 1$) solutions are included in bold.*

ranges for the boundary conditions arise as requirements for the problem to be solved.

Finally, it is important to highlight again the advantages of the ADF model:

1. It has a very low computational cost (one order of magnitude lower than the DF model).

2. Due to its low computational cost a better discretization of the controlling variables can be achieved, e.g. strain rate, leading to a local description of the turbulent flame.

3. It can manage chemical schemes of any complexity since the homogeneous reactors calculation is very fast avoiding the use of skeletal mechanisms as a way to keep suitable computational times. This is relevant in diesel spray for parameters like ignition delay or lift-off length and pollutants, which are highly dependent on chemistry.

4. Attending to the high impact of the strain rate on the ignition delay and the combustion structure ((Z, Y_c) profiles), as shown in section 3.3.2, it seems that the losses related to neglecting the effect of diffusion on the chemical source terms in the auto-ignition range[36] are probably not so critical as other possible alternatives like solving a very reduced number of flamelets with the DF model which act as 'average' flamelets in the CFD calculation.

3.4 Conclusions

In this chapter the flamelet concept has been thoroughly reviewed. The equations derived for this model have been explained and the different approaches found in the literature have been sketched. The chapter has followed with a detailed description of the developed model in the current work. To do so, first the complete DF model has been explained and the simplifications that lead to the ADF model have been developed. In addition, some corrections related to the chemical source term have been described in order to improve the ability of the ADF model. The theoretical part of the chapter has been closed with the description of the generation of the turbulent combustion manifold and its coupling with CFD.

In the second part of the chapter the ADF model has been validated by its direct comparison with the DF solutions. The steady and transient regimes have been assessed for a set of fuels of different chemical complexity. In addition, the effect of the progress variable in the ADF solutions has been investigated.

It has been shown that the ADF model reproduces solutions provided by the DF model in terms of ignition delay and combustion structure in the auto-ignition range if the corrections explained in the chapter are applied when necessary. Moreover, in this range the progress variable has no sharp effect on ADF solutions.

The positive results obtained in the validation in conjunction with the considerable decrease of computational cost leads to confirm that the ADF model is of great interest when the auto-ignition range predominates during the combustion process.

[36] The comparison with DF solutions shows that the effects of such simplification are very limited in terms of ignition delay and combustion structure.

References

[1] Barths H., Hasse C., Bikas G. and Peters N. "Simulation of combustion in direct injection diesel engines using a eulerian particle flamelet model". *Proceedings of the Combustion Institute*, Vol. 28 n^o 1, pp. 1161–1168, 2000.

[2] Dhuchakallaya I., Rattanadecho P. and Watkins P. "Auto-ignition and combustion of diesel spray using unsteady laminar flamelet model". *Applied Thermal Engineering*, Vol. 52 n^o 2, pp. 420–427, 2013.

[3] Tillou J., Michel J. B., Angelberger C., Bekdemir C. and Veynante D. "Large-Eddy Simulation of Diesel Spray Combustion with Exhaust Gas Recirculation". *Oil & Gas Science and Technology-Revue de l'IFP*, Vol. 69 n^o 1, pp. 155–165, 2014.

[4] Winklinger J. F. *Implementation of a combustion model based on the flamelet concept and its application to turbulent reactive sprays*. Doctoral Thesis, Universitat Politècnica de València, 2015.

[5] Kahila H., Wehrfritz A., Kaario O., Masouleh M. G., Maes N., Somers B. and Vuorinen V. "Large-eddy simulation on the influence of injection pressure in reacting spray A". *Combustion and Flame*, Vol. 191, pp. 142–159, 2018.

[6] Williams F. A. *Recent advances in theoretical descriptions of turbulent diffusion flames*. Springer, 1975.

[7] Peters N. *Turbulent combustion*. Cambridge University Press, 2000.

[8] Peters N. "Laminar diffusion flamelet models in non-premixed turbulent combustion". *Progress in Energy and Combustion Science*, Vol. 10 n^o 3, pp. 319–339, 1984.

[9] Peters N. "Laminar flamelet concepts in turbulent combustion". In *Symposium (International) on Combustion*, volume 21, pp. 1231–1250. Elsevier, 1988.

[10] Pope S. B. "Ten questions concerning the large-eddy simulation of turbulent flows". *New journal of Physics*, Vol. 6 n^o 1, pp. 35, 2004.

[11] Pitsch H. "Large-eddy simulation of turbulent combustion". *Annu. Rev. Fluid Mech.*, Vol. 38, pp. 453–482, 2006.

[12] Peters N. *Combustion theory*. CEFRC Summer School, Princeton, 2010.

[13] Poinsot T. and Veynante D. *Theoretical and numerical combustion*. RT Edwards Inc., 2005.

[14] Burke S. P. and Schumann T. E. W. "Diffusion flames". *Industrial & Engineering Chemistry*, Vol. 20 n^o 10, pp. 998–1004, 1928.

[15] Liñán A. "The asymptotic structure of counterflow diffusion flames for large activation energies". *Acta Astronautica*, Vol. 1 n^o 7-8, pp. 1007–1039, 1974.

[16] Kirkbey L. L. and Schmitz R. A. "An analytical study of the stability of a laminar diffusion flame". *Combustion and Flame*, Vol. 10 n^o 3, pp. 205–220, 1966.

[17] Schmitz R. A. "A further study of diffusion flame stability". *Combustion and Flame*, Vol. 11 n^o 1, pp. 49–62, 1967.

[18] Naud B., Novella R., Pastor J. M. and Winklinger J. F. "RANS modelling of a lifted H2/N2 flame using an unsteady flamelet progress variable approach with presumed PDF". *Combustion and Flame*, Vol. 162 n^o 4, pp. 893–906, 2015.

[19] Kim J. S. and Williams F. A. "Structures of flow and mixture-fraction fields for counterflow diffusion flames with small stoichiometric mixture fractions". *SIAM Journal on Applied Mathematics*, Vol. 53 n^o 6, pp. 1551–1566, 1993.

[20] van Oijen J. A. and de Goey L. P. H. "Modelling of premixed laminar flames using flamelet-generated manifolds". *Combustion Science and Technology*, Vol. 161 n^o 1, pp. 113–137, 2000.

[21] de Goey L. P. H., van Oijen J. A., Bongers H. and Groot G. R. A. "New flamelet based reduction methods: the bridge between chemical reduction techniques and flamelet methods". In *European Combustion Meeting, Orléans (France)*, 2003.

[22] Pitsch H. and Peters N. "A consistent flamelet formulation for non-premixed combustion considering differential diffusion effects". *Combustion and Flame*, Vol. 114 n^o 1-2, pp. 26–40, 1998.

[23] Pera C., Colin O. and Jay S. "Development of a FPI detailed chemistry tabulation methodology for internal combustion engines". *Oil & Gas Science and Technology-Revue de l'IFP*, Vol. 64 n^o 3, pp. 243–258, 2009.

[24] D'Errico G., Lucchini T., Contino F., Jangi M. and Bai X. S. "Comparison of well-mixed and multiple representative interactive flamelet approaches for diesel spray combustion modelling". *Combustion Theory and Modelling*, Vol. 18 n^o 1, pp. 65–88, 2014.

[25] Maas U. and Pope S. B. "Simplifying chemical kinetics: intrinsic low-dimensional manifolds in composition space". *Combustion and flame*, Vol. 88 n^o 3-4, pp. 239–264, 1992.

[26] Gicquel O., Darabiha N. and Thévenin D. "Laminar premixed hydrogen/air counterflow flame simulations using flame prolongation of ILDM with differential diffusion". *Proceedings of the Combustion Institute*, Vol. 28 n^o 2, pp. 1901–1908, 2000.

[27] Pierce C. D. and Moin P. "Progress-variable approach for large-eddy simulation of non-premixed turbulent combustion". *Journal of fluid Mechanics*, Vol. 504, pp. 73–97, 2004.

[28] Lehtiniemi H., Mauss F., Balthasar M. and Magnusson I. "Modeling diesel engine combustion with detailed chemistry using a progress variable approach". *SAE Technical Paper*, 2005.

[29] Fiorina B., Gicquel O., Vervisch L., Carpentier S. and Darabiha N. "Approximating the chemical structure of partially premixed and diffusion counterflow flames using FPI flamelet tabulation". *Combustion and flame*, Vol. 140 n^o 3, pp. 147–160, 2005.

[30] Prüfert U., Hartl S., Hunger F., Messig D., Eiermann M. and Hasse C. "A constrained control approach for the automated choice of an optimal progress variable for chemistry tabulation". *Flow, Turbulence and Combustion*, Vol. 94 n^o 3, pp. 593–617, 2015.

[31] Pastor J. V., López J. J., García J. M. and Pastor J. M. "A 1D model for the description of mixing-controlled inert diesel sprays". *Fuel*, Vol. 87 n^o 13-14, pp. 2871–2885, 2008.

[32] Michel J. B., Colin O. and Veynante D. "Modeling ignition and chemical structure of partially premixed turbulent flames using tabulated chemistry". *Combustion and Flame*, Vol. 152 n^o 1, pp. 80–99, 2008.

[33] Livengood J. C. and Wu P. C. "Correlation of autoignition phenomena in internal combustion engines and rapid compression machines". In *Symposium (international) on combustion*, volume 5, pp. 347–356. Elsevier, 1955.

[34] Pope S. B. *Turbulent flows*. IOP Publishing, 2001.

[35] Pitsch H., Chen M. and Peters N. "Unsteady flamelet modeling of turbulent hydrogen-air diffusion flames". In *Symposium (international) on combustion*, volume 27, pp. 1057–1064. Citeseer, 1998.

[36] Effelsberg E. and Peters N. "Scalar dissipation rates in turbulent jets and jet diffusion flames". In *Symposium (International) on Combustion*, volume 22, pp. 693–700. Elsevier, 1989.

[37] Jones W. P. and Musonge P. "Closure of the Reynolds stress and scalar flux equations". *The Physics of fluids*, Vol. 31 n^o 12, pp. 3589–3604, 1988.

[38] Janicka J. and Peters N. "Prediction of turbulent jet diffusion flame lift-off using a PDF transport equation". *Symposium (International) on Combustion*, Vol. 19 n^o 1, pp. 367–374, 1982.

[39] Desantes J. M., Novella R., Pastor J. M. and Pérez-Sánchez E. J. "Analysis of the approximated diffusion flamelet approach using fuels with different chemical complexity". In *Mathematical Modelling in Engineering & Human Behaviour 2014. 16th Edition of the Mathematical Modelling Conference Series at the Institute for Multidisciplinary Mathematics, Valencia, Spain*, pp. 228–233, 2014.

[40] Payri F., Novella R., Pastor J. M. and Pérez-Sánchez E. J. "Evaluation of the approximated diffusion flamelet concept using fuels with different chemical complexity". *Applied Mathematical Modelling*, Vol. 49, pp. 354–374, 2017.

[41] Saxena P. and Williams F. A. "Testing a small detailed chemical-kinetic mechanism for the combustion of hydrogen and carbon monoxide". *Combustion and Flame*, Vol. 145 n^o 1-2, pp. 316–323, 2006.

[42] Smith G. P., Golden D. M., Frenklach M., Moriarty N. W., Eiteneer B., Goldenberg M., Bowman C. T., Hanson R. K., Song S., Gardiner Jr. W. C. and others. "GRI mechanism for methane/air, version 3.0". *URL www. me. berkeley. edu/gri_mech*, 1999.

[43] Cabra R., Myhrvold T., Chen J. Y., Dibble R. W., Karpetis A. N. and Barlow R. S. "Simultaneous laser Raman-Rayleigh-LIF measurements and numerical modeling results of a lifted turbulent H2/N2 jet flame in a vitiated coflow". *Proceedings of the Combustion Institute*, Vol. 29 n^o 2, pp. 1881–1888, 2002.

[44] Cabra R., Chen J. Y., Dibble R. W., Karpetis A. N. and Barlow R. S. "Lifted methane–air jet flames in a vitiated coflow". *Combustion and Flame*, Vol. 143 n^o 4, pp. 491–506, 2005.

[45] Zeuch T., Moréac G., Ahmed S. S. and Mauss F. "A comprehensive skeletal mechanism for the oxidation of n-heptane generated by chemistry-guided reduction". *Combustion and Flame*, Vol. 155 n^o 4, pp. 651–674, 2008.

[46] Pickett L. M., Bruneaux G. and Payri R. "Engine combustion network". *Sandia National Laboratories, Livermore, CA, https://ecn.sandia.gov/*, 2018.

[47] Naud B., Novella R., Pastor J. M. and Winklinger J. F. "Comparison of different assumptions for tabulated chemistry based on laminar igniting and extinguishing diffusion flamelets". In *European Combustion Meeting 2013*, 2013.

[48] Novoselov A. G., Law C. K. and Mueller M. E. "Direct Numerical Simulation of turbulent nonpremixed "cool" flames: applicability of flamelet models". *Proceedings of the Combustion Institute (in press)*, 2018.

[49] Michel J. B. and Colin O. "A tabulated diffusion flame model applied to diesel engine simulations". *International Journal of Engine Research*, pp. 346–369, 2013.

[50] Petzold L. R. "Description of DASSL: a differential/algebraic system solver". *Sandia National Labs., Livermore, CA (USA)*, 1982.

[51] Tillou J., Michel J. B., Angelberger C. and Veynante D. "Assessing LES models based on tabulated chemistry for the simulation of diesel spray combustion". *Combustion and Flame*, Vol. 161 n^o 2, pp. 525–540, 2014.

Chapter 4

Analysis of the diesel spray in the RANS framework

Contents

4.1 Introduction

The aim of this thesis is to analyse and understand how combustion occurs and develops in a diesel-like reactive spray, that is, how spray auto-ignites

and which are the morphology and internal structure of the spray at quasi-steady conditions. To reach this goal, the developed advanced combustion model, based on the flamelet concept and with the simplifications that the ADF approach introduces, as described in chapter 3, is applied in the frame of RANS and LES turbulence models. This chapter deals with the simulation of a diesel spray using a RANS model to describe turbulence while its description in the LES context is postponed to next chapter.

To achieve this objective the problem is analysed in the light of different aspects:

1. The influence of the boundary conditions on the spray structure. It is intended to understand how the reactivity of the mixture, modified by means of the ambient temperature and/or the oxygen concentration, impacts on auto-ignition and spray morphology.

2. The influence of the chemical mechanism. It is clear that the oxidation scheme is one of the major uncertainties in combustion modelling, especially for long chain alkanes where it is necessary to simplify the number of species and reactions in order to obtain manageable mechanisms. Although the mechanism is experimentally assessed, it is important to note that little or non-existing information is available for rich mixtures and high pressures ignition, where combustion typically occurs in diesel sprays.

3. How combustion is modified when adding different layers of physical content. The homogeneous reactors solutions, where only chemistry occurs without any kind of transport, are first analysed. Subsequently, the laminar flames solutions, where transport phenomena are introduced and coexist with chemistry, are assessed. The impact of the interaction between diffusion and chemistry is evaluated based on previous homogeneous reactors solutions. Finally, the turbulent spray is described in the light of the homogeneous reactors and the laminar flames solutions.

   The description of the turbulent flame solution based on the behaviour of laminar flames, or in this context flamelets, arises as a natural step when a flamelet based combustion model is applied since it describes the turbulent flame as an ensemble of strained laminar flames. In addition, the application of the ADF model invites to carry out this gradual description from the homogeneous reactors to the turbulent spray, where in each stage new physical and delimited content is added and, in fact, it corresponds to the own model workflow.

It is considered that each of the previous points complements each other and adds relevant information that is necessary in order to provide a complete picture of the combustion process.

Regarding the diesel spray, it is clear that lots of processes concur in a direct injection diesel engine. These can be summarized in the following:

1. Liquid vein atomization and droplets break-up.
2. Turbulent flow including additional flow movements like swirl usually induced in order to enhance mixing.
3. Fuel and air mixing.
4. Fuel oxidation.
5. Heat transfer due to conduction, convection and radiation.
6. Wall impingement and flame extinction.
7. Pollutant emissions formation. In a diesel spray the most important are soot and nitrogen oxides (NO_x).
8. Several injections. Interaction between them.
9. Several injectors and interaction between sprays.
10. Piston movement.

This makes patent that measuring in a real engine is a task far from being straightforward and that the detailed study of combustion in such complex configuration by means of experimental techniques may derive in uncertainties whose cause is not easily devised.

If the objective is the understanding of the intrinsic nature of diesel spray combustion, it would be desirable to conceive some kind of simplified experimental configuration in order to minimize additional and undesired effects that do not add relevant information but only distort measurements. In addition, simplifying the experimental set-up leads to obtain a greater diversity and more accurate measurements.

The need to achieve a deeper insight of diesel sprays due to the reasons advocated in chapter 1 has prompted that the Engine Combustion Network (ECN) [1] designed a set of experiments to be performed in specific combustion chambers in order to measure diesel-like sprays. For this purpose, special

facilities with fixed walls positioned far from the diesel spray, in order to reduce heat transfer by radiation and avoid wall impingement, are used. Two types of installations exist, namely, constant-volume pre-burn combustion vessels (CVP) and constant-pressure flow rigs (CPF) [2, 3].

In the first one, the spray is injected in a combustion chamber of constant volume. High temperature and pressure conditions, as those found close to the top dead center (TDC) in a diesel engine, are generated by means of a previous premixed combustion with a specified composition. Then, combustion products cool down due to heat transfer to the walls during a long period of time (around 1 s) and, when the desired temperature and pressure conditions are achieved, fuel is injected and auto-ignites in diesel-like conditions. Injection extends 5 ms at most in order to achieve the quasi-steady regime. On the contrary, in the CPF rig, a constant flow of compressed and pre-heated air, at the desired thermal conditions, is supplied into the combustion chamber where fuel is injected and auto-ignites.

The ranges of the boundary conditions that may be covered depend on the facility too. In general, higher ambient temperatures and pressures are achieved with a CVP in comparison with a CPF. However, the CPF allows a higher frequency of injections and does not contain in the supplied air products from a previous combustion as it happens in the CVP. Notwithstanding, contrarily to the CVP, heat release cannot be measured in the CPF since it works at constant pressure.

Comparisons of measured data in different chambers confirm that they provide very similar spray parameters and variables [4, 5], although some of such parameters show slight differences depending on the type of facility.

From the ECN set of experiments, one of the spray configurations that has attracted greater attention in the scientific community is the so-called spray A. It is a single nozzle spray with boundary conditions corresponding to modern diesel-like sprays. The ranges over which the parametric sweeps extend comprise large variations of the most relevant boundary conditions, that is, moderate/high injection pressures (between 50 and 150 MPa), low/intermediate air temperature (between 750 and 1000 K), moderate/high oxygen concentration (between 0.13 and 0.21), etc. Fuel for spray A is dodecane, which is a diesel surrogate fuel. Nozzles used for spray A have very reduced diameters of the order of 90 μm that improve atomization and break-up of the liquid fuel.

A large amount of scientific literature in the experimental [2, 3, 6–10] as well as the modelling fields [11–19] is found for spray A.

The analysis and description of spray A, from the different angles exposed at the beginning of this chapter, is one of the main objectives of this thesis in order to contribute to the understanding of diesel flames. This is carried out in the context of RANS simulations in the current chapter.

The results obtained in this chapter can be found in the author's works [16, 18, 20].

4.2 Boundary conditions

In this section the boundary conditions for the simulated cases in the RANS framework are described. The nominal case for spray A is defined by the boundary conditions given by an ambient temperature $T_{amb} = 900$ K, an oxygen molar concentration $X_{O_2} = 0.15$ and a density $\rho = 22.8$ kg/m^3. In this work, three parametric sweeps are carried out, namely, two in the ambient temperature direction from 750 to 900 K keeping $X_{O_2} = 0.15$ and 0.21 while a third study spans in the oxygen concentration direction (simulating the effect of EGR) from 0.13 to 0.21 with an ambient temperature fixed at 900 K. In all the cases density is kept at $\rho = 22.8$ kg/m^3, injection pressure, p_{inj}, at a value of 150 MPa and fuel temperature at 363 K. Fuel is injected in quiescent air only composed of oxygen and nitrogen.

In addition, a fuel injection rate, obtained from a virtual injection rate generator [21], which lasts for more than 4 ms is imposed in order to reach quasi-steady state in an extensive region of the spray. The nozzle injector, with ECN reference nozzle code 210675 [1], has a nominal diameter of 90 μm and an estimated discharge coefficient of 0.9 [22].

Table 4.1 gathers the boundary conditions for the simulated cases, where p_{amb} is the pressure in the combustion chamber, Z_{st} is the stoichiometric mixture fraction and Z_s is the saturation mixture fraction. Experimental results correspond to those measured in a CPF rig at CMT - Motores Térmicos unless otherwise stated [7, 8, 21].

4.3 Mesh and model description

To solve turbulence a standard $k - \varepsilon$ model was used adjusting $C_{\varepsilon 1}$ to 1.52 in order to reduce the spreading rate overestimation found for round jets [23, 24] described in section 2.5.1. For the other parameters, standard values appearing in table 2.1 were used.

Table 4.1. *Definition of spray A simulated parametric studies.*

X_{O2}	T_{amb} (K)	ρ_{amb}(kg/m^3)	p_{amb} (MPa)	p_{inj} (MPa)	Z_{st}	Z_s
0.13	900	22.8	5.98	150	0.040	0.326
0.15	750	22.8	4.97	150	0.046	0.251
0.15	800	22.8	5.3	150	0.046	0.278
0.15	850	22.8	5.63	150	0.046	0.303
0.15	900	22.8	5.96	150	0.046	0.326
0.21	750	22.8	4.93	150	0.063	0.250
0.21	800	22.8	5.26	150	0.063	0.277
0.21	900	22.8	5.91	150	0.063	0.325

Regarding the liquid phase, it was solved by means of the Discrete Droplet Model (DDM). Atomization and break-up were solved modelling Kelvin-Helmholtz and Rayleigh-Taylor instabilities by means of the Reitz model [25]. According to Desantes et al. [26], model constants were chosen equal to $B_0 = 0.61$, $B_1 = 40$, $C_\tau = 1$, $CBU = 3$. Ranz-Marshall model was used for droplet evaporation with exponents equal to 1/2 and 1/3 for Reynolds and Prandtl numbers, respectively. No collision neither coalescence were accounted for in the simulation. The flow of parcels was taken equal to $5.4 \cdot 10^7$ parcels/s.

The ADF model, as described in chapter 3, has been adopted for the calculations described in this chapter. For all the simulated mechanisms an exponent of $\alpha = 2$ has been chosen for the chemical source terms limitation (see chapter 3), except for Yao mechanism (described in the following) where a value of 10 was taken due to the extremely short ignition delays (see sections 4.4.1 and 4.4.3.2). Moreover, the chosen progress variable for these calculations was defined by $Y_c = Y_{\mathrm{CO}} + Y_{\mathrm{CO_2}}$, which has been already used in chapter 3.

To generate the flamelet manifold around 160 mixtures fraction values were taken, depending on the boundary conditions, with 504 points in the progress variable direction to describe very accurately the whole ignition process.

For results shown in this chapter, integrations were performed with a beta PDF for mixture fraction while a log-normal defined by $\sigma = \sqrt{2}$ for scalar dissipation rate was used and a Dirac delta for time. The turbulent flame manifold contains around 32 values for $\widetilde{Z}$, 17 for S and 35 for $\widetilde{\chi}_{st}$ depending on the boundary conditions. Finally, 51 values with a parabolic distribution were used for $\widetilde{Y_c}$ (or equivalently d).

The transported species were H, OH, CO, CO_2, H_2O, $C_{12}H_{26}$, CH_2O, C_2H_2, HO_2, H_2O_2, N_2, C_7H_{14}, H_2, O_2 being the last three used as sink species

in order to fulfil mass conservation [27] (see section 3.2.4). The coupling between the manifold and the turbulent spray corresponds to a weak coupling where species chemical source terms are obtained from tabulated species mass fractions according to option 2 (see section 3.2.4).

Regarding the chemical mechanisms, whose influence is one of the objectives of this work, three well-known dodecane oxidation schemes were applied to spray A calculations. Narayanaswamy et al. [28] is the largest one with 255 species and 2289 reactions while the Yao et al. scheme [29] is a skeletal mechanism with a reduced number of species and reactions (54 and 269, respectively). Finally, Wang et al. [30] scheme, with an intermediate extension, has 100 species and 432 reactions.

The CFD equations were solved in the open tool-box OpenFOAM environment [31], which is a finite volume code, using an in-house code. A cylinder of height 108 mm and radius 54 mm represented the domain but, as cylindrical symmetry was imposed in the RANS frame, only a meridian cut was solved. The mesh was structured with a constant cell size of 0.5 (axial direction) $\times$ 0.25 (radial direction) mm [26]. The time step was fixed constant and equal to 0.1 μs. As domain dimensions were large and spray was far from border domain, typical boundary conditions were imposed at walls.

A PISO algorithm[1] was applied to solve transport equations in CFD. Gradients, divergences and Laplacians were calculated with second order schemes while an implicit first order scheme was used for the temporal derivative.

4.4 Results and discussion

This section is the principal part of the chapter and is devoted to analyse the three previous described objectives, namely, the influence of the boundary conditions, the impact of the chemical mechanism and, finally, how combustion is modified when adding new physical content.

These paragraphs are structured following the own combustion model workflow: a first analysis in homogeneous reactor conditions, a subsequent description of the flamelet solutions where diffusion effects are added to the chemical evolution and, finally, a study of the turbulent flame. In each of the different parts of the analysis, special attention is devoted to the impact of the boundary conditions and the chemical scheme on combustion structure.

[1]PISO stands for Pressure Implicit with Splitting of Operators and is one of the most extended algorithms to solve transient flows.

4.4.1 Homogeneous reactor results

As in a turbulent flame there exists a diversity of possible uncertainties due to the different hypotheses required to formulate the models, it is convenient to carry out a previous evaluation of the response given by the mechanisms in stirred or homogeneous reactor conditions in order to limit, in some sense, which are the causes of latter discrepancies observed in the turbulent spray.

The ignition delay (ID) for the auto-ignition of a set of homogeneous reactors is plotted in figure 4.1 as a function of the inverse of temperature for the three mechanisms, including the experimental data measured in shock tubes [32]. Auto-ignition in a shock tube is modelled as a homogeneous reactor that evolves with adiabatic and constant volume evolution[2] [32] with an initial pressure equal to 20 atm and equivalence ratios of $\phi = 0.5$ and 1 as in the experiment. Then, ignition delay is defined as the time for which the derivative of pressure is maximum, corresponding this definition to that used in the experiment [32].

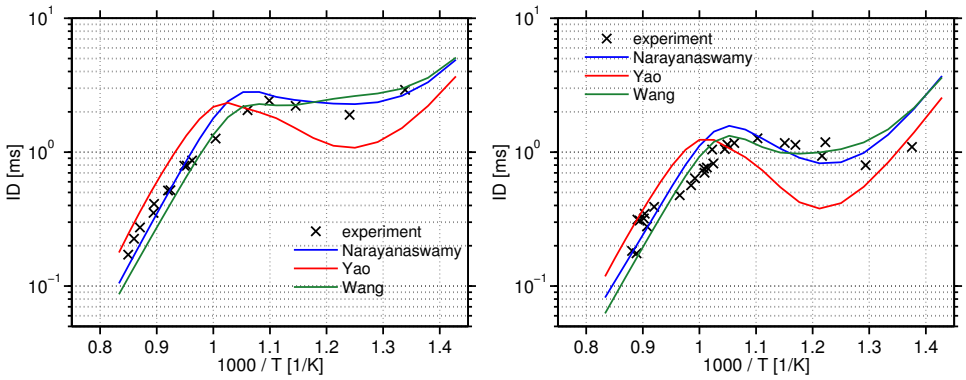

Figure 4.1. *Experimental (crosses) and modelled (Narayanaswamy blue, Yao red, Wang green) ignition delays as a function of temperature for $\phi = 0.5$ (left) and 1 (right). Calculations for initial pressure $p = 20$ atm.*

From figure 4.1, it is observed that Yao mechanism is the one that shows greater differences compared with the experiment. For temperatures lower than 1000 K it under-predicts ignition delay, especially for the stoichiometric mixture, nevertheless, for temperatures higher than 1000 K it overestimates ignition delay. On the contrary, Narayanaswamy and Wang schemes provide

[2]Different to this, homogeneous reactors are computed at constant pressure in the ADF combustion model.

very similar ignition delays and their predicted values are quite close to the measured ones.

It is worth mentioning that there exists a mild NTC region (see section 2.4.1) for temperatures in the interval of 800 and 900 K, which in spite of the higher scattering, seems to be intensified when enriching the mixture (at least in relative terms). Yao scheme predicts a very strong NTC region that is far from fitting experimental data. On the contrary, Wang mechanism is the one that provides a softer NTC region being non-existing for $\phi = 0.5$.

It is important to note that the experimental data from shock tubes is in general very limited in pressure and mixture richness. It is difficult to have measurements for rich mixtures, which as will be seen later, are the mixtures where ignition mainly develops in diesel-like sprays. However, with the available data, it is expected that Yao predicts faster ignition than Narayanaswamy and Wang since, at the simulated conditions, ignition develops at initial temperatures lower than 1000 K. This is confirmed in the following analysis.

With this previous evaluation of the capabilities of the chemical mechanisms we can undertake the subsequent analysis of spray A. This analysis is started describing the homogeneous reactors solutions from two points of view, the ignition delays and the chemical source terms maps in terms of Z and c. The understanding of the behaviour of the homogeneous reactors is considered of paramount importance since they are the base of the present combustion model. Notwithstanding, even for the DF model or other flamelet approaches, their fundamental relevance is still evident since, even diffusion may modify chemical evolution, they provide a global picture of the most important features of chemistry in the auto-ignition range. Motivated by these observations, the homogeneous reactors results for spray A nominal conditions are shown in the following[3].

First, ignition delay is represented as a function of mixture fraction at nominal conditions for the three mechanisms in figure 4.2. As long chain alkanes ignite in two stages, two ignition delays are used to characterize the mixtures: ID_1 is the time spent by each mixture to reach its initial temperature plus 30 K while ID_2 is the ignition delay related to an increment of the initial temperature of 400 K. Clearly, ID_1 and ID_2 characterize low and high temperature ignition delays, respectively.

[3]As these solutions are used for subsequent calculations, they are performed imposing constant pressure, which is a boundary condition for homogeneous reactors calculations used in the ADF model, as described in section 3.2.2.2

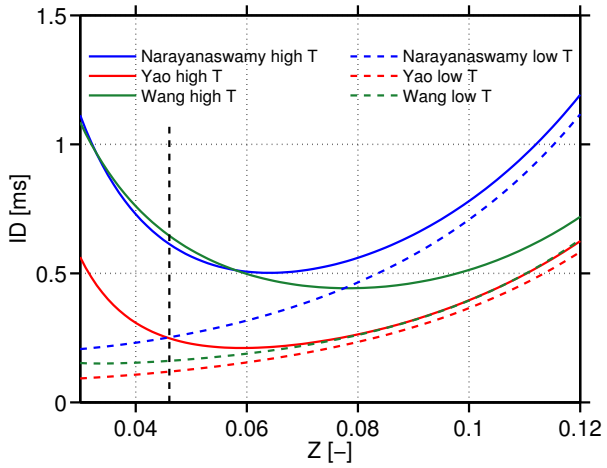

Figure 4.2. *Homogeneous reactors ignition delays for low and high temperature stages for Narayanaswamy (blue), Yao (red) and Wang (green) mechanisms at nominal conditions. Vertical black dashed line indicates stoichiometric mixture fraction.*

It is observed in figure 4.2 that ID_1 and its slope are increasing with the mixture fraction. On the contrary, ID_2 shows a minimum positioned at the most reactive mixture fraction Z_{MR}. Yao mechanism is the one that predicts the most reduced ID_1, followed by Wang which in turn is followed by Narayanaswamy. In fact, ID_1 for Yao and Wang are remarkably similar as they move parallel at a very short distance, different to Narayanaswamy, which predicts a substantially more dilated ID_1 that tends to diverge from Yao and Wang solutions when enriching the mixture.

Regarding the cool flame period, that is the temporal interval for which global species production freezes between low and high temperature stages, it is almost non-existing for rich mixtures according to Yao scheme. Narayanaswamy shows moderate cool flame periods but it is the Wang mechanism which predicts the most dilated ones. For all the three oxidation schemes, the longest cool flames are found at lean mixtures and this period is reduced when enriching the mixture.

Finally, it is the Yao scheme the one which provides the most reduced ID_2 values for all the mixture fractions. Wang and Narayanaswamy show similar ID_2 for lean and slightly rich mixtures, in agreement with results from figure 4.1 where it was shown that this agreement holds for a wide interval of

temperatures. However, for $Z > 0.06$ Wang ID_2 profile shows a completely different evolution from that predicted by Narayanaswamy with even shorter ID_2 delays than ID_1 Narayanaswamy solutions.

Z_{MR} is found at similar rich mixture fractions for Yao and Narayanaswamy (0.059 and 0.063, respectively) but it is very different for Wang, which provides a richer Z_{MR} (0.077). In addition, it seems that there exists an asymmetry for ID_2 at both sides of Z_{MR} being the slope of the curve (in absolute value) lower for $Z > Z_{MR}$ than for $Z < Z_{MR}$.

Regarding how combustion proceeds, all the three mechanisms predict that the first ignition kernels are found at lean mixtures since their higher initial temperature promotes auto-ignition, as it is revealed by the reduced ID_1 compared with rich mixtures. However, the reduction of the cool flame period when enriching the mixture favours the displacement of ignition to rich mixtures, that is, as seen from figure 4.2, ID_2 is lower for rich mixtures indicating that these are the fastest mixtures to reach the high temperature stage and, therefore, overtake lean mixtures during their auto-ignition [33]. This reason is argued in order to explain the displacement of ignition from lean to rich mixtures observed in experiments and simulations for spray A [11].

These considerations reveal that the position of Z_{MR} at rich mixtures as well as the reduced ID_2 for rich mixtures compared to lean and stoichiometric mixtures have a clear influence on the combustion development and explain where it takes place in terms of mixture richness as we shall see later in detail.

In order to gain more insight in the homogeneous reactors auto-ignition, their chemical source term $\dot{\omega}_{Y_c}^{HR}$ is represented as a function of (Z, c) for the three mechanisms at the nominal spray A boundary condition. Figure 4.3 shows these maps represented in a logarithmic scale to better visualize the different regions. In addition, several level curves for the chemical source term have been added for reference.

All the maps show a region of intense chemical activity at low c values in a wide region of rich mixture fractions which corresponds with the low temperature ignition stage. Advancing in the map in the c direction, a strong reduction of the chemical source term occurs which is caused by the cool flame stage where chemical activity is almost frozen. In terms of c this reduction of chemical activity lasts for a short interval since during the cool flame the increase of temperature and progress variable are marginal. Then, the high temperature stage initiates and the chemical source term increases again with a strength that depends on the mechanism. Nevertheless, all of them predict a region of very intense chemical source terms at high c values (around 0.8) and slight rich mixtures (around 0.05).

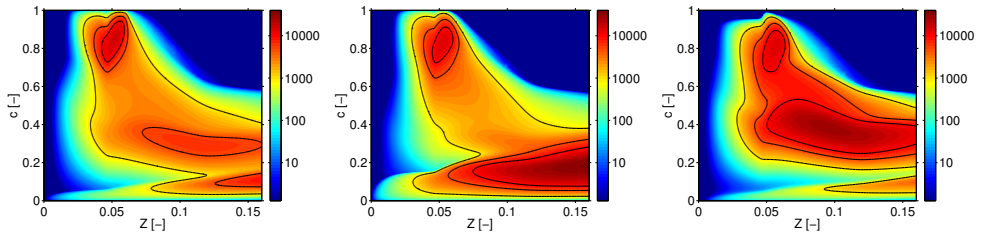

Figure 4.3. *Homogeneous reactors progress variable chemical source terms at nominal condition for Narayanaswamy (left), Yao (centre) and Wang (right) mechanisms. Level curves for values 1000, 5000 and 10000 1/s are represented. Scales common for all figures.*

Although the previous behaviour is similarly described by all the mechanisms, important discrepancies in the morphology of the maps are detected. Yao mechanism predicts a zone of extremely high chemical source terms in the region of low c values in a very wide interval of mixture fractions. Then, the chemical source term drops drastically and only reaches high chemical source terms again for c values around 0.8.

On the contrary, Wang scheme provides a very different picture of combustion. The chemical source terms for low temperature ignition are extremely low compared with Yao solution as well as the source terms during the cool flame. This is corroborated by the analysis of the ignition delays in figure 4.2 where the longest cool flames were observed for Wang. However, Wang shows a region of very intense chemical activity for $c > 0.2$ with two maxima, different to Yao which after the first ignition stage predicted moderate source terms and only high chemical terms were reached for very high c values. Finally, Narayanaswamy scheme predicts an intermediate solution between Yao and Wang solutions.

As will be seen later, the behaviour during the cool flame period is of paramount importance when introducing additional transport effects, such as diffusion. Low chemical activity during this period implies a frozen chemical activity that limits, during the period it lasts, the advancement of combustion to only diffusion transport. This is the case of Wang mechanism. However, if chemical activity is moderate, as it is the case of Yao scheme, the flame may advance, during the cool flame period, not only due to diffusion but to chemistry too. Clearly, this has a strong influence on the mixtures where combustion extends before starting the second ignition, that is, the high temperature stage.

It is worth mentioning that, although combustion is a complex matter due to the very different phenomena that simultaneously occur, notwithstanding, it can be characterized in its general trends with very few variables. Figures 4.2 and 4.3 gather and condensate such variables and give a general picture of how combustion develops for laminar flames as well as turbulent flames as we shall see in the following.

It is also relevant to analyse how species and temperature evolve during combustion and compare them between the different chemical schemes. In order to describe this evolution omitting the temporal dependence, figure 4.4 gathers the profiles for the temperature and mass fractions for several species as a function of the normalized progress variable c during the auto-ignition of several mixture fractions at nominal conditions. The chosen species are formaldehyde (CH_2O), hydrogen peroxide (H_2O_2), carbon monoxide (CO) and carbon dioxide (CO_2). Mass fractions are scaled with fixed factors in order to share all the species the same axis. In addition, the c values reached for the times ID_1 and ID_2 are indicated for reference.

From figure 4.4 it is clear that temperature and some intermediate and final products, such as CO and CO_2, are almost identical for all the mechanisms. However, initial and other intermediate species like CH_2O, which is a tracer of low temperature combustion, and H_2O_2, that delimits the end of the cool flame, are clearly affected by the choice of the mechanism since they show non-negligible discrepancies in their profiles.

The differences for H_2O_2 are related to the cool flame interval which is differently predicted by each of the mechanisms. In line with this, it is worth mentioning that Yao scheme is the one that generates the lowest H_2O_2 concentrations and is the mechanism with the shortest cool flame interval. On the contrary, Wang mechanism, which showed the most dilated cool flames, predicts the highest H_2O_2 accumulation. Narayanaswamy provides intermediate production of H_2O_2 as well as intermediate cool flame periods[4].

As a consequence, it is observed that there exists a strong dependence between the low temperature combustion characteristics and the chosen mechanism due to the large amount of radicals with small mass and the variety of chemical paths that may be found at these low temperatures [20]. Therefore, care must be taken when comparing different mechanisms in terms of global parameters, such as ignition delay, since their agreement does not

[4]However, with this we do not intend to establish a relation of cause and effect between the cool flame period and the maximum accumulated H_2O_2 mass fraction since, to do this, the chemical reaction rates of this species should be analysed too.

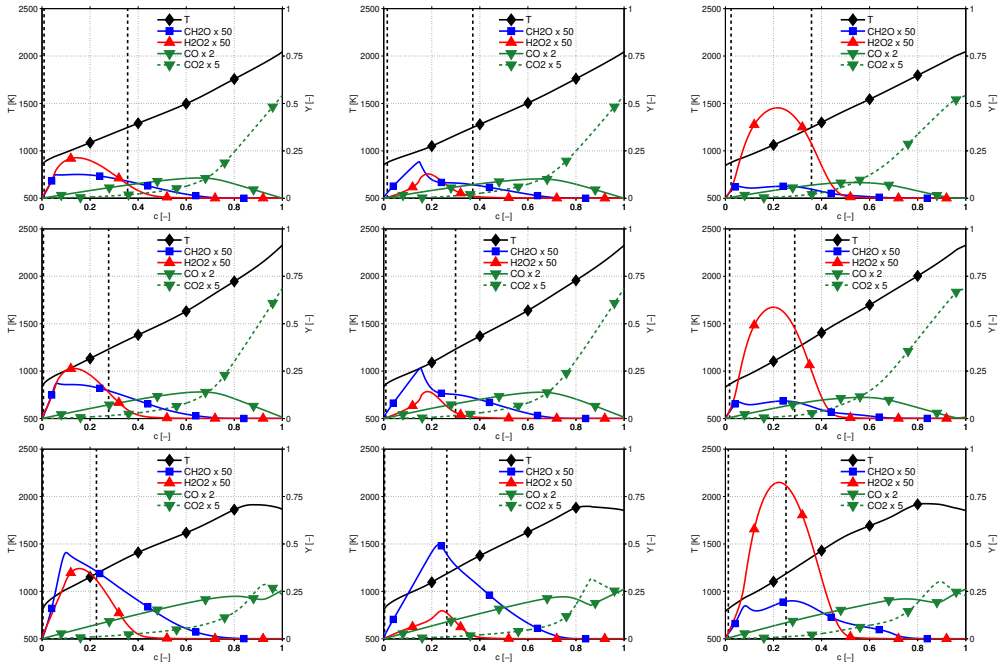

Figure 4.4. *Temperature and species mass fractions evolution as a function of c for Narayanaswamy (left column), Yao (central column), Wang (right column) for Z = 0.035 (first row), 0.046 (second row), 0.08 (third row) at nominal conditions. Vertical lines correspond to the c values for the low and high temperature ignition delays criteria from figure 4.2. Calculations for homogeneous reactor conditions.*

imply similar evolutions for other variables, especially if these are related to the low temperature stage.

Finally, it is meaningful to note that there exists a soft relationship between temperature as well as the most important species and the progress variable. This implies that the chosen progress variable has the ability to trace accurately the auto-ignition process and, hence, it is suitable for the following calculations. In addition, as it shows representative changes in the regions where there exists important heat release it can be used or, if preferred, its source term, to trace the different combustion stages in the turbulent reacting spray.

4.4.2 Flamelet results

Once homogeneous reactors auto-ignition has been described, it is natural to follow this study with the analysis of the flamelets. In laminar flames chemistry coexists and interacts with transport processes, like diffusion, whose intensity is determined by the strain rate. In addition, the description of the turbulent flame as an ensemble of laminar flames (flamelet concept) makes almost prescriptive to devote some attention to flamelet combustion.

As described in chapter 3, flamelets are calculated according to the ADF approach, which was shown to reproduce correctly the combustion development in laminar flames, and, hence, solutions provided by this approximation are analysed in the following.

The structure of combustion during transient ignition is represented in figure 4.5 in the $Z-T$ map for strain rates 10, 100 and 1000 1/s, which cover the auto-ignition range, for the three mechanisms at nominal conditions. The represented profiles correspond to c_2 values of 0.05 and 0.15 for strain rates 10 and 100 1/s while 0.1 and 0.3 were chosen for $a = 1000$ 1/s. From the profiles obtained for Y_c, the temperature profiles were interpolated from the relationship $T = T(Z, Y_c)$ given by the homogeneous reactors calculations. In the same way as the analysis carried out in section 3.3.2, the discussion is focused on the propagation of combustion across the flame.

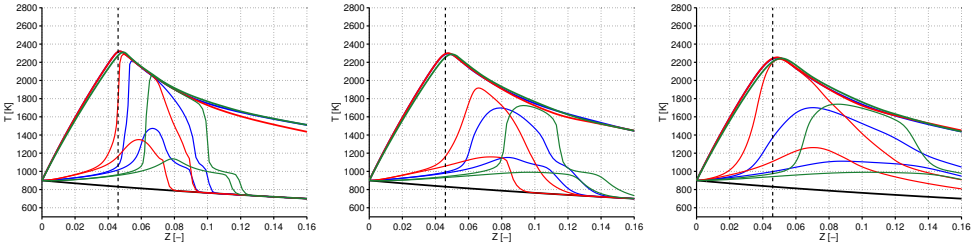

Figure 4.5. *Z - T flamelet profiles for Narayanaswamy (blue), Yao (red) and Wang (green) mechanisms at nominal conditions. The figures correspond to strain rates 10 1/s (left), 100 1/s (centre) and 1000 1/s (right). Black dashed line indicates stoichiometric mixture fraction.*

According to figure 4.5, all mechanisms predict the start of combustion at lean mixtures during the first stage of combustion followed by a subsequent displacement to rich mixtures. This fact was revealed with the analysis of the ignition delay in figure 4.2 where it is observed that the lowest ID_1 values are found at lean mixtures owing to their higher initial temperature [11, 17].

However, lean mixtures show a very dilated cool flame period and, during this period, rich mixtures have time to reach the first ignition stage and even burn in the high temperature stage since the cool flame tends to disappear when enriching the mixture.

The initiation of the second ignition stage occurs close to Z_{MR} [34] and this second stage leads to the steady solution. It is a very fast ignition that generates strong gradients in the mixture fraction space between mixtures that have reached steady conditions and mixture fractions that still remain in their first ignition or cool flame. Clearly, the strength of this gradient depends on the strain rate. For low strain rates very high gradients are observed in a small region where the jump between mixtures at very different states is produced. However, gradients intensity is mitigated but spreads on a wider region for higher strain rates. This gradient provokes an imbalance of species and enthalpy and, as consequence, a diffusion flux that tends to propagate the ignition to other mixtures.

Comparing the different mechanisms, very distinct combustion structures are predicted by each of them whose differences are due to the Z_{MR} value as well as the cool flame latency period. For Yao scheme, Z_{MR} appears in the slightly rich mixtures ($Z_{MR} \simeq 0.06$) and shows an almost non-existing cool flame for $Z > Z_{MR}$. The second ignition is an intense and fast combustion centred at slightly rich mixtures that generates strong gradients that favour the ignition of the surrounding mixtures due to temperature and species diffusion. As moderate chemical source terms are observed during the cool flame (see figure 4.3), the slope of the Z - T profiles is decreased (in absolute value) since combustion develops and advances due to both chemical and diffusion effects.

On the contrary, for Wang mechanism, Z_{MR} is found at richer mixtures and this, together with the fact that it predicts a very long cool flame period, allows that a wide range of rich mixtures have time to reach the cool flame period prior to the second ignition in the surroundings of Z_{MR}. As very low chemical source terms are found during the cool flame interval (see figure 4.3), diffusion is the basic mechanism to propagate combustion and very sharp instantaneous profiles are generated in the Z - T map between the reacting mixtures (during their second ignition stage) and their surroundings[5]. This behaviour contrasts with that found for Yao mechanism. Finally, again Narayanaswamy predicts an intermediate behaviour between those given by Yao and Wang.

[5]This means that when the second ignition is initiated for any mixture Z^*, the mixtures found at one side of Z^* are still during the cool flame period and show very reduced chemical source terms. Z^* advances very fast during second ignition while the other mixtures remain at an intermediate state. In this case, the only propagation mechanism is diffusion and sharp gradients are generated between Z^* and its surroundings.

Therefore, the behaviour during the cool flame period in terms of chemical reactivity determines the sharpness of the slope of the Z - T profiles and the region of mixtures where first ignition extends before the main ignition.

Regarding the strain rate, it is clearly observed that its increase smooths the profiles due to the reduction of the velocity of advancement of the most reactive mixtures during the second ignition stage. This is because the increase of strain rate promotes the transport of part of their enthalpy and species production to the surrounding mixture fractions which in turn accelerate their ignition as was explained in section 3.3.2. This allows that wider mixture fraction intervals reach the cool flame period prior to the most reactive mixture fractions attain the second ignition stage, leading to soft Z - T profiles which extend until very rich mixtures.

Figures 4.6 and 4.7 represent similar profiles than those shown for the nominal case in figure 4.5 but for the cases T_{amb} = 800 K and X_{O_2} = 0.15 and T_{amb} = 900 K and X_{O_2} = 0.21, respectively. In this way, the effect of the boundary conditions on the flame structure is assessed. Same values for c_2 and a than those used in figure 4.5 are used in these figures.

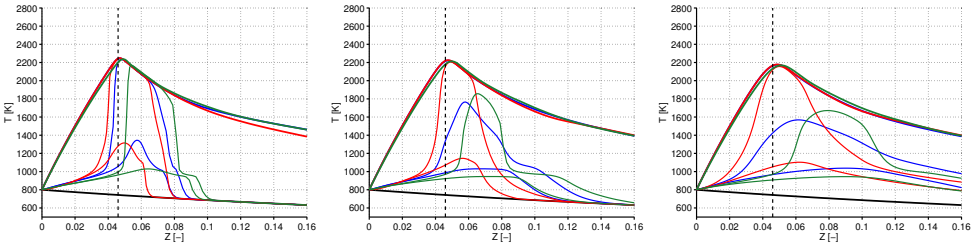

Figure 4.6. *Z - T profiles for Narayanaswamy (blue), Yao (red) and Wang (green) mechanisms at T_{amb} = 800 K and X_{O_2} = 0.15. The figures correspond to strain rates 10 1/s (left), 100 1/s (centre) and 1000 1/s (right). Black dashed line indicates stoichiometric mixture fraction.*

Regarding how combustion develops during the different ignition stages and the shape of Z - T profiles between the chemical mechanisms and the effect of the strain rate, similar conclusions to those established for the nominal case are valid for the different boundary conditions.

On the one hand, comparing figures 4.5 and 4.6, it arises that decreasing ambient temperature displaces combustion to leaner mixtures implying a loss of reactivity of rich mixtures. Consequently, Z - T profiles become sharper when reducing the ambient temperature.

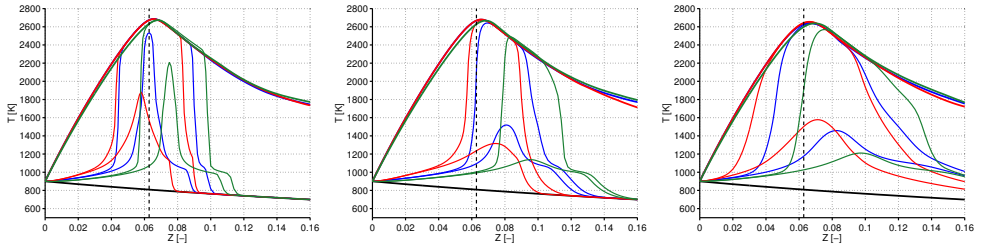

Figure 4.7. *Z - T profiles for Narayanaswamy (blue), Yao (red) and Wang (green) mechanisms at T_{amb} = 900 K and X_{O_2} = 0.21. The figures correspond to strain rates 10 1/s (left), 100 1/s (centre) and 1000 1/s (right). Black dashed line indicates stoichiometric mixture fraction.*

On the other hand, the increase of oxygen concentration provokes that the most reactive mixtures show faster progressions producing extremely fast second ignition stages that in turn sharpen Z - T profiles. Moreover, the increased reactivity of the mixture extends the maximum level of diffusion or strain rate supported by the flamelet before entering in the reignition-extinction range. Finally, say that, according to figures 4.5 and 4.7, Z_{MR} does not depend on the oxygen concentration.

All the results shown until this point make patent the extreme importance of the low temperature ignition stage and subsequent cool flame period in order to determine how and where flame ignition occurs. In addition, different to the high temperature ignition, this first stage shows a strong dependence on the choice of the mechanism due to the complex low temperature chemistry that complicates its modelling.

4.4.3 Turbulent diesel-like flame

In this section, turbulent spray combustion is described in terms of flame metrics, auto-ignition and quasi-steady regime structure in the light of the influence of the boundary conditions and the chemical mechanism. Analysis in previous paragraphs has provided the grounds for the explanation of the behaviour of the turbulent diesel-like flame.

However, and prior to this analysis, it is necessary to configure the CFD model constants in order to achieve accurate results, as described in next section. Then, a global analysis of the flame is carried out exploring ignition delay and lift-off length trends. After this validation the auto-ignition and

quasi-steady flame structure are investigated in order to deepen in the diesel flames knowledge.

4.4.3.1 Set-up of the model

The set-up of the model is carried out for inert conditions for which there exists abundant experimental data, such as vapour penetration, liquid length and some spatial fields, in order to adjust the spray behaviour, with special attention to the fields that describe the state of the mixture. This model configuration is based on the work developed by Desantes et al. [26] and has been used in different analysis developed by the author of this work [18, 20].

First, the spray is described in terms of vapour penetration and liquid length comparing experimental data [8] and simulations. Vapour penetration is defined as the maximum distance to the nozzle where mixture fraction equals 0.001 while liquid length is the distance to the nozzle where 95% of the liquid fuel is enclosed [1]. Results are gathered in figure 4.8 at inert nominal conditions.

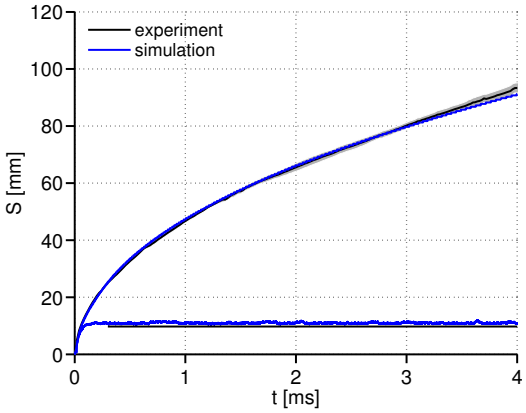

Figure 4.8. *Vapour penetration and liquid length at the inert nominal condition for the experiment (black) and the simulation (blue). For experiments, uncertainty of measurements is delimited with shadows.*

It is shown that the current configuration, described in section 4.3, provides an excellent agreement in terms of vapour penetration for which experimental and simulated curves are overlapped. In addition, liquid length is well-captured, as the proximity between both values show.

In order to proceed with a more detailed comparison, average and root mean square (rms) mixture fraction fields, that is, $\widetilde{Z}$ and Z_{rms}, as well as axial velocity ($\widetilde{u}$) are shown in figure 4.9 for the experiment and the simulation. Experimental data is extracted from [6, 10, 35, 36]. As different nozzles have been used when measuring, nozzle diameter is normalized with the equivalent diameter defined as $d_{eq} = d_0\sqrt{\rho_f/\rho_a}$ where d_0 is the nozzle diameter and ρ_f and ρ_a are fuel and air densities, respectively. Radial cuts at 50 and 90 d_{eq} correspond to axial distances of 25 and 45 mm, approximately.

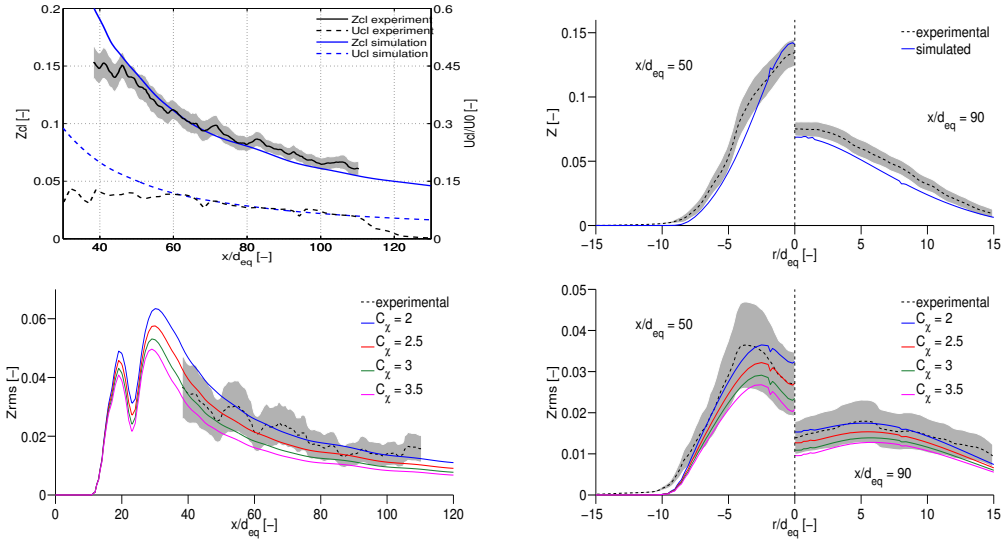

Figure 4.9. *Comparison between simulated and experimental mixture formation results at very advanced instants for inert nominal condition. Top left: $\widetilde{Z}$ and normalized $\widetilde{u}$ on the centerline. Top right: $\widetilde{Z}$ radial profiles at 50 and 90 d_{eq}. Bottom left: Z_{rms} on the centerline. Bottom right: Z_{rms} radial profiles at 50 and 90 d_{eq}. Experimental uncertainties are shown with shadowed regions and simulated profiles with different C_χ values are included in rms plots.*

Figure 4.9 shows that there exists an excellent agreement between averaged mixture fraction and velocity fields on the axis as well as on the radial cuts. In addition, bottom figures demonstrate that an excellent agreement may be obtained for the mixture fraction rms if constant C_χ, which relates $\widetilde{Z''^2}$ and its dissipation $\widetilde{\chi}$, is chosen properly (see equation 3.59). For current calculations,

a value of $C_\chi = 2$ has been taken as the value that best fits experimental profiles as also suggested in the literature [37, 38]. This value is applied for subsequent reactive computations.

The excellent results obtained so far encourage a comparison of the simulated reactive spray against experimental results. Unfortunately, there exist very few experimental information in reactive conditions so the comparison is quite limited.

Figure 4.10 shows tip penetration and liquid length for the reactive nominal spray for the experiment [8] and the simulation. Both parameters share the same definitions than those given in inert conditions for vapour penetration and liquid length.

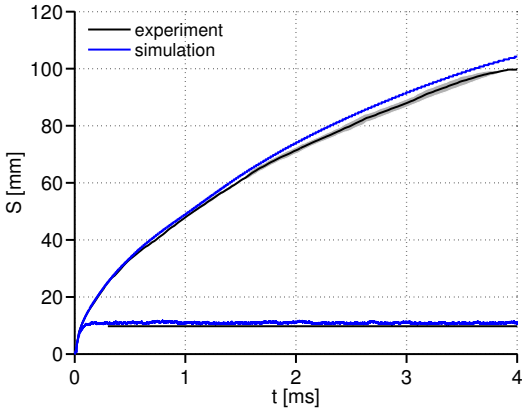

Figure 4.10. *Tip penetration and liquid length for the reactive case for the experiment (black) and the simulation (blue). For experiments, uncertainty of measurements is delimited with shadows.*

Although there exists a slight deviation of the tip penetration between the experiment and the simulation due to the flow thermal expansion that provokes an over-prediction of the tip penetration by the simulation, it is considered that a very good agreement between both is also achieved. Regarding the liquid length, the same values are reached for inert and reactive conditions because of the spatial split between liquid evaporation and combustion regions for spray A.

Moreover, figure 4.11, which shows the axial velocity on the axis at the reactive nominal condition for the experiment and the simulation, reveals the good agreement between both profiles in the interval $[50, 90]d_{eq}$ where measurements are reliable [10].

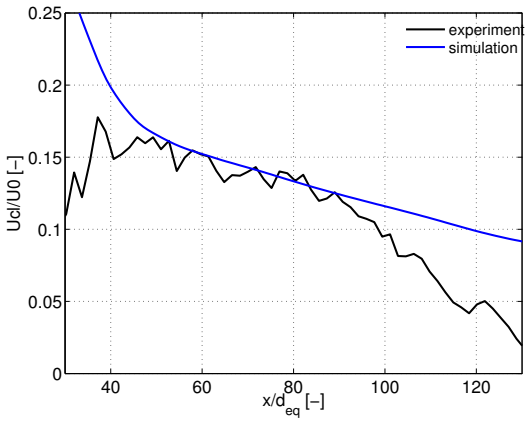

Figure 4.11. *Normalized axial velocity on the axis for the reactive nominal case.*

In addition, a drastic change in the slope of the simulated velocity profile at $45d_{eq}$, which corresponds to 22.5 mm, approximately, is observed. This acceleration of the flow compared to inert conditions is due to the reduction of density as a consequence of the temperature increase owing to the heat release caused by combustion. As will be seen later, this distance is a little downstream of the lift-off length position since the point at the base of the flame that provides the lift-off length measurement is radially displaced and, hence, the contour of the flame is shaped like a W.

4.4.3.2 Flame metrics

Once it has been demonstrated that the current set-up provides reasonable results in terms of liquid and spray tip penetration as well as local fields we are in position to continue the validation by the analysis of the flame metrics.

On the one hand, as diesel flames auto-ignite spontaneously due to the high pressure and temperature found in the combustion chamber it is natural to characterize the flame by its ignition delay, ID. On the other hand, due to the high injection velocities, diesel flames are lifted. The axial distance from the nozzle to the point where the diesel flame stabilizes is known as the lift-off length, LOL.

Both ignition delay and lift-off length are representative values that characterize the diesel flame and, in this text, are referred to as flame metrics.

Clearly, these parameters are of paramount importance since they summarize two of the most important characteristics of the flame.

According to the ECN, ignition delay and lift-off length are defined experimentally by means of OH* (OH in its excited state) chemiluminescence. Ignition delay corresponds to the time spent until reaching 50% of the high-temperature chemiluminescence level while lift-off length is the minimum axial location where 50% of the leveling-off value of OH* chemiluminescence is observed [1].

Although some mechanisms include OH*, in general, it is not contained in the oxidation schemes. For this reason and for modelling purposes, different criteria are found in the literature in order to compute ignition delay and lift-off length.

In the frame of the ECN, ignition delay is defined as the time spent from start of injection (SOI) until the maximum rise of maximum Favre-averaged temperature ($\widetilde{T}_{max}$) occurs. However, in this work it has been found that this definition provides ignition delays for which $\widetilde{T}_{max}$ is close to 2000 K, that is, the end of auto-ignition. This is especially critical for low reactive cases where spray ignition is slow and may take several hundreds microseconds. In addition, a definition based on a temporal derivative may be subjected to small numerical perturbations that may distort the value. For this reason, in this work, ignition delay is defined as the time spent from SOI to the instant in which $\widetilde{T}_{max}$ reaches the ambient temperature plus 400 K [24]. An increment of 400 K is too high to measure a cool flame and too low be related to the last stages of ignition.

Regarding lift-off length, several definitions are found based on OH or temperature fields [1, 39]. In this work, ECN criterion, which defines lift-off length as the minimum axial distance from the nozzle to the level curve/surface of the 14% of the maximum $\widetilde{Y_{\mathrm{OH}}}$ value of the domain ($\mathrm{LOL}_{14\%\mathrm{OH}}$), is adopted [1]. Other definitions in the literature are based on the same criterion but changing 14% by 2% ($\mathrm{LOL}_{2\%\mathrm{OH}}$) while other one computes this distance based on the ambient temperature plus 400 K (LOL_{400K}) [6].

In one of the author's works [18], the three definitions were investigated and it was found that the relationship $\mathrm{LOL}_{2\%\mathrm{OH}} < \mathrm{LOL}_{14\%\mathrm{OH}} < \mathrm{LOL}_{400K}$ is preserved for all the spray A boundary conditions. The criterion based on $14\%Y_{\mathrm{OH}}$ is the one that best fitted experimental results since the other criteria are related to too low or too high temperatures to define this distance.

[6] In the following and if not otherwise stated, we will refer always to the lift-off length defined by 14% of the maximum $\widetilde{Y_{\mathrm{OH}}}$ value in the domain and will omit subscripts.

Figures 4.12, 4.13 and 4.14 show ignition delay and lift-off length results for the different parametric studies with the three simulated mechanisms and the experimental measurements, which belong to CMT - Motores Térmicos database [7].

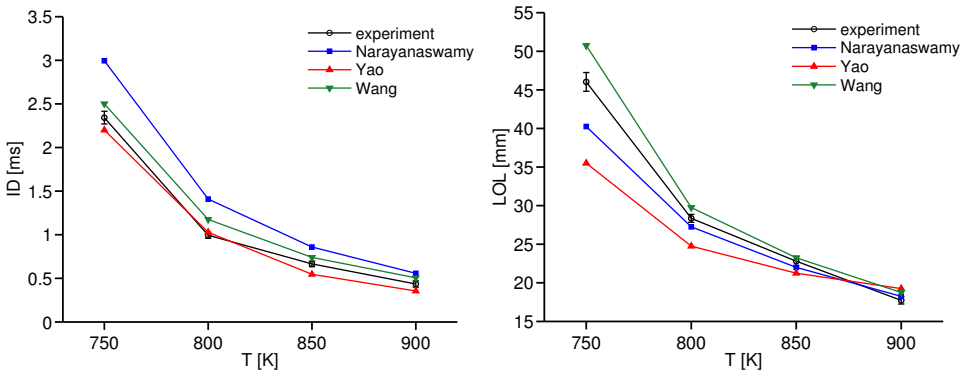

Figure 4.12. *Ignition delay (left) and lift-off length (right) for the parametric temperature variation with* $X_{O_2} = 0.15$. *In both figures error bars indicate experimental uncertainty.*

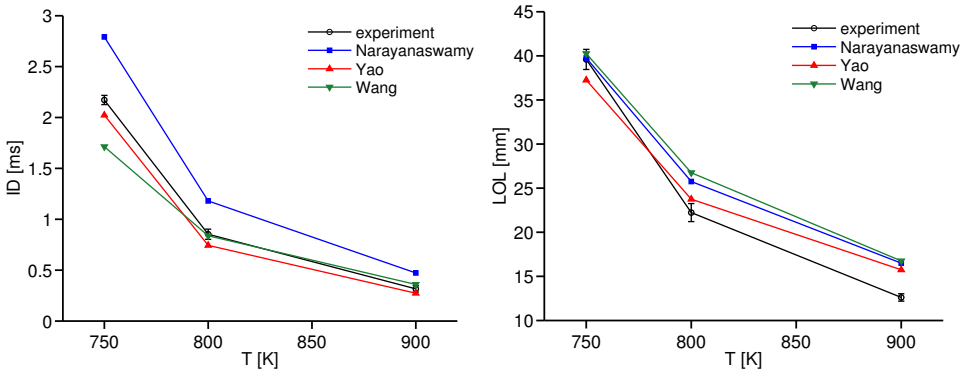

Figure 4.13. *Ignition delay (left) and lift-off length (right) for the parametric temperature variation with* $X_{O_2} = 0.21$. *In both figures error bars indicate experimental uncertainty.*

From figures 4.12, 4.13 and 4.14 it is observed that, in general, there exists a very good agreement between simulated and experimental results for both

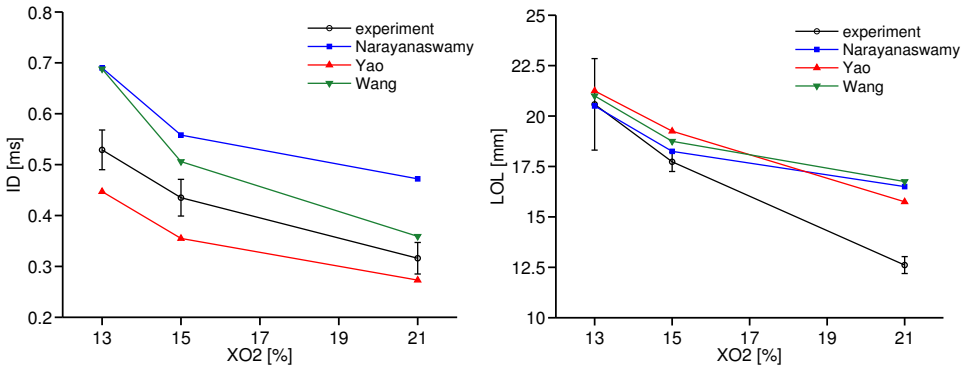

Figure 4.14. *Ignition delay (left) and lift-off length (right) for the parametric oxygen variation with $T_{amb} = 900$ K. In both figures error bars indicate experimental uncertainty.*

ignition delay and lift-off length, although this agreement depends on the direction of the parametric sweep.

In general, Narayanaswamy mechanism provides the longest ignition delays (compared to experiments and other schemes) followed by Wang scheme which in turn is slower than Yao, which predicts the shortest ignition delays. This ordering was already observed in homogeneous reactor results in figures 4.1 and 4.2 and, as seen, it is preserved at all the stages of combustion.

Notwithstanding, this ordering is not observed in lift-off length figures, where it arises that Narayanaswamy predicts intermediate lift-off length values compared to other mechanisms. Consequently, it cannot be deduced that shorter ignition delays imply shorter lift-off lengths in the context of chemical mechanisms comparisons. This is caused by different factors that may be summarized in the distinct thermochemical paths described by each scheme.

In the case of the oxygen variation there exists a lack of sensitivity when changing from $X_{O_2} = 0.15$ to 0.21 in terms of lift-off length. In addition, this fact is similarly reproduced by all the three schemes. A possible reason to explain such lack of sensitivity could be some kind of interaction between the liquid evaporation and combustion zones, which are separated by a short distance in the $X_{O_2} = 0.21$ case, since no chemical source terms are allowed in the region where liquid is found and no source term due to evaporation is included in the mixture fraction variance transport equation which could affect such field downstream. However, more work is needed in order to elucidate the causes of this behaviour.

As a final remark, figure 4.15 shows the cloud of points defined by the pair (ID, LOL) for experimental and simulated results for the whole set of parametric variations. It is patent that a reduction of ignition delay by the increase of reactivity in any direction (ambient temperature or oxygen concentration) shortens lift-off length [40] in agreement with experimental results [41]. This suggests that spray ignition together with the flame base location are affected by chemical kinetics and show some kind of relationship. More precisely, this seems an argument in favour of auto-ignition as one of the flame stabilization mechanism in diesel sprays [12, 19, 41] which can be modulated by additional mechanisms such as flame propagation [14]. Notwithstanding, this argument is not completely conclusive in order to establish such implication and requires further investigation.

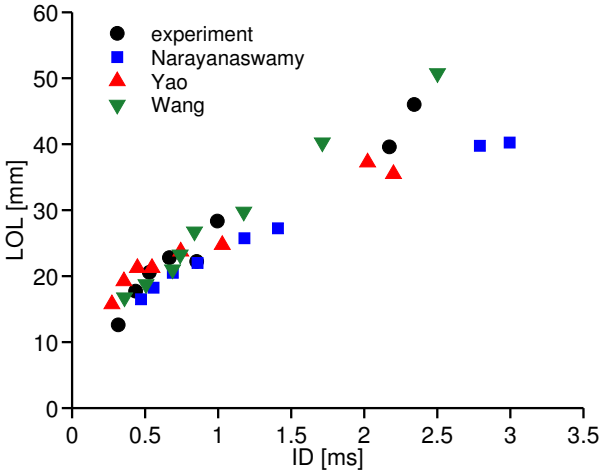

Figure 4.15. *Cloud of points defined by the pair (ID, LOL) for experiments and simulations for the whole set of boundary conditions.*

4.4.3.3 Spray auto-ignition

In this section spray auto-ignition is described in terms of different relevant variables that characterize the reacting spray. Again the influence of the chemical mechanism and the boundary conditions are widely studied as a way to elucidate their impact.

First, temperature fields for different instants during spray auto-ignition are gathered in figure 4.16 for the nominal case solved with Narayanaswamy

mechanism. Fields have been saturated and scale modified in each of the figures in order to better visualize the region where combustion is taking place.

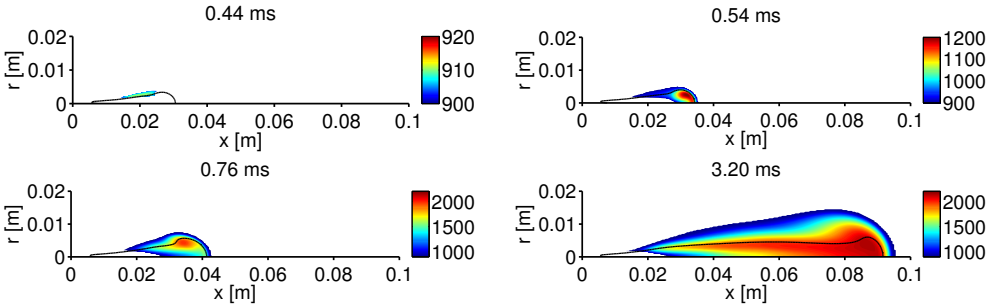

Figure 4.16. *Temperature spatial fields for different instants. Black solid line corresponds to stoichiometric mixture fraction level curve. Results for nominal case with Narayanaswamy mechanism.*

It is observed that ignition starts at the periphery of the spray in the region of slightly lean mixtures during the first steps of combustion (top left) due to their higher initial temperatures that allows a faster low temperature ignition for these mixtures [9, 33]. This was observed in figures 4.2 and 4.5 too. However, the region of highest temperatures is rapidly displaced to rich mixtures whose ignition is probably promoted by the emergent lean mixture reaction kernels due to the intense mixing induced by the turbulent flow [11, 15]. There exist experimental evidences [9] as well as simulations in the frame of LES [14] that confirm this behaviour.

Ignition develops in the rich mixtures and occurs rapidly since the maximum temperature increases from 1200 K to more than 2000 K in barely 200 μs. When advancing in time the point with maximum temperature is found closer to the stoichiometric mixture.

More insight is gained when representing variables $\widetilde{Z''^2}$ and $\widetilde{\chi}$ and their normalized values, S and $\widetilde{\chi_{st}}$, versus time for the point with the highest temperature in the domain, as is shown in figure 4.17 for the nominal case calculated with Narayanaswamy mechanism.

It is observed that after spray auto-ignition, the point of maximum temperature tends to be displaced rapidly to regions of low mixture fraction variance and scalar dissipation rate. In terms of the segregation factor S, which represents a normalized mixture fraction variance, the maximum

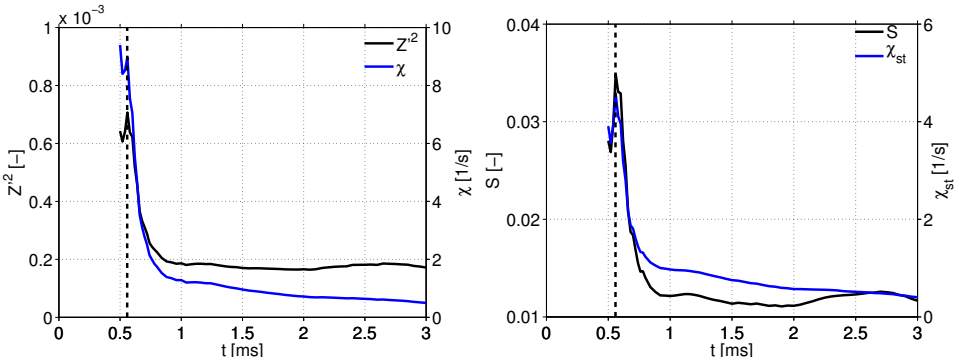

Figure 4.17. *Temporal evolution of $\widetilde{Z''^2}$ and $\widetilde{\chi}$ (left) and S and $\widetilde{\chi}_{st}$ (right) for the point with the highest temperature in the domain. Vertical black dashed line indicates spray ignition delay. Results for the nominal case with Narayanaswamy mechanism.*

value does not reach 0.04 while the stoichiometric scalar dissipation rate is bounded by 5 1/s. Considering that flamelet auto-ignition range extends until a stoichiometric scalar dissipation rate of 106 1/s, this implies that the first ignition kernels are observed at very low values for these variables [15, 34]. Finally, as time advances the point with maximum temperature moves downstream and stabilizes in regions of lower mixture fraction variance and scalar dissipation rate.

Similar figures are represented for the case of $T_{amb} = 800$ K and $X_{O_2} = 0.15$ in figure 4.18 and for the case of $T_{amb} = 900$ K and $X_{O_2} = 0.21$ in figure 4.19.

Figures 4.18 and 4.19 demonstrate how variations in mixture reactivity displace first ignition kernels to regions of different mixture fraction variance and scalar dissipation rate in order to adapt fuel oxidation tendency to flow dynamics. Ignition kernels are observed at higher values of $\widetilde{Z''^2}$ and $\widetilde{\chi}$ as well as S and $\widetilde{\chi}_{st}$ when increasing mixture reactivity.

This section is closed showing the temporal mass evolution for relevant species and heat release integrated in the whole domain for the different chemical mechanisms and several boundary conditions. Figure 4.20 shows this representation for the three chemical schemes for nominal conditions. The chosen species are CH_2O, as a low temperature combustion tracer, CO and CO_2, as intermediate and final species, and, finally, C_2H_2 as a soot precursor[7]. The profiles are multiplied by a fixed factor in order to share the same scale.

[7] As soot is not modelled in these simulations, C_2H_2, that it is a soot precursor, will be used instead in the following to discuss some experimental trends observed for soot.

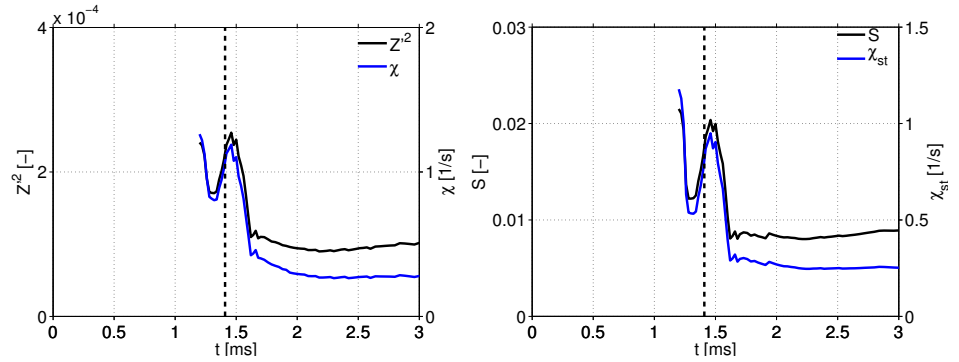

Figure 4.18. *Temporal evolution of* $\widetilde{Z''^2}$ *and* $\widetilde{\chi}$ *(left) and* S *and* $\widetilde{\chi}_{st}$ *(right) for the point with the highest temperature in the domain. Vertical black dashed line indicates spray ignition delay. Results for the* $T_{amb} = 800\ K$ *and* $X_{O_2} = 0.15$ *case with Narayanaswamy mechanism.*

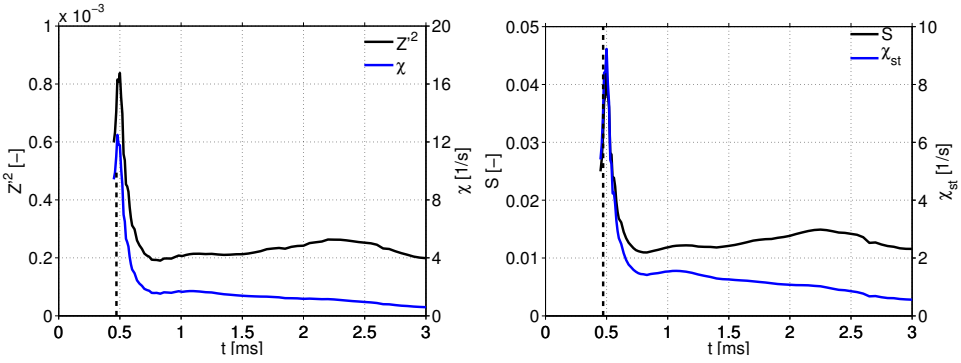

Figure 4.19. *Temporal evolution of* $\widetilde{Z''^2}$ *and* $\widetilde{\chi}$ *(left) and* S *and* $\widetilde{\chi}_{st}$ *(right) for the point with the highest temperature in the domain. Vertical black dashed line indicates spray ignition delay. Results for the* $T_{amb} = 900\ K$ *and* $X_{O_2} = 0.21$ *case with Narayanaswamy mechanism.*

Due to the extremely short ignition delay calculated with Yao mechanism, it is observed a weak premixed flame (premixed-burn period) compared with the other mechanisms. For the other schemes the more dilated ignition delays lead to a higher fuel injected mass and, consequently, higher heat release during premixed-burn phase, especially for Wang.

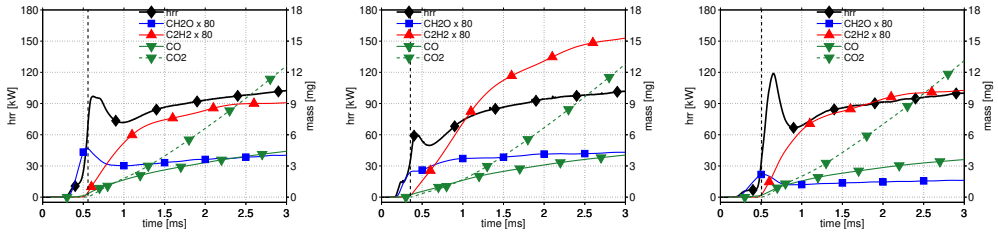

Figure 4.20. *Integrated mass for different species and heat release temporal evolutions for the nominal case with Narayanaswamy (left), Yao (center) and Wang (right). Vertical dashed line corresponds to the ignition delay for each mechanism.*

Regarding CH_2O as it is a species produced during the first stages of combustion, it is detected from the beginning of combustion and is positioned close to the nozzle. As a consequence, it stabilizes after the premixed-burn phase finishes. Different to CH_2O, CO and CO_2 are mostly produced at more advanced stages of combustion during the diffusion combustion phase and are spatially found in the vicinity of the diffusion flame. Hence, their appearance is postponed and CO stabilization has not been reached at 3 ms. Regarding C_2H_2, it is revealed that it can be strongly affected by the chemical mechanism as the discrepancies between Yao and the other mechanisms make patent.

Figure 4.20 clearly shows that initial and intermediate species evolution, such as C_2H_2, are strongly affected by the chemical oxidation scheme as well as the premixed-burn period. These species are temporally produced during the premixed-burn phase and are spatially found in the vicinity of the partially premixed combustion zone. However, for other species that appear at more advanced stages of combustion, such as CO and CO_2, the chemical mechanism choice has almost no effect on their prediction. These species are related to the temporal diffusion phase and are spatially found in the vicinity of the diffusion flame. This is completely in agreement with conclusions extracted from figure 4.4.

Similar profiles are shown in figures 4.21 and 4.22 where the boundary conditions effects are analysed. For the sake of brevity only results for Narayanaswamy are gathered in these figures.

Regarding heat release, figure 4.21 shows that the reduction of temperature induces a more intense premixed combustion as a consequence of the longer ignition delays that allow greater injected fuel mass prior to this event. On

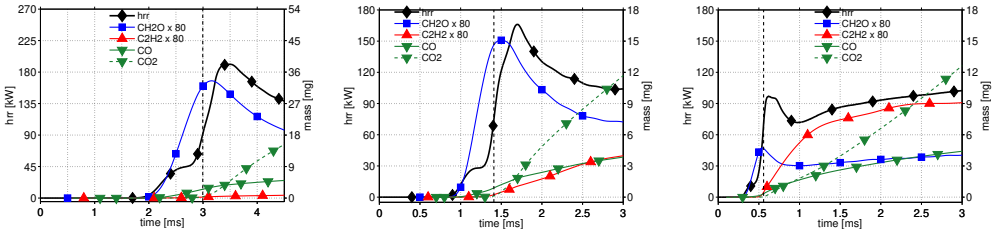

Figure 4.21. *Integrated mass for different species and heat release temporal evolutions. Temperature sweep: T_{amb} = 750 (left), 800 (centre) and 900 (right) K with X_{O_2} = 0.15. Vertical dashed line corresponds to the ignition delay for each condition. Scales are common for all the figures except for the 750 K case. Calculations performed with Narayanaswamy mechanism.*

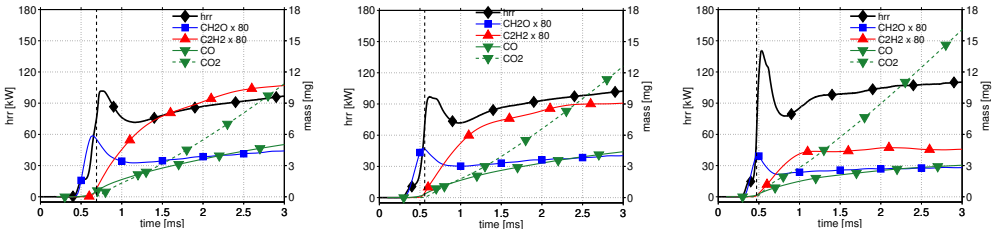

Figure 4.22. *Integrated mass for different species and heat release temporal evolutions. Oxygen sweep: X_{O_2} = 0.13 (left), 0.15 (centre) and 0.21 (right) with T_{amb} = 900 K. Vertical dashed line corresponds to the ignition delay for each condition. Calculations performed with Narayanaswamy mechanism.*

the contrary, increasing oxygen concentration (figure 4.22) derives in a more violent premixed phase despite shortening the ignition delay and, hence, reducing the injected fuel mass at the moment of ignition. This has been observed experimentally [42] and the explanation is found in the larger oxygen mass entrained in the spray as a consequence of the higher oxygen concentration in spite of the reduction of the ignition delay.

Regarding C_2H_2, it is observed that reducing the ambient temperature decreases its total production being almost negligible for the 750 K case (figure 4.21) and suggesting that this case is a non-sooting flame. This is in agreement with experimental results where no soot precursors are detected for such low

temperatures [3]. This behaviour is explained by the displacement of the combustion region to leaner mixtures where no soot is formed owing to the high lift-off lengths as a consequence of the very dilated ignition delays [42].

Nevertheless, the oxygen parametric sweep shows that the increase of oxygen in air produces less C_2H_2 mass and, in consequence, lower soot formation is expected. This behaviour corresponds to the well-known trade-off between EGR and soot in diesel sprays explained in section 2.5.4.

In order to gain more insight in this aspect, figure 4.23 shows $Y_{C_2H_2}$ on the axis for the oxygen variation for advanced instants and Narayanaswamy mechanism. It is observed that increasing the oxygen concentration increases the peak value and moves this peak upstream as well as the point where acetylene is started to be produced in agreement with experimental measured soot mass profiles [43]. In addition, augmenting X_{O_2} increases the formation and consumption rates of $Y_{C_2H_2}$.

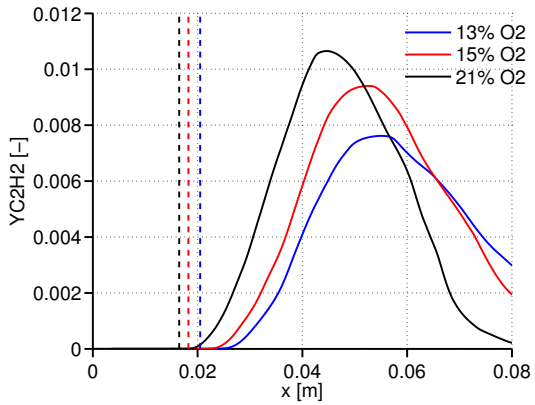

Figure 4.23. C_2H_2 *mass fraction on the axis for the oxygen parametric variation. Dashed line indicates simulated lift-off length position for each case. Results for very advanced instants and Narayanaswamy mechanism.*

However, although the peak $Y_{C_2H_2}$ value increases when augmenting X_{O_2} a reduction of the total C_2H_2 mass is observed as shown in figure 4.22. To explain this, figure 4.24 shows C_2H_2 mass fraction field for the three cases of the oxygen sweep for advanced instants and Naryanaswamy mechanism.

Although an increase of C_2H_2 mass fraction peak is observed when augmenting oxygen concentration, the narrowing in radial and axial directions where non-negligible amounts of $Y_{C_2H_2}$ are found leads to a global reduction of the total mass found in the domain. This manifests the relevance of

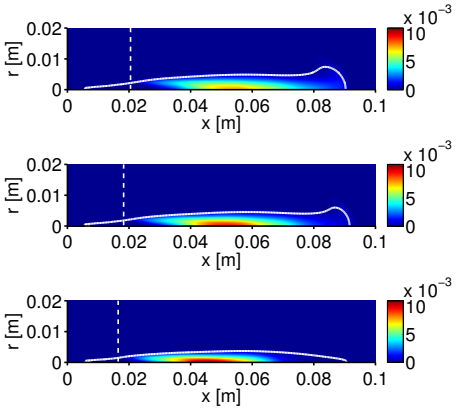

Figure 4.24. *$Y_{C_2H_2}$ spatial fields for the oxygen concentration sweep with $X_{O_2} = 0.13$ (top), 0.15 (center) and 0.21 (bottom). White solid line corresponds to stoichiometric mixture fraction level curve and white dashed line indicates simulated lift-off length position for each case. Results for very advanced instants and Narayanaswamy mechanism.*

the spatial region where species are produced since, when accounting for cylindrical symmetry, the contribution of species found very close to the axis may lead to marginal increments. In a similar way, the region of CH_2O is narrowed when augmenting oxygen concentration producing lower integrated mass in the domain.

Finally, it is observed from figure 4.22 that augmenting oxygen concentration accelerates the initial CO_2 rate production due to the increase of reaction rates with X_{O_2}. The higher rate of CO_2 mass production at times around 3 ms is caused by transient phenomena since the flame length has not stabilized yet for all the cases.

As a final comment, as expected, heat release stabilizes around the same value independently of the oxygen concentration or the ambient temperature since the injection mass rate is the same in all the cases.

4.4.3.4 Flame structure during quasi-steady regime

In the previous section, spray was analysed during its transient evolution, that is, during its auto-ignition. In this section, the flame is described after reaching the quasi-steady regime, that is, for advanced instants where it shows

a steady statistical behaviour in an extensive region. The internal structure of the flame is analysed comparing between the different chemical mechanisms and assessing the effect of the boundary conditions. As the structure of the flame is described from different points of view, the section is divided in different paragraphs.

Spatial fields

As a preliminary step and as part of the spray validation, formaldehyde and hydroxide fields are compared with experimental data [10] in figure 4.25. Modelling results correspond to Narayanaswamy mechanism.

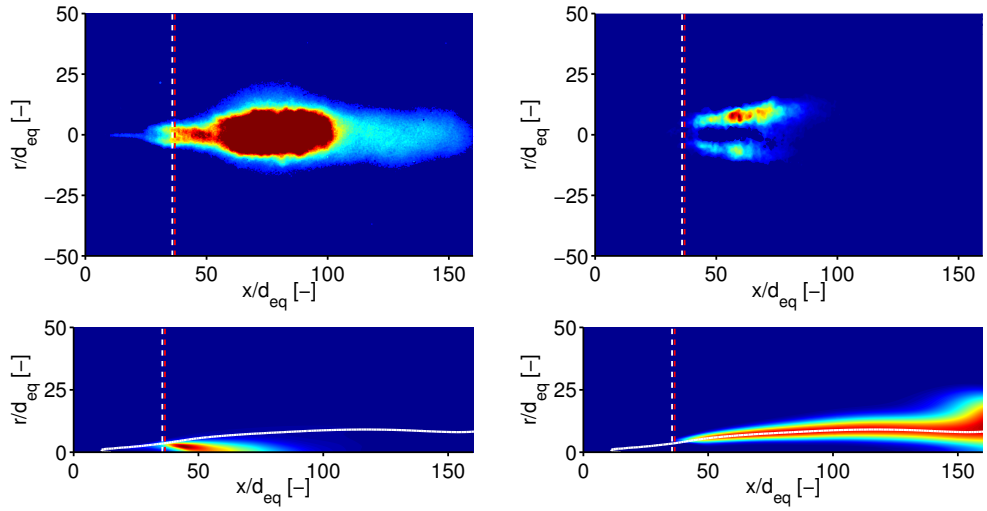

Figure 4.25. *Comparison of CH_2O and OH fields for nominal case. First row corresponds to experimental results while second row is for simulations. Left column shows 355 nm LIF signal from the experiment and CH_2O field for the simulation while right column is derived from OH LIF signal from the experiment and shows OH field for the simulation. Lift-off length values for experiment (white dashed) and simulation (red dashed) are shown and the stoichiometric level curve is included for the modelled results which are calculated with Narayanaswamy mechanism.*

Experimental data were measured with Laser Induced Fluorescence (LIF) and is averaged in time for advanced instants where the spray is developed [10]. Again, as the nozzle diameter is different in the experiment than in the simulation, results are normalized with the equivalent diameter. In

the experiment the laser sheet only extends until $92\,d_{eq}$, approximately, and, hence, the analysis is only limited to this region.

Formaldehyde is detected in the vicinity of lift-off length in both cases. The experimental image is saturated in the region downstream of $50\,d_{eq}$ since, as explained in [10], the possible interference of polycyclic aromatic hydrocarbons (PAHs) would prevent from visualizing the weaker formaldehyde signal. Therefore, it seems that the simulated field shows a good qualitative agreement with the measured experimental signal. As a final note, although both formaldehyde fields seem to extend some millimetres upstream of the lift-off length, this is more evident for the experimental signal.

Regarding hydroxide, both fields appear downstream of the lift-off length and are qualitatively similar in the region that extends until $92d_{eq}$, although the simulation predicts a zone of high hydroxide concentration nearby the stoichiometric level curve independently of the axial location. In the case of the experiment there exists a scattering in the signal that makes the LIF signal not to be uniform in the region of the stoichiometric line, where it is expected to be found with the greatest intensity due to the high temperatures.

Clearly this validation is limited to a qualitative comparison but it shows that the model has the ability to reproduce fields measured experimentally and encourages to continue the analysis provided by calculations.

As a next step in the analysis, spatial fields for the nominal condition calculated with the three mechanisms are shown for temperature, hydroxide, formaldehyde and acetylene mass fractions in figures 4.26 and 4.27.

Figures 4.26 and 4.27 reveal the structure of the diesel flame for advanced instants. From the temperature field it is observed that temperature rapidly increases at a distance of 20 mm, approximately, where lift-off length is positioned, changing from low temperature (given by the mixing between air and fuel) to very high temperatures, around 2000 K, in few millimetres. Heat released in this region is due to the partially premixed combustion region that, as observed from the temperature field, adopts a lobular or W shape since mixture richness on the axis prevents from reacting and forces combustion to be radially displaced. Downstream of the partially premixed combustion zone, reactions are completed with a slow reaction rate at the diffusion flame.

Moreover, species fields show how these species are spatially distributed. As formaldehyde is a species appearing during the first steps of combustion, it is detected, as described in previous validation, in the close region downstream of the lift-off length in the rich mixtures region since it is enclosed by the stoichiometric level curve. In addition, it is found in low/intermediate

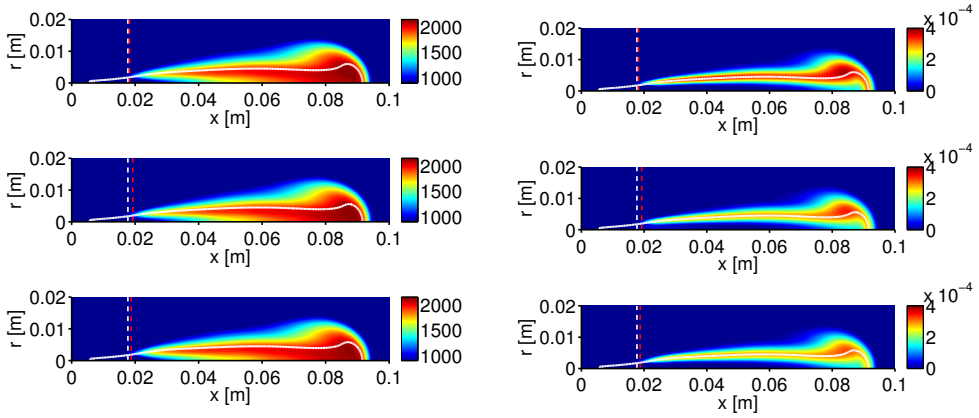

Figure 4.26. *Temperature (left column) and species mass fractions fields of OH (right column) for Narayanaswamy (first row), Yao (second row) and Wang (third row). Lift-off lengths are included with white dashed line for experiment and red dashed line for simulations corresponding to each mechanism. White line represents stoichiometric level curve. Results for nominal case.*

temperatures since it is positioned in the rich mixtures close to the lift-off length.

Moving downstream, acetylene is still observed in the rich mixtures but at higher temperatures than formaldehyde. Its concentration decreases when moving away from the axis. Finally, hydroxide, which is a tracer of high temperature combustion, is found downstream of the partially premixed combustion zone along the stoichiometric level curve and in its proximities, where very high temperatures are reached. On this level curve the diffusion flame is established wrapping the whole spray. Hydroxide extends from the lean mixtures to the slightly rich mixtures and its maximum mass fraction value seems to be slightly displaced to the lean mixtures. This structure is in line with results found in the literature [15, 44, 45].

Regarding the effect of the chemical mechanism, it is observed that neither temperature nor hydroxide fields seem to be affected by the oxidation scheme. On the contrary, formaldehyde field is strongly modified by the mechanism especially when comparing Narayanaswamy or Wang with Yao. For this last scheme, formaldehyde extends in a wider region spreading in leaner mixtures in comparison to the others.

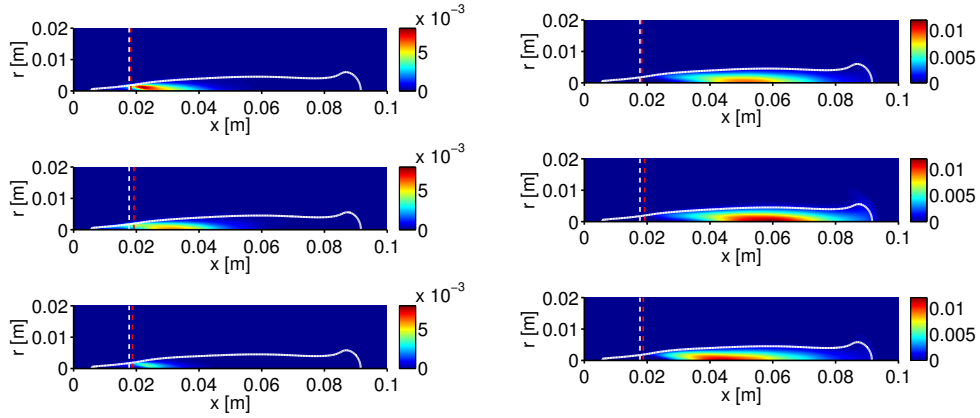

Figure 4.27. *Species mass fractions fields of CH_2O (left column) and C_2H_2 (right column) for Narayanaswamy (first row), Yao (second row) and Wang (third row). Lift-off lengths are included with white dashed line for experiment and red dashed line for simulations corresponding to each mechanism. White line represents stoichiometric level curve. Results for nominal case.*

In the same way, the impact of the mechanism on the acetylene field is not negligible since its position, in terms of mixture fraction, is modified and the peak values are slightly different. In line with this, figure 4.20 showed that Yao scheme is the one that highest acetylene mass produces while Narayanaswamy and Wang predict similar values.

These results were expectable since, as it was shown in previous section, the choice of the chemical mechanism influences only on the variables related to the first and intermediate stages of combustion but not on more advanced stages.

In the following, the effect of the boundary conditions is described. For such purpose, figures 4.28 and 4.29 show the temperature field for the ambient temperature parametric study at $X_{O_2} = 0.15$ and the oxygen sweep at $T_{amb} = 900$ K, respectively. For the sake of brevity, species fields description is postponed to next section where they will be analysed by means of the Z - T maps. Only results for Narayanaswamy mechanism are shown.

Regarding the air temperature sweep, it arises that has a very strong impact on the morphology of the flame. Decreasing the ambient temperature reduces the axial distance where the flame extends since the lift-off length

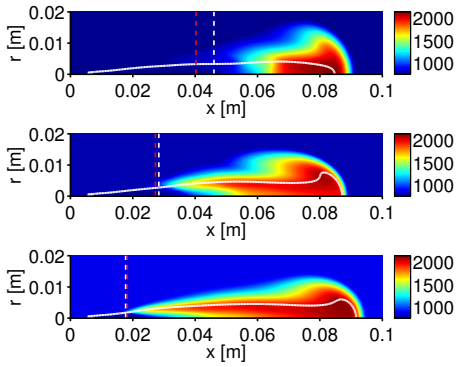

Figure 4.28. *Temperature field for air temperature sweep: T_{amb} = 750 (top), 800 (centre) and 900 (bottom) K with X_{O_2} = 0.15. Lift-off lengths are included with white dashed line for experiments and red dashed line for simulations corresponding to each case. White line represents the stoichiometric level curve. Results for Narayanaswamy mechanism.*

is increased but the flame length is barely modified. In addition, the W shape observed at the partially premixed combustion region is not so clearly distinguished when lowering the ambient temperature since mixtures on the axis tend to be more reactive in comparison with other mixtures at the same axial distance as they are closer to stoichiometry. Finally, reactions in the partially premixed combustion region are not so fast and the transformation from fresh gases to burnt products takes longer spatial paths.

Observing the oxygen variation, it seems that the W shape at the height of the partially premixed combustion is less sharp when reducing oxygen in air. The increment of the oxygen concentration narrows the flame as the stoichiometric mixture increases and its level curve is found closer to the axis. As expected the oxygen variation has a strong impact on the maximum temperature reached in the domain, different to the temperature sweep which has a mild effect on this maximum.

In order to deepen in the morphology of the flame, the profiles for different variables are represented in next figures. The curves show the evolution of several variables along different level curves of fixed equivalence ratios projected on the axis for the nominal, T_{amb} = 800 K with X_{O_2} = 0.15 and T_{amb} = 900 K with X_{O_2} = 0.21 cases calculated with Narayanaswamy

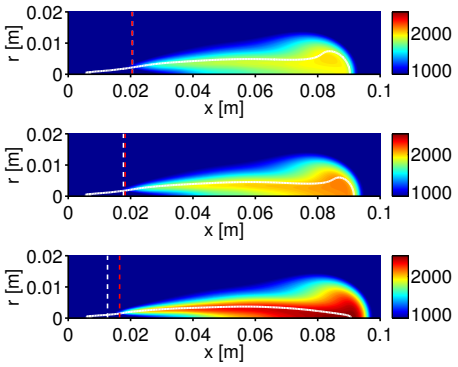

Figure 4.29. *Temperature field for the oxygen concentration sweep with X_{O_2} = 0.13 (top), 0.15 (center) and 0.21 (bottom). Lift-off lengths are included with white dashed line for experiments and red dashed line for simulations corresponding to each case. White line represents the stoichiometric level curve. Results for Narayanaswamy mechanism.*

mechanism. As the stoichiometric mixture fraction is not the same for all the three cases, equivalence ratio is used instead of mixture fraction and profiles are represented for fixed equivalence ratios common for all the cases.

Figure 4.30 shows these profiles for variables $\widetilde{Z''^2}$ and $\widetilde{\chi}$ while figure 4.31 gathers the same profiles for the normalized parameters S and $\widetilde{\chi_{st}}$. All these variables are used to describe the state of the mixture. This description is complemented with figure 4.32 that represents these profiles for the variables $\widetilde{c}$ [8] and $\widetilde{T}$, which describe the advancement of combustion.

Figure 4.30 shows that $\widetilde{Z''^2}$ and $\widetilde{\chi}$ decrease when moving downstream as well as moving away from the axis (reducing the equivalence ratio) due to the reduction of velocity and the consequent decrease of fluctuations and gradients. Although the values are similar in all the cases, there is an increment of these mixing related variables when increasing the oxygen concentration as a consequence of the higher stoichiometric mixture fraction value that displaces combustion to regions closer to the axis.

[8] In fact, it is represented the progress variable normalized to the corresponding steady values for the local $(\widetilde{Z}, \widetilde{Z''^2}, \widetilde{\chi_{st}})$, that is, variable d.

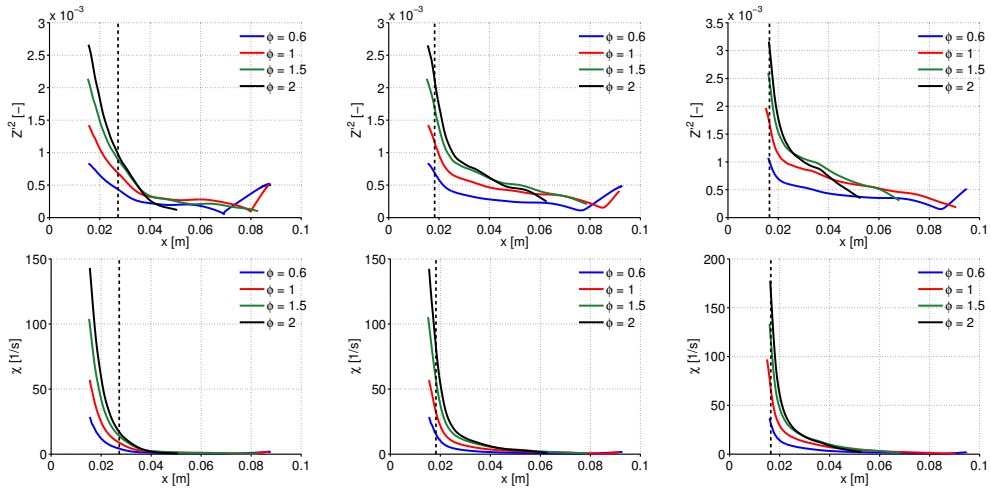

Figure 4.30. *$\widetilde{Z''^2}$ (top) and $\widetilde{\chi}$ (bottom) along equivalence ratio level curves projected on the axis. Results for $T_{amb} = 800$ K with $X_{O_2} = 0.15$ (left), nominal (center) and $T_{amb} = 900$ K with $X_{O_2} = 0.21$ (right) cases. Black dashed line represents simulated lift-off length. Calculations performed with Narayanaswamy mechanism.*

The scalar dissipation rate suffers a very strong decay and only the region of the partially premixed combustion for the cases with $T_{amb} = 900$ K is submitted to high $\widetilde{\chi}$. In addition, it is very interesting to observe that profiles for S and, particularly, $\widetilde{\chi}_{st}$ tend to appear almost collapsed on a single curve for the represented range of equivalence ratios in a certain interval of axial distances.

Finally, figure 4.32 shows how the partially premixed combustion region appears in the vicinity of the lift-off length. In this region $\widetilde{c}$ experiments a strong increase due to the intense combustion that takes place and, later, it tends to unity with a slow rate caused by combustion in the diffusion flame which is substantially much weaker in chemical terms. Similar profiles are described by temperature where the stabilization value depends on the richness of the mixture[9]. Different to the nominal case where $\widetilde{c}$ curves are collapsed, the rate at which they grow for the other boundary conditions depends on the equivalence ratio.

[9]The peaks observed in temperature profiles are due to transient effects on the head of the spray.

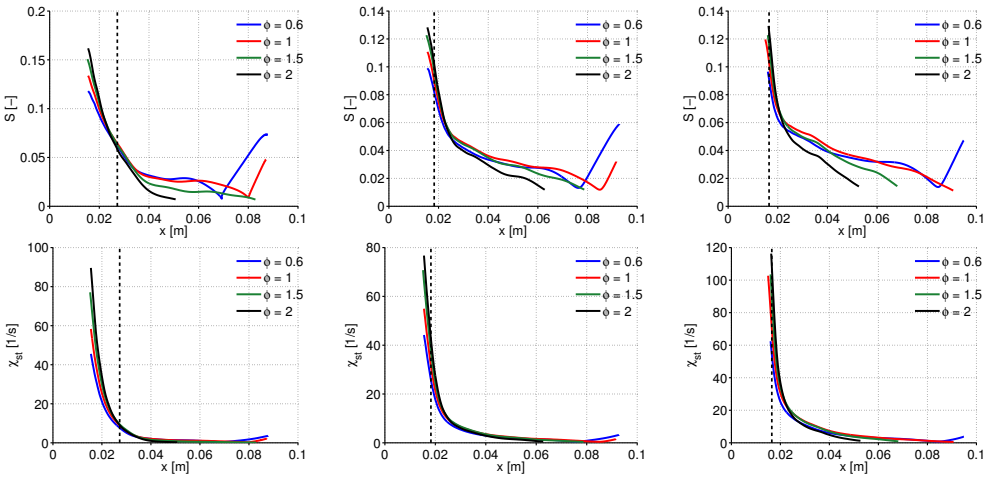

Figure 4.31. *S (top) and $\widetilde{\chi}_{st}$ (bottom) along equivalence ratio level curves projected on the axis. Results for $T_{amb} = 800$ K with $X_{O_2} = 0.15$ (left), nominal (center) and $T_{amb} = 900$ K with $X_{O_2} = 0.21$ (right) cases. Black dashed line represents simulated lift-off length. Calculations performed with Narayanaswamy mechanism.*

The section is closed showing the spatial maps for the progress variable source term $\partial\widetilde{Y}_c/\partial t$, used to advance in the turbulent flame manifold, for nominal condition and $T_{amb} = 800$ K with $X_{O_2} = 0.15$ and $T_{amb} = 900$ K with $X_{O_2} = 0.21$ cases in figure 4.33. In order to better visualize the different parts of the flame a logarithmic scale is used.

The flame is described in terms of the progress variable source term since, as was pointed out previously, this variable traces the whole combustion process and, hence, can be used as a tracer of zones where heat is released.

Figure 4.33 reinforces the concepts explained with previous results, that is, the diesel flame is composed of a partially premixed combustion found in the vicinity of the lift-off length. It is revealed that the high burning rates found in this region lead to transform unburned mixtures to products close to the steady solution, as observed in figure 4.32. The most intense burning rate is found in the rich mixtures around an equivalence ratio of 1.5 in a position radially displaced from the axis.

The progress variable source term suffers a sharp fall when moving downstream of the partially premixed combustion region, especially in the

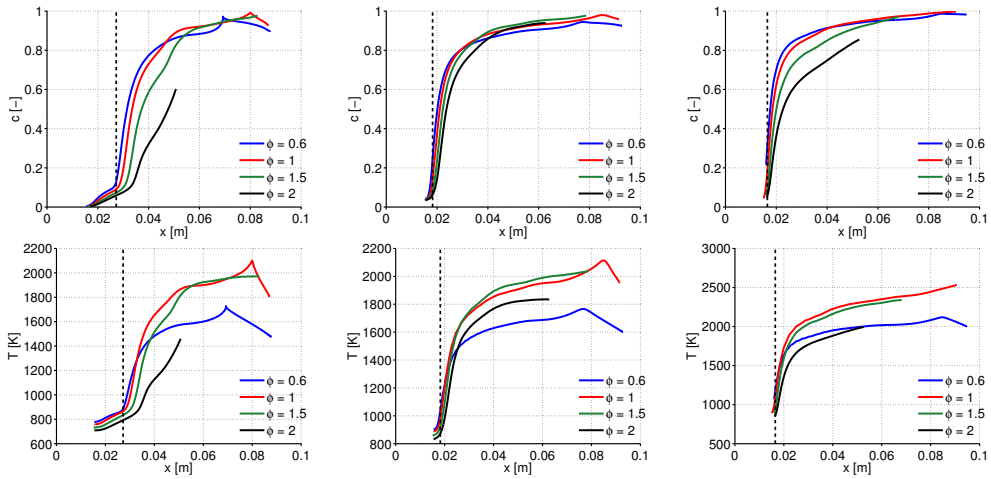

Figure 4.32. *$\widetilde{c}$ (top) and $\widetilde{T}$ (bottom) along equivalence ratio level curves projected on the axis. Results for $T_{amb} = 800$ K with $X_{O_2} = 0.15$ (left), nominal (center) and $T_{amb} = 900$ K with $X_{O_2} = 0.21$ (right) cases. Black dashed line represents simulated lift-off length. Calculations performed with Narayanaswamy mechanism.*

zone close to the axis. Combustion is completed in the diffusion flame, which wraps the spray, and is characterized by its relative low source terms compared to those found in the partially premixed combustion[10]. This means that the diffusion flame is slower than the partially premixed combustion as a consequence of the mixing controlled combustion limitations. This picture of the reactive diesel flame agrees with that given by Dec [44], summarized in section 2.5.4.

In addition, note that the diffusion flame is not strictly limited to the stoichiometric level curve due to the turbulent fluctuations that, in the RANS context, are captured. Clearly these fluctuations are retained by means of the presumed PDFs which in the current model are accounted for the mixture fraction and the scalar dissipation rate. This produces a distributed turbulent flame brush where soft profiles extend in contrast with other approaches that do not retain this kind of interactions [40, 46].

The comparison between boundary conditions shows that decreasing mixture reactivity spreads the region affected by the partially premixed

[10]Their difference is of one or two orders of magnitude.

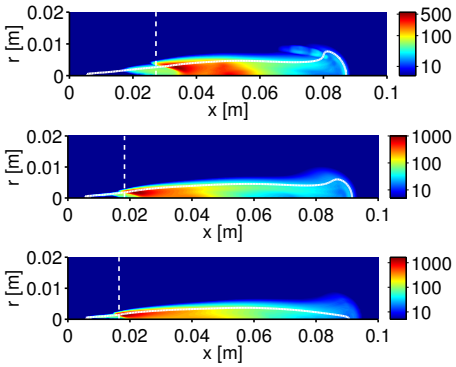

Figure 4.33. *$\partial\widetilde{Y}_c/\partial t$ spatial field for an advanced instant for $T_{amb} = 800$ K with $X_{O_2} = 0.15$ (upper), nominal (center) and $T_{amb} = 900$ K with $X_{O_2} = 0.21$ (bottom) cases. A logarithmic scale is used for $\partial\widetilde{Y}_c/\partial t$. White solid line corresponds to the stoichiometric mixture fraction level curve. Simulated lift-off lengths are included with white dashed lines. Results for Narayanaswamy mechanism.*

combustion which, owing to the decreased chemical rates and the reduction of velocity due to the increase of the lift-off length, takes longer times and lengths to partially oxidise the mixture. In the same way, there is a clear decrease of the maximum progress variable source term when reducing reactivity.

In addition, when reducing mixture reactivity, the partially premixed combustion is not only limited to a region radially displaced from the axis but combustion pockets appear on the axis too. Displacement of lift-off length downstream allows rich mixtures found on the axis to be diluted enough to be potentially reactive. This is clearly seen when comparing $T_{amb} = 900$ K with $X_{O_2} = 0.21$ case, where the extremely reduced lift-off length prevents combustion on the axis, with $T_{amb} = 800$ K with $X_{O_2} = 0.15$ case, where due to the dilated lift-off length rich mixtures on the axis are lean enough to react.

Z - T maps

More insight is gained when describing flame structure in terms of mixture fraction and temperature by means of the Z - T maps.

First, different species of interest are represented in the Z - T maps for the three mechanisms and nominal conditions for advanced instants. Figure

4.34 gathers these results for species CH_2O, C_2H_2 and OH. In order to avoid showing non-representative points, only those that fulfil $\widetilde{Y}_i \geq 0.25\,\widetilde{Y}_i^{max}$ are included, being $\widetilde{Y}_i^{max}$ the maximum mass fraction for species i in the domain. Moreover, the initial mixing line and the contour of the map, understood as the set of points with maximum temperature for each mixture fraction, are included.

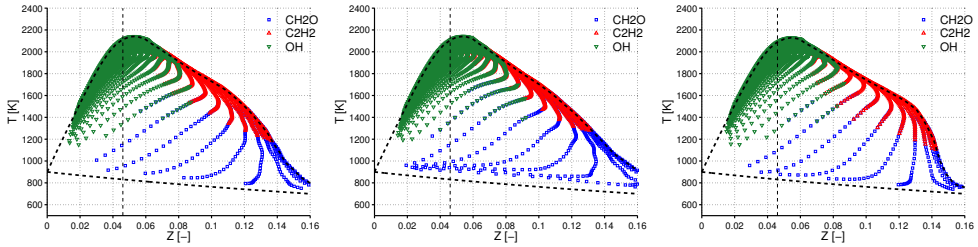

Figure 4.34. CH_2O, C_2H_2 *and* OH *species in Z - T maps for the nominal case with Narayanaswamy (left), Yao (center) and Wang (right). Black dashed line corresponds to the initial adiabatic mixing line and the upper contour of the map. Vertical black dashed line indicates the stoichiometric mixture fraction.*

Figure 4.34 shows that OH is predicted in a similar way by the three mechanisms although it extends in lower temperature regions with Narayanaswamy and Wang mechanisms than with Yao. As expected, species related to low/intermediate temperatures, CH_2O and C_2H_2, are the most affected by the mechanism choice. Narayanaswamy and Wang predict similar fields although for the last one C_2H_2 reaches lower temperatures. On the contrary, Yao shows the most important differences since C_2H_2 only appears in the very close region to the upper contour of the map and CH_2O spreads over very low temperatures.

Yao scheme predicts a very smooth fall of the contour of the map for very rich mixtures compared to the other mechanisms, especially when comparing with Wang that shows an extremely abrupt contour. These sharp profiles were observed for Wang flamelet solutions in figure 4.5 where it was explained that this behaviour is caused by the low chemical source terms during the cool flame, while for Yao mechanism the more moderate source terms lead to softer profiles. As observed, the behaviour observed for the flamelet solutions is retained in the spray.

In order to analyse the influence of the boundary conditions, figures 4.35 and 4.36 show similar maps for advanced instants for the air temperature

sweep with $X_{O_2} = 0.15$ and the oxygen parametric variation. Results are for Narayanaswamy mechanism.

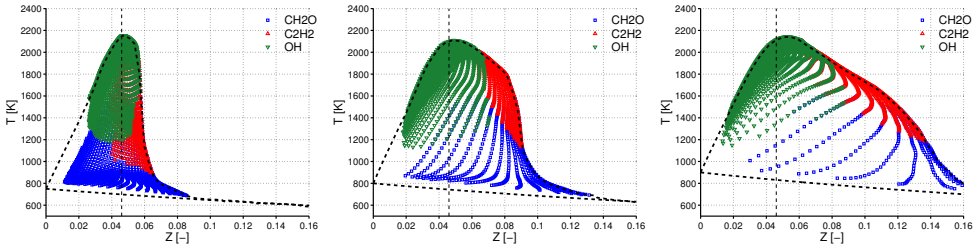

Figure 4.35. CH_2O, C_2H_2 *and* OH *species in Z - T maps. Air temperature sweep:* $T_{amb} = 750$ *(left), 800 (centre) and 900 (right) K with* $X_{O_2} = 0.15$*. Black dashed line corresponds to the initial adiabatic mixing line and the upper contour of the map. Vertical black dashed line indicates the stoichiometric mixture fraction. Calculations performed with Narayanaswamy mechanism.*

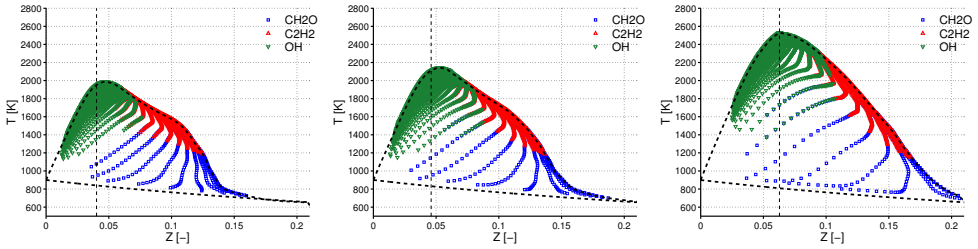

Figure 4.36. CH_2O, C_2H_2 *and* OH *species in Z - T maps. Oxygen concentration sweep:* $X_{O_2} = 0.13$ *(left), 0.15 (center) and 0.21 (right). Black dashed line corresponds to the initial adiabatic mixing line and the upper contour of the map. Vertical black dashed line indicates the stoichiometric mixture fraction. Calculations performed with Narayanaswamy mechanism.*

One of the most important conclusions from figures 4.35 and 4.36 is that the increase of reactivity by air temperature or oxygen concentration extends the region of reactive mixtures owing to the intensification of the chemical activity. The most extreme case is that for 750 K (and $X_{O_2} = 0.15$) for which combustion is limited to $\widetilde{\phi} < 1.5$. This generates very small amounts of C_2H_2 mass as was shown in figure 4.21. Therefore, the increase of ambient

temperature provokes an extension of the range of reactive rich mixtures yielding higher soot precursors formation[11].

This reasoning cannot be directly applied to the oxygen sweep since, even the range of reactive mixtures is slightly enlarged, the total C_2H_2 mass is reduced with the oxygen concentration as was shown in figure 4.22. The explanation was given in section 4.4.3.3 and is due to the different spatial structure of the flame when changing oxygen concentration. Owing to the increase of the stoichiometric mixture fraction, the maximum $\widetilde{\phi}$ value where acetylene is detected is similar (around 3.3) for the cases of $X_{O_2} = 0.13$ and 0.21. The narrowing of the region where C_2H_2 spreads when increasing oxygen concentration provokes that the mass contributions for C_2H_2 are lower when considering cylindrical symmetry even if the peak value for $Y_{C_2H_2}$ increases.

Moreover, the upper contour of the map becomes smoother when increasing the mixture reactivity and the sharp profiles in the rich region tend to disappear. In addition, increasing oxygen concentration leads to an important increase of the maximum temperature reached in the domain, however, only a moderate rise is found when changing air temperature.

In order to reach a deeper understanding of the partially premixed combustion, contour levels for variables describing the state of the mixture and the reaction are represented in the Z - T map. The variables chosen to describe the state of the mixture are $\widetilde{Z''^2}$ and $\widetilde{\chi}$ together with $\widetilde{Z}$, that corresponds to one of the axis. The chemical state is described by the contour levels of $\partial\widetilde{Y}_c/\partial t$ and $\widetilde{T}$, that corresponds to the other axis. These figures are of great interest because they condensate the most important aspects of combustion since they are build upon the reactive flow controlling variables.

The values corresponding to the level curves for the different variables and boundary conditions are gathered in table 4.2. For a given variable all the level curves are plotted with the same colour and they are distinguished by means of markers: square markers are used for the lowest value, circles for next value and triangles for the third and greatest value (if three different values are included). For each boundary condition representative values have been chosen.

As in previous Z - T map figures, the initial mixing line and the upper contour of the map are included for reference together with the stoichiometric mixture fraction.

[11] As was explained in chapter 2 soot is formed in temperatures of the order of 1300 K and equivalence ratios higher than 2.

Table 4.2. *Values of the variables for the represented level curves for the different boundary conditions.*

Variable	750K 15% O2	800K 15% O2	900K 15% O2	900K 13% O2	900K 21% O2
$\widetilde{Z''^2} \times 10^4$	1.3, 2	3.3, 4.5, 5.5	7, 10, 14	5, 7, 9	12, 18, 25
$\widetilde{\chi}$ (1/s)	0.3, 0.4, 0.8	2.5, 4	3, 20, 30	3, 10, 20	10, 50, 80
$\partial\widetilde{Y_c}/\partial t$ (1/s)	150, 350	200, 500	300, 600, 900	300, 600	600, 1500

In order to simplify representation, two blocks of figures, one containing only mixing variables, that is, $\widetilde{Z''^2}$ and $\widetilde{\chi}$, while the other one related to the reacting variable $\partial\widetilde{Y}_c/\partial t$, are plotted. Figures 4.37 and 4.38 contain these figures for the nominal case and the three analysed mechanisms for advanced instants.

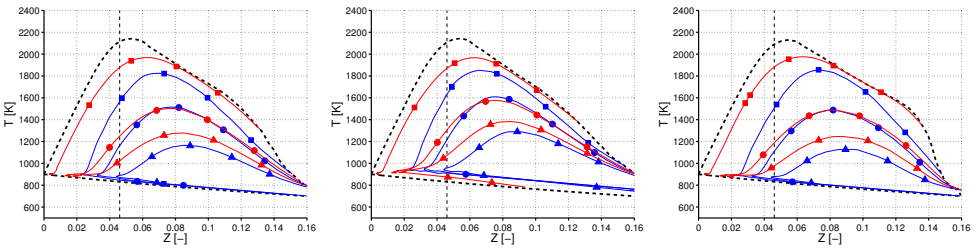

Figure 4.37. *Z - T maps with level curves for $\widetilde{Z''^2}$ (blue) and $\widetilde{\chi}$ (red) for the nominal case with Narayanaswamy (left), Yao (center) and Wang (right). Markers distinguish between different level curve values (see table 4.2). Black dashed lines correspond to the initial adiabatic mixing line and the upper contour of the map. Vertical black dashed line indicates the stoichiometric mixture fraction.*

As seen from figures 4.37 and 4.38, they allow to analyse in detail the partially premixed combustion. On the contrary, the diffusion flame is not clearly distinguished in this kind of representation since it is very close to the contour of the map and shows very low source terms compared to the partially premixed combustion.

Regarding the partially premixed combustion, it extends over a wide region of mixture fractions and temperatures. The most vigorous zone is found for $\widetilde{Z}$ between 0.07 and 0.09 (although this depends on the mechanism too), that corresponds to $\widetilde{\phi}$ between 1.5 and 2 and temperatures ranging from 1200 to 1400 K. These results are in agreement with experimental results [44].

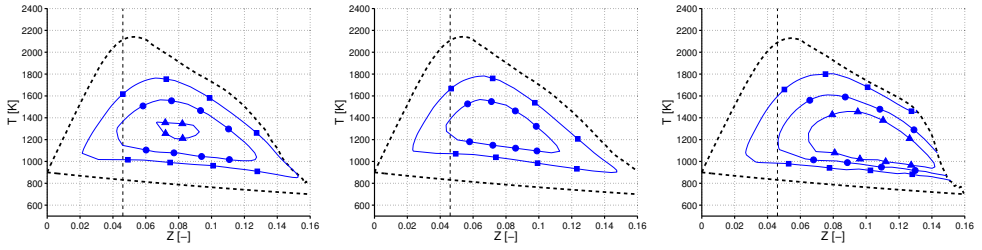

Figure 4.38. *Z - T maps with level curves for $\partial\widetilde{Y}_c/\partial t$ for the nominal case with Narayanaswamy (left), Yao (center) and Wang (right). Markers distinguish between different level curve values (see table 4.2). Black dashed lines correspond to the initial adiabatic mixing line and the upper contour of the map. Vertical black dashed line indicates the stoichiometric mixture fraction.*

According to figure 4.37, in this region $\widetilde{Z''^2}$ reaches values around $1.2 \cdot 10^{-3}$ while $\widetilde{\chi}$ around 25 1/s (that, in this case, corresponds to $\widetilde{\chi}_{st} = 25$ 1/s).

From this, it is deduced that the partially premixed combustion is found in a region of rich mixtures with instantaneous mixture fraction estimated in the interval 0.07 ± 0.035 (taking $\widetilde{Z''^2} = 1.2 \cdot 10^{-3}$) and a flame defined by $\widetilde{\chi}_{st} = 25$ 1/s. Therefore, it is presumed that this combustion ranges over moderate values for the scalar dissipation rate considering that flamelets auto-ignition range extends until $\chi_{st} = 106$ 1/s, approximately[12].

In order to demonstrate this, the log-normal PDF defined by $\widetilde{\chi}_{st} = 25$ 1/s and $\sigma = \sqrt{2}$ is represented in figure 4.39. With this PDF, the probability of reaching values greater than $\widetilde{\chi}_{st} = 106$ 1/s is 4.16%, which is marginal, and demonstrates that the log-normal PDF promotes weakly strained flamelets. Therefore, it is not expected that extinction phenomena are important for the partially premixed combustion. This corroborates that the behaviour of the diesel flame can be modelled only accounting for the flamelet auto-ignition range [47] reinforcing ADF approach suitability for this configuration.

Analysing the impact of the chemical mechanism, it is observed that Yao and Narayanaswamy predict the zone of intense reaction from the partially premixed combustion in a region of similar temperatures and mixture fractions. On the contrary, Wang shows a very intense reaction that, additionally, is displaced to the very rich mixtures region. This is in

[12] In fact, non-null chemical source terms would be still obtained for $\widetilde{\chi}_{st}$ higher than 106 1/s when considering a log-normal PDF for the scalar dissipation rate and, in consequence, 106 1/s is a low boundary.

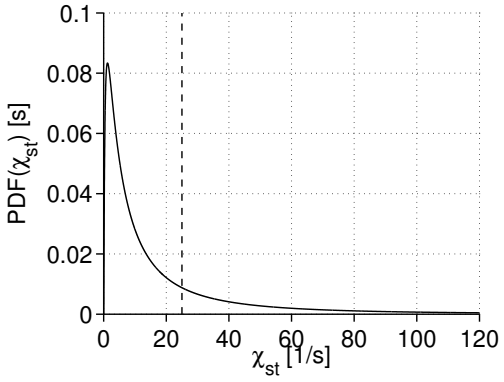

Figure 4.39. *Log-normal PDF defined by* $\widetilde{\chi}_{st} = 25$ *1/s and* $\sigma = \sqrt{2}$*. Black vertical dashed line indicates* $\widetilde{\chi}_{st} = 25$ *1/s.*

agreement with flamelet calculations (see section 4.4.2) which showed for this mechanism an ignition displaced to richer mixtures compared to other schemes. Nevertheless, different to the chemical aspects, mixing variables take similar values for all the three mechanisms[13].

Figures 4.40 and 4.41, on the one hand, and 4.42 and 4.43, on the other hand, show the corresponding level curves in the Z - T maps for the temperature sweep with $X_{O_2} = 0.15$ and the oxygen parametric variation, respectively. Figures are for advanced instants and correspond to results computed with Narayanaswamy mechanism.

Previous to the analysis of the figures, it is worth mentioning that table 4.2, that gathers the values of the represented level curves, is a preliminary reflection of the effect of the boundary conditions. It is observed that there exists a strong variation of the non-reactive variables, deeply connected with the displacement of the lift-off length, together with the burning rate $\partial\widetilde{Y}_c/\partial t$ that, although is patent in both parametric variations, is possibly more accentuated for the air temperature variation.

As expected, increasing the ambient temperature enriches the mixture where the partially premixed combustion develops. Different to the air

[13]This was expected since the only way by which combustion modifies these non-reactive variables is by the change of density and viscosity induced by temperature, which in turn is caused by heat release. Although the flame structure may be notably different between mechanisms the differences are not so significant to substantially modify density and viscosity fields between them and, hence, non-reactive variables.

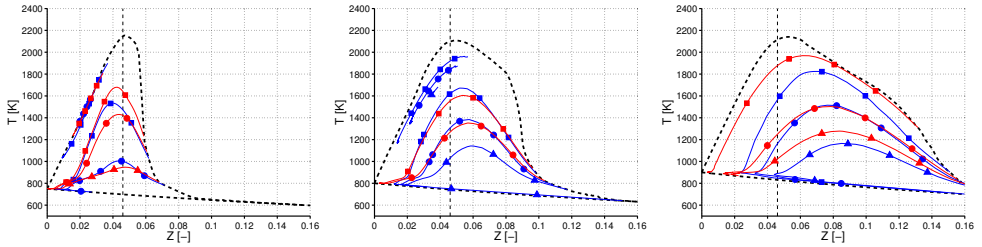

Figure 4.40. *Z - T maps with level curves for $\widetilde{Z''^2}$ (blue), $\widetilde{\chi}$ (red). Air temperature sweep (X_{O_2} = 0.15): T_{amb} = 750 (left), 800 (centre) and 900 (right) K. Markers distinguish between different level curve values (see table 4.2). Black dashed lines correspond to the initial adiabatic mixing line and the upper contour of the map. Vertical black dashed line indicates the stoichiometric mixture fraction. Calculations performed with Narayanaswamy mechanism.*

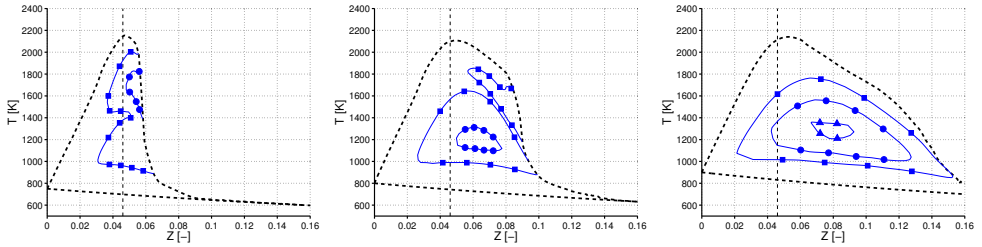

Figure 4.41. *Z - T maps with level curves for $\partial\widetilde{Y}_c/\partial t$. Temperature sweep ($X_{O_2}$ = 0.15): T_{amb} = 750 (left), 800 (centre) and 900 (right) K. Markers distinguish between different level curve values (see table 4.2). Black dashed lines correspond to the initial adiabatic mixing line and the upper contour of the map. Vertical black dashed line indicates the stoichiometric mixture fraction. Calculations performed with Narayanaswamy mechanism.*

temperature variation, the oxygen sweep has a slight influence on the position of the most intense combustion region. Again this is in line with flamelet results where it was indicated that Z_{MR} is clearly enriched when increasing the ambient temperature but remains almost identical when modifying the oxygen concentration. From this, it is deduced that the partially premixed combustion develops at slightly leaner equivalence ratios when augmenting the oxygen concentration.

The increase of the non-reacting variables when increasing mixture reactivity is in deep connection with the reduction of the lift-off length. On

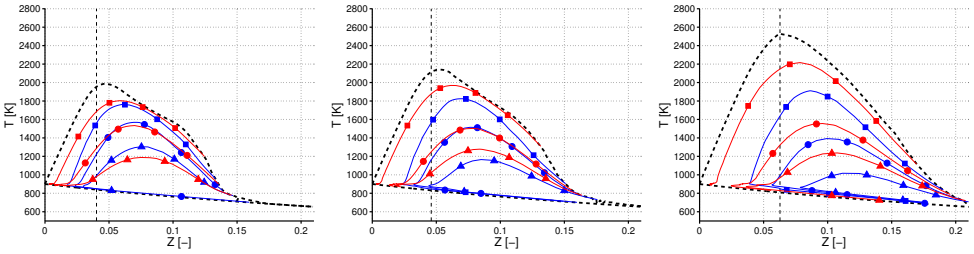

Figure 4.42. *Z - T maps with level curves for $\widetilde{Z''^2}$ (blue), $\widetilde{\chi}$ (red). Oxygen sweep (T_{amb} = 900 K): X_{O_2} = 0.13 (left), 0.15 (centre) and 0.21 (right). Markers distinguish between different level curve values (see table 4.2). Black dashed lines correspond to the initial adiabatic mixing line and the upper contour of the map. Vertical black dashed line indicates the stoichiometric mixture fraction. Calculations performed with Narayanaswamy mechanism.*

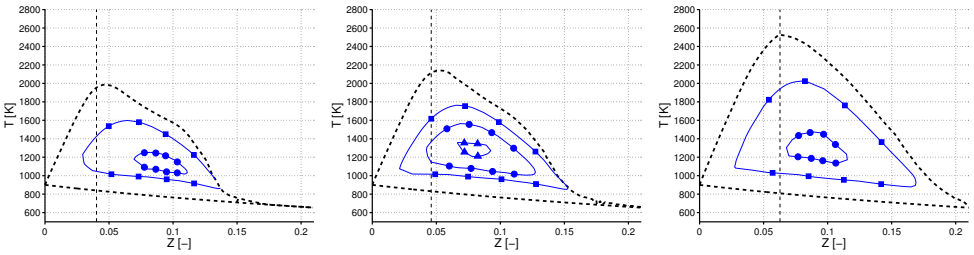

Figure 4.43. *Z - T maps with level curves for $\partial\widetilde{Y}_c/\partial t$. Oxygen sweep ($T_{amb}$ = 900 K): X_{O_2} = 0.13 (left), 0.15 (centre) and 0.21 (right). Markers distinguish between different level curve values (see table 4.2). Black dashed lines correspond to the initial adiabatic mixing line and the upper contour of the map. Vertical black dashed line indicates the stoichiometric mixture fraction. Calculations performed with Narayanaswamy mechanism.*

the one hand, the reduction of the lift-off length is very strong when increasing air temperature producing a sharp rise of the non-reacting variables. On the other hand, although the lift-off length sensitivity is relatively moderate to oxygen concentration, non-reacting variables experiment a sharper variation close to the nozzle. This explains that in both sweeps there exists a non-negligible variation of these variables, which, notwithstanding, seems to be more sensitive to the air temperature.

As a consequence, the increase of reactivity enables the mixture to sustain combustion in less favourable regions, that is, zones with higher variances and scalar dissipation rates.

Moreover, for low air temperature cases, the partially premixed combustion seems to be composed of two regions with intense burning rate. As observed from figure 4.41, a second peak is found in the richest reactive mixtures and high temperatures around 1600 K for the 750 and 800 K air temperature cases. In spatial coordinates this second peak is found very close to the axis and can be observed in figure 4.33 for $T_{amb} = 800$ K at 50 mm, approximately. When increasing mixture reactivity this second peak disappears. This fact suggests that the structure of the low reactive diesel sprays is complex and requires further investigation.

As a final observation, to say that $\widetilde{Z''^2}$ and $\widetilde{\chi}$ level curves are approximately overlapped as deduced from figures 4.37, 4.40 and 4.42. Since the explanation for this observation is not straightforward and this feature of the spray occurs in inert conditions too, its analysis is given in the appendix of this chapter.

Some additional comments

With a similar procedure that it was done in the previous section, probability of reaching extinction conditions in the partially premixed combustion region is quantified when changing the boundary conditions. These probabilities are shown in figure 4.44 and the values $\widetilde{\chi}_{st}$ used to define the log-normal functions in order to calculate such probabilities are measured at the lift-off length. All the results in this section are for Narayanaswamy calculations[14].

It is observed that the decrease of ambient temperature, which augments lift-off length, as well as the increase of oxygen concentration, that reduces lift-off length, decrease substantially the probability of reaching the flamelets extinction zone in the partially premixed combustion region.

This probability does not only depend on how the lift-off length is modified, but how the maximum flamelet stoichiometric scalar dissipation rate in the auto-ignition range $\chi_{st,i}$ changes with boundary conditions too. This makes that when increasing oxygen concentration, even reducing lift-off length, the probability is decreased as a consequence of the strong increase in $\chi_{st,i}$. Figure 4.45 shows how $\chi_{st,i}$ is modified with boundary conditions. It is observed that the same increase in air temperature produces higher increase in $\chi_{st,i}$ for a higher level of oxygen concentration.

[14]These probabilities are expected to show some dependency with the mechanism since they predict different lift-off lengths.

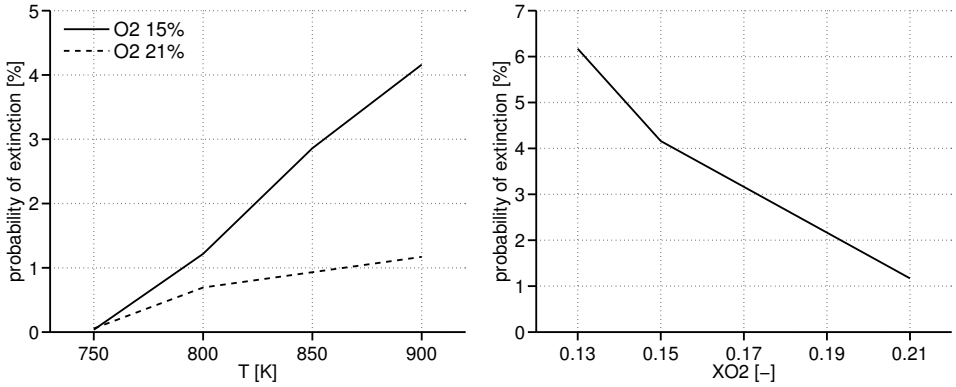

Figure 4.44. *Probability of reaching extincition conditions at the lift-off length for both temperature parametric variations (left) and oxygen sweep (right).*

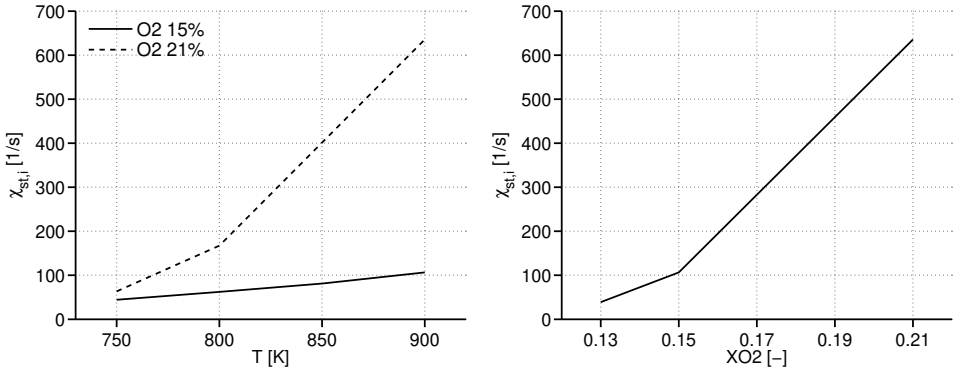

Figure 4.45. *$\chi_{st,i}$ values in the auto-ignition range for both temperature parametric variations (left) and oxygen sweep (right).*

The most important conclusion of this comparison is that, in all the cases, extremely low probabilities of extinction are found in the partially premixed combustion region discarding extinction phenomena as the main stabilization mechanism in diesel flames.

4.4.3.5 Influence of C_χ

The chapter is closed analysing the effect of the constant of proportionality C_χ. In this work, this constant was adjusted fitting experimental mixture fraction variance profiles for inert conditions. A value $C_\chi = 2$ was found suitable and retained for subsequent reactive calculations. The following analysis does not intend to improve reactive spray calculations, since it is assumed that the variations in the mixture fraction variance induced by the flame are accounted for by density changes and, then, constant C_χ does not need to be recalibrated, but to analyse which is the effect of this constant in the reactive flow when modified. For this purpose, calculations with $C_\chi = 5$ are compared with previous results. All the calculations are carried out with Narayanaswamy mechanism.

As a first step, Z_{rms} and $\widetilde{\chi}$ profiles on the axis are compared in inert conditions between calculations with $C_\chi = 2$ and 5 for nominal case as shown in figure 4.46.

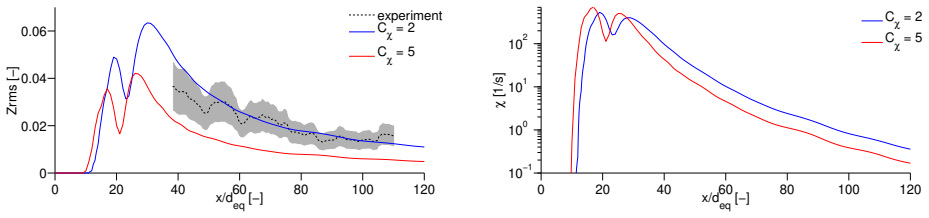

Figure 4.46. *Comparison of Z_{rms} and $\widetilde{\chi}$ profiles on the axis for different C_χ values. For Z_{rms} experimental information is included where shadowed regions delimit experimental uncertainty. Results for inert nominal case.*

It is observed that increasing C_χ value reduces $\widetilde{Z''^2}$ in the whole domain except in a very close region to the nozzle while increases $\widetilde{\chi}$ in a region close to the nozzle and reduces it far away. This was expected since C_χ amplifies the effect of the dissipation for mixture fraction variance[15]. Then, close to the nozzle as the variables are still not strongly affected by the change in parameters, dissipation $\widetilde{\chi}$ increases when augmenting C_χ and reduces faster $\widetilde{Z''^2}$. Downstream, as $\widetilde{Z''^2}$ has been decreased upstream, the rate at which it

[15]It is also deduced that increasing C_χ provokes the reduction of mixing characteristic times ($\widetilde{Z''^2}/\widetilde{\chi}$) since it is expected that the turbulent characteristic time k/ε is not affected by C_χ in inert conditions (see equation 3.59)

may be dissipated is reduced too, providing lower $\widetilde{\chi}$ values when increasing C_χ.

The effect on ignition delay and lift-off length for the temperature and oxygen sweeps is shown in figures 4.47 and 4.48, respectively. Increasing C_χ reduces ignition delay, probably, as a consequence of the reduction of $\widetilde{Z''^2}$ which inhibits turbulent transport between mixtures and enhances combustion in the most reactive mixtures. However, there exists an increase of the lift-off length whose explanation is postponed to the following analysis of the spatial fields.

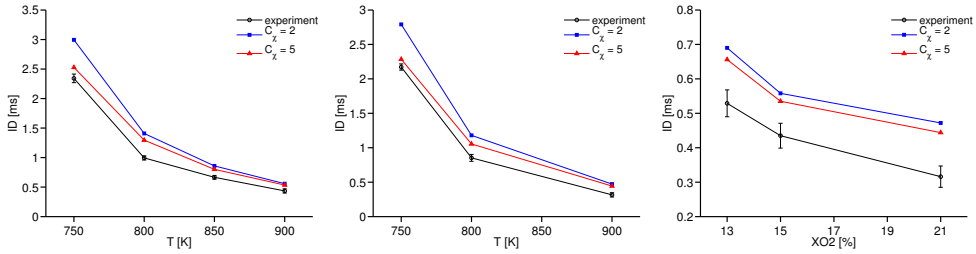

Figure 4.47. *Ignition delay for the ambient temperature parametric variations at* $\mathrm{X_{O_2}} = 0.15$ *(left),* $\mathrm{X_{O_2}} = 0.21$ *(center) and oxygen sweep (right). Error bars indicate experimental uncertainties. Results for Narayanaswamy mechanism.*

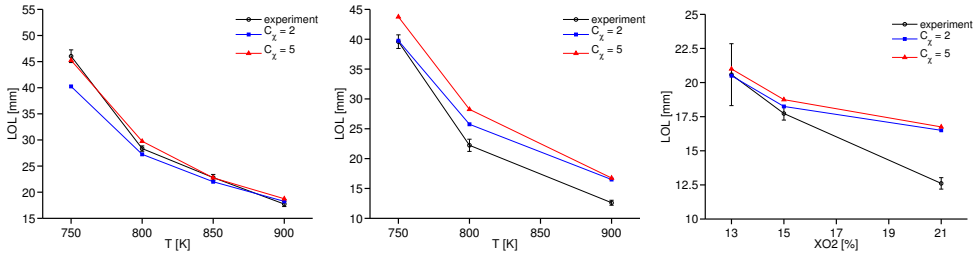

Figure 4.48. *Lift-off length for the ambient temperature parametric variations at* $\mathrm{X_{O_2}} = 0.15$ *(left),* $\mathrm{X_{O_2}} = 0.21$ *(center) and oxygen sweep (right). Error bars indicate experimental uncertainties. Results for Narayanaswamy mechanism.*

Figures 4.49 and 4.50 show the effect of constant C_χ on the spatial fields for temperature, hydroxide, formaldehyde and acetylene for reactive nominal condition. Similar fields are obtained for the different variables for both C_χ values, however, it is observed that the peak values are increased when augmenting C_χ, again, as a consequence of the reduction of transport between

mixtures. Therefore, very reactive mixtures are more easily ignited while less reactive mixtures are more reluctant to ignite. This is especially remarkable for hydroxide probably due to the differences in maximum temperature reached with C_χ 2 and 5 which are of the order of 100 K. This increase may have a strong impact on NO_x predictions since they are produced at the last stages of combustion and are very sensitive to temperature. In addition, it seems that formaldehyde extends on a wider region when increasing C_χ and has a second peak at 40 mm.

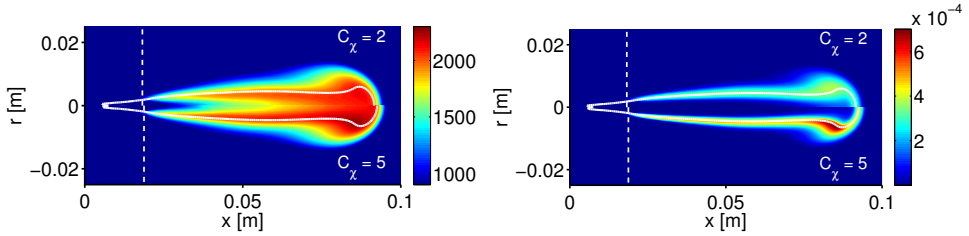

Figure 4.49. *Temperature (left) and species mass fraction for OH (right) fields for advanced instants. In each representation top figure corresponds to $C_\chi = 2$ and bottom to $C_\chi = 5$. Results for Narayanaswamy mechanism and nominal case.*

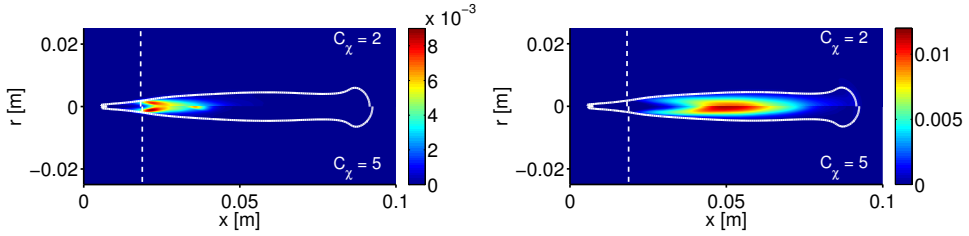

Figure 4.50. *Species mass fraction for CH_2O (left) and C_2H_2 (right) fields for advanced instants. In each representation top figure corresponds to $C_\chi = 2$ and bottom to $C_\chi = 5$. Results for Narayanaswamy mechanism and nominal case.*

In order to analyse the effect of the boundary conditions a similar representation to that shown in figures 4.49 and 4.50 is shown in figures 4.51 and 4.52 at $T_{amb} = 800$ K and $X_{O_2} = 0.15$.

Similar observations to those extracted for the nominal case are established in this case. However, the wider extension of formaldehyde and the second peak when augmenting C_χ are more evident for this low temperature case. In

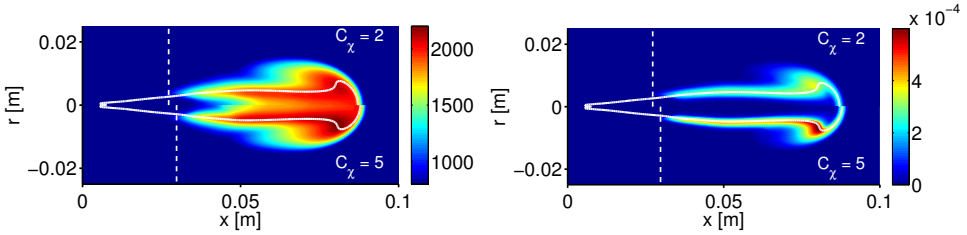

Figure 4.51. *Temperature (left) and species mass fraction for OH (right) fields for advanced instants. In each representation top figure corresponds to* $C_\chi = 2$ *and bottom to* $C_\chi = 5$*. Results for Narayanaswamy mechanism and* $T_{amb} = 800$ *K and* $X_{O_2} = 0.15$ *case.*

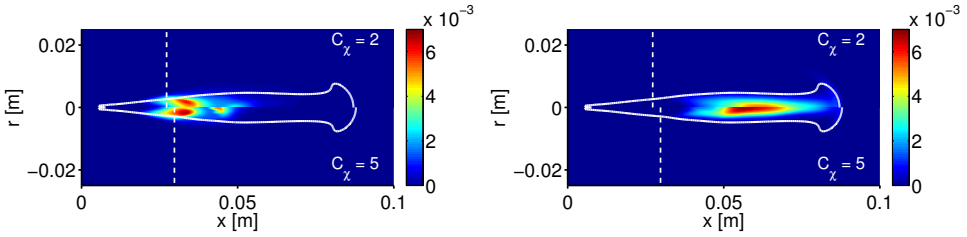

Figure 4.52. *Species mass fraction for* CH_2O *(left) and* C_2H_2 *(right) fields for advanced instants. In each representation top figure corresponds to* $C_\chi = 2$ *and bottom to* $C_\chi = 5$*. Results for Narayanaswamy mechanism and* $T_{amb} = 800$ *K and* $X_{O_2} = 0.15$ *case.*

addition, it is observed a substantial increase of the peak mass fraction for acetylene with C_χ.

Finally, the increase of the lift-off length is revealed in the light of this representation for both boundary conditions, namely, it is due to the increase of the peak hydroxide value that occurs in the diffusion flame. As lift-off length is based on a relative value of this maximum, its increase provokes a displacement of the base of the flame in the downstream direction.

4.5 Conclusions

In this chapter, spray A, representative of diesel-like sprays, has been thoroughly analysed. To accomplish this objective, the analysis is based on the

study of three aspects: the influence of the boundary conditions, the impact of the chemical mechanism and the modifications that new flow aspects induce in combustion structure when included.

First, it has been emphasized the importance of low temperature ignition and subsequent cool flame period in homogeneous conditions since this determines further combustion development when introducing other physical aspects. A first picture of this can be achieved analysing ignition delays and chemical source terms for homogeneous reactors.

For all the mechanisms and boundary conditions, it has been observed that ignition at low temperatures starts at lean mixtures and then, displaces to rich mixtures where it develops. This behaviour is observed not only for homogeneous reactors and flamelets but also for the spray, although the relevance of ignition at lean mixtures for the spray is clearly mitigated.

How ignition develops during the first combustion stages has a strong dependence on the mechanism choice while high temperature chemistry shows a remarkable agreement between the different chemical schemes.

Regarding the effect on species, it is emphasized that the model reproduces the expected trends, as in the case of acetylene, when modifying the boundary conditions.

For all the boundary conditions it has been observed that ignition kernels are first localized in regions of low mixture fraction variance and scalar dissipation rate in agreement with literature. Once the flame stabilizes, it is observed that is composed of a partially premixed combustion positioned near the lift-off length in the rich mixtures side and intermediate temperatures and a diffusion flame in the vicinity of the stoichiometric mixture fraction. The partially premixed combustion shows a vigorous combustion compared to the diffusion flame, where burning rates are moderate or low. When decreasing mixture reactivity, the rich flame tends to spread from a radially displaced position to regions closer to the axis flattening the flame base.

In addition, an extremely low probability to reach extinction is observed in the partially premixed combustion region. This suggests that extinction phenomena is an aspect of second order and does not strongly affect the stabilization mechanism. In fact, a dependence between ignition delay and lift-off length is observed for the set of boundary conditions suggesting that auto-ignition plays a role in flame stabilization.

Moreover, C_χ has a strong impact on mixture fraction variance and scalar dissipation rate. Low C_χ values enhance mixing at the small scales softening

reactive scalars fields. However, high values inhibit micro-mixing and produce sharp profiles for such reactive scalars fields.

Finally, the agreement between model results and other experimental and modelling works together with the rest of findings that, in spite of the lack of measurements to compare with, show an internal logic, lead to state that the flamelet concept in its particular ADF formulation is suitable for diesel spray combustion description.

Appendix

This appendix is addressed to explain the overlapping between the fields $\widetilde{Z''^2}$ and $\widetilde{\chi}$ in terms of their level curves observed in figures 4.37, 4.40 and 4.42. It is an interesting feature since it affects directly to mixing variables which define the state of combustion in models like those based on the flamelet concept.

In addition, as the variables to be analysed are related to the state of the mixture, the analysis is carried out for the inert configuration in order to simplify. As this analysis is out of the scope of this thesis only a sketch of the reasons of this behaviour is given here.

The first aspect to be mentioned is the formal similarity between the equations for turbulent kinetic energy k and mixture fraction variance $\widetilde{Z''^2}$, as was explained in section 2.3.2. The equations solved in the present simulations for k and $\widetilde{Z''^2}$ are reproduced here[16].

$$\frac{\partial(\overline{\rho}\,k)}{\partial t}+\frac{\partial(\overline{\rho}\,\widetilde{u}_i\,k)}{\partial x_i}=\frac{\partial}{\partial x_i}\left(\left(\mu+\frac{\mu_T}{\sigma_k}\right)\frac{\partial k}{\partial x_i}\right)+\overline{\rho}\,\wp-\overline{\rho}\,\varepsilon-\frac{2}{3}\overline{\rho}\,k\,\frac{\partial\widetilde{u}_i}{\partial x_i} \tag{4.1}$$

$$\frac{\partial(\overline{\rho}\,\widetilde{Z''^2})}{\partial t}+\frac{\partial(\overline{\rho}\,\widetilde{u}_i\,\widetilde{Z''^2})}{\partial x_i}=\frac{\partial}{\partial x_i}\left(\frac{\mu+\mu_T}{Sc_v}\frac{\partial\widetilde{Z''^2}}{\partial x_i}\right)+\overline{\rho}\wp_z-\overline{\rho}\,\chi \tag{4.2}$$

where Sc_v is the Schmidt number related to $\widetilde{Z''^2}$ and the production terms are equal to

[16]The equations are obtained applying Boussinesq hypothesis since k equation is taken from $k-\varepsilon$ model.

$$\wp = 2\overline{\rho}\,\nu_T \widetilde{s_{ij}}\ \widetilde{s_{ij}} = \overline{\rho}\,\nu_T \frac{\partial \widetilde{u_i}}{\partial x_j}\frac{\partial \widetilde{u_i}}{\partial x_j} + \overline{\rho}\,\nu_T \frac{\partial \widetilde{u_i}}{\partial x_j}\frac{\partial \widetilde{u_j}}{\partial x_i} \tag{4.3}$$

$$\wp_z = 2\overline{\rho}\,\frac{\nu_T}{Sc_v}\frac{\partial \widetilde{Z}}{\partial x_i}\frac{\partial \widetilde{Z}}{\partial x_i} \tag{4.4}$$

Equations 4.1 and 4.2 corroborate that variables k and $\widetilde{Z''^2}$ are governed by equations formally identical. Analysing the equations we first observe that they are composed of a transient, convective and diffusive terms that are identical in form.

The production terms $\wp$ and $\wp_z$, given by equations 4.3 and 4.4, respectively, show a similar structure[17]. In fact, the similarity for these terms becomes obvious if applying the boundary layer approximation for a round jet [48]

$$\wp = \overline{\rho}\nu_T \left(\frac{\partial \widetilde{u}}{\partial r}\right)^2 \tag{4.5}$$

$$\wp_z = 2\overline{\rho}\,\frac{\nu_T}{Sc_v}\left(\frac{\partial \widetilde{Z}}{\partial r}\right)^2 \tag{4.6}$$

where the nomenclature given in section 2.5.1 has been adopted.

The dissipation for k is measured by ε while for $\widetilde{Z''^2}$ values $\widetilde{\chi}$, which are defined by equations

$$\begin{aligned}\frac{\partial(\overline{\rho}\,\varepsilon)}{\partial t} + \frac{\partial(\overline{\rho}\,\widetilde{u_i}\,\varepsilon)}{\partial x_i} =& \frac{\partial}{\partial x_i}\left(\left(\mu + \frac{\mu_T}{\sigma_\varepsilon}\right)\frac{\partial \varepsilon}{\partial x_i}\right) + C_{\varepsilon 1}\,\overline{\rho}\frac{\varepsilon}{k}\,\wp - C_{\varepsilon 2}\,\overline{\rho}\,\frac{\varepsilon^2}{k} - \\ & - \left(\frac{2}{3}C_{\varepsilon 1} + C_{\varepsilon 3}\right)\overline{\rho}\,\varepsilon\,\frac{\partial \widetilde{u_i}}{\partial x_i}\end{aligned} \tag{4.7}$$

$$\widetilde{\chi} = C_\chi\,\frac{\varepsilon}{k}\,\widetilde{Z''^2} \tag{4.8}$$

Although equations 4.7 and 4.8 are completely different, equations for $\widetilde{\chi}$ has a very physical meaning if we note that k/ε and $\widetilde{Z''^2}/\widetilde{\chi}$ are characteristic

[17] The absence of the 2 in last equality of equation 4.3 is caused by the definition of k which values $1/2\,\widetilde{u_i''\,u_i''}$. It would be recovered if we defined the variable $\widetilde{u_i''\,u_i''} = 2\,k$ (in a similar way that $\widetilde{Z''^2}$).

times for turbulence and mixing, respectively. Equation 4.8 states that the time required for vortexes to dissipate variances[18] for turbulence and mixing are proportional.

Finally, equation 4.1 shows a term related to compressibility (it is generated by non-null velocity divergences) that does not appear in equation 4.2 (the last term of equation 4.7 corresponds to compressibility effects too). For the following reasoning we will neglect this contribution since it is expected not to be determinant downstream of some distance from the nozzle.

This analysis shows that both equations 4.1 and 4.2 are governed by similar processes and, hence, their equations are formally similar. However, they have some parameters (σ_k, Sc_v, C_χ) that may intensify some phenomena. It is expected that if these coefficients are properly chosen in order to provide similar weights to the different contributions of the equations, then k and $\widetilde{Z''^2}$ will show a similar behaviour[19]. In addition, as explained in section 2.5.1, fields $\widetilde{u}$ and $\widetilde{Z}$ collapse when normalized (this aspect have been checked for the present calculations) and, in consequence, $\wp$ and $\wp_z$ are proportional.

Based on this reasoning we describe in the following a numerical experiment where Sc_v and C_χ are taken equal to 1 [20,21]. Assuming $C_\chi = 1$ makes that the time scales are not only proportional but equal for both turbulence and mixing.

Figure 4.53 shows some level curves in the physical space for k, ε, $\widetilde{Z''^2}$ and $\widetilde{\chi}$ for this configuration.

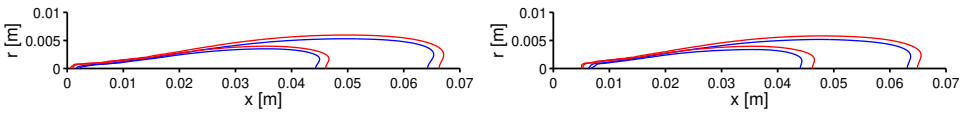

Figure 4.53. *Level curves for k (blue) and ε (red) in left figure and $\widetilde{Z''^2}$ (blue) and $\widetilde{\chi}$ (red) in right figure for inert nominal condition and Sc_v and C_χ equal to 1.*

It is clearly observed that the level curves for each of the variables (k and ε by one side and $\widetilde{Z''^2}$ and $\widetilde{\chi}$ by the other side) are overlapped. Even between

[18] k can be understood as the variance for velocity.

[19] That is, they should be proportional.

[20] σ_k has been taken equal to 1 in all the simulations of this thesis.

[21] The purpose of this experiment is not the improvement of the calculations but to evaluate how similar the fields are when taking the models parameters equal for k and $\widetilde{Z''^2}$.

the pair $(k, \widetilde{Z''^2})$ and $(\varepsilon, \widetilde{\chi})$ it is observed that the shape of the level curves is almost identical.

In order to gain more knowledge, axial and radial profiles are represented for these variables. As the values that they take differ by several orders of magnitude and in order to evaluate self-similarity, the following normalized variables are defined

$$\phi_{norm}(x, r/r_{\phi,0.01}(x)) = \frac{\phi(x,r)}{\phi(x,0)} \tag{4.9}$$

and

$$\phi_{norm,2}(x) = \frac{\phi(x,0)}{\phi(x^*,0)} \tag{4.10}$$

where ϕ is any variable, $r_{\phi,0.01}(x)$ is the radius where ϕ reaches 1 % of its value on the axis for the axial position x and x^* is a prescribed distance. Equation 4.9 normalizes the radial profiles by the corresponding value on the axis while equation 4.10 defines a normalization based on the value at some point on the axis for the axial profile. In the following figure x^* is taken equal to 15 mm.

Figure 4.54 compares similar variables (k and $\widetilde{Z''^2}$ by one side and ε and $\widetilde{\chi}$ by the other side) for the axial profiles while figure 4.55 is a similar representation for radial profiles at distances 30 and 60 mm.

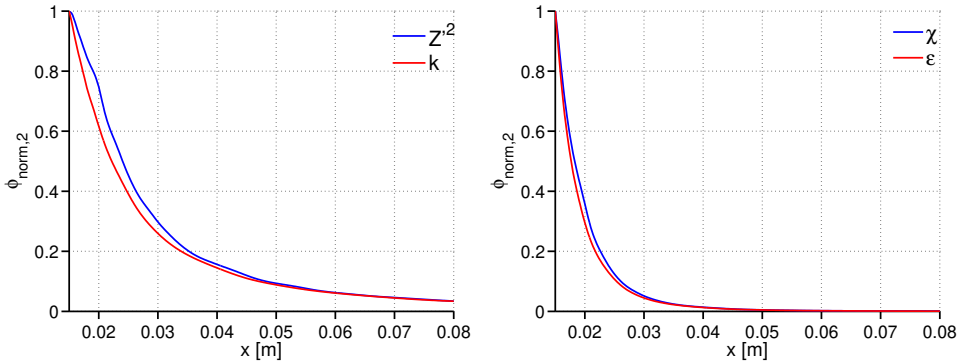

Figure 4.54. *Normalized axial profiles for k and $\widetilde{Z''^2}$ (left) and ε and $\widetilde{\chi}$ (right) for inert nominal condition and Sc_v and C_χ equal to 1.*

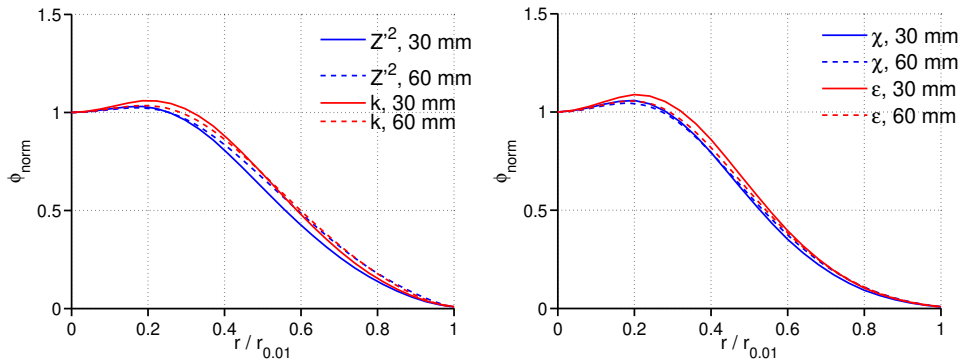

Figure 4.55. *Normalized radial profiles for k and $\widetilde{Z''^2}$ (left) and ε and $\widetilde{\chi}$ (right) at distances 30 and 60 mm for inert nominal condition and Sc_v and C_χ equal to 1.*

Figures 4.54 and 4.55 show that the curves for the pairs $(k, \widetilde{Z''^2})$ and $(\varepsilon, \widetilde{\chi})$ are almost collapsed in both axial and radial directions and this similarity means that variables of each pair are approximately related by a constant. Consequently, with this choice for the model parameters, equations 4.1 and 4.2 are not only formally identical but the values of their terms are approximately proportional.

In addition, it is verified that the radial profiles for the variances (k and $\widetilde{Z''^2}$) and dissipations (ε and $\widetilde{\chi}$) are self-similar. Self-similarity for k and ε was expected since, as explained in section 2.5.1 it has been experimentally verified that self-similarity does not only hold for mean variables, such as $\widetilde{u}$, but for Reynolds stresses ($\widetilde{u_i'' u_j''}$) too [48–50].

However, when considering the values taken for the configuration case of the calculations from this chapter, that is, Schmidt numbers equal to 0.9 and $C_\chi = 2$ the intensities of the different phenomena concurring in equations 4.1 and 4.2 take a different relative weight between those belonging to equation k and $\widetilde{Z''^2}$ and the proportionality between variables is lost. In order to analyse this, similar representations as those shown previously are gathered in figures 4.56, 4.57 and 4.58 for such configuration case.

The changes in the Schmidt number and C_χ do not have any effect on variables k and ε and, in consequence, their profiles are the same as those shown in figures 4.53, 4.54 and 4.55. Even if the changes in the model parameters do not have a strong effect on the level curves of $\widetilde{Z''^2}$ and $\widetilde{\chi}$, which as shown in figure 4.56 still remain almost overlapped, their axial profiles differ

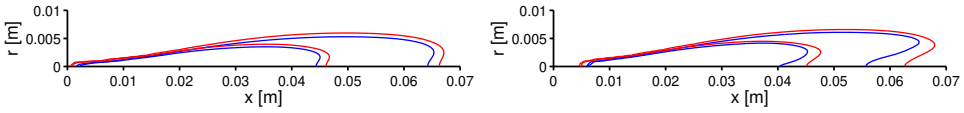

Figure 4.56. *Level curves for k (blue) and ε (red) in left figure and $\widetilde{Z''^2}$ (blue) and $\widetilde{\chi}$ (red) in right figure for inert nominal condition and $Sc_v = 0.9$ and $C_\chi = 2$.*

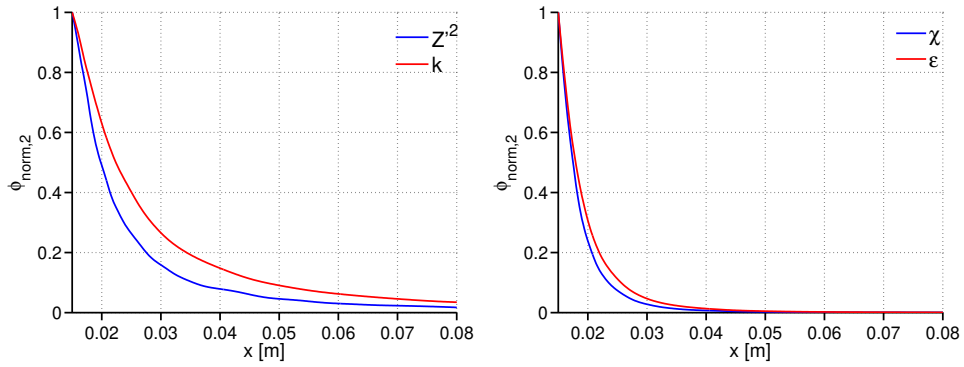

Figure 4.57. *Normalized axial profiles for k and $\widetilde{Z''^2}$ (left) and ε and $\widetilde{\chi}$ (right) for inert nominal condition and $Sc_v = 0.9$ and $C_\chi = 2$.*

from k and ε and the most prominent differences are observed in the radial profiles. In addition, self-similarity does not hold for these turbulent mixing variables ($\widetilde{Z''^2}$ and $\widetilde{\chi}$).

In this case even if equations 4.1 and 4.2 are still formally identical the different phenomena that describe k and $\widetilde{Z''^2}$ fields have different intensities and, hence, the proportionality between such fields does not hold.

In summary, even if the proportionality between k and $\widetilde{Z''^2}$ is lost when taking proportional but different time scales for the vortex dissipation and slightly distinct diffusivity, it seems that such changes do not have a strong impact on the overlapping of the level curves for $\widetilde{Z''^2}$ and $\widetilde{\chi}$ as was observed in section 4.4.3.4. Notwithstanding, it is emphasized that this is only a preliminary explanation and the profound causes of this phenomenology require further investigation.

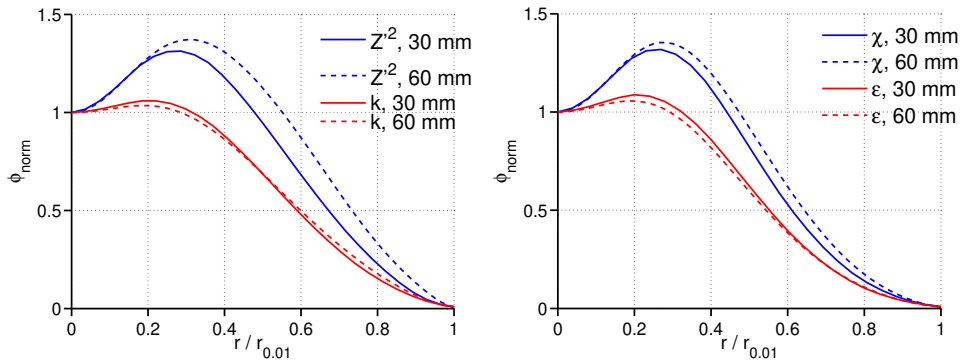

Figure 4.58. *Normalized radial profiles for k and $\widetilde{Z''^2}$ (left) and ε and $\widetilde{\chi}$ (right) at distances 30 and 60 mm for inert nominal condition and $Sc_v = 0.9$ and $C_\chi = 2$.*

References

[1] Pickett L. M., Bruneaux G. and Payri R. "Engine combustion network". *Sandia National Laboratories, Livermore, CA, https://ecn.sandia.gov/*, 2018.

[2] Bardi M., Payri R., Malbec L. M., Bruneaux G., Pickett L. M., Manin J., Bazyn T. and Genzale C. L. "Engine Combustion Network: comparison of spray development, vaporization, and combustion in different combustion vessels". *Atomization and Sprays*, Vol. 22 n^o 10, 2012.

[3] Maes N., Meijer M., Dam N., Somers B., Toda H. B., Bruneaux G., Skeen S. A., Pickett L. M. and Manin J. "Characterization of spray A flame structure for parametric variations in ECN constant-volume vessels using chemiluminescence and laser-induced fluorescence". *Combustion and Flame*, Vol. 174, pp. 138–151, 2016.

[4] Pickett L. M., Genzale C. L., Bruneaux G., Malbec L. M., Hermant L., Christiansen C. and Schramm J. "Comparison of diesel spray combustion in different high-temperature, high-pressure facilities". *SAE Int. J. Engines*, Vol. 3 n^o 2, pp. 156–181, 2010.

[5] Meijer M., Somers B., Johnson J., Naber J., Lee S. Y., Malbec L. M. C., Bruneaux G., Pickett L. M., Bardi M., Payri R. and Bazyn T. "Engine Combustion Network (ECN): characterization and comparison of boundary conditions for different combustion vessels". *Atomization and Sprays*, Vol. 22 n^o 9, 2012.

[6] Meijer M., Malbec L. M., Bruneaux G. and Somers L. M. T. "Engine Combustion Network: Spray A Basic Measurements and Advanced Diagnostics". In *12th Triennial International Conference on Liquid Atomization and Spray Systems (ICLASS 2012), Heidelberg, Germany, September*, pp. 2–6, 2012.

[7] Benajes J., Payri R., Bardi M. and Martí-Aldaraví P. "Experimental characterization of diesel ignition and lift-off length using a single-hole ECN injector". *Applied Thermal Engineering*, Vol. 58 n^o 1, pp. 554–563, 2013.

[8] Payri R., García-Oliver J. M., Xuan T. and Bardi M. "A study on diesel spray tip penetration and radial expansion under reacting conditions". *Applied Thermal Engineering*, Vol. 90, pp. 619–629, 2015.

[9] Skeen S. A., Manin J. and Pickett L. M. "Simultaneous formaldehyde PLIF and high-speed schlieren imaging for ignition visualization in high-pressure spray flames". *Proceedings of the Combustion Institute*, Vol. 35 n^o 3, pp. 3167–3174, 2015.

[10] García-Oliver J. M., Malbec L. M., Toda H. B. and Bruneaux G. "A study on the interaction between local flow and flame structure for mixing-controlled Diesel sprays". *Combustion and Flame*, Vol. 179, pp. 157–171, 2017.

[11] Gong C., Jangi M. and Bai X. S. "Large eddy simulation of n-dodecane spray combustion in a high pressure combustion vessel". *Applied Energy*, Vol. 136, pp. 373–381, 2014.

[12] Pei Y., Davis M. J., Pickett L. M. and Som S. "Engine combustion network (ECN): global sensitivity analysis of Spray A for different combustion vessels". *Combustion and Flame*, Vol. 162 n^o 6, pp. 2337–2347, 2015.

[13] Pei Y., Hawkes E. R., Kook S., Goldin G. M. and Lu T. "Modelling n-dodecane spray and combustion with the transported probability density function method". *Combustion and Flame*, Vol. 162 n^o 5, pp. 2006–2019, 2015.

[14] Pei Y., Som S., Pomraning E., Senecal P. K., Skeen S. A., Manin J. and Pickett L. M. "Large eddy simulation of a reacting spray flame with multiple realizations under compression ignition engine conditions". *Combustion and Flame*, Vol. 162 n^o 12, pp. 4442–4455, 2015.

[15] Pei Y., Hawkes E. R., Bolla M., Kook S., Goldin G. M., Yang Y., Pope S. B. and Som S. "An analysis of the structure of an n-dodecane spray flame using TPDF modelling". *Combustion and Flame*, Vol. 168, pp. 420–435, 2016.

[16] Akkurt B., Akargun H. Y., Somers L. M. T., Deen N. G., Novella R. and Pérez-Sánchez E. J. "An insight on the spray-A combustion characteristics by means of RANS and LES simulations using flamelet-based combustion models". *SAE Technical Paper 2017-01-0577, 2017, doi:10.4271/2017-01-0577*, 2017.

[17] Dahms R. N., Paczko G. A., Skeen S. A. and Pickett L. M. "Understanding the ignition mechanism of high-pressure spray flames". *Proceedings of the Combustion Institute*, Vol. 36 n^o 2, pp. 2615–2623, 2017.

[18] Desantes J. M., García-Oliver J. M., Novella R. and Pérez-Sánchez E. J. "Application of an unsteady flamelet model in a RANS framework for spray A simulation". *Applied Thermal Engineering*, Vol. 117, pp. 50–64, 2017.

[19] Kahila H., Wehrfritz A., Kaario O., Masouleh M. G., Maes N., Somers B. and Vuorinen V. "Large-eddy simulation on the influence of injection pressure in reacting spray A". *Combustion and Flame*, Vol. 191, pp. 142–159, 2018.

[20] Payri F., García-Oliver J.M., Novella R. and Pérez-Sánchez E. J. "Influence of the chemical mechanism in the frame of diesel-like CFD reacting spray simulations using a presumed PDF flamelet-based combustion model". In *ILASS Europe. 28th european conference on liquid atomization and spray systems*, pp. 678–685, 2017.

[21] CMT Motores Térmicos. "Universitat Politècnica de València, Spain". *http://www.cmt.upv.es/ECN03.aspx*, 2018.

[22] Kastengren A. L., Tilocco F. Z., Powell C. F., Manin J., Pickett L. M., Payri R. and Bazyn T. "Engine combustion network (ECN): measurements of nozzle geometry and hydraulic behavior". *Atomization and Sprays*, Vol. 22 n^o 12, pp. 1011–1052, 2012.

[23] Pope S. B. "An explanation of the turbulent round-jet/plane-jet anomaly". *AIAA journal*, Vol. 16 n^o 3, pp. 279–281, 1978.

[24] Novella R., García A., Pastor J. M. and Domenech V. "The role of detailed chemical kinetics on CFD diesel spray ignition and combustion modelling". *Mathematical and Computer Modelling*, Vol. 54 n^o 7, pp. 1706–1719, 2011.

[25] Beale J. C. and Reitz R. D. "Modeling spray atomization with the Kelvin-Helmholtz/Rayleigh-Taylor hybrid model". *Atomization and sprays*, Vol. 9 n^o 6, 1999.

[26] Desantes J. M., García-Oliver J. M., Pastor J. M. and Pandal A. "A comparison of diesel sprays CFD modeling approaches: DDM versus Σ-Y Eulerian atomization model". *Atomization and Sprays*, Vol. 26 n^o 7, 2016.

[27] Pera C., Colin O. and Jay S. "Development of a FPI detailed chemistry tabulation methodology for internal combustion engines". *Oil & Gas Science and Technology-Revue de l'IFP*, Vol. 64 n^o 3, pp. 243–258, 2009.

[28] Narayanaswamy K., Pepiot P. and Pitsch H. "A chemical mechanism for low to high temperature oxidation of n-dodecane as a component of transportation fuel surrogates". *Combustion and Flame*, Vol. 161 n^o 4, pp. 866–884, 2014.

[29] Yao T., Pei Y., Zhong B. J., Som S. and Lu T. "A hybrid mechanism for n-dodecane combustion with optimized low-temperature chemistry". In *9th US National Combustion Meeting, Cincinnati, Ohio*, pp. 17–20, 2015.

[30] Wang H., Ra Y., Jia M. and Reitz R. D. "Development of a reduced n-dodecane-PAH mechanism and its application for n-dodecane soot predictions". *Fuel*, Vol. 136, pp. 25–36, 2014.

[31] "OpenFOAM". *http://www.openfoam.com/*, 2017.

[32] Vasu S. S., Davidson D. F., Hong Z., Vasudevan V. and Hanson R. K. "n-Dodecane oxidation at high-pressures: measurements of ignition delay times and OH concentration time-histories". *Proceedings of the Combustion Institute*, Vol. 32 n^o 1, pp. 173–180, 2009.

[33] Skeen S., Manin J. and Pickett L. M. "Visualization of ignition processes in high-pressure sprays with multiple injections of n-dodecane". *SAE International Journal of Engines*, Vol. 8 n^o 2, pp. 696–715, 2015.

[34] Epaminondas M. "Ignition of turbulent non-premixed flames". *Progress in Energy and Combustion Science*, Vol. 35 n^o 1, pp. 57–97, 2009.

[35] Pickett L. M., Manin J., Genzale C. L., Siebers D. L., Musculus M. P. B. and Idicheria C. A. "Relationship between diesel fuel spray vapor penetration/dispersion and local fuel mixture fraction". *SAE International Journal of Engines*, Vol. 4 n^o 2011-01-0686, pp. 764–799, 2011.

[36] Eagle W. E., Musculus M. P. B., Malbec L. M. C. and Bruneaux G. "Measuring transient entrainment rates of a confined vaporizing diesel jet". In *ILASS Americas 26th Annual Conference on Liquid Atomization and Spray Systems, Portland, OR*, 2014.

[37] Barths H., Hasse C., Bikas G. and Peters N. "Simulation of combustion in direct injection diesel engines using a eulerian particle flamelet model". *Proceedings of the Combustion Institute*, Vol. 28 n^o 1, pp. 1161–1168, 2000.

[38] Dhuchakallaya I., Rattanadecho P. and Watkins P. "Auto-ignition and combustion of diesel spray using unsteady laminar flamelet model". *Applied Thermal Engineering*, Vol. 52 n^o 2, pp. 420–427, 2013.

[39] Winklinger J. F. *Implementation of a combustion model based on the flamelet concept and its application to turbulent reactive sprays*. Doctoral Thesis, Universitat Politècnica de València, 2015.

[40] Bhattacharjee S. and Haworth D. C. "Simulations of transient n-heptane and n-dodecane spray flames under engine-relevant conditions using a transported PDF method". *Combustion and Flame*, Vol. 160 n^o 10, pp. 2083–2102, 2013.

[41] Pickett L. M., Siebers D. L. and Idicheria C. A. "Relationship between ignition processes and the lift-off length of diesel fuel jets". *SAE technical paper*, 2005.

[42] Idicheria C. A. and Pickett L. M. "Effect of EGR on diesel premixed-burn equivalence ratio". *Proceedings of the Combustion Institute*, Vol. 31 n^o 2, pp. 2931–2938, 2007.

[43] Idicheria C. A. and Pickett L. M. "Soot formation in diesel combustion under high-EGR conditions". *SAE Technical Paper*, 2005.

[44] Dec J. E. "A conceptual model of DI diesel combustion based on laser-sheet imaging". *SAE Technical paper*, 1997.

[45] Idicheria C. A. and Pickett L. M. "Formaldehyde visualization near lift-off location in a diesel jet". *SAE Technical Paper*, 2006.

[46] Poinsot T. and Veynante D. *Theoretical and numerical combustion*. RT Edwards Inc., 2005.

[47] Michel J. B. and Colin O. "A tabulated diffusion flame model applied to diesel engine simulations". *International Journal of Engine Research*, pp. 346–369, 2013.

[48] Pope S. B. *Turbulent flows*. IOP Publishing, 2001.

[49] Tennekes H. and Lumley J. L. *A first course in turbulence*. MIT press, 1972.

[50] Hussein H. J., Capp S. P. and George W. K. "Velocity measurements in a high-Reynolds-number, momentum-conserving, axisymmetric, turbulent jet". *Journal of Fluid Mechanics*, Vol. 258, pp. 31–75, 1994.

Chapter 5

Analysis of the diesel spray in the LES framework

Contents

5.1 Introduction

Chapter 4 analysed a diesel-like spray in the context of RANS simulations in order to figure out the flame temporal and spatial structure. RANS turbulence models may offer a great variety of advantages for engineering problems since, generally speaking, they provide a good ratio between accuracy and computational requirements. Although all the turbulence scales are modelled and this may be an impediment for their application if the turbulence

model is not suited for a given problem, their computational cost is remarkably low compared to other approaches.

However, their lack of accuracy for complex flow configuration problems[1] and the impossibility of modelling intermittent phenomena, which may be only partially devised if transporting scalar variances, may not compensate its advantages in computational cost.

In this context, the continuous increasing computational power that has been experimented for decades invites to apply other approaches that, despite their penalty in computational resources, provide a new spectrum of possibilities. In this way, LES calculations have been receiving increasing attention during the last years, especially in the present research field.

Two aspects contribute to an expectable improvement of computations accuracy for LES calculations. The first one is that the largest eddies are not modelled but solved. The second one is that, according to the classical turbulence theory, vortexes tend to be isotropic when decreasing in size and, therefore, the small eddies modelling is expected to be more universal and less subjected to the particular flow boundary conditions. Other interesting LES strong point is its ability to reproduce flow intermittency which may be important in problems that show high variability like cyclic dispersion in gasoline engines [1].

However, these advantages are not exempt of cost. Solving a wide range of vortexes requires decreasing the cell size and, consequently, decreasing the time step too in order to limit Courant numbers. In addition, symmetry simplifications cannot be applied. Finally, finding representative initial and boundary conditions may be more difficult in LES than in RANS and their accuracy may have a stronger impact on flow results. All these facts produce an increase in computational cost of several orders of magnitude when compared with solving the same problem with RANS turbulence models.

In the case of diesel sprays, as a particular type of free shear flows, transport phenomena are mainly controlled by the motion of the large scales which are solved in LES simulations [2]. However, chemical reactions occur at the smallest scales of the flow since they take place when species are mixed at molecular level. Therefore, LES simulations cannot solve chemical reactions but have to model them [2, 3] allowing to directly extend RANS combustion models to LES.

[1] Problems with strong gradients in one of the directions that derive in highly anisotropic flows, flows with recirculation, etc. are still challenging in the context of RANS turbulence models.

Although it may seem that there is no clear advantage in applying LES simulation to diesel sprays, this is not the case since the non-reactive scalars are better predicted and the accuracy of flamelet combustion models rely on the ability to reproduce these fields. In addition, it is expected that the shape of the filtered probability density function (FPDF) has less effect on results than in RANS [3].

The deeper understanding that can be achieved with LES simulations in the research of diesel-like sprays encourages to apply this approach to spray A simulation. Thus, spray A modelling is accomplished in this chapter by means of an LES turbulence model and the ADF approach explained in chapter 3 in order to analyse this spray and complement the investigation carried out in chapter 4.

5.2 Boundary conditions

As in chapter 4 the problem to be solved is spray A from ECN [4]. Here only the temperature parametric variation with $X_{O_2} = 0.15$ is calculated. Since the characterization of the problem has been already specified in section 4.2 from chapter 4 it is omitted here and only the boundary conditions are summarized in table 5.1 for the sake of completeness.

Table 5.1. *Definition of spray A simulated parametric study.*

X_{O2}	T_{amb} (K)	ρ_{amb}(kg/m^3)	p_{amb} (MPa)	p_{inj} (MPa)	Z_{st}	Z_s
0.15	750	22.8	4.97	150	0.046	0.251
0.15	800	22.8	5.3	150	0.046	0.278
0.15	850	22.8	5.63	150	0.046	0.303
0.15	900	22.8	5.96	150	0.046	0.326

5.3 Mesh and model description

In this work, the LES turbulence model used for calculations is the Dynamic Structure model (DS) [5–8] described in section 2.3.3.4. It is not based on Boussinesq hypothesis and transports the subgrid kinetic energy k_{sgs} allowing the use of coarser meshes [5]. This is extremely useful when applying the Discrete Droplet Model (DDM) since this formulation assumes that the liquid concentration does not exceed a threshold value in order to fulfil some

hypotheses and, therefore, large cells are more compatible with this type of modelling.

The DDM is composed of different models in order to describe the different aspects of injection. The Reitz model [9] is used to describe Kelvin-Helmholtz and Rayleigh-Taylor instabilities. Droplets are injected according to a Rosin-Rammler distribution with droplet diameter ranging from 10 μm to the nozzle diameter. As droplets size follows a distribution it is not necessary to use atomization model since no liquid vein exists in the simulation. Ranz-Marshall model is used for droplet evaporation and O'Rourke model to describe collision. Finally, to say that DS model contains a source term in k_{sgs} transport equation that accounts for subgrid interactions between gas phase and liquid droplets.

Regarding the combustion model, the ADF model in the form described in chapter 3 is applied. As in previous calculations the progress variable $Y_c = Y_{\mathrm{CO}} + Y_{\mathrm{CO_2}}$ is used [10]. For these calculations only Narayanaswamy mechanism (255 species and 2289 reactions) has been used [11].

The FPDFs applied to the LES simulations are a beta function (see section 3.2.3) for the mixture fraction and Dirac deltas for the scalar dissipation rate and time. To describe accurately the turbulent flame manifold, and depending on the boundary conditions, around 32 values for $\widetilde{Z}$, 17 for S and 35 for $\widetilde{\chi}_{st}$ are used. To retain ignition accurately, 51 values are used for $\widetilde{Y}_c$ (or more precisely d) that follow a parabolic distribution.

The coupling between the turbulent flame manifold and CFD was explained in section 3.2.4 and is the same that the one used for RANS simulations, that is, a weak coupling where species chemical source terms are obtained from species mass fractions according to option 2 (see section 3.2.4). The transported species are H, OH, CO, CO_2, H_2O, $C_{12}H_{26}$, CH_2O, C_2H_2, N_2, C_7H_{14}, H_2 and O_2, where the last three act as sink species.

CFD equations are solved in the open tool-box OpenFOAM environment [12] using an in-house developed code. A PISO algorithm is applied with second order schemes to discretize temporal derivative as well as Laplacian and divergence terms.

Finally, the mesh is a cylinder divided into 3.6 Million cells, approximately, where the cell size and distribution are based upon spray geometry. Its radius is 23.5 mm while its height is 108 mm. Open boundary conditions are imposed for all the faces except for the base of the cylinder, where the injector is positioned, which is a wall. To better solve the spray, the mesh is refined in the interior of an internal prism with its axis coincident with the cylinder one. This prism has square base with side 1.688 mm and is divided in cells with square base of 62.5 μm according to [13, 14].

The rest of the mesh is discretized in a cylindrical coordinate system with 108, 108 and 292 cells in radial, azimuthal and axial directions, respectively. Expansion ratios between cells of 1.015 and 1.01 for the radial and the axial directions, respectively, are imposed. Figures 5.1 and 5.2 show different views and cuts of the mesh.

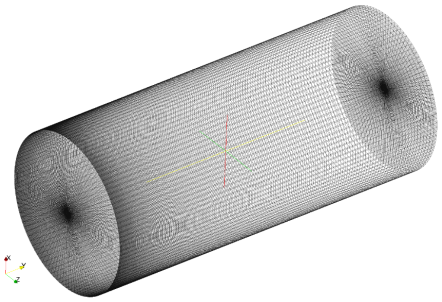

Figure 5.1. *3D view of the mesh and the domain.*

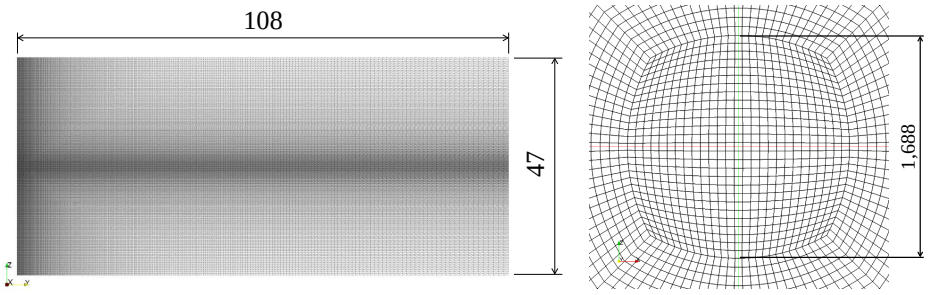

Figure 5.2. *Different cuts of the mesh used for calculations. Left figure shows a cut to the cylinder containing its axis. Right figure shows a perpendicular cut to the cylinder axis with a zoom at the inner prism. Dimensions in mm.*

Moreover, the time step has been taken equal to 0.02 μs, deemed to be small enough, since it ensures low Courant numbers and allows a very accurate description of the physical and chemical phenomena.

5.4 Results and discussion

In a similar way that it was done in chapter 4, first, the set-up of the model together with the analysis of the main reactive parameters are described in order to appreciate the capabilities of the model prior to the fields study and effect of the boundary conditions. As the behaviour of homogeneous reactors as well as flamelets was given in chapter 4 we directly focus the study on CFD analysis. The following discussion can be found in the author's work [15].

5.4.1 Set-up of the model

As in chapter 4, spray is first calibrated in inert conditions comparing vapour penetration and liquid length between experiments [16] and simulations for inert nominal case as shown in figure 5.3. Vapour penetration and liquid length follow the same definitions than those given in section 4.4.3.1.

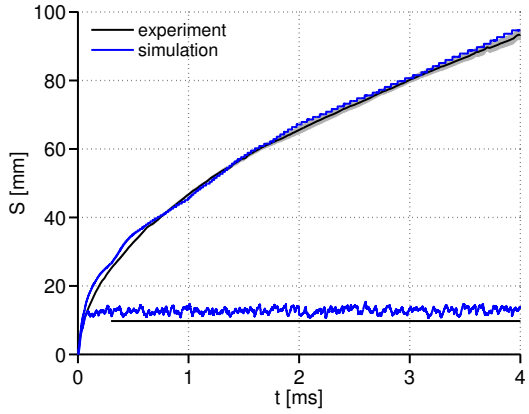

Figure 5.3. *Vapour penetration and liquid length for experimental and simulated inert nominal condition. For experiment, uncertainty of measurements is delimited with shadows.*

Although a slight over-prediction of the liquid length is observed, an excellent agreement exists for the vapour penetration. Due to the spatial separation that exists between the liquid zone and the combustion region for spray A conditions (see chapter 4.4.3.1), it is deemed that the slight over-prediction of the liquid length is not critical if fields related to mixture fraction are well-captured, as we shall see in the following. Figure 5.3 is a first confirmation of the ability of the simulation to reproduce spray characteristics.

The validation continues comparing simulated profiles for mixture fraction $\langle \widetilde{Z} \rangle$ and its variance or, in this case, its root mean square (rms), $\sqrt{\langle \widetilde{Z''^2} \rangle}$ or Z_{rms}, as well as the axial velocity $\langle \widetilde{U} \rangle$ with experimental results in figure 5.4 for the inert spray. It is reminded that the symbol $\langle\rangle$ is used to denote average in LES context and can be performed in different directions (see section 2.3.3.1). In this work, both azimuthal and temporal averages are considered when using the symbol $\langle\rangle$ unless otherwise stated. Mixture fraction variances are calculated as the sum of the variance of the solved mixture fraction field and the subgrid mixture fraction variance component as explained in section 2.3.3.1.

Rayleigh imaging was used to obtain experimental fields related to mixture fraction while Particle Image Velocimetry (PIV) technique was used for velocity [17–20]. In the same way that in chapter 4, the discrepancies between nozzle diameters force to normalize distance by the equivalent diameter. Velocity is normalized with the estimated nozzle exit velocity. Radials cuts for 50 and 90 d_{eq} correspond to distances of 25 and 45 mm, approximately.

Figure 5.4 shows an excellent agreement for both $\langle \widetilde{Z} \rangle$ and $\langle \widetilde{U} \rangle$. Different to RANS simulations, constant C_χ has not strong impact on Z_{rms} LES profiles since this constant only affects to the modelled part (see equation 3.60). A slight decrease of Z_{rms} is found when increasing C_χ since this increase enhances mixture fraction variance dissipation (see section 4.4.3.5). It is deemed that a value of $C_\chi = 5$ provides similar profiles than those measured and is adopted for subsequent calculations.

In order to assess the accuracy of the simulation it is convenient to compare the modelled and solved quantities. For this purpose, figure 5.5 shows the modelled and total $\langle \widetilde{Z''^2} \rangle$ and $\langle \widetilde{\chi} \rangle$.

It is observed that an important percentage of the total $\langle \widetilde{Z''^2} \rangle$ is solved in the simulation especially when moving downstream. However, for $\langle \widetilde{\chi} \rangle$ almost all its content is modelled and only a very small amount is solved. This was expected since the scalar dissipation rate is a variable related to the smallest scales of the flow and, therefore, it is foreseeable that an LES simulation only solves a small portion of such variable. In addition, close to the nozzle the DDM spray model imposes a minimum cell value of 62.5 μm [13, 14] which is probably large considering the characteristic length and velocity of the problem nearby the nozzle. In conclusion, these results are considered a positive validation of the simulation since a large fraction of $\langle \widetilde{Z''^2} \rangle$ is solved.

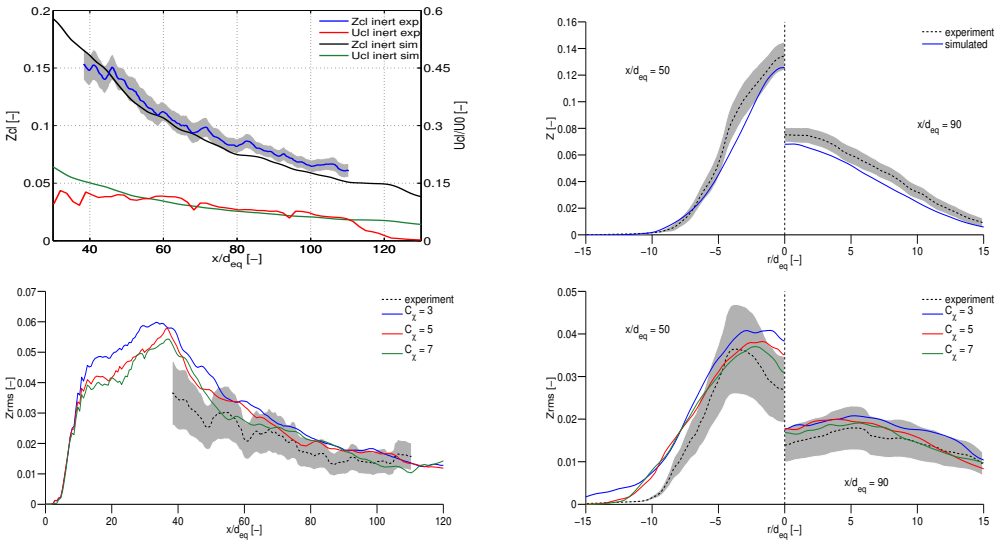

Figure 5.4. *Spray validation for very advanced instants. Top left:* $\langle \widetilde{Z} \rangle$ *and normalized* $\langle \widetilde{U} \rangle$ *on the centerline. Top right:* $\langle \widetilde{Z} \rangle$ *radial profiles at* 50 *and* 90 d_{eq}*. Bottom left:* Z_{rms} *on the centerline for different* C_χ *values. Bottom right:* Z_{rms} *radial profiles at* 50 *and* 90 d_{eq} *for different* C_χ *values. Experimental uncertainties delimited with shadowed regions. Results for inert nominal condition.*

As a complementary aspect, the energetic spectral content of turbulence is shown in figure 5.6 for inert nominal case. The spectra are obtained in two points on the axis and other radially displaced.

The spectrum is obtained in the frequency domain from the axial velocity signal registered during several milliseconds at a fixed point once the turbulent statistics stabilize, as described in section 2.3.2, but applying the concepts to variable time instead of space [21].

Figure 5.6 shows that there exists a range of frequencies, where spectrum slope is almost flat, that matches with the energy-containing range of the flow. For higher frequencies it is observed that, despite the signal noise, the spectrum falls with a slope close to -5/3, as described by the classical turbulence theory [22–24], that corresponds with the inertial subrange. Such subrange extends from 10^4 to 10^5 Hz, approximately.

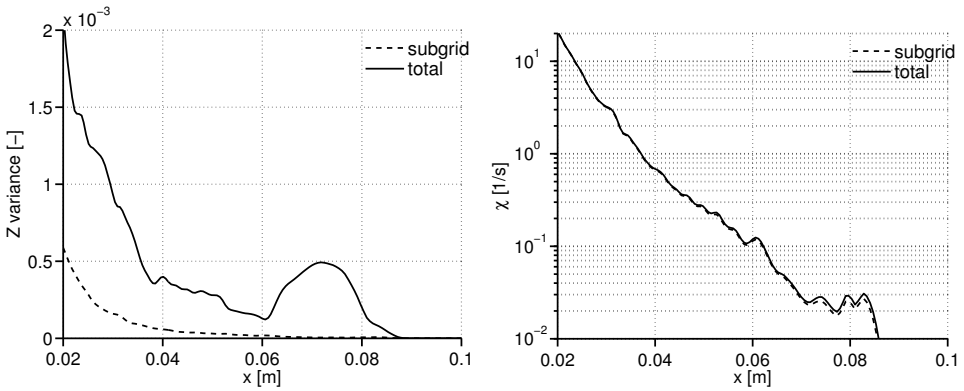

Figure 5.5. *Total and subgrid* $\langle \widetilde{Z''^2} \rangle$ *and* $\langle \widetilde{\chi} \rangle$ *variables on the axis. Results for inert nominal case.*

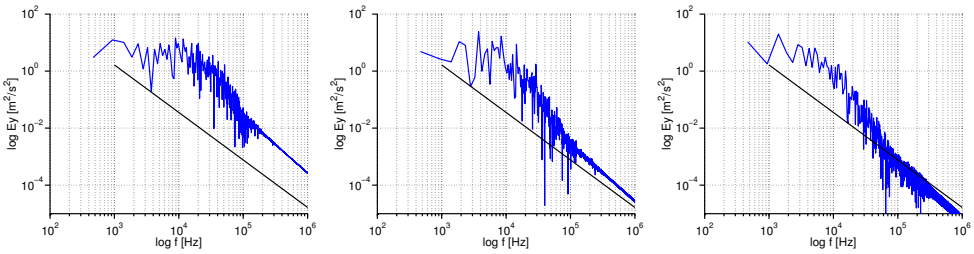

Figure 5.6. *Energy spectra in the frequency domain for two points on the axis at a distance of 20 (left) and 30 mm (center) and a 2 mm radially displaced point positioned 30 mm from the nozzle (right). For reference a straight line with slope -5/3 is included too. Results for inert nominal case.*

In LES simulations, it is intended to solve partially or completely the inertial subrange [2]. However, in the current simulations, it is possible that this range is not completely solved since the application of the DDM formulation forces to impose relatively coarse cell sizes in order to fulfil its hypotheses. As explained in section 5.3, the minimum cell size is 62.5 μm following results given in literature for similar models and calculations[2] [13, 14].

It is worth mentioning that, as observed from figure 5.6, moving downstream on the axis or moving away from the axis at a fixed axial position

[2]Note that the nozzle diameter is 90 μm, approximately.

provokes a displacement of the inertial subrange to lower frequencies since the flow dynamics become slower due to the reduction of velocities.

After the previous satisfactory inert spray calibration, some preliminary results for the reactive spray are shown to validate it too. Figure 5.7 compares tip penetration and liquid length for experiments [16] and simulations for the reactive nominal case. Again the definitions given in 4.4.3.1 are applied.

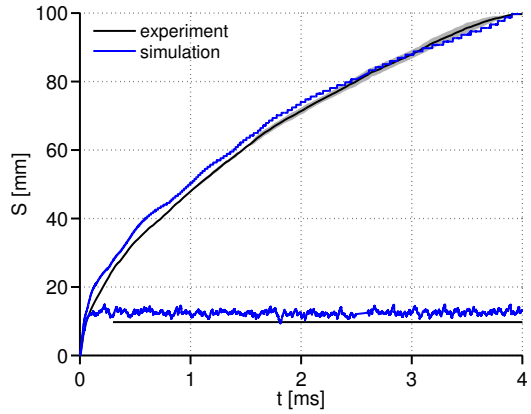

Figure 5.7. *Tip penetration and liquid length for experimental and simulated reactive nominal condition. For experiment, uncertainty of measurements is delimited with shadows.*

In a similar way to the inert spray, simulated tip penetration shows an excellent agreement with the experimental profile. Liquid length is slightly overestimated, but as was explained previously, as it is spatially isolated from the flame region it is expected that this overestimation will not affect subsequent results.

Figure 5.8 gathers the average axial velocity on the axis normalized by the nozzle exit velocity for the reactive nominal condition. Although velocity is slightly underestimated when comparing with the experiment, it is considered that results are acceptable.

To close this validation, a qualitative comparison of formaldehyde and hydroxide fields with fields measured with LIF technique [20] is carried out in a similar way as described in section 4.4.3.4 with figure 4.25. Results are shown in figure 5.9, where experimental and simulated averaged fields are included. For LES, fields are temporally and azimuthally averaged. In addition, and for illustrative purposes, instantaneous LES fields are included too. Lengths are normalized with the equivalent diameter.

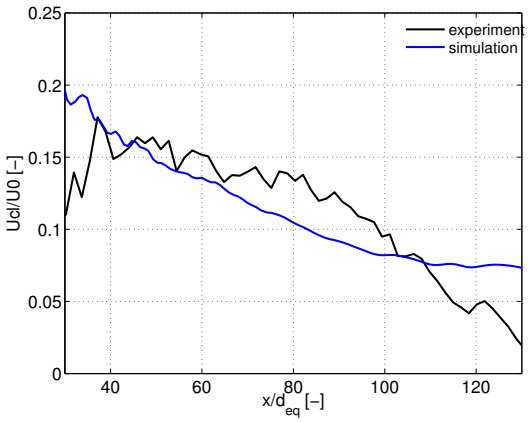

Figure 5.8. *Experimental and simulated normalized $\langle \widetilde{U} \rangle$ on the centerline for reactive nominal condition.*

As explained in section 4.4.3.4, image measured with 355 nm LIF technique is saturated in order to visualize formaldehyde field since according to [20] there exists possible interferences with PAHs.

In agreement with experimental results, LES simulations predict CH_2O in the zone of rich mixtures close to the lift-off length between 30 and 50 d_{eq}. Different to the experiment where formaldehyde seems to extend upstream of the lift-off length, in the simulation it is limited to the region downstream of this distance.

Hydroxide fields are qualitatively similar and spread in the same region downstream of the lift-off length. Unfortunately, the laser sheet extends until 92 d_{eq} and not further information is available.

This comparison only intends to be qualitative but it shows a good agreement between experiments and simulations.

The results obtained so far for inert and reactive conditions provide a preliminary validation of the simulations which show a remarkable agreement with experimental data. The validation is complemented with some reactive flame parameters in next section.

5.4.2 Flame metrics

In this section, flame metrics, namely, ignition delay and lift-off length, are compared between experiments and simulations. Definitions for ignition delay

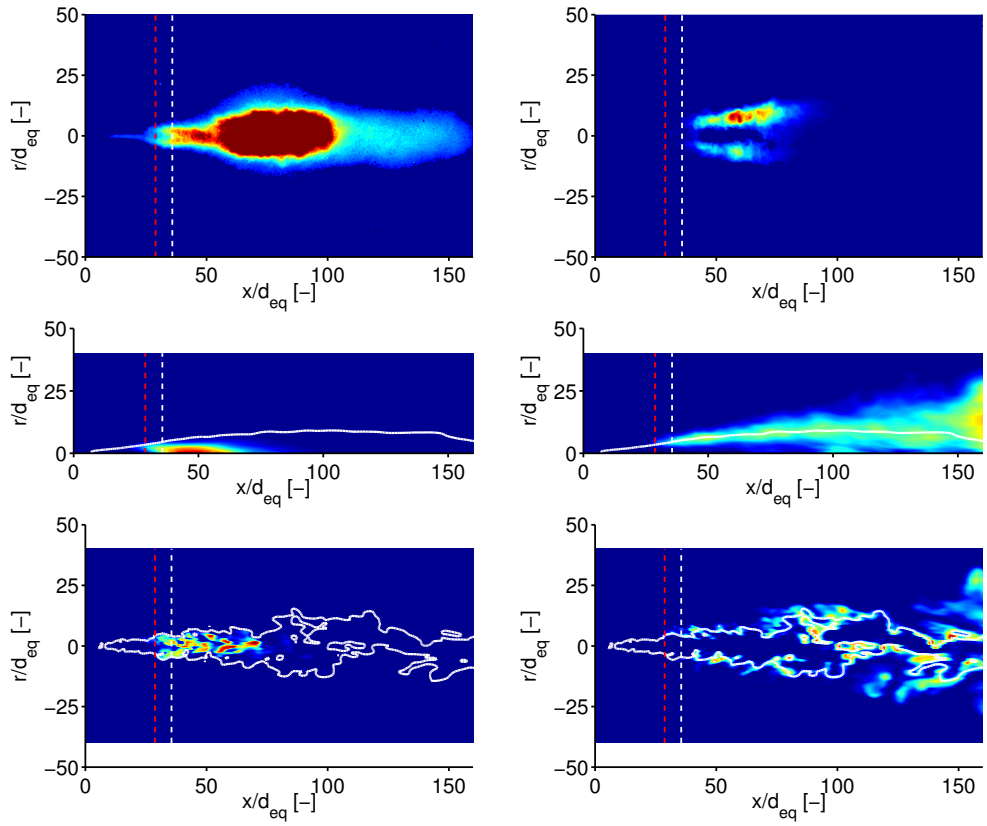

Figure 5.9. *Comparison of CH_2O and OH fields for the nominal case. First row corresponds to experimental results, second row is for LES averaged solutions and third row is for instantaneous LES fields. Left column shows 355 nm LIF signal for the experiment and CH_2O field for the simulation while right column is derived from OH LIF signal for the experiment and shows OH field for the simulation. Lift-off length values for experiment (white dashed line) and simulation (red dashed line) are included and the stoichiometric level curve is shown for the modelled results.*

and lift-off length were given in section 4.4.3.2. However, in LES simulations, lift-off length criterion requires some additional considerations.

As in LES simulations filtered fields are solved, we can define two lift-off length values: the first one is the minimum axial distance from the nozzle to the surface level given by the averaged Favre filtered OH mass fraction corresponding to the 14 % of the maximum value reached in this field. We

label this criterion as 'LES OH aver.'[3]. The second definition is given by the average of the minimum axial distance from the nozzle to the surface level of the Favre filtered OH mass fraction corresponding to the 14 % of the maximum value reached in this field. We refer to this criterion as 'LES OH instant.'.

Note that the difference between both definitions is the order of the operations (averaging the instantaneous field and measuring or measuring the instantaneous field and averaging). This makes possible to evaluate the effect of altering the order of the operations. Figure 5.10 gathers the flame metrics when changing the ambient temperature.

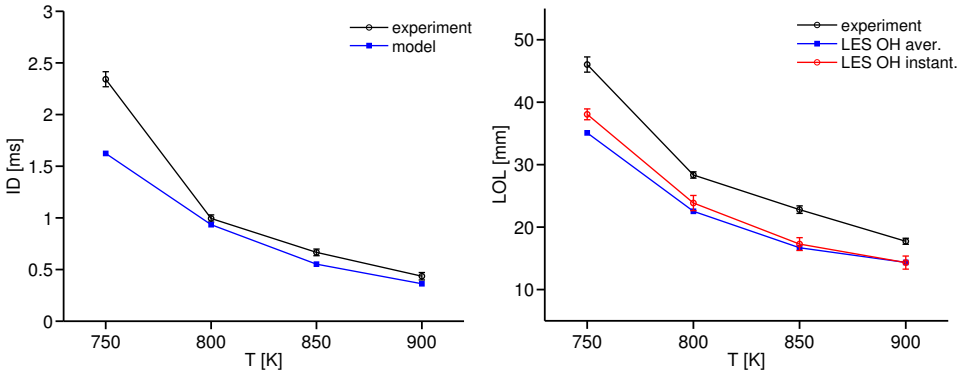

Figure 5.10. *Ignition delay (left) and lift-off length (LOL) for the temperature parametric sweep. Error bars delimit the standard deviation of the variable.*

Figure 5.10 shows an excellent agreement for ignition delay except for the lowest temperature for which LES predicts a too fast ignition. Regarding lift-off length, both definitions underestimate measured values although they reproduce the experimental trend since they move almost parallel to the experimental curve. Moreover, both definitions provide very close values though some discrepancies arise when decreasing mixture reactivity.

As an instantaneous lift-off length position is computed from the filtered hydroxide field, a standard deviation for the criterion 'LES OH instant.' can be calculated, which is included in figure 5.10 by means of error bars in a similar way to the experiment standard deviation. This lift-off length variability is computed from resolved motions and does not consider a subgrid component. Notwithstanding, it is considered that this fact does not change subsequent

[3]This corresponds to lift-off length ECN criterion.

conclusions. From figure 5.10, it is observed that the fluctuation levels are not high and, as the experiments, remain in the order of ±1mm.

To deepen more in this feature, figure 5.11 shows how lift-off length evolves in time according to the instantaneous filtered hydroxide mass fraction field. In addition, 'LES OH aver.' is included too.

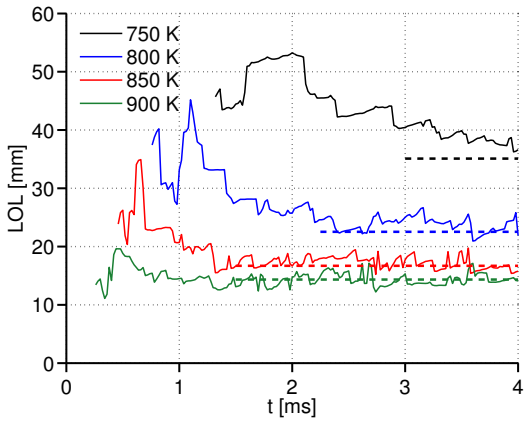

Figure 5.11. *Instantaneous lift-off length evolutions for the different ambient temperature cases (solid line) and 'LES OH aver.' lift-off length (dashed line). Lines with same colour correspond to same boundary conditions.*

From figure 5.11, it emerges that the first ignition kernels appear downstream of the stabilized lift-off length value since, as observed, lift-off length suffers a recession after spray auto-ignition, in agreement with experimental and modelling results [25–27].

Corroborating figure 5.10, lift-off length fluctuations are small (±1 mm) and do not show a clear dependence with air temperature.

It is interesting to note that lift-off length position suffers some rapid and sharp jumps, similar to discontinuities once it has stabilized, e.g. at 3.5 ms for 800 K or 2.7 ms for 900 K. This is not caused by a rapid recession of the base of the flame but to the apparition of isolated ignition kernels that burn spontaneously in the vicinity and upstream of the base of the flame. This phenomenon will be analysed in more detail in section 5.4.3.

Summarizing, results from figure 5.11 establish that the base of the flame, defined by the lift-off length position, is anchored in the vicinity of a fixed point and does not suffer intense fluctuations for any of the analysed boundary conditions. From this, it is deduced that, in a diesel spray, even when mixture

reactivity is not high, flame dynamics adapt to the local flow conditions in order to generate a stable and vigorous flame. This is caused by a chemical activity that is weak upstream of the lift-off length but is triggered at the base of the flame with a so high intensity that is not strongly affected by local flow variations provoking low lift-off length fluctuations. Connecting this with the conceptual diesel flame description [28] as well as the results provided by this combustion model in the RANS framework (chapter 4), this intense chemistry produces a partially premixed combustion established at the lift-off length distance, where reactants burn rapidly into intermediate products and release important amounts of heat. More insight about these ignition kernels is provided in next section.

5.4.3 Instantaneous filtered fields

In this section the instantaneous fields for temperature and some relevant species are shown in the spatial and Z - T representations. The analysis is followed by the description of the formation of ignition kernels at the base of the flame.

Fields $\widetilde{T}$, $\widetilde{Y_{CH_2O}}$, $\widetilde{Y_{C_2H_2}}$ and $\widetilde{Y_{OH}}$ are shown for instants 3500, 3800 and 4000 μs for the reactive nominal case in figure 5.12.

Figure 5.12 reveals the structure of the flame which is composed of a partially premixed combustion zone anchored at the lift-off length distance. Ignition kernels are observed and stabilize the flame burning into products and reaching temperatures close to 2000 K on the stoichiometric level curve. The partially premixed combustion region adopts a W shape where the lobes are separated by an inert or less reactive mass on the axis that does not ignite so fast due to its mixture richness.

Downstream of the partially premixed combustion, a diffusion flame, with a less vigorous burning rate, is established in the vicinity of the stoichiometric level curve that wraps the spray and where the maximum temperature in the domain is found due to the completeness of chemical reactions. Nevertheless, pockets with high and low temperature alternate in the head of the spray as a consequence of the inhomogeneities induced by the turbulent flow.

Regarding the different species, formaldehyde appears in the vicinity of the lift-off length since it is related to the low temperature chemistry. The field is enclosed by the stoichiometric level curve and, hence, is limited to rich mixtures that are found close to the axis. High variability is found in this field between instants as a consequence of the high velocities of this

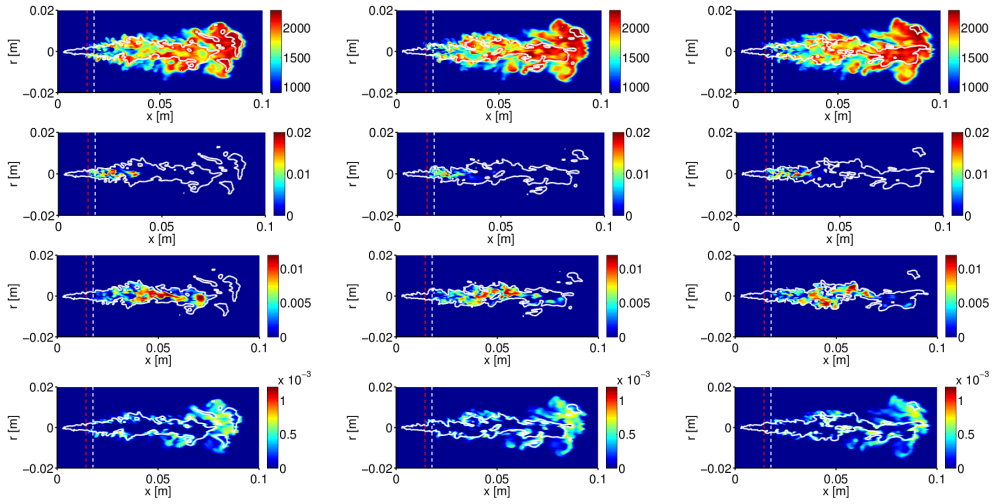

Figure 5.12. *Instantaneous fields for $\widetilde{T}$ (first row), $\widetilde{Y_{CH_2O}}$ (second row), $\widetilde{Y_{C_2H_2}}$ (third row) and $\widetilde{Y_{OH}}$ (last row) for the instants 3500 (left), 3800 (center) and 4000 μs (right). The level curve $\widetilde{Z} = Z_{st}$ is included in white line. Lift-off length values for experiment (white dashed line) and simulation (red dashed line) are shown too. Results for nominal case.*

region. Downstream of formaldehyde, acetylene is found, which is limited to rich mixtures and shows a high variability in its morphology too.

Finally, as was expected, hydroxide, a tracer of high temperature chemistry, is found in the vicinity of the stoichiometric level curve where the highest temperature in the domain is reached. The stoichiometric level curve shows a high variability between the different instants even far from the nozzle, where velocities are moderate provoking in turn a high variability of hydroxide since this species shows a strong dependence on the mixture fraction.

It is worth mentioning that although the fields show strong variations in their morphology their peak values are remarkably similar between instants. This means that, although the flame shows strong local variations, its global picture is hardly altered along time.

Moreover, LES simulations reproduce the small eddies generated in the periphery of the spray responsible of the intense mixing between spray and quiescent air, as a consequence of the very high gradients that are produced [29]. High fluctuations are found in the proximities of the lift-off length

that are moderated when moving downstream due to the deceleration of the spray caused by the momentum exchange between the spray and air. This produces in turn an increase of the characteristic time scales of the eddies. This is important when averaging since forces to take large temporal windows in order to obtain representative signals.

Thus, the model is able to reproduce the internal structure of the diesel flame [20, 28] in the LES context.

In order to deepen in previous results the instantaneous filtered fields are represented in the Z - T maps for the nominal case in figure 5.13 for the same instants that those shown in figure 5.12. To include representative points, only those that fulfil that $\widetilde{Y}_i$ is higher than 0.25 times the maximum mass fraction for that species and instant are plotted. Figures gather formaldehyde, acetylene and hydroxide.

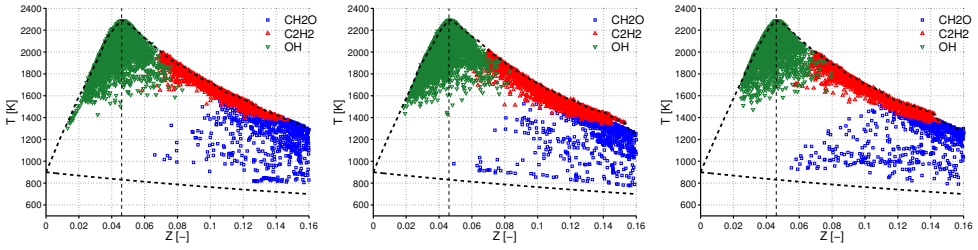

Figure 5.13. *Z - T maps for 3500 (left), 3800 (center) and 4000 μs (right) for the* $\widetilde{Y_{CH_2O}}$, $\widetilde{Y_{OH}}$ *and* $\widetilde{Y_{C_2H_2}}$ *fields. The initial adiabatic mixing line and the upper contour of the map are included with black dashed lines. The stoichiometric value is shown with a vertical line. Results for nominal case.*

As was previously explained, formaldehyde appears at intermediate temperatures and rich mixtures while hydroxide is found in the vicinity of stoichiometry and high temperatures. Acetylene is limited to a narrow fringe of points close to equilibrium for rich mixtures.

In addition, there exists a clear variability in the maps in terms of points cloud density and position of the points for acetylene and, especially, formaldehyde. In the case of formaldehyde this is due to the high turbulence levels that are found in the region close to the lift-off length. However, the contour of the map does not seem to change between instants due to the fluctuations, meaning that there exist always points at equilibrium in the whole range of reactive mixtures.

Once the nominal case has been analysed, we focus on the effect of the boundary conditions. Figure 5.14 shows the spatial representations for the instantaneous filtered fields $\widetilde{T}$, $\widetilde{Y_{CH_2O}}$, $\widetilde{Y_{C_2H_2}}$ and $\widetilde{Y_{OH}}$ for the cases 750, 800 and 900 K of the air temperature parametric variation for 4000 μs.

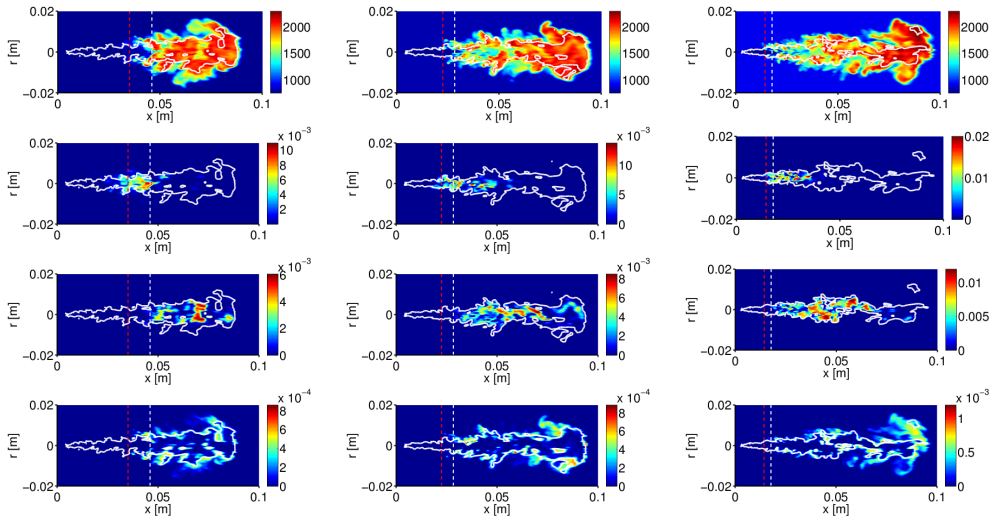

Figure 5.14. *Instantaneous fields for $\widetilde{T}$ (first row), $\widetilde{Y_{CH_2O}}$ (second row), $\widetilde{Y_{C_2H_2}}$ (third row) and $\widetilde{Y_{OH}}$ (last row) for the cases 750 (left), 800 (center) and 900 K (right). The level curve $\widetilde{Z} = Z_{st}$ is included in white line. Lift-off length values for experiment (white dashed line) and simulation (red dashed line) are shown too. Results for very advanced instants.*

The reduction of reactivity by means of the air temperature has a clear impact on the morphology of the flame. Observing temperature fields from figure 5.14, it arises that the base of the flame, with the characteristic W shape of the partially premixed combustion region, is flattened when decreasing ambient temperature. Different to the nominal case, where downstream but close to the lift-off length only points on the stoichiometric level curve reach temperatures close to 2000 K, in the 750 K case a broad region of mixtures reach these very high temperatures some few millimetres downstream of the lift-off length.

This is probably due to the fact that the lift-off length in the 750 K case is positioned in a region where mixture has been homogenized due to the dilution of fuel with air. This dilution provokes that the range of mixtures

downstream of the lift-off length is narrowed and, consequently, they show more similar chemical characteristics including ignition delay. On the contrary, at the height of the lift-off length in the nominal case, only a very narrow interval of mixtures is potentially ignitable while, for the rest of mixtures downstream and close to the lift-off length, combustion cannot proceed.

In addition, although pockets of low and high temperature are seen to alternate in the 750 K case, it seems that the temperature field shows a uniformity that tends to disappear when increasing the ambient temperature. This is in connection with the stoichiometric level surface that is highly fragmented in the nominal case (see figure 5.12) while in the 750 K case, except for some holes inside the flame, is a contorted but continuous line.

Regarding formaldehyde, further from its position in the low/intermediate temperatures and rich mixtures range, non-negligible amounts of this species are observed upstream of the lift-off length (red dashed line in figure 5.14) for the 750 K case. When increasing air temperature, the apparition of formaldehyde upstream of lift-off length tends to be mitigated being almost not observable in this region for the nominal case.

As expected, acetylene is found downstream of the partially premixed combustion where temperature is close to equilibrium. Finally, hydroxide appears close to the stoichiometric level curve, spreading in the lean and slightly rich mixtures region and very high temperatures independently of the air temperature. Moreover, the enhancement of chemistry by air temperature increment provokes an increase of the peak values for species and temperature.

In order to gain more insight, previous species fields are represented in the Z - T space and shown in figure 5.15. The same criterion to include representative points that that given for figure 5.13 is applied to this case.

Figure 5.15 reinforces previous ideas and shows that there exists an important enlargement of the reactive mixture range when increasing the ambient temperature. As has been emphasized along this work this is of critical importance for soot formation. In addition, there exists an increase of the maximum temperature reached in the domain with the air temperature.

Although species relative position does not change in the Z - T map with ambient temperature, it is remarkable that lift-off length for the 750 K case is so long that the partially premixed combustion is displaced to slightly rich mixtures and formaldehyde is even found in the lean region.

This section is closed providing some understanding about combustion at the base of the flame and the stabilization mechanism. In the literature it is

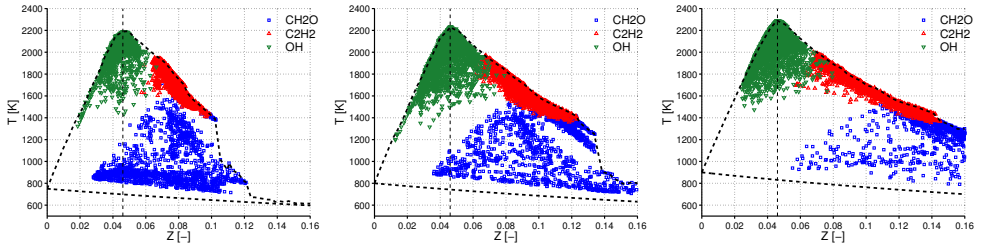

Figure 5.15. *Z - T maps for 750 (left), 800 (center) and 900 K (right) for the* $\widetilde{Y_{CH_2O}}$, $\widetilde{Y_{OH}}$ *and* $\widetilde{Y_{C_2H_2}}$ *fields. The initial adiabatic mixing line and the upper contour of the map are included with black dashed lines. The stoichiometric value is shown with a vertical line. Results for very advanced instants.*

found, as explained in section 2.5.4, that auto-ignition plays a role as one of the stabilization mechanism in diesel flames [30–33].

In order to contribute to this issue, figure 5.16 shows LES instantaneous filtered temperature fields for 750, 800 and 900 K cases in the region of the lift-off length for several instants. The instantaneous lift-off length value together with the stoichiometric mixture fraction level curve are included. As a reference, level curves for air temperature plus 500 K are depicted too.

It is observed that there exists a thin well-defined interface bordering the temperature level curve that separates the unburned and burnt mixtures. This sharp jump in the temperature field is caused by the intense burning rates found in the partially premixed combustion.

In the three cases ignition kernels are observed upstream of the base of the flame (to improve their visualization rectangles mark where they are found). These hot pockets, that appear isolated and upstream of the main flame, ignited due to the local mixture conditions, increase in size, owing to the heat release and species diffusion to their surroundings, and are convected until they merge with the base of the flame.

This phenomenology has been experimentally observed and led to conclude the relevance of auto-ignition as stabilization mechanism [30]. Additionally, modelling works have reported similar results about ignition, growth and attachment of isolated ignition kernels to the main flame [32, 33].

Finally, it is also observed that two branches of high temperature may enclose a volume of fresh mixture when they get close and merge. In this way, pockets of unburned mixture are observed inside the flame due to the turbulent

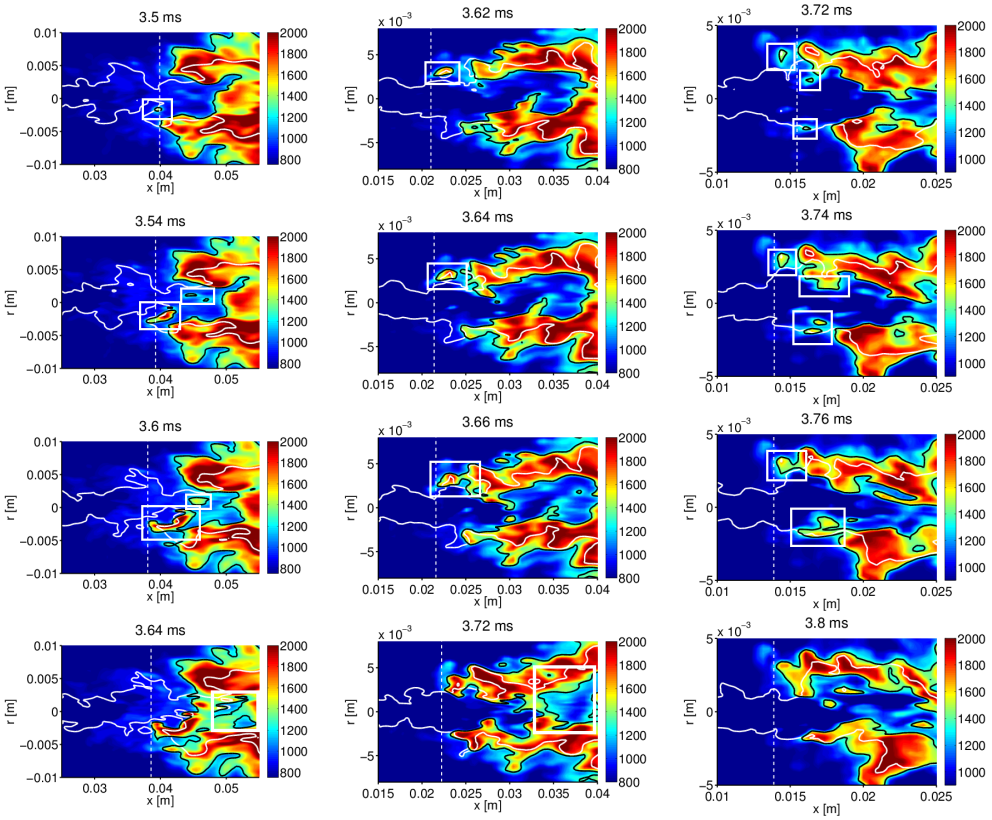

Figure 5.16. *Instantaneous temperature fields for T_{amb} = 750 (left), 800 (center) and 900 K (right). Vertical white line shows the instantaneous lift-off length position while the solid white line indicates the stoichiometric level curve. Black lines are level curves for $T_{amb} + 500$ K.*

motion as is shown for the last represented instants of the 750 and 800 K cases in figure 5.16, where again rectangles are used to mark their position.

5.4.4 Comparison between RANS and LES simulations

In this section, results for RANS (from chapter 4) and LES simulations are compared using Narayanaswamy mechanism. The comparative has to be understood taking some perspective since the turbulence models may have

some impact on the behaviour of the spray as well as the modelling of some terms of the transport equations.

The first differences found between both reactive spray calculations, further from a slight overestimation of the tip penetration for RANS that is not observed for LES, are related to the flame metrics. LES modelled ignition delay is lower than that given by RANS simulations (compare figures 4.12 and 5.10). In terms of lift-off lengths, although LES provides shorter values, both simulations predict similar distances.

Although the structure of the flame is described by both RANS and LES simulations, the range of reactive mixtures is larger for LES compared to RANS. One of the causes is that the lift-off length for LES is shorter than in RANS providing an enrichment of the reactive mixtures.

Figures 5.17 and 5.18 show the comparison of temperature, hydroxide, formaldehyde and acetylene spatial fields of for both RANS and LES at nominal conditions. LES fields are temporally averaged during 1 ms (from 3.5 to 4.5 ms in order to only average once the spray is developed) and azimuthally with 32 meridian planes[4].

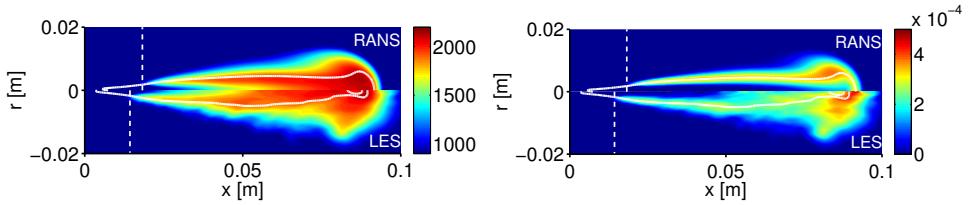

Figure 5.17. *Temperature (left) and species mass fraction for OH (right) fields for advanced instants. In each representation top figure corresponds to RANS and bottom to LES. Results for Narayanaswamy mechanism and nominal case.*

Figures 5.17 and 5.18 show that similar peak values are reached in the domain in both simulations although for some fields, such as formaldehyde, the maximum value is higher for LES. Clearly, the shorter lift-off length for LES is reflected in the fields which extend closer to the nozzle. Pictures show that, in spite of the azimuthal and temporal averages (32 planes and 1 ms, respectively), these are not enough to obtain completely converged fields.

In order to analyse the impact of the boundary conditions figures 5.19 and 5.20 show a similar representation for the case $T_{amb} = 800$ K and $X_{O_2} = 0.15$.

[4]It has been checked that 32 planes are enough to reach convergence in azimuthal direction.

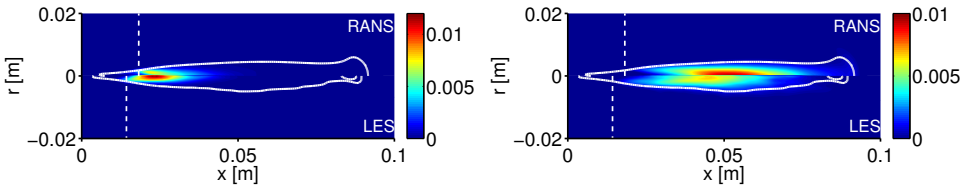

Figure 5.18. *Species mass fraction for* CH_2O *(left) and* C_2H_2 *(right) fields for advanced instants. In each representation top figure corresponds to RANS and bottom to LES. Results for Narayanaswamy mechanism and nominal case.*

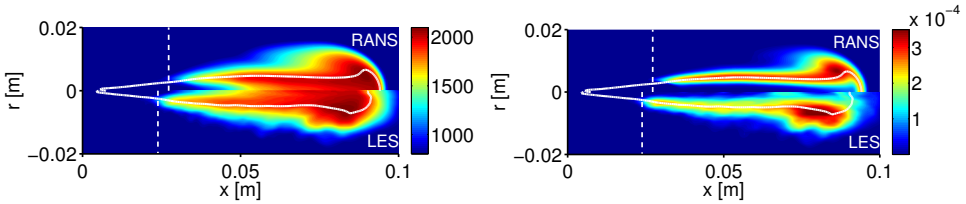

Figure 5.19. *Temperature (left) and species mass fraction for OH (right) fields for advanced instants. In each representation top figure corresponds to RANS and bottom to LES. Results for Narayanaswamy mechanism and* $T_{amb} = 800$ *K and* $X_{O_2} = 0.15$ *case.*

Conclusions are very similar to those corresponding to the nominal case. For this lower temperature the discrepancies between formaldehyde fields are stronger in both field spatial extension and maximum value.

5.5 Conclusions

In this chapter spray A has been modelled in the frame of LES simulations by means of the DS turbulence model and the ADF flamelet model. Due to the high computational cost, only the temperature parametric variation at $X_{O_2} = 0.15$ has been carried out in order to study the capabilities of the model when changing mixture reactivity.

A first calibration was carried out where excellent agreement with experimental data was obtained and a constant $C_\chi = 5$ was chosen.

Ignition delay was well-captured for all the boundary conditions except for the less reactive case, while lift-off length, although was slightly

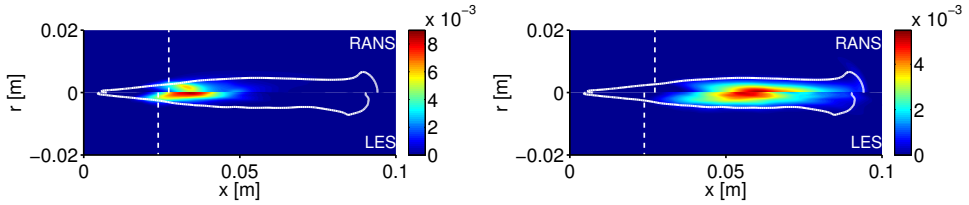

Figure 5.20. *Species mass fraction for* CH_2O *(left) and* C_2H_2 *(right) fields for advanced instants. In each representation top figure corresponds to RANS and bottom to LES. Results for Narayanaswamy mechanism and* $T_{amb} = 800$ *K and* $X_{O_2} = 0.15$ *case.*

underestimated, showed a clear parallelism with the experimental curve. Compared with RANS, LES provides a remarkable faster ignition and lower lift-off length values. This fact provokes that the range of reactive mixtures is larger in LES than in RANS.

In addition, very low fluctuations are observed for the lift-off length as a consequence of the intense burning that develops at the base of the flame that allows flame dynamics to adapt to the local flow conditions. Such fluctuation does not show a clear dependence with the ambient temperature.

The flame structure was properly described by the simulations showing that there exists a vigorous partially premixed combustion with an intense burning rate where reactants are rapidly oxidised reaching temperatures around 2000 K. The rest of the spray is wrapped by a diffusion flame with a moderate chemical activity. The morphology of the partially premixed combustion zone is flattened when decreasing mixture reactivity and combustion tends to be spatially more uniform with level curves less fragmented.

In addition, high fluctuations are observed in both spatial and Z - T representations for species positioned close to the nozzle due to the intense turbulence.

Finally, ignition kernels appear close to the lift-off length generating discontinuities in its instantaneous signal. They ignite spontaneously, detached and upstream of the flame, and grow until they merge with the base of the flame. This is supported by experimental and modelling work and demonstrates that auto-ignition is one of the stabilization mechanisms in diesel flames.

Summarizing, the ADF flamelet combustion model provides satisfactory results when applied in the context of LES turbulence models and describes spray structure in its different stages. Hence, it is suitable for diesel flame analysis and arises as a tool to be applied to further investigation.

References

[1] Poinsot T. and Veynante D. *Theoretical and numerical combustion.* RT Edwards Inc., 2005.

[2] Pope S. B. "Ten questions concerning the large-eddy simulation of turbulent flows". *New journal of Physics*, Vol. 6 n^o 1, pp. 35, 2004.

[3] Pitsch H. "Large-eddy simulation of turbulent combustion". *Annu. Rev. Fluid Mech.*, Vol. 38, pp. 453–482, 2006.

[4] Pickett L. M., Bruneaux G. and Payri R. "Engine combustion network". *Sandia National Laboratories, Livermore, CA, https://ecn.sandia.gov/*, 2018.

[5] Pomraning E. and Rutland C. J. "A dynamic one-equation nonviscosity large-eddy simulation model". *AIAA journal*, Vol. 40 n^o 4, pp. 689–701, 2002.

[6] Bharadwaj N., Rutland C. J. and Chang S. M. "Large eddy simulation modelling of spray-induced turbulence effects". *International Journal of Engine Research*, Vol. 10 n^o 2, pp. 97–119, 2009.

[7] Bharadwaj N. and Rutland C. J. "A large-eddy simulation study of sub-grid two-phase interaction in particle-laden flows and diesel engine sprays". *Atomization and Sprays*, Vol. 20 n^o 8, 2010.

[8] Mompó Laborda J. M. *Engineering Large Eddy Simulation of Diesel Sprays.* Doctoral Thesis, Universitat Politècnica de València, 2014.

[9] Beale J. C. and Reitz R. D. "Modeling spray atomization with the Kelvin-Helmholtz/Rayleigh-Taylor hybrid model". *Atomization and sprays*, Vol. 9 n^o 6, 1999.

[10] Fiorina B., Gicquel O., Vervisch L., Carpentier S. and Darabiha N. "Approximating the chemical structure of partially premixed and diffusion counterflow flames using FPI flamelet tabulation". *Combustion and flame*, Vol. 140 n^o 3, pp. 147–160, 2005.

[11] Narayanaswamy K., Pepiot P. and Pitsch H. "A chemical mechanism for low to high temperature oxidation of n-dodecane as a component of transportation fuel surrogates". *Combustion and Flame*, Vol. 161 n^o 4, pp. 866–884, 2014.

[12] "OpenFOAM". *http://www.openfoam.com/*, 2017.

[13] Senecal P. K., Pomraning E., Richards K. J. and Som S. "An investigation of grid convergence for spray simulations using an LES turbulence model". *SAE Technical Paper*, 2013.

[14] Xue Q., Som S., Senecal P. K. and Pomraning E. "A Study of Grid Resolution and SGS Models for LES Under Non-Reacting Spray Conditions". In *25th Annual Conference on Liquid Atomization and Spray Systems, Pittsburgh, PA*, 2013.

[15] Desantes J. M., García-Oliver J. M., Novella R. and Pérez-Sánchez E. J. "Application of a flamelet-based CFD combustion model to the LES simulation of a diesel-like reacting spray". In *Tenth International Conference on Computational Fluid Dynamics (ICCFD10), Barcelona, Spain*, 2018.

[16] Payri R., García-Oliver J. M., Xuan T. and Bardi M. "A study on diesel spray tip penetration and radial expansion under reacting conditions". *Applied Thermal Engineering*, Vol. 90, pp. 619–629, 2015.

[17] Pickett L. M., Manin J., Genzale C. L., Siebers D. L., Musculus M. P. B. and Idicheria C. A. "Relationship between diesel fuel spray vapor penetration/dispersion and local fuel mixture fraction". *SAE International Journal of Engines*, Vol. 4 n^o 2011-01-0686, pp. 764–799, 2011.

[18] Meijer M., Malbec L. M., Bruneaux G. and Somers L. M. T. "Engine Combustion Network: Spray A Basic Measurements and Advanced Diagnostics". In *12th Triennial International Conference on Liquid Atomization and Spray Systems (ICLASS 2012), Heidelberg, Germany, September*, pp. 2–6, 2012.

[19] Eagle W. E., Musculus M. P. B., Malbec L. M. C. and Bruneaux G. "Measuring transient entrainment rates of a confined vaporizing diesel jet". In *ILASS Americas 26th Annual Conference on Liquid Atomization and Spray Systems, Portland, OR*, 2014.

[20] García-Oliver J. M., Malbec L. M., Toda H. B. and Bruneaux G. "A study on the interaction between local flow and flame structure for mixing-controlled Diesel sprays". *Combustion and Flame*, Vol. 179, pp. 157–171, 2017.

[21] Tennekes H. and Lumley J. L. *A first course in turbulence*. MIT press, 1972.

[22] Kolmogorov A. N. "The local structure of turbulence in incompressible viscous fluid for very large Reynolds numbers". *Proc. R. Soc. Lond. A*, Vol. 434 n^o 1890, pp. 9–13, 1991.

[23] Kolmogorov A. N. "Dissipation of energy in the locally isotropic turbulence". *Proc. R. Soc. Lond. A*, Vol. 434 n^o 1890, pp. 15–17, 1991.

[24] Pope S. B. *Turbulent flows*. IOP Publishing, 2001.

[25] Idicheria C. A. and Pickett L. M. "Effect of EGR on diesel premixed-burn equivalence ratio". *Proceedings of the Combustion Institute*, Vol. 31 n^o 2, pp. 2931–2938, 2007.

[26] Novella R., García A., Pastor J. M. and Domenech V. "The role of detailed chemical kinetics on CFD diesel spray ignition and combustion modelling". *Mathematical and Computer Modelling*, Vol. 54 n^o 7, pp. 1706–1719, 2011.

[27] Bhattacharjee S. and Haworth D. C. "Simulations of transient n-heptane and n-dodecane spray flames under engine-relevant conditions using a transported PDF method". *Combustion and Flame*, Vol. 160 n^o 10, pp. 2083–2102, 2013.

[28] Dec J. E. "A conceptual model of DI diesel combustion based on laser-sheet imaging". *SAE Technical paper*, 1997.

[29] Duwig C. and Fuchs L. "Large eddy simulation of a H2/N2 lifted flame in a vitiated co-flow". *Combustion Science and Technology*, Vol. 180 n^o 3, pp. 453–480, 2008.

[30] Pickett L. M., Siebers D. L. and Idicheria C. A. "Relationship between ignition processes and the lift-off length of diesel fuel jets". *SAE technical paper*, 2005.

[31] Gong C., Jangi M. and Bai X. S. "Large eddy simulation of n-dodecane spray combustion in a high pressure combustion vessel". *Applied Energy*, Vol. 136, pp. 373–381, 2014.

[32] Pei Y., Som S., Pomraning E., Senecal P. K., Skeen S. A., Manin J. and Pickett L. M. "Large eddy simulation of a reacting spray flame with multiple realizations under compression ignition engine conditions". *Combustion and Flame*, Vol. 162 n^o 12, pp. 4442–4455, 2015.

[33] Kahila H., Wehrfritz A., Kaario O., Masouleh M. G., Maes N., Somers B. and Vuorinen V. "Large-eddy simulation on the influence of injection pressure in reacting spray A". *Combustion and Flame*, Vol. 191, pp. 142–159, 2018.

Chapter 6

Conclusions and future works

Contents

6.1 Conclusions

As was explained in chapter 1, the main objective of this thesis is to investigate and model, in the frame of RANS and LES turbulence models, a diesel-like spray by means of an advanced combustion model assessing the boundary condition effects as well as other critical modelling aspects. For this purpose, spray A from ECN has been analysed in the light of different aspects: the internal changes in the flame structure when adding transport phenomena with different intensity, the influence of combustion to the boundary conditions and the impact of the chemical mechanism.

In addition, as a simplified laminar flamelet model has been used[1], as a first step, it was validated for fuels with different chemical complexity in steady and transient regimes.

Consequently, although the main conclusions have been established in their corresponding chapters, it is positive to gather the main results in some brief lines in order to take perspective and synthesize the contributions of the work. The main conclusions obtained in this investigation are summarized in the

[1]Which, however, is able to account for complex phenomena and manage complex chemical mechanisms.

following and are divided into two blocks. The first one corresponds to the performance of the ADF model while the second one describes the conclusions related to the ECN spray A analysis in both RANS and LES frameworks[2].

ADF validation

1. The comparison between DF and ADF models leads to state that the ADF approach provides similar results than the DF model for steady and transient regimes in the auto-ignition range when including the suggested chemical source terms limitation for complex fuels.

2. This validation has been accomplished successfully by the comparison of S-curves, ignition delays and flame propagation for fuels with different chemical complexity that ranged from hydrogen, the simplest fuel, to complex alkanes, like heptane used as a diesel surrogate.

3. The influence of the definition of the progress variable is of a second order.

4. It has been shown that this approach reduces drastically the computational cost compared to the complete solution of the flame.

5. Taking into account such reduction and considering that diesel combustion develops mainly in the auto-ignition range it has been proved that the ADF model is suitable for diesel engine simulations.

Spray A analysis

1. Auto-ignition is composed of two stages at low and high temperature separated by a cool flame. The duration of the first stage and the cool flame and their sensitivity to mixture fraction are critical in order to determine how combustion develops when adding convection and diffusion phenomena.

2. All the simulated mechanisms predict an ignition at low temperatures that starts at lean mixtures and is later displaced to rich mixtures. The time elapsed for the cool flame determines to which degree combustion is displaced to rich mixtures.

[2] Although they are accomplished with different turbulence approaches, it is deemed that they belong to the same conceptual problem and this justifies that their conclusions are given together. This point of view is reinforced when considering that their conclusions, far from being contradictory, complement each other.

3. All the simulated mechanisms show a noticeable agreement for high temperature chemistry while remarkable discrepancies appear in the low temperature stage.

4. Low mixture fraction variances and scalar dissipation rates are observed in the region where ignition starts and develops in the turbulent spray.

5. Focusing more particularly on the spray, flame metrics, namely, ignition delay and lift-off length, are modelled satisfactorily for both RANS and LES simulations.

6. During quasi-steady regime, modelling shows a spray structure composed of a partially premixed combustion at the height of the lift-off length and a diffusion flame that wraps the reactive zone.

7. Different to the diffusion flame, which is established in the vicinity of the stoichiometric level surface and temperatures close to equilibrium and shows low chemical rates, the partially premixed combustion encompasses a wide range of mixtures and temperatures although is centred at rich mixtures and intermediate temperatures that are submitted to an intense burning rate. In these mixtures, mixture fraction variance and scalar dissipation rate are low and LES simulations shows that the base of the flame (lift-off length) suffers low fluctuations.

8. Boundary conditions have an important effect on the morphology of the flame that is flattened when reducing the reactivity by ambient temperature since the base of the flame is displaced to more diluted mixtures. Reducing of oxygen concentration broadens the flame, but its effect on the morphology is less accentuated that the variation of air temperature since it has less impact on the lift-off length.

9. Constant C_χ inhibits turbulent transport and leads to sharper fields where the flame brush is narrowed.

10. Variation of lift-off length with ignition delay and apparition of detached ignition kernels upstream of the lift-off length that grow and merge with the base of the flame are characteristic of a stabilization mechanism where auto-ignition plays a role.

The successful capabilities of the model to reproduce so different aspects, at least qualitatively, and its agreement with results found in literature in the experimental and modelling fields lead to state that the combustion model developed in this work is suitable for diesel flame simulations.

6.2 Future works

As in any research work the analysis is far from being finished and some lines for future works are suggested in the following.

1. As the models based on the flamelet concept rely their accuracy on the capabilities of the CFD simulation to predict mixing variables, it would be interesting to perform a deep analysis of such variables (including variances, dissipation and turbulent budgets) and relate them to the turbulent kinetic energy and its dissipation.

2. It would be interesting to complete spray A parametric studies in the LES context especially for the oxygen sweep.

3. Analysis of heat radiation effects on the flame. Although this heat transfer is low in the energetic combustion balance for a diesel engine (between 3 and 5%), it may be important for maximum temperature as well as NO_x emissions.

4. NO_x and soot modelling. As said in the previous point, NO_x are very affected by the highest temperatures and, therefore, inclusion of radiation may be important. In addition, their chemistry is very slow complicating the progress variable choice.

   Regarding soot, the other major pollutant in diesel engines, the models that predict its formation do not cover all the complex mechanisms that participate in its nucleation and growth. In addition, its coupling with the combustion model is not straightforward.

5. A detailed study of combustion in the zone close to the lift-off length which improved the knowledge about the stabilization mechanisms and determined the relevance of each of such mechanisms as a function of the boundary conditions.

6. Coupling of the current combustion model with other spray atomization models, such as Eulerian spray models, which have been demonstrated to be more suitable for diesel sprays than DDM approaches.

7. Finally, the final objective of the model is its application to the simulation of diesel engine combustion in order to provide a reliable tool with the ability to describe this complex process.

References

-.
OpenFOAM.
http://www.openfoam.com/, 2017. (cited on pp. 171, 236)

-.
https://www.dieselnet.com/, 2018. (cited on p. 2)

Agarwal A. K., Singh A. P. and Maurya R. K.
Evolution, challenges and path forward for low temperature combustion engines.
Progress in Energy and Combustion Science, Vol. 61, pp. 1–56, 2017. (cited on pp. 3, 88)

Akkurt B., Akargun H. Y., Somers L. M. T., Deen N. G., Novella R. and Pérez-Sánchez E. J.
An insight on the spray-A combustion characteristics by means of RANS and LES simulations using flamelet-based combustion models.
SAE Technical Paper 2017-01-0577, 2017, doi:10.4271/2017-01-0577, 2017.
(cited on pp. 168, 169)

Bardi M., Payri R., Malbec L. M., Bruneaux G., Pickett L. M., Manin J., Bazyn T. and Genzale C. L.
Engine Combustion Network: comparison of spray development, vaporization, and combustion in different combustion vessels.
Atomization and Sprays, Vol. 22 n^o 10, 2012. (cited on p. 168)

Bardina J., Ferziger J. and Reynolds W.
Improved subgrid-scale models for large-eddy simulation.
In *13th Fluid and Plasma Dynamics Conference*, pp. 1357–1357, 1980. (cited on p. 48)

Barths H., Hasse C., Bikas G. and Peters N.
Simulation of combustion in direct injection diesel engines using a eulerian particle flamelet model.
Proceedings of the Combustion Institute, Vol. 28 n^o 1, pp. 1161–1168, 2000.
(cited on pp. 6, 98, 102, 105, 107, 185)

Batchelor G. K.
An introduction to fluid dynamics.
Cambridge university press, 2000. (cited on p. 15)

Beale J. C. and Reitz R. D.
Modeling spray atomization with the Kelvin-Helmholtz/Rayleigh-Taylor hybrid model.
Atomization and sprays, Vol. 9 n^o 6, 1999. (cited on pp. 170, 236)

Benajes J., Payri R., Bardi M. and Martí-Aldaraví P.
Experimental characterization of diesel ignition and lift-off length using a single-hole ECN injector.
Applied Thermal Engineering, Vol. 58 n^o 1, pp. 554–563, 2013.
(cited on pp. 168, 169, 188)

Bharadwaj N. and Rutland C. J.
A large-eddy simulation study of sub-grid two-phase interaction in particle-laden flows and diesel engine sprays.
Atomization and Sprays, Vol. 20 n^o 8, 2010. (cited on pp. 47, 235)

Bharadwaj N., Rutland C. J. and Chang S. M.
Large eddy simulation modelling of spray-induced turbulence effects.
International Journal of Engine Research, Vol. 10 n^o 2, pp. 97–119, 2009.
(cited on pp. 47, 235)

Bhattacharjee S. and Haworth D. C.
Simulations of transient n-heptane and n-dodecane spray flames under engine-relevant conditions using a transported PDF method.
Combustion and Flame, Vol. 160 n^o 10, pp. 2083–2102, 2013.
(cited on pp. 70, 87, 88, 190, 206, 246)

Bilger R. W.
Conditional moment closure for turbulent reacting flow.
Physics of Fluids A: Fluid Dynamics, Vol. 5 n^o 2, pp. 436–444, 1993. (cited on p. 74)

Bolla M., Gudmundsson T., Wright Y. M. and Boulouchos K.
Simulations of diesel sprays using the conditional moment closure model.
SAE International Journal of Engines, Vol. 6 n^o 2013-01-1618, pp. 1249–1261, 2013.
(cited on p. 75)

Borghesi G., Krisman A., Lu T. and Chen J. H.
Direct numerical simulation of a temporally evolving air/n-dodecane jet at low-temperature diesel-relevant conditions.
Combustion and Flame, 2018. (cited on p. 33)

Borghi R.
On the structure and morphology of turbulent premixed flames.
In *Recent advances in the Aerospace Sciences*, pp. 117–138. Springer, 1985.
(cited on p. 64)

Broadwell J. E., Dahm W. J. A. and Mungal M. G.
Blowout of turbulent diffusion flames.
In *Symposium (international) on combustion*, volume 20, pp. 303–310. Elsevier, 1985.
(cited on p. 69)

Burke S. P. and Schumann T. E. W.
Diffusion flames.
Industrial & Engineering Chemistry, Vol. 20 n^o 10, pp. 998–1004, 1928.
(cited on pp. 60, 83, 100, 103)

Cabra R., Chen J. Y., Dibble R. W., Karpetis A. N. and Barlow R. S.
Lifted methane–air jet flames in a vitiated coflow.
Combustion and Flame, Vol. 143 n^o 4, pp. 491–506, 2005. (cited on pp. 27, 138)

Cabra R., Myhrvold T., Chen J. Y., Dibble R. W., Karpetis A. N. and Barlow R. S.
Simultaneous laser Raman-Rayleigh-LIF measurements and numerical modeling results of a lifted turbulent H2/N2 jet flame in a vitiated coflow.
Proceedings of the Combustion Institute, Vol. 29 n^o 2, pp. 1881–1888, 2002.
(cited on pp. 27, 138)

Dahms R. N. and Oefelein J. C.
On the transition between two-phase and single-phase interface dynamics in multicomponent fluids at supercritical pressures.
Physics of Fluids, Vol. 25 n^o 9, pp. 092103, 2013. (cited on p. 14)

Dahms R. N., Paczko G. A., Skeen S. A. and Pickett L. M.
Understanding the ignition mechanism of high-pressure spray flames.
Proceedings of the Combustion Institute, Vol. 36 n^o 2, pp. 2615–2623, 2017.
(cited on pp. 168, 179)

Damköhler G.
Der einfluss der turbulenz auf die flammengeschwindigkeit in gasgemischen.
Zeitschrift für Elektrochemie und angewandte physikalische Chemie, Vol. 46 n^o 11, pp. 601–626, 1940. (cited on p. 65)

Darrieus G.
Propagation d'un front de flamme.
La Technique Moderne, Vol. 30, pp. 18, 1938. (cited on p. 57)

de Goey L. P. H., van Oijen J. A., Bongers H. and Groot G. R. A.
New flamelet based reduction methods: the bridge between chemical reduction techniques and flamelet methods.
In *European Combustion Meeting, Orléans (France)*, 2003. (cited on pp. 105, 107)

Dec J. E.
A conceptual model of DI diesel combustion based on laser-sheet imaging.
SAE Technical paper, 1997. (cited on pp. 54, 85, 86, 200, 206, 211, 247, 249)

Demuren A. O. and Rodi W.
Calculation of turbulence-driven secondary motion in non-circular ducts.
Journal of Fluid Mechanics, Vol. 140, pp. 189–222, 1984. (cited on p. 44)

Desantes J. M., García-Oliver J. M., Novella R. and Pérez-Sánchez E. J.
Application of an unsteady flamelet model in a RANS framework for spray A simulation.
Applied Thermal Engineering, Vol. 117, pp. 50–64, 2017.
(cited on pp. 168, 169, 183, 187)

Desantes J. M., García-Oliver J. M., Novella R. and Pérez-Sánchez E. J.
Application of a flamelet-based CFD combustion model to the LES simulation of a diesel-like reacting spray.
In *Tenth International Conference on Computational Fluid Dynamics (ICCFD10), Barcelona, Spain*, 2018. (cited on pp. 88, 238)

Desantes J. M., García-Oliver J. M., Pastor J. M. and Pandal A.
A comparison of diesel sprays CFD modeling approaches: DDM versus Σ-Y Eulerian atomization model.
Atomization and Sprays, Vol. 26 n^o 7, 2016. (cited on pp. 82, 170, 171, 183)

Desantes J. M., Novella R., Pastor J. M. and Pérez-Sánchez E. J.
Analysis of the approximated diffusion flamelet approach using fuels with different chemical complexity.
In *Mathematical Modelling in Engineering & Human Behaviour 2014. 16th Edition of the Mathematical Modelling Conference Series at the Institute for Multidisciplinary Mathematics, Valencia, Spain*, pp. 228–233, 2014. (cited on p. 137)

Desantes J. M., Payri R., Salvador F. J. and Gil A.
Development and validation of a theoretical model for diesel spray penetration.
Fuel, Vol. 85, pp. 910–917, 2006. (cited on p. 80)

Dhuchakallaya I., Rattanadecho P. and Watkins P.
Auto-ignition and combustion of diesel spray using unsteady laminar flamelet model.
Applied Thermal Engineering, Vol. 52 n^o 2, pp. 420–427, 2013. (cited on pp. 6, 98, 185)

Diesel R.
Internal combustion engine.
U.S. Patent 608845, 1898. (cited on p. 1)

Dukowicz J. K.
A particle-fluid numerical model for liquid sprays.
Journal of computational Physics, Vol. 35 n^o 2, pp. 229–253, 1980. (cited on p. 82)

Duwig C. and Fuchs L.
Large eddy simulation of a H2/N2 lifted flame in a vitiated co-flow.
Combustion Science and Technology, Vol. 180 n^o 3, pp. 453–480, 2008. (cited on p. 248)

D'Errico G., Lucchini T., Contino F., Jangi M. and Bai X. S.
Comparison of well-mixed and multiple representative interactive flamelet approaches for diesel spray combustion modelling.
Combustion Theory and Modelling, Vol. 18 n^o 1, pp. 65–88, 2014. (cited on p. 107)

Eagle W. E., Musculus M. P. B., Malbec L. M. C. and Bruneaux G.
Measuring transient entrainment rates of a confined vaporizing diesel jet.
In *ILASS Americas 26th Annual Conference on Liquid Atomization and Spray Systems, Portland, OR*, 2014. (cited on pp. 184, 239)

Effelsberg E. and Peters N.
Scalar dissipation rates in turbulent jets and jet diffusion flames.
In *Symposium (International) on Combustion*, volume 22, pp. 693–700. Elsevier, 1989. (cited on p. 128)

Eickhoff H., Lenze B. and Leuckel W.
Experimental investigation on the stabilization mechanism of jet diffusion flames.
In *Symposium (International) on Combustion*, volume 20, pp. 311–318. Elsevier, 1985. (cited on p. 68)

Epaminondas M.
Ignition of turbulent non-premixed flames.
Progress in Energy and Combustion Science, Vol. 35 n^o 1, pp. 57–97, 2009. (cited on pp. 87, 180, 192)

Falgout Z., Rahm M., Wang Z. and Linne M.
Evidence for supercritical mixing layers in the ECN spray A.
Proceedings of the Combustion Institute, Vol. 35 n^o 2, pp. 1579–1586, 2015. (cited on p. 14)

Favre A. J.
The equations of compressible turbulent gases.
Aix-Marseille University (France). Inst. de Mecanique Statistique de la Turbulence, 1965. (cited on p. 26)

Fiorina B., Gicquel O., Vervisch L., Carpentier S. and Darabiha N.
Approximating the chemical structure of partially premixed and diffusion counterflow flames using FPI flamelet tabulation.
Combustion and flame, Vol. 140 n^o 3, pp. 147–160, 2005. (cited on pp. 108, 139, 236)

García-Oliver J. M., Malbec L. M., Toda H. B. and Bruneaux G.
A study on the interaction between local flow and flame structure for mixing-controlled Diesel sprays.
Combustion and Flame, Vol. 179, pp. 157–171, 2017.
(cited on pp. 88, 168, 184, 185, 198, 199, 239, 242, 243, 249)

Germano M., Piomelli U., Moin P. and Cabot W. H.
A dynamic subgrid-scale eddy viscosity model.
Physics of Fluids A: Fluid Dynamics, Vol. 3 n^o 7, pp. 1760–1765, 1991. (cited on p. 45)

Gicquel O., Darabiha N. and Thévenin D.
Laminar premixed hydrogen/air counterflow flame simulations using flame prolongation of ILDM with differential diffusion.
Proceedings of the Combustion Institute, Vol. 28 n^o 2, pp. 1901–1908, 2000.
(cited on pp. 76, 107)

Glassman I., Yetter R. A. and Glumac N. G.
Combustion.
Academic press, 2014. (cited on pp. 15, 51, 52, 54, 81)

Gong C., Jangi M. and Bai X. S.
Large eddy simulation of n-dodecane spray combustion in a high pressure combustion vessel.
Applied Energy, Vol. 136, pp. 373–381, 2014.
(cited on pp. 69, 85, 88, 168, 175, 179, 191, 252)

Higgins B., Siebers D. L. and Aradi A.
Diesel-spray ignition and premixed-burn behavior.
SAE Technical Paper, 2000. (cited on p. 85)

Hirschfelder J. O., Curtiss C. F. and Bird R. B.
Molecular theory of gases and liquids, volume 26.
Wiley New York, 1969. (cited on p. 17)

Hussein H. J., Capp S. P. and George W. K.
Velocity measurements in a high-Reynolds-number, momentum-conserving, axisymmetric, turbulent jet.
Journal of Fluid Mechanics, Vol. 258, pp. 31–75, 1994. (cited on pp. 80, 227)

Idicheria C. A. and Pickett L. M.
Soot formation in diesel combustion under high-EGR conditions.
SAE Technical Paper, 2005. (cited on pp. 85, 88, 196)

Idicheria C. A. and Pickett L. M.
Formaldehyde visualization near lift-off location in a diesel jet.
SAE Technical Paper, 2006. (cited on pp. 87, 200)

Idicheria C. A. and Pickett L. M.
Effect of EGR on diesel premixed-burn equivalence ratio.
Proceedings of the Combustion Institute, Vol. 31 n^o 2, pp. 2931–2938, 2007.
(cited on pp. 87, 195, 196, 246)

Idicheria C. A. and Pickett L. M.
Quantitative mixing measurements in a vaporizing diesel spray by Rayleigh imaging.
SAE Technical Paper, 2007. (cited on p. 88)

Janicka J. and Peters N.
Prediction of turbulent jet diffusion flame lift-off using a PDF transport equation.
Symposium (International) on Combustion, Vol. 19 n^o 1, pp. 367–374, 1982.
(cited on p. 136)

Jones W. P. and Musonge P.
Closure of the Reynolds stress and scalar flux equations.
The Physics of fluids, Vol. 31 n^o 12, pp. 3589–3604, 1988. (cited on p. 136)

Kahila H., Wehrfritz A., Kaario O., Masouleh M. G., Maes N., Somers B. and Vuorinen V.
Large-eddy simulation on the influence of injection pressure in reacting spray A.
Combustion and Flame, Vol. 191, pp. 142–159, 2018.
(cited on pp. 6, 69, 88, 98, 168, 190, 252)

Kastengren A. L., Tilocco F. Z., Powell C. F., Manin J., Pickett L. M., Payri R. and Bazyn T.
Engine combustion network (ECN): measurements of nozzle geometry and hydraulic behavior.
Atomization and Sprays, Vol. 22 n^o 12, pp. 1011–1052, 2012. (cited on p. 169)

Kerstein A. R.
A linear-eddy model of turbulent scalar transport and mixing.
Combustion Science and Technology, Vol. 60 n^o 4-6, pp. 391–421, 1988. (cited on p. 75)

Kim J., Moin P. and Moser R.
Turbulence statistics in fully developed channel flow at low Reynolds number.
Journal of fluid mechanics, Vol. 177, pp. 133–166, 1987. (cited on pp. 29, 33)

Kim J. S. and Williams F. A.
Structures of flow and mixture-fraction fields for counterflow diffusion flames with small stoichiometric mixture fractions.
SIAM Journal on Applied Mathematics, Vol. 53 n^o 6, pp. 1551–1566, 1993.
(cited on p. 104)

Kirkbey L. L. and Schmitz R. A.
An analytical study of the stability of a laminar diffusion flame.
Combustion and Flame, Vol. 10 n^o 3, pp. 205–220, 1966. (cited on pp. 62, 103)

Klimenko A. Y.
Multicomponent diffusion of various admixtures in turbulent flow.
Fluid dynamics, Vol. 25 n^o 3, pp. 327–334, 1990. (cited on p. 74)

Klimenko A. Y. and Bilger R. W.
Conditional moment closure for turbulent combustion.
Progress in energy and combustion science, Vol. 25 n^o 6, pp. 595–687, 1999.
(cited on p. 75)

Kolmogorov A. N.
Dissipation of energy in the locally isotropic turbulence.
Proc. R. Soc. Lond. A, Vol. 434 n^o 1890, pp. 15–17, 1991. (cited on pp. 24, 240)

Kolmogorov A. N.
The local structure of turbulence in incompressible viscous fluid for very large Reynolds numbers.
Proc. R. Soc. Lond. A, Vol. 434 n^o 1890, pp. 9–13, 1991. (cited on pp. 24, 240)

Landau L. D.
On the theory of slow combustion.
Acta Physicochim (USSR), Vol. 19, pp. 77–85, 1944. (cited on p. 57)

Launder B. E., Reece G. Jr. and Rodi W.
Progress in the development of a Reynolds-stress turbulence closure.
Journal of fluid mechanics, Vol. 68 n^o 3, pp. 537–566, 1975. (cited on p. 44)

Launder B. E. and Spalding D. B.
The numerical computation of turbulent flows.
In *Numerical Prediction of Flow, Heat Transfer, Turbulence and Combustion*, pp. 96–116. Elsevier, 1983. (cited on p. 42)

Le H., Moin P. and Kim J.
Direct numerical simulation of turbulent flow over a backward-facing step.
Journal of fluid mechanics, Vol. 330, pp. 349–374, 1997. (cited on p. 33)

Lehtiniemi H., Mauss F., Balthasar M. and Magnusson I.
Modeling diesel engine combustion with detailed chemistry using a progress variable approach.
SAE Technical Paper, 2005. (cited on p. 108)

Leonard A.
Energy cascade in large-eddy simulations of turbulent fluid flows.
In *Advances in geophysics*, volume 18, pp. 237–248. Elsevier, 1975. (cited on p. 36)

Liñán A.
The asymptotic structure of counterflow diffusion flames for large activation energies.
Acta Astronautica, Vol. 1 n^o 7-8, pp. 1007–1039, 1974. (cited on p. 103)

Livengood J. C. and Wu P. C.
Correlation of autoignition phenomena in internal combustion engines and rapid compression machines.
In *Symposium (international) on combustion*, volume 5, pp. 347–356. Elsevier, 1955. (cited on pp. 55, 122)

López Pintor D.
Theoretical and experimental study on the autoignition phenomena of homogeneous reactive mixtures.
Doctoral Thesis, Universitat Politècnica de València, 2017. (cited on pp. 51, 52, 55)

Lucchini T., d'Errico G., Ettorre D. and Ferrari G.
Numerical investigation of non-reacting and reacting diesel sprays in constant-volume vessels.
SAE International Journal of Fuels and Lubricants, Vol. 2 n^o 1, pp. 966–975, 2009. (cited on p. 70)

Lyons K. M.
Toward an understanding of the stabilization mechanisms of lifted turbulent jet flames: experiments.
Progress in Energy and Combustion Science, Vol. 33 n^o 2, pp. 211–231, 2007.
(cited on pp. 68, 69)

Maas U. and Pope S. B.
Simplifying chemical kinetics: intrinsic low-dimensional manifolds in composition space.
Combustion and flame, Vol. 88 n^o 3-4, pp. 239–264, 1992. (cited on pp. 76, 107)

Maes N., Meijer M., Dam N., Somers B., Toda H. B., Bruneaux G., Skeen S. A., Pickett L. M. and Manin J.
Characterization of spray A flame structure for parametric variations in ECN constant-volume vessels using chemiluminescence and laser-induced fluorescence.
Combustion and Flame, Vol. 174, pp. 138–151, 2016. (cited on pp. 168, 196)

Magnussen B. F. and Hjertager B.
On mathematical modeling of turbulent combustion with special emphasis on soot formation and combustion.
In *Symposium (international) on Combustion*, volume 16, pp. 719–729. Elsevier, 1977.
(cited on p. 71)

Mallard E. and Le Chatelier H.
Combustion of explosive gas mixtures.
Ann. mines, Vol. 8, pp. 274, 1883. (cited on p. 58)

Marble F. E. and Broadwell J. E.
The coherent flame model for turbulent chemical reactions.
Purdue University Lafayette, 1977. (cited on p. 73)

Markstein G. H.
Nonsteady flame propagation, volume 75.
Elsevier, 2014. (cited on p. 57)

McDonough J. M.
Introductory lectures on turbulence: physics, mathematics and modeling.
University of Kentucky, 2007. (cited on p. 20)

McMurthy P. A., Menon S. and Kerstein A. R.
A linear eddy sub-grid model for turbulent reacting flows: application to hydrogen-air combustion.
In *Symposium (International) on Combustion*, volume 24, pp. 271–278. Elsevier, 1992.
(cited on p. 75)

Meijer M., Malbec L. M., Bruneaux G. and Somers L. M. T.
Engine Combustion Network: Spray A Basic Measurements and Advanced Diagnostics.
In *12th Triennial International Conference on Liquid Atomization and Spray Systems (ICLASS 2012), Heidelberg, Germany, September*, pp. 2–6, 2012.
(cited on pp. 168, 184, 239)

Meijer M., Somers B., Johnson J., Naber J., Lee S. Y., Malbec L. M. C., Bruneaux G., Pickett L. M., Bardi M., Payri R. and Bazyn T.
Engine Combustion Network (ECN): characterization and comparison of boundary conditions for different combustion vessels.
Atomization and Sprays, Vol. 22 n^o 9, 2012. (cited on p. 168)

Menter F. R.
Improved Two-Equation k-ε Turbulence Models for Aerodynamic Flows.
NASA Technical Memorandum, Vol. 103975, 1992. (cited on p. 43)

Menter F. R.
Two-equation eddy-viscosity turbulence models for engineering applications.
AIAA journal, Vol. 32 n^o 8, pp. 1598–1605, 1994. (cited on p. 43)

Miake-Lye R. C. and Hammer J. A.
Lifted turbulent jet flames: a stability criterion based on the jet large-scale structure.
In *Symposium (International) on Combustion*, volume 22, pp. 817–824. Elsevier, 1989.
(cited on p. 69)

Michel J. B. and Colin O.
A tabulated diffusion flame model applied to diesel engine simulations.
International Journal of Engine Research, pp. 346–369, 2013. (cited on pp. 147, 212)

Michel J. B., Colin O. and Veynante D.
Modeling ignition and chemical structure of partially premixed turbulent flames using tabulated chemistry.
Combustion and Flame, Vol. 152 n^o 1, pp. 80–99, 2008.
(cited on pp. 6, 113, 114, 120, 122, 137, 149, 157)

Molina S. A.
Estudio de la influencia de los parámetros de inyección y la recirculación de gases de escape sobre el proceso de combustión, las prestaciones y las emisiones de un motor diésel de 1.8 litros de cilindrada.
Doctoral Thesis, Universitat Politècnica de València, 2003. (cited on p. 87)

Mompó Laborda J. M.
Engineering Large Eddy Simulation of Diesel Sprays.
Doctoral Thesis, Universitat Politècnica de València, 2014. (cited on pp. 47, 235)

Naot D. and Rodi W.
Calculation of secondary currents in channel flow.
Journal of the Hydraulics Division, Vol. 108 n^o 8, pp. 948–968, 1982. (cited on p. 44)

Narayanaswamy K., Pepiot P. and Pitsch H.
A chemical mechanism for low to high temperature oxidation of n-dodecane as a component of transportation fuel surrogates.
Combustion and Flame, Vol. 161 n^o 4, pp. 866–884, 2014. (cited on pp. 171, 236)

Naud B., Novella R., Pastor J. M. and Winklinger J. F.
Comparison of different assumptions for tabulated chemistry based on laminar igniting and extinguishing diffusion flamelets.
In *European Combustion Meeting 2013*, 2013. (cited on pp. 140, 147)

Naud B., Novella R., Pastor J. M. and Winklinger J. F.
RANS modelling of a lifted H2/N2 flame using an unsteady flamelet progress variable approach with presumed PDF.
Combustion and Flame, Vol. 162 n^o 4, pp. 893–906, 2015.
(cited on pp. 104, 139, 140, 147)

Novella R., García A., Pastor J. M. and Domenech V.
The role of detailed chemical kinetics on CFD diesel spray ignition and combustion modelling.
Mathematical and Computer Modelling, Vol. 54 n^o 7, pp. 1706–1719, 2011.
(cited on pp. 80, 169, 187, 246)

Novoselov A. G., Law C. K. and Mueller M. E.
Direct Numerical Simulation of turbulent nonpremixed "cool" flames: applicability of flamelet models.
Proceedings of the Combustion Institute (in press), 2018. (cited on p. 144)

O'Brien E. E.
The probability density function (pdf) approach to reacting turbulent flows.
Springer, 1980. (cited on p. 75)

Okude K., Mori K., Shiino S. and Moriya T.
Premixed compression ignition (PCI) combustion for simultaneous reduction of NOx and soot in diesel engine.
SAE Technical Paper, 2004. (cited on p. 4)

Olsson J. O., Tunestål P. and Johansson B.
Closed-loop control of an HCCI engine.
SAE Technical Paper, 2001. (cited on p. 4)

Panchapakesan N. R. and Lumley J. L.
Turbulence measurements in axisymmetric jets of air and helium. Part 1. Air jet.
Journal of Fluid Mechanics, Vol. 246, pp. 197–223, 1993. (cited on p. 80)

Pao Y. H.
Structure of turbulent velocity and scalar fields at large wavenumbers.
The Physics of Fluids, Vol. 8 n^o 6, pp. 1063–1075, 1965. (cited on p. 31)

Pastor J. V., López J. J., García J. M. and Pastor J. M.
A 1D model for the description of mixing-controlled inert diesel sprays.
Fuel, Vol. 87 n^o 13-14, pp. 2871–2885, 2008. (cited on p. 110)

Payri F., Desantes J. M. and Arrègle J.
Characterization of D.I. diesel sprays in high density conditions.
SAE Technical Paper, 1996. (cited on p. 81)

Payri F., García-Oliver J.M., Novella R. and Pérez-Sánchez E. J.
Influence of the chemical mechanism in the frame of diesel-like CFD reacting spray simulations using a presumed PDF flamelet-based combustion model.
In *ILASS Europe. 28th european conference on liquid atomization and spray systems*, pp. 678–685, 2017. (cited on pp. 169, 177, 183)

Payri F., Novella R., Pastor J. M. and Pérez-Sánchez E. J.
Evaluation of the approximated diffusion flamelet concept using fuels with different chemical complexity.
Applied Mathematical Modelling, Vol. 49, pp. 354–374, 2017. (cited on p. 137)

Payri R., García-Oliver J. M., Xuan T. and Bardi M.
A study on diesel spray tip penetration and radial expansion under reacting conditions.
Applied Thermal Engineering, Vol. 90, pp. 619–629, 2015.
(cited on pp. 83, 168, 169, 183, 185, 238, 242)

Pei Y., Davis M. J., Pickett L. M. and Som S.
Engine combustion network (ECN): global sensitivity analysis of Spray A for different combustion vessels.
Combustion and Flame, Vol. 162 n^o 6, pp. 2337–2347, 2015. (cited on pp. 88, 168, 190)

Pei Y., Hawkes E. R., Bolla M., Kook S., Goldin G. M., Yang Y., Pope S. B. and Som S.
An analysis of the structure of an n-dodecane spray flame using TPDF modelling.
Combustion and Flame, Vol. 168, pp. 420–435, 2016.
(cited on pp. 69, 76, 85, 87, 88, 168, 191, 192, 200)

Pei Y., Hawkes E. R., Kook S., Goldin G. M. and Lu T.
Modelling n-dodecane spray and combustion with the transported probability density function method.
Combustion and Flame, Vol. 162 n^o 5, pp. 2006–2019, 2015. (cited on pp. 76, 168)

Pei Y., Som S., Pomraning E., Senecal P. K., Skeen S. A., Manin J. and Pickett L. M.
Large eddy simulation of a reacting spray flame with multiple realizations under compression ignition engine conditions.
Combustion and Flame, Vol. 162 n^o 12, pp. 4442–4455, 2015.
(cited on pp. 85, 88, 168, 190, 191, 252)

Pera C., Colin O. and Jay S.
Development of a FPI detailed chemistry tabulation methodology for internal combustion engines.
Oil & Gas Science and Technology-Revue de l'IFP, Vol. 64 n^o 3, pp. 243–258, 2009.
(cited on pp. 107, 117, 133, 134, 171)

Peters N.
Laminar diffusion flamelet models in non-premixed turbulent combustion.
Progress in Energy and Combustion Science, Vol. 10 n^o 3, pp. 319–339, 1984.
(cited on pp. 98, 127)

Peters N.
Laminar flamelet concepts in turbulent combustion.
In *Symposium (International) on Combustion*, volume 21, pp. 1231–1250. Elsevier, 1988.
(cited on p. 98)

Peters N.
The turbulent burning velocity for large-scale and small-scale turbulence.
Journal of Fluid mechanics, Vol. 384, pp. 107–132, 1999. (cited on pp. 64, 73)

Peters N.
Turbulent combustion.
Cambridge University Press, 2000. (cited on pp. 15, 60, 63, 66, 67, 68, 70, 71, 73, 75, 84, 88, 98, 101, 104, 105, 107, 111, 127, 128)

Peters N.
Combustion theory.
CEFRC Summer School, Princeton, 2010. (cited on pp. 99, 126)

Peters N. and Williams F. A.
Liftoff characteristics of turbulent jet diffusion flames.
AIAA journal, Vol. 21 n^o 3, pp. 423–429, 1983. (cited on p. 69)

Petzold L. R.
Description of DASSL: a differential/algebraic system solver.
Sandia National Labs., Livermore, CA (USA), 1982. (cited on p. 147)

Phillips H.
Flame in a buoyant methane layer.
In *Symposium (International) on Combustion*, volume 10, pp. 1277–1283. Elsevier, 1965. (cited on p. 69)

Pickett L. M., Bruneaux G. and Payri R.
Engine combustion network.
Sandia National Laboratories, Livermore, CA, https://ecn.sandia.gov/, 2018. (cited on pp. 5, 139, 167, 169, 183, 187, 235)

Pickett L. M., Genzale C. L., Bruneaux G., Malbec L. M., Hermant L., Christiansen C. and Schramm J.
Comparison of diesel spray combustion in different high-temperature, high-pressure facilities.
SAE Int. J. Engines, Vol. 3 n^o 2, pp. 156–181, 2010. (cited on p. 168)

Pickett L. M., Manin J., Genzale C. L., Siebers D. L., Musculus M. P. B. and Idicheria C. A.
Relationship between diesel fuel spray vapor penetration/dispersion and local fuel mixture fraction.
SAE International Journal of Engines, Vol. 4 n^o 2011-01-0686, pp. 764–799, 2011. (cited on pp. 184, 239)

Pickett L. M., Siebers D. L. and Idicheria C. A.
Relationship between ignition processes and the lift-off length of diesel fuel jets.
SAE technical paper, 2005. (cited on pp. 69, 85, 88, 190, 252)

Pierce C. D. and Moin P.
Progress-variable approach for large-eddy simulation of non-premixed turbulent combustion.
Journal of fluid Mechanics, Vol. 504, pp. 73–97, 2004. (cited on p. 108)

Pitsch H.
Large-eddy simulation of turbulent combustion.
Annu. Rev. Fluid Mech., Vol. 38, pp. 453–482, 2006. (cited on pp. 63, 99, 234, 235)

Pitsch H., Chen M. and Peters N.
Unsteady flamelet modeling of turbulent hydrogen-air diffusion flames.
In *Symposium (international) on combustion*, volume 27, pp. 1057–1064. Citeseer, 1998. (cited on p. 128)

Pitsch H. and Peters N.
A consistent flamelet formulation for non-premixed combustion considering differential diffusion effects.
Combustion and Flame, Vol. 114 n^o 1-2, pp. 26–40, 1998. (cited on p. 105)

Poinsot T. and Veynante D.
Theoretical and numerical combustion.
RT Edwards Inc., 2005.
(cited on pp. 15, 17, 18, 60, 68, 76, 100, 101, 106, 107, 127, 133, 206, 234)

Pomraning E. and Rutland C. J.
A dynamic one-equation nonviscosity large-eddy simulation model.
AIAA journal, Vol. 40 n^o 4, pp. 689–701, 2002. (cited on pp. 40, 45, 47, 235)

Pope S. B.
A more general effective-viscosity hypothesis.
Journal of Fluid Mechanics, Vol. 72 n^o 2, pp. 331–340, 1975. (cited on p. 44)

Pope S. B.
An explanation of the turbulent round-jet/plane-jet anomaly.
AIAA journal, Vol. 16 n^o 3, pp. 279–281, 1978. (cited on pp. 43, 80, 169)

Pope S. B.
PDF methods for turbulent reactive flows.
Progress in energy and combustion science, Vol. 11 n^o 2, pp. 119–192, 1985.
(cited on p. 75)

Pope S. B.
Computationally efficient implementation of combustion chemistry using in situ adaptive tabulation.
Combustion theory and modelling, 1997. (cited on p. 76)

Pope S. B.
Turbulent flows.
IOP Publishing, 2001.
(cited on pp. 15, 22, 26, 33, 37, 40, 41, 75, 79, 80, 126, 224, 227, 240)

Pope S. B.
Ten questions concerning the large-eddy simulation of turbulent flows.
New journal of Physics, Vol. 6 n^o 1, pp. 35, 2004. (cited on pp. 38, 63, 99, 234, 241)

Prüfert U., Hartl S., Hunger F., Messig D., Eiermann M. and Hasse C.
A constrained control approach for the automated choice of an optimal progress variable for chemistry tabulation.
Flow, Turbulence and Combustion, Vol. 94 n^o 3, pp. 593–617, 2015. (cited on p. 109)

Richardson L. F.
Weather prediction by numerical process.
Cambridge University Press, 1922. (cited on p. 22)

Ryan T. W. and Callahan T. J.
Homogeneous charge compression ignition of diesel fuel.
SAE Technical Paper, 1996. (cited on p. 4)

Saddoughi S. G. and Veeravalli S. V.
Local isotropy in turbulent boundary layers at high Reynolds number.
Journal of Fluid Mechanics, Vol. 268, pp. 333–372, 1994. (cited on pp. 25, 31)

Saxena P. and Williams F. A.
Testing a small detailed chemical-kinetic mechanism for the combustion of hydrogen and carbon monoxide.
Combustion and Flame, Vol. 145 n^o 1-2, pp. 316–323, 2006. (cited on p. 138)

Schlichting H. and Gersten K.
Boundary-layer theory.
Springer, 2016. (cited on pp. 15, 78)

Schmitz R. A.
A further study of diffusion flame stability.
Combustion and Flame, Vol. 11 n^o 1, pp. 49–62, 1967. (cited on pp. 62, 103)

Semenov N. N.
Thermal Theory of Combustion and Explosion: III. Theory of Normal Flame Propagation.
Technical Memorandums National Advisory Committee for Aeronautics, 1942.
(cited on p. 58)

Senecal P. K., Pomraning E., Richards K. J. and Som S.
An investigation of grid convergence for spray simulations using an LES turbulence model.
SAE Technical Paper, 2013. (cited on pp. 236, 239, 241)

Shen H. P. S., Steinberg J., Vanderover J. and Oehlschlaeger M. A.
A shock tube study of the ignition of n-heptane, n-decane, n-dodecane, and n-tetradecane at elevated pressures.
Energy & Fuels, Vol. 23 n^o 5, pp. 2482–2489, 2009. (cited on p. 52)

Siebers D.
Liquid-phase fuel penetration in Diesel sprays.
SAE Technical paper, 1998. (cited on pp. 83, 85)

Siebers D. L., Higgins B. and Pickett L.
Flame lift-off on direct-injection diesel fuel jets: oxygen concentration effects.
SAE Technical Paper, 2002. (cited on p. 88)

Skeen S., Manin J. and Pickett L. M.
Visualization of ignition processes in high-pressure sprays with multiple injections of n-dodecane.
SAE International Journal of Engines, Vol. 8 n^o 2, pp. 696–715, 2015.
(cited on pp. 175, 191)

Skeen S. A., Manin J. and Pickett L. M.
Simultaneous formaldehyde PLIF and high-speed schlieren imaging for ignition visualization in high-pressure spray flames.
Proceedings of the Combustion Institute, Vol. 35 n^o 3, pp. 3167–3174, 2015.
(cited on pp. 168, 191)

Smith G. P., Golden D. M., Frenklach M., Moriarty N. W., Eiteneer B., Goldenberg M., Bowman C. T., Hanson R. K., Song S., Gardiner Jr. W. C. and others.
GRI mechanism for methane/air, version 3.0.
URL www. me. berkeley. edu/gri_mech, 1999. (cited on p. 138)

Smith T. and Menon S.
Model simulations of freely propagating turbulent premixed flames.
In *Symposium (International) on Combustion*, volume 26, pp. 299–306. Elsevier, 1996.
(cited on p. 75)

Spalart P. R.
Direct simulation of a turbulent boundary layer up to Rθ = 1410.
Journal of Fluid Mechanics, Vol. 187, pp. 61–98, 1988. (cited on p. 33)

Spalart P. R. and Allmaras S. R.
A one-equation turbulence model for aerodynamic flows.
In *30th Aerospace Sciences Meeting and Exhibit*, pp. 439–439, 1992. (cited on p. 43)

Spalding D. B.
Mixing and chemical reaction in steady confined turbulent flames.
In *Symposium (International) on Combustion*, volume 13, pp. 649–657. Elsevier, 1971. (cited on p. 71)

Spalding D. B.
Development of the eddy-break-up model of turbulent combustion.
In *Numerical Prediction of Flow, Heat Transfer, Turbulence and Combustion*, pp. 194–200. Elsevier, 1983. (cited on p. 71)

Speziale C. G.
On nonlinear k-l and k-ε models of turbulence.
Journal of Fluid Mechanics, Vol. 178, pp. 459–475, 1987. (cited on p. 44)

Sreenivasan K. R.
On the universality of the Kolmogorov constant.
Physics of Fluids, Vol. 7 n^o 11, pp. 2778–2784, 1995. (cited on p. 25)

Subramaniam S.
Lagrangian-Eulerian methods for multiphase flows.
Progress in Energy and Combustion Science, Vol. 39 n^o 2-3, pp. 215–245, 2013. (cited on p. 82)

Tagliante F., Malbec L. M., Bruneaux G., Pickett L. M. and Angelberger C.
Experimental study of the stabilization mechanism of a lifted Diesel-type flame using combined optical diagnostics and laser-induced plasma ignition.
Combustion and Flame, Vol. 197, pp. 215–226, 2018. (cited on p. 88)

Tavoularis S. and Corrsin S.
Experiments in nearly homogenous turbulent shear flow with a uniform mean temperature gradient. Part 1.
Journal of Fluid Mechanics, Vol. 104, pp. 311–347, 1981. (cited on p. 41)

Tennekes H. and Lumley J. L.
A first course in turbulence.
MIT press, 1972. (cited on pp. 15, 20, 29, 31, 80, 227, 240)

Tillou J., Michel J. B., Angelberger C., Bekdemir C. and Veynante D.
Large-Eddy Simulation of Diesel Spray Combustion with Exhaust Gas Recirculation.
Oil & Gas Science and Technology-Revue de l'IFP, Vol. 69 n^o 1, pp. 155–165, 2014. (cited on pp. 6, 98)

Tillou J., Michel J. B., Angelberger C. and Veynante D.
Assessing LES models based on tabulated chemistry for the simulation of diesel spray combustion.
Combustion and Flame, Vol. 161 n^o 2, pp. 525–540, 2014. (cited on p. 149)

CMT Motores Térmicos.
Universitat Politècnica de València, Spain.
http://www.cmt.upv.es/ECN03.aspx, 2018. (cited on p. 169)

Vallet A. and Borghi R.
Modélisation Eulerienne de l'atomisation d'un jet liquide.
Comptes Rendus de l'Académie des Sciences-Series IIB-Mechanics-Physics-Astronomy, Vol. 327 n^o 10, pp. 1015–1020, 1999. (cited on p. 82)

van Oijen J. A. and de Goey L. P. H.
Modelling of premixed laminar flames using flamelet-generated manifolds.
Combustion Science and Technology, Vol. 161 n^o 1, pp. 113–137, 2000.
(cited on pp. 76, 105, 107)

Vanquickenborne L. and Van Tiggelen A.
The stabilization mechanism of lifted diffusion flames.
Combustion and Flame, Vol. 10 n^o 1, pp. 59–69, 1966. (cited on p. 68)

Vasu S. S., Davidson D. F., Hong Z., Vasudevan V. and Hanson R. K.
n-Dodecane oxidation at high-pressures: measurements of ignition delay times and OH concentration time-histories.
Proceedings of the Combustion Institute, Vol. 32 n^o 1, pp. 173–180, 2009.
(cited on p. 172)

Venugopal R. and Abraham J.
A review of fundamental studies relevant to flame lift-off in diesel jets.
SAE technical paper, 2007. (cited on p. 68)

Versteeg H. K. and Malalasekera W.
An introduction to computational fluid dynamics: the finite volume method.
Pearson Education, 2007. (cited on pp. 15, 20, 26, 33, 40, 42, 44)

Veynante D. and Vervisch L.
Turbulent combustion modeling.
Progress in Energy and Combustion Science, Vol. 28 n^o 3, pp. 193–266, 2002.
(cited on p. 58)

Wang H., Ra Y., Jia M. and Reitz R. D.
Development of a reduced n-dodecane-PAH mechanism and its application for n-dodecane soot predictions.
Fuel, Vol. 136, pp. 25–36, 2014. (cited on p. 171)

Wilcox D. C.
Reassessment of the scale-determining equation for advanced turbulence models.
AIAA journal, Vol. 26 n^o 11, pp. 1299–1310, 1988. (cited on p. 43)

Williams F. A.
Recent advances in theoretical descriptions of turbulent diffusion flames.
Springer, 1975. (cited on pp. 71, 98)

Williams F. A.
Combustion theory.
Benjamin Cummings, Menlo Park, CA, 1985. (cited on p. 17)

Winklinger J. F.
Implementation of a combustion model based on the flamelet concept and its application to turbulent reactive sprays.
Doctoral Thesis, Universitat Politècnica de València, 2015. (cited on pp. 98, 187)

Wohl K., Kapp N. M. and Gazley C.
The stability of open flames.
In *Symposium on Combustion and Flame, and Explosion Phenomena*, volume 3, pp. 3–21.
Elsevier, 1948. (cited on p. 68)

Xue Q., Som S., Senecal P. K. and Pomraning E.
A Study of Grid Resolution and SGS Models for LES Under Non-Reacting Spray Conditions.
In *25th Annual Conference on Liquid Atomization and Spray Systems, Pittsburgh, PA*, 2013.
(cited on pp. 236, 239, 241)

Yakhot V., Orszag S. A., Thangam S., Gatski T. B. and Speziale C. G.
Development of turbulence models for shear flows by a double expansion technique.
Physics of Fluids A: Fluid Dynamics, Vol. 4 n^o 7, pp. 1510–1520, 1992. (cited on p. 44)

Yang B. and Pope S. B.
Treating chemistry in combustion with detailed mechanisms— In situ adaptive tabulation in principal directions— Premixed combustion.
Combustion and Flame, Vol. 112 n^o 1-2, pp. 85–112, 1998. (cited on p. 76)

Yao T., Pei Y., Zhong B. J., Som S. and Lu T.
A hybrid mechanism for n-dodecane combustion with optimized low-temperature chemistry.
In *9th US National Combustion Meeting, Cincinnati, Ohio*, pp. 17–20, 2015.
(cited on p. 171)

Yoshizawa A. and Horiuti K.
A statistically-derived subgrid-scale kinetic energy model for the large-eddy simulation of turbulent flows.
Journal of the Physical Society of Japan, Vol. 54 n^o 8, pp. 2834–2839, 1985.
(cited on p. 46)

Zeldovich Y. B.
Acta Physicochim.
USSR, Vol. 21, pp. 577, 1946. (cited on p. 54)

Zeuch T., Moréac G., Ahmed S. S. and Mauss F.
A comprehensive skeletal mechanism for the oxidation of n-heptane generated by chemistry-guided reduction.
Combustion and Flame, Vol. 155 n^o 4, pp. 651–674, 2008. (cited on p. 138)